Developments and Numerical Simulations for the Electron-Proton-Telescope Onboard Solar Orbiter

Dissertation
zur Erlangung des Doktorgrades
der Mathematisch-Naturwissenschaftlichen Fakultät
der Christian-Albrechts-Universität zu Kiel

vorgelegt von
Rolf Paspirgilis

Kiel im November 2012

Erster Gutachter : Prof. Dr. Robert F. Wimmer-Schweingruber

Zweiter Gutachter : Prof. Dr. Sebastian Wolf

Tag der mündlichen Prüfung : 17.12.2012

Zum Druck genehmigt : 17.12.2012

---

gez. Prof. Dr. Wolfgang J. Duschl, Dekan

Abstract

The Solar Orbiter spacecraft is an ESA M-class mission that is designated to launch in 2017 to reach an orbit around the sun. At its perihelion, Solar Orbiter will be as close to the sun as 0.28 AU and will nearly co-rotate for almost a complete solar rotation. During its journey, Solar Orbiter will also leave the ecliptic plane to examine higher latitudes of the sun including the polar regions. The spacecraft will be equipped with a unprecedented combination of in-situ and remote sensing instruments enabling us to get a full insight into the physical processes on the sun and in the heliosphere at very close distances where the pristine properties of the solar wind and solar energetic particle events have not yet been smeared out by acceleration and transport processes.

As a part of the Energetic Particle Detector (EPD), the Electron Proton Telescope (EPT) will measure the electron and proton intensities in an energy range from 20 keV to 400 keV for electrons and from 20 keV to 7 MeV for protons. EPT is the successor of the Solar Electron Proton Telescope (SEPT) of the STEREO mission at 1 AU. From SEPT EPT inherits the design as a two double-ended telescope and the magnet/foil-technique to separate electrons from protons before they reach one of the two silicon detectors inside the aluminum housing.

Although EPT is derived from SEPT, there are still some modifications to be made to adapt the instrument to the much different solar environment at 0.28 AU. This will be the scope of this work. For this, we will consider a strong SEP event measured at 1 AU and extrapolate the intensities to 0.28 AU and examine how the instrument must be designed to withstand even such high intensities.

We will further use GEANT4 simulations to see how the mechanical design must be changed to reduce the background noise from scattering electrons and from relativistic protons from the galactic cosmic radiation.

In addition, we will determine the setup of the rescaled magnet system that is employed to deflect electrons away from the detector that should only detect protons. And since EPT is accompanied by the magnetometer instrument MAG onboard Solar Orbiter, we must prove that the magnetic far field of the two EPT magnet systems does not disturb the functionality of MAG. We do this by measuring the near field of the magnet systems and extrapolating the field to the MAG positions.

Finally, we will demonstrate the functionality of our instrument (including the particle separation technique) by performing first measurements with an EPT demo model using a radioactive ^{207}Bi electron source.

Zusammenfassung

Solar Orbiter ist eine ESA-Mission der Klasse M, bei der im Jahr 2017 eine Raumsonde auf einen Orbit um die Sonne geschossen werden soll. An ihrem Perihel wird sich diese Sonde der Sonne bis auf 0,28 AU nähern und dabei für etwa eine Sonnenrotationsdauer synchron mit der Sonne rotieren. Im weiteren Orbit wird Solar Orbiter die Ekliptikebene verlassen um höhere Breiten inklusive der Polregionen der Sonne zu beobachten. An Bord der Sonde werden sich In-Situ- und Fernerkundungsinstrumente befinden, die in dieser Kombination noch nie auf einem Satelliten unser Zentralgestirn in solcher Nähe beobachtet haben. Der Vorteil der großen Nähe zur Sonne ergibt sich dadurch, dass die interessanten ursprünglichen Eigenschaften des Sonnenwinds und der Teilchenereignisse noch nicht durch Transport- und Beschleunigungsprozesse verfälscht und verwischt worden sind.

Als Teil des Energetic Particle Detectors (EPD) wird das Electron Proton Telescope (EPT) die Teilchenflüsse von Elektronen und Protonen im Energiebereich von 20 keV bis 400 keV für Elektronen und von 20 keV bis 7 MeV für Protonen messen. EPT ist der Nachfolger des Solar Electron Proton Telescopes (SEPT), welches an Bord der STEREO-Mission bei 1 AU Elektronen- und Protonenintensitäten misst. EPT übernimmt dabei von SEPT das grundlegende Design als Instrumentenduo zweier Doppelteleskope, die in beide antiparallele Richtungen schauen. Zudem erbt EPT von SEPT die Technik der Magnet-/Folienkombination zur Separation der Teilchenarten bevor die Teilchen einen der zwei Siliziumdetektoren im Inneren des Aluminiumgehäuses treffen.

Trotz der Anlehnung an SEPT müssen an EPT Modifikationen vorgenommen werden, um das Instrument an die schärferen Bedingungen bei 0.28 AU anzupassen. Dies wird das Thema dieser Arbeit sein. Dazu nehmen wir uns Messungen eines starken SEP-Ereignisses bei 1 AU und extrapolieren diese auf 0.28 AU, um zu sehen, wie wir das Instrument neu skalieren müssen, damit die Verarbeitungselektronik ein solch großes aber auch interessantes Ereignis auflösen und messen kann.

Des Weiteren werden wir GEANT4-Simulation benutzen, um heraus zu finden, wie wir das mechanische Design des Instruments anpassen müssen, um das Hintergrundrauschen, das von streuenden Elektronen und von relativistischen Protonen der kosmischen Hintergrundstrahlung verursacht wird, minimieren können.

Ferner werden wir die Zusammensetzung des Magnetsystems, welches zur Ablenkung von Elektronen benutzt wird, berechnen und die Magnetfelder der fertigen Systeme ausmessen. Da EPT an Bord von Solar Orbiter von dem Magnetometerinstrument MAG begleitet wird, stehen wir in der Pflicht, zu beweisen, dass die Felder der beiden Magnetsysteme von EPT1 und EPT2 die Messungen von MAG nicht negativ beeinträchtigen. Wir tun dies, indem wir Messungen der Nahfelder der Systeme durchführen, die wir dann auf die Position des Magnetometers extrapolieren.

Schließlich werden wir die Funktionalität des Instruments (inklusive der Teilchenseparation) demonstrieren, indem wir mittels eines radioaktiven ^{207}Bi-Präparats als Elektronenquelle erste Messungen durchühren.

Contents

1. Introduction

1.1. The ESA Mission Solar Orbiter

The ESA M-class mission Solar Orbiter is a project to launch a probe that is designed to observe the sun and it's coupling to the heliosphere. The launch of the Solar Orbiter spacecraft from Cape Canaveral is planned for 2017 at the top of an Atlas V rocket provided by the NASA. The computed orbit will take the spacecraft to very close distances to our central star. At its perihelion, Solar Orbiter will be only 0.28 AU away from the sun nearly co-rotating with the star for almost a complete solar rotation. Furthermore, the probe will also leave the ecliptical plane increasing its inclination up to 25° (nominal mission; extended mission: 34°- 36°) to make observations of higher latitudes of the sun including the poles. The mission duration is set to be 7 years for nominal mission including the cruise phase with a possible extended mission time of 3 years.

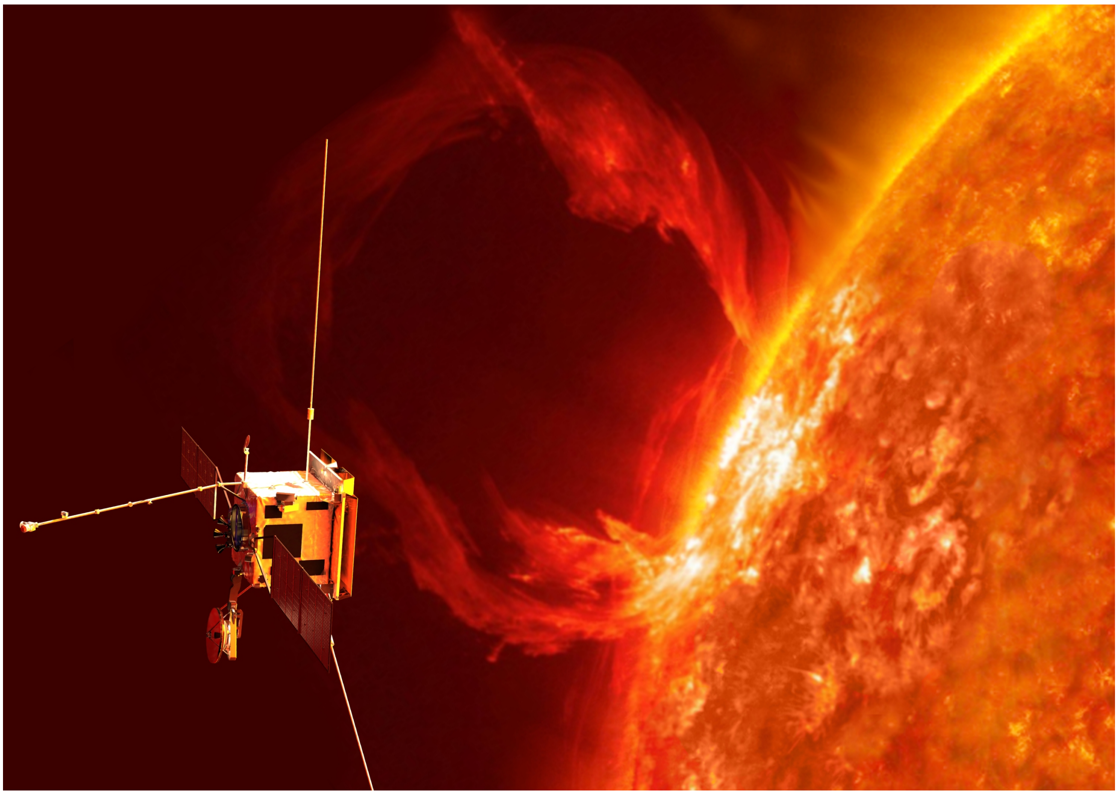

Figure 1.1.: An illustration of the Solar Orbiter spacecraft observing the sun. (Taken from: `http://sci.esa.int/solarorbiter`)

The big benefit of an orbit this close to the sun is that the primordial physical conditions smear out with growing distances which makes it harder to analyze the ongoing processes. The probes Helios-1 and especially Helios-2 also approached the sun very close (0.3 AU and 0.29 AU), but did not carry the unique and varied ensemble of both in-situ and remote sensing instruments as Solar Orbiter will (Porsche 1977). Using the latest advanced detector technology with Solar Orbiter, we will have the ability to carry out remote and in-situ measurements of the plasma, the electromagnetic fields, the energetic particles and the waves in the heliosphere at locations where their properties and distributions are still pristine and not yet stirred up by mutual interactions in an unprecedented way.

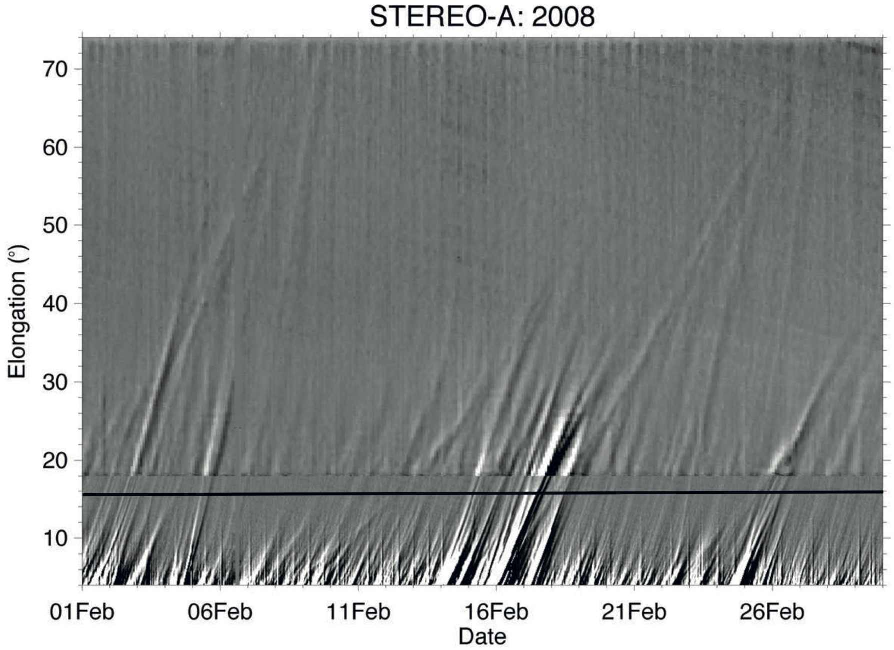

Figure 1.2.: This image from the Heliospheric Imager onboard STEREO-A shows structures in the solar wind that are flowing away from the sun to higher elongations. One can see that structures with a higher velocity (a steeper incline) collide with slower structures and interfere with them. As a result, the flows are blurred and lose the information about their relative origins. The black line depicts the closest elongation where Solar Orbiter will travel. We see that it becomes possible to regain this information and to measure the physical properties of the unmixed structures. (Courtesy J. Davies, Rutherford Appleton Laboratory, UK, Taken from Mueller et al. (2012))

Of course, there have been missions that covered the link between the sun and the heliosphere like:

- Helios (Start: 1974)
- Ulysses (1990)
- Yohkoh (1991)
- SOHO (1995)

- TRACE (1998)
- RHESSI (2002)
- Hinode (2006)
- STEREO (2006)

Each of these missions was extremely successful in achieving deeper insights into the heliosphere. But none of them showed the unique instrumental combination of both in-situ and remote detectors or covered a comparable wide range of energies and frequencies or approached the sun so close as Solar Orbiter will.

1.1.1. Mission Objectives

The main question that is to be answered by the mission is: **How does the sun create and control the heliosphere?** This can be broken down into four more detailed questions (Mueller et al. 2012):

How and where do the solar wind plasma and magnetic field originate in the corona?

The sun fills the heliosphere with two kinds of solar wind: the *slow* (≈300 - 500 km/s) and the *fast* (≈700 km/s) solar wind. Both types differ in mass flux and composition. While the sources of the fast wind are reckoned to be coronal holes from where the wind travels along open magnetic field lines into the heliosphere, the slow solar wind originates from a region around the solar equator and expands out along closed field lines. The escape mechanism that unleashes the slow solar wind is still unknown and can not be determined as long as the exact initial points and physical processes can not be analyzed from 1 AU. Additionally, the turbulent fluctuations engulfed in the solar winds carry the physical footprints of their origins with them. These fluctuations are suspected to be the causes of the differences in the heating and acceleration processes between different solar wind streams.

How do solar transients drive heliospheric variability?

Coronal Mass Ejections (CMEs) are big transient events containing hot plasma and turbulent magnetic fields and are cast away from the sun at velocities up to 2000 km/s. When traveling through the solar system, a CME becomes a so-called *Interplanetary* CME (ICME). When such an ICME hits the earth it can have a crucial impact on the geomagnetic field and can cause geomagnetic storms which are dangerous to the international communication network and the complicated power grids. In order to predict whether these kinds of events become perilous for earth, it is important to understand the evolution of CMEs during their journey through interplanetary space.

How do solar eruptions produce energetic particle radiation that fills the heliosphere?

As we will see later (in section 2.3), several processes exist that can accelerate particles to very high energies. Unfortunately, at 1 AU it becomes difficult to examine the multiple processes that play a role in impelling charged particles since the accelerated ions get scattered by inhomogeneities in the interplanetary magnetic field. This scattering destroys much of the information carried by the particle distribution about the acceleration processes that take place closer to the sun.

How does the solar dynamo work and drive connections between the Sun and the heliosphere?

The large-scale solar magnetic field is produced by a huge dynamo inside the convection zone of the sun and permeates the heliosphere and influences the interplanetary space. This field is also dominated by the 11-year cycle with which the solar activity varies. To better understand the solar magnetism and its variation, we need to observe the transport of fluxes at high latitudes and to examine the physical properties of the poles' magnetic field in more detail.

To answer all these questions, one must observe the concerning properties simultaneously with combined in-situ and remote measurements covering a wide range of energies (when measuring energetic particles) and frequencies (measurements of fields, imaging, spectroscopy). But most important is the close proximity to the target. It is known that at 1 AU most of the interesting structures and activities already are mixed up and that their origins cannot be retraced anymore (see fig. 1).

1.1.2. Instruments Onboard Solar Orbiter

To answer all the scientific questions with which Solar Orbiter will be sent on its journey around the sun, it carries an unprecedented array of in-situ and remote sensing instruments. We will now briefly introduce these instruments.

In-situ Sensing Instruments

RPW: Radio and Plasma Waves (Plettemeier et al. 2009): This instrument consists of three monopole antennas that are deployed from two corners and one side of the spacecraft. After deployment, the antennas span a plane that is perpendicular to the sun-spacecraft axis. In this plane the antennas are equally aligned with an angle of 120° to each other. Also with RPW comes a fluxgate magnetometer which is located on the instrument boom behind Solar Orbiter. With this setup, RPW will be able to measure magnetic and electric fields including the concerning waves in the solar wind with a high time resolution from almost DC to 20 Mhz. RPW could as well be listed among the remote sensing instruments, since it is also able to remotely detect solar radio emissions.

SWA: Solar Wind Plasma Analyser (Bruno et al. 2009): This instrument will portray the solar wind between 0.23 AU and 1.4 AU in order to explore the link between the sun's atmosphere and the solar wind during both quiet and disturbed phases. SWA will measure the three-dimensional velocity distributions of the main particle types in the solar wind (protons, alpha particles and electrons). Also determined will be the densities, the temperatures and the heat flux vectors of the solar wind constituents to identify the fluid and kinetic properties of the solar wind.

MAG: Magnetometer (Carr et al. 2006): The two magnetometers MAG IBS (Magnetometer Inboard Sensor) and MAG OBS (Magnetometer Outboard Sensor) are two digital fluxgate sensors mounted on the instrument boom of Solar Orbiter that are designed to measure the heliospheric magnetic field in order to investigate how the solar magnetic field reaches into spaces and varies over the solar cycle. Also of interest are the generation and dissipation of magnetic waves and turbulences and the development of heliospheric structures in the inner solar system. MAG IBS is mounted on the boom closer to the spacecraft than MAG OBS to detect possible magnetic disturbances originating in the spacecraft itself. These disturbances can then be removed in the data analyzation process.

EPD: Energetic Particle Detector (Wimmer-Schweingruber et al. 2010): This detector suite contains 5 instruments that are designed to measure the composition, timing, and distribution functions of suprathermal and energetic particles. EPT is one of the 5 sensors of EPD. We will later (in section 1.2) introduce EPD in more detail.

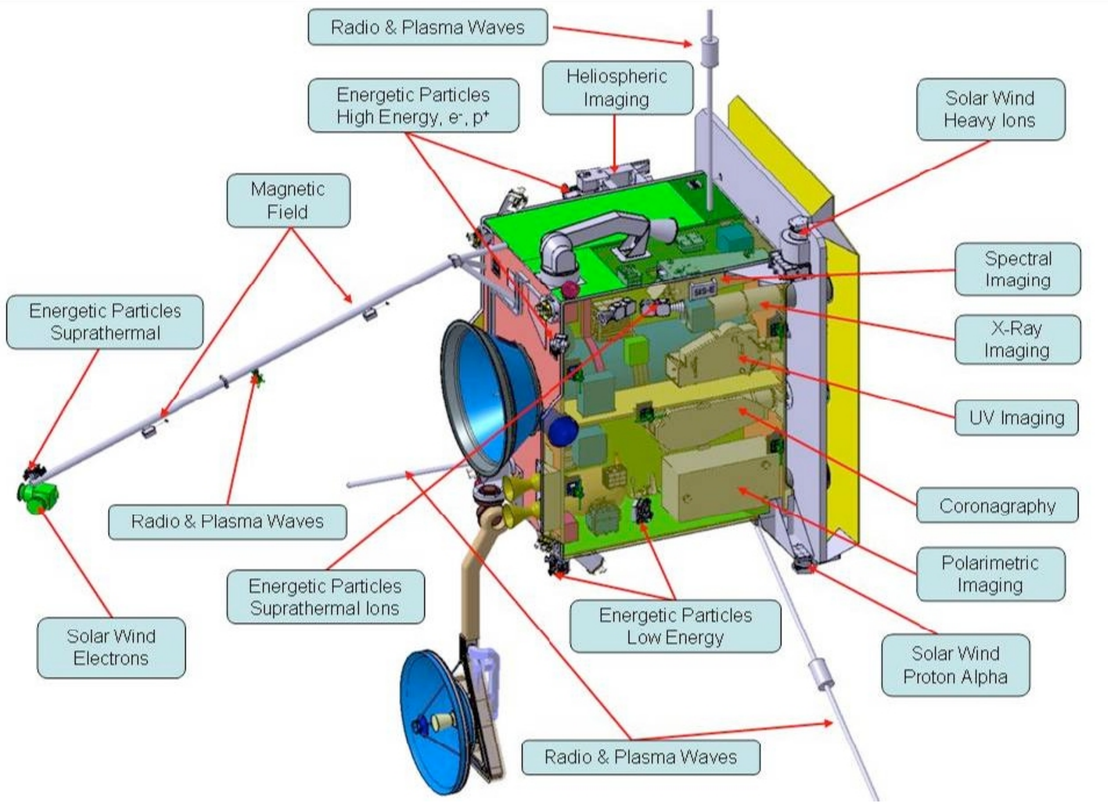

Figure 1.3.: The various instruments onboard Solar Orbiter. (Picture taken from Solar Orbiter website (`http://sci.esa.int/solarorbiter`))

Remote Sensing Instruments

PHI: Polarimetric and Helioseismic Imager (Gandorfer et al. 2011): The PHI will measure the vector magnetic field and the line-of-sight velocity of the photosphere to allow for an investigation of the solar convection zone. The continuum intensity in the visible wavelength will also be determined.

EUI: Extreme Ultraviolet Imager (Hochedez et al. 2006): EUI will take images of the solar atmospheric layers above the photosphere to examine the link between the solar surface and the corona. It will also deliver the first images of the sun from out of the ecliptic ever. The aim is to investigate the fine-scale processes in the solar atmosphere and the low atmosphere analogues of large-scale eruptive events like CMEs.

SPICE: Spectral Imaging of the Coronal Environment (Hassler et al. 2011): SPICE is an EUV imaging spectrograph that will observe the solar disk and the corona to determine the plasma properties at the sun and its vicinity. Its main tasks are to find correlations between solar wind streams and their origins on the solar surface, to examine the processes that inject plasma from closed structures into the solar wind and to image the suprathermal ions that are suspect to be the seed populations of SEPs.

STIX: Spectrometer/Telescope for Imaging X-rays (Hurford et al. 2010): This contribution to Solar Orbiter is responsible for the imaging spectroscopy of thermal and non-thermal x-ray emission in the energy range from 4 keV to 150 keV. STIX will determine the timing, location, intensity, and spectra of accelerated electrons and the high temperature plasma that is mostly found in flares and micro flares.

METIS: Multi Element Telescope for Imaging and Spectroscopy (Schuehle 2012): To examine the structure of the corona and the processes inside, METIS is designed as a coronograph to take polarized broad-band images of the visible K-corona and narrow-band images of the UV- and the EUV-corona.

SoloHI: Solar Orbiter Heliospheric Imager (Howard et al. 2010): SoloHI will detect the visible sunlight that is scattered by electrons and thus is designed to observe the quasi-steady flow and transient disturbances in the solar wind. This allows for a detailed analysis of the SEP acceleration processes by imaging CMEs and CME-driven shocks. Furthermore, the development of CMEs and corotating interaction regions (CIRs) in the heliosphere is investigated as well as the development and origins of the solar wind by measuring the solar wind's structure and turbulences. Last, but not least, SoloHi will provide context for the other in-situ and remote sensing instruments.

1.2. The EPD Instrument Suite Onboard Solar Orbiter

The EPD instrument suite onboard Solar Orbiter consists of 5 different sensors (EPT, HET, STEIN, SIS, LET) that combine their measurements to examine particle acceleration, transport and distributions near the sun over a wide energy range (from 2 keV up to 200 MeV/nucleon) and for various particle types (electrons, protons and ions from helium to iron).

The energy coverage for the different particle types is as follows:

- 0.002 MeV to 20 MeV for electrons
- 0.003 MeV to 100 MeV for protons
- 0.008 MeV/nuc to 200 MeV/nuc for heavy ions (species-dependent)

The individual energy ranges of each sensor of EPD are shown in fig. 1.4.

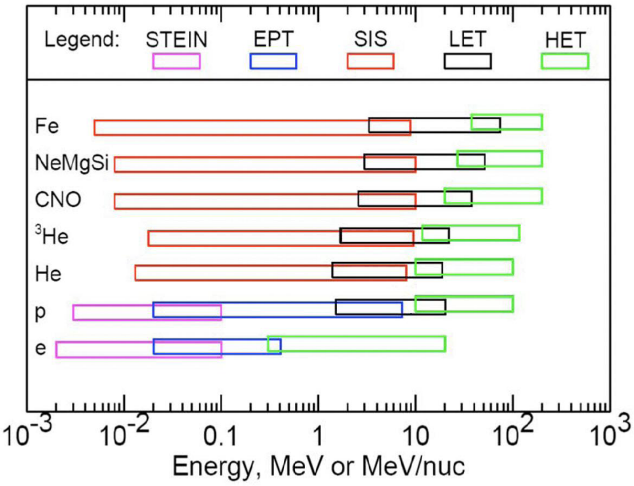

Figure 1.4.: Energy coverage of EPD arranged by instruments and particle types. Marked in blue is the energy range of EPT. (Taken from Rodriguez-Pacheco, 2011)

The scientific objectives that are especially targeted by EPD are the acceleration and transportation processes of energetic particles and their origins. Also examined will be the magnetic connectivity by using the suprathermal particles as field line tracers. Furthermore, EPD will analyze the radial evolution of CME-driven shocks and associated particle populations.

The sensor heads of EPD are distributed at different locations on the spacecraft covering various fields of view (see fig. 1.5). Multiple viewing directions of single instruments enable us to determine the pitch angle distribution of the particles.

1.2.1. The Single Instruments of EPD

We will now briefly introduce the 5 separate sensors of EPD including EPT which we will also describe later in more detail.

STEIN (SupraThermal Electrons Ions and Neutrals Telescope): STEIN is designed to measure suprathermal particles from 3 keV to 100 keV coming from two antiparallel directions using passively cooled silicon semiconductor detectors. An electrostatic deflection system enables STEIN to distinguish between the electrons and ions up to 100 keV and neutrals up to 40 keV. STEIN is mounted on the spacecraft's instrument boom.

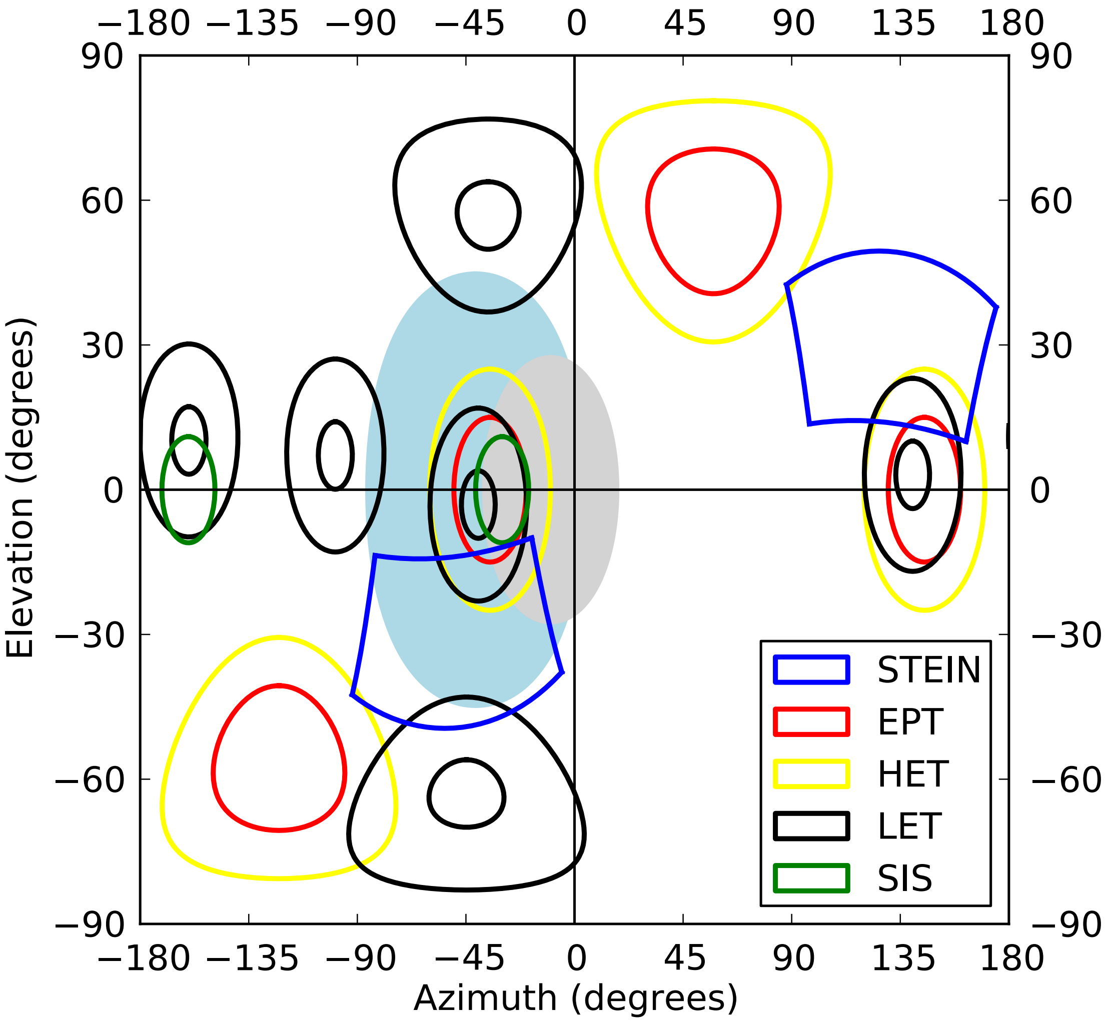

Figure 1.5.: EPD fields of view distribution (by Christoph Terasa). The origin of this plot represents the direction of the sun as seen from the Solar Orbiter spacecraft. The red loops show the fields of view of the two EPT instruments. The light blue ellipse represents the area of the expected direction of the Parker spiral at 0.8 AU whereas the grey ellipse depicts the Parker spiral at 0.3 AU.

SIS (Suprathermal Ion Spectrograph): The two telescopes of SIS will measure the composition of heavy ions from helium to iron in the energy range of 8 keV/nucleon to 10 MeV/nucleon. Below 1 MeV/nuc SIS is also able to detect ions with $Z > 26$ in ^{3}He-rich solar flare events.

LET (Low Energy Telescope): These two telescopes measure the abundances of elements from H to Ni ($1 \leq Z \leq 28$) in the energy range from 1.5 MeV/nuc to 60 MeV/nuc. In addition, LET can separate ^{3}He from ^{4}He down to levels of approx. 1% and it can also resolve Ne and Mg isotopes. The broad dynamic range of LET will provide us with the ability to detect trans-Fe elements with $30 \leq Z \leq 83$ that are often highly enriched in impulsive SEP events.

HET (High-Energy Telescope): The neighbor of EPT onboard Solar Orbiter will measure electrons (300 keV - 20 MeV), protons (10 MeV - 100 MeV), and heavy ions (20 MeV/nuc - 200 MeV/nuc). The instrument is designed similar to EPT as two double-ended telescopes one pointing sun/anti-sunward, the other out of the ecliptic. Inside one sensor head, an array of solid state detectors and a high-density calorimeter scintillator use the dE/dx vs. total E technique for particle identification and energy measurement.

EPT (Electron Proton Telescope): EPT measures electrons and protons in the range from 20 keV to 400 keV (electrons) and from 20 keV to 7 MeV (protons) and thus covers the energy gap between STEIN and LET concerning protons and the gap between STEIN and HET concerning electrons. A more detailed introduction into EPT will be given in section 1.2.3.

1.2.2. Scientific Objectives of EPD

The deployment of EPD onboard Solar Orbiter aims for the answer to the Solar Orbiter objective number three **"How do solar eruptions produce energetic particle radiation that fills the heliosphere?"** (see section 1.1.1) which can be broken down to the following two questions:

1. **What are the sources of energetic particles and how are they accelerated to high energies?**
2. **How are solar energetic particles released from their sources and distributed in time?**

These questions ask for detailed measurements of SEP sources, acceleration mechanisms, seed populations, and distributions in space and time.

The sources can be flaring loops, CMEs and impulsive processes from which the energetic particles are accelerated by Fermi acceleration at shock waves, by stochastic acceleration, by wave-particle interactions or by direct accelerations in electric fields (Aschwanden 2006; Grupen 2005). The particles that are energized in these ways can be hot material in solar magnetic loops, heated solar wind or suprathermal ions from various sources. The observation of the evolution in space and time of the energetic particles could lead to a more detailed description of the transport and acceleration processes in the solar atmosphere and heliosphere which could yield a better forecast of the behavior of SEP events.

Together with in-situ measurements of the magnetic field and the plasma environment near the sun, EPD will provide us with a closer look at the large-scale structure of the coronal magnetic fields and the three dimensional anatomy of MHD turbulence. As we will later see in section 2.2.1 , the paths of charged particles along magnetic field lines is affected by adiabatic cooling of the plasma as it thins out into space and by pitch angle scattering off the small scale irregularities. As we will see in eqn. (2.10), one important parameter of this motion is the diffusion coefficient $D_{\mu\mu}$, that can be determined from the particle's scattering mean free path if the power spectrum of the turbulence is known. In co-operation with MAG and RPW EPD will be able to map the power spectrum of the magnetic turbulences with respect to the heliocentric distance.

1.2.3. EPT as a Part of EPD

This work focuses on the Electron Proton Telescope (EPT). EPT is a heritage of the Solar Electron Proton Telescope (SEPT) that is already flying successfully onboard the two STEREO probes at 1 AU around the sun and measures the proton and electron fluxes there. Like SEPT, EPT is a two-sided double-ended telescope that uses the magnet/foil-technique to cleanly separate electrons from protons before the are detected in two solid state detectors.

As a part of the EPD suite, EPT covers the energy gap between STEIN and LET concerning protons and the gap between STEIN and HET concerning electrons (see fig. 1.4). With its high energy and time resolution EPT is optimized to deliver important measurements that will help to describe the acceleration and transport processes of energetic particles.

The setup of two dual double-ended telescopes EPT1 and EPT2 enables us to determine possible particle anisotropies. For this, EPT1 points in the orbital plane approximately along the Parker spiral towards and away from the sun while EPT2 looks into the direction perpendicular to that plane in the north and south direction.

A detailed description of the EPT and its functionality can be found in section 3.

2. Transport and Acceleration Processes

Before we deal with EPT, we want to discuss the main transport and acceleration processes in the heliosphere.

2.1. The Trajectories of Particles in a Magnetic Field

Before coming to the transportation and acceleration processes, we need to discuss the movement of charged particles in magnetic fields. The knowledge gained here will be important in the later discussions in section 2.2 and in section 2.3.

We will only treat this topic sketchily but detailed enough for the understanding of the transport and acceleration processes. Deeper insights into the propagation of charged particles in magnetic fields are offered in any good textbook about plasma physics such as Chen et al. 1985.

2.1.1. A Particle's Trajectory Along a Magnetic Field Line

The Lorentz force acting on a charged particle in a magnetic field forces the particle on a helical path around a field line as seen on the left side of fig. 2.1. As long as the field is constant (direction and magnitude) the shape of the helical path also stays the same. Especially the Larmor radius r_L (the radius of the perpendicular motion around the field line) and the pitch angle φ (the angle between the two components of the particle's velocity $\varphi = \sphericalangle \left(v_\parallel, v_\perp\right)$) stay constant. r_L is directly dependent on the magnetic field:

$$r_L = \frac{mv_\perp}{qB} \tag{2.1}$$

where m is the mass of the particle, $v_\perp$ its velocity perpendicular to the magnetic field, q the particle's charge and B is the magnetic flux density. As long as the magnetic field line does not change significantly the particle will follow its original field line and will not drift away from it.

The situation changes when the field line varies due to waves in the magnetic field (see right side of fig. 2.1). The wave is described by the wave frequency ω and the wave vector $\vec{k}$. A particle with the velocity $\vec{v}$ and the gyration frequency Ω can interact with the wave when the following condition is fulfilled (Tsurutani et al. 1997):

$$\omega - \vec{k} \cdot \vec{v} = n\Omega \tag{2.2}$$

where $n \in \mathbb{Z}$. The interaction can change the two velocity components $v_\parallel$ and $v_\perp$ which changes the Larmor radius and the pitch angle. This process can affect an exchange of energy and momentum between a wave and a particle in the solar wind frame.

When the particle travels through a region with significant magnetic turbulence, poorly understood processes can lead a charged particle to apparently jump to another

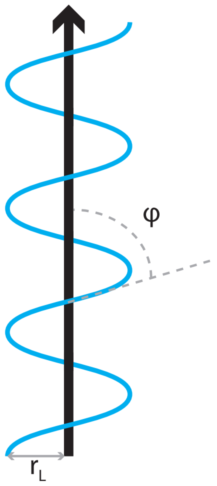

Figure 2.1.: The particle on the left follows the black magnetic field line on a helical path with the pitch angle φ and the Larmor radius r_L. Since the field is constant both the Larmor radius and the pitch angle are too. The situation on the right is different: Here the field shows minor turbulences. These variations have a direct influence on the Larmor radius and the pitch angle.

field line, so that this particle appears to perform a random walk across field lines in the turbulent region.

2.1.2. Magnetic Mirror

As we saw in section 2.1.1, a charged particle stays on its helical path around a magnetic field line as long as the field shows no relevant variations. The effect we want to discuss now occurs when the magnetic field increases along the particle's movement parallel to the magnetic field. Fig. 2.2 shows this configuration. There, we see two charged particles (red and blue) with different pitch angles (φ_m and φ_e) but with a common movement of a downward spiral towards the bottom of the figure.

At the top, the field lines are parallel arranged and there is no component perpendicular to the particle's downward movement: $B_\perp = 0$. With growing density towards the bottom, the field lines also begin to show a curvature and with this a non-zero magnetic field in the perpendicular direction: $B_\perp \neq 0$. With increasing $B_\perp$, a Lorentz force begins to build up that points into the opposite direction of the particle's movement downwards and thus decelerates the particle and can even invert the particle movement upwards. The pitch angle of the particle's path determines whether the particle will be reflected by the magnetic mirror or not. Here, the initial pitch angle of the particle on the blue path is too high to escape the mirror so that the particle is reflected. The particle following the red path on the other hand can penetrate the mirror since it's pitch angle is low enough. When B_M is the maximum magnetic field at the end of the mirror, B_0 is the field at the starting point of the particle's path and φ_0 the pitch angle of the path at this point, the particle can penetrate the magnetic mirror when the following condition is fulfilled:

$$\sin \varphi_0 < \sqrt{\frac{B_0}{B_\mathrm{M}}} \tag{2.3}$$

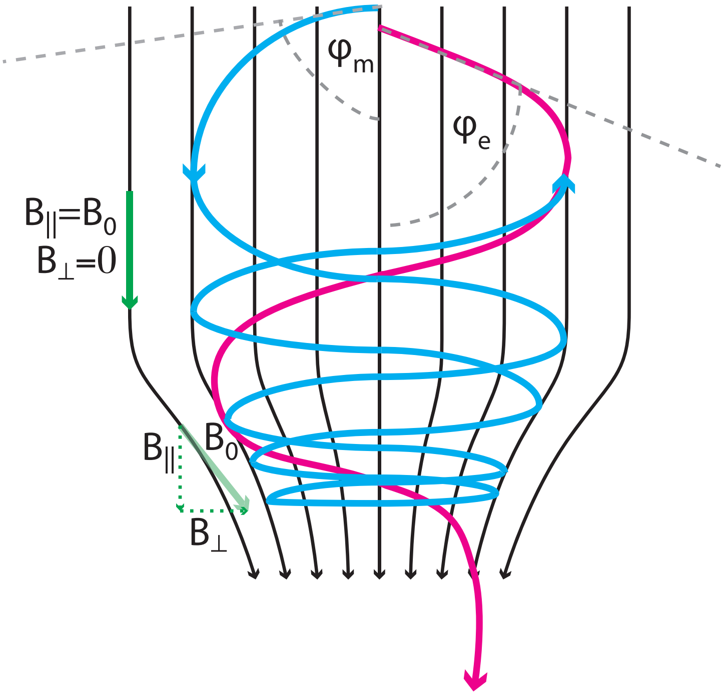

Figure 2.2.: Principle of a magnetic mirror: The increasing density of the magnetic field lines represents the increasing magnetic field towards the bottom of the picture.

Additionally to the deceleration of the particle, the Larmor radius decreases with increasing magnetic flux density as we see in fig. 2.2 and in eqn. (2.1).

Particle-wave interaction as described in section 2.1.1 and especially in eqn. (2.2) can change the pitch angle in a way that it becomes possible for a formerly trapped particle to penetrate a magnetic mirror. This process is called pitch angle scattering and will be of importance when we will discuss the motion of a charged particle in a region of magnetic turbulences in section 2.3.4.

2.2. Particle Transport

So far we have discussed the movement of charged particles in magnetic field in a microscopic way – i.e. we considered a single particle on a rather short path. Although this knowledge is essential for the understanding of the propagation of electrons and ions in the heliosphere, we also need to learn how an ensemble of many particles travels through space covering distances of a few AUs.

Since it is not feasible to give the equation of movement for every single particle of an ensemble, it is more reasonable to determine the probability to detect a particle at the location $\vec{r}$ with the velocity $\vec{v}$ in an infinitely small section $d\vec{r}d\vec{v}$ of the six dimensional phase space:

$$f\left(\vec{r},\vec{v},t\right)d\vec{r}d\vec{v} \tag{2.4}$$

This quantity f is also called the phase space density and is scaled in the effect that a particle must be found somewhere in the phase space which leads to the number N of particles in the ensemble when integrating over the whole phase space:

$$\int_{-\infty}^{+\infty}\int_{-\infty}^{+\infty} f\left(\vec{r},\vec{v},t\right) d\vec{r}d\vec{v} = N \tag{2.5}$$

We will introduce two transport equations that give a partial differential equation system for the phase space density (2.4) that are both based on the well-known *Fokker-Planck equation* (Baumjohann et al. 1996):

$$\frac{\partial f}{\partial t} + \vec{v}\cdot\nabla_{\vec{r}} f + \frac{q}{m}\left(\vec{E} + \vec{v}\times\vec{B}\right)\cdot\nabla_{\vec{v}} f = \nabla_{\vec{v}}\cdot\left(\mathbf{D}\cdot\nabla_{\vec{v}} f\right) \tag{2.6}$$

where q is the charge of the considered particle, m is its mass, $\vec{E}$ is a possible electric field and $\vec{B}$ the magnetic field. The right hand side of (2.6) describes the variation of f due to velocity variations which lead to a diffusion in phase space. $\mathbf{D}$ is a diffusion tensor that reflects the mean values $\langle\Delta v\rangle$ (first order) and $\langle\Delta v\Delta v\rangle$ (second order) of these velocity variations.

Next we want to briefly introduce two important transport equations that describe the propagation of charged particles in the heliosphere and that are based on (2.6). Each equation focuses on different physical transport processes and effects and relies on specific coefficients. With the measurements from EPD we will be able to determine these coefficients and to examine the validity of the different transport equations.

2.2.1. Focused Transport

The focused transport equation takes care of pitch angle diffusion by magnetic irregularities along a field line and the focusing effect that shows when the magnetic field lines diverge.

In plasma physics there are three adiabatic invariants. For a charged particle that moves in a nearly constant magnetic field, the magnetic moment $\frac{T_\perp}{B}$ with T as the kinetic energy of the charged particle perpendicular to the magnetic field is called the *first adiabatic invariant* and thus is constant when the magnetic field B does only vary on greater times scales compared to the gyration period of the particle:

$$\frac{T_\perp}{B} = \text{const.} \tag{2.7}$$

As a consequence of this, the perpendicular kinetic energy drops with decreasing magnetic flux density which means that the particle's velocity perpendicular to the field also decreases while the parallel velocity grows to fulfill the conservation of energy principle. This has a direct effect on the pitch angle $\varphi = \sphericalangle\left(v_{\parallel}, v_\perp\right)$ in the way that its value decreases until the motion of the charged particle is nearly parallel to the magnetic field lines. The particle motion is focused along B.

When we take a look at the interplanetary magnetic field, we see that it is diverging which may be considered as a reverse magnetic mirror which we discussed in section 2.1.2. The change of the pitch angle cosine $\mu = \cos\varphi$ is determined by (Roelof 1969):

$$\frac{d\mu}{dt} = \frac{v}{2L}\left(1-\mu^2\right) \tag{2.8}$$

where v is the velocity of the particle, $\mu = \cos\varphi$ is the cosine of the pitch angle and the so-called focusing length L is defined as:

$$L = -\frac{B}{\frac{\partial B}{\partial z}} \tag{2.9}$$

The motion of the particles is described using cylindrical coordinates along the magnetic field lines pointing in the z-direction.

Based on (2.6) together with (2.8) and (2.9) Roelof derived the *Focused Transport equation* (also called the *Roeloff Transport equation*) (Roelof 1969):

$$\frac{\partial f}{\partial t} + \underbrace{\mu v \frac{\partial f}{\partial z}}_{\text{Advection}} + \underbrace{\frac{v\left(1-\mu^2\right)}{2L}\frac{\partial f}{\partial \mu}}_{\text{Focussing}} = \underbrace{\frac{\partial}{\partial \mu}\left(D_{\mu\mu}\frac{\partial f}{\partial \mu}\right)}_{\text{Diffusion}} + Q\left(z,\mu,t\right) \tag{2.10}$$

where the second term determines the advection process of the solar wind traveling at the velocity v. The third term characterizes the change of the density distribution due to the focussing effect and the fourth term describes the pitch angle diffusion of the particles with the diffusion coefficients $D_{\mu\mu}$. Q represents possible particle sources (for example solar flares) or sinks.

2.2.2. Parker's Transport Equation

E.N. Parker developed a transport equation 1964 that was named after him in which he considered three different transport processes (Parker 1965):

1. ***Diffusion*** Parker showed that particles that get scattered in magnetic irregularities (as described in section 2.1.1) perform a random walk which can be looked at as a diffusion process that is described by the Fokker-Planck equation. He introduced the diffusion tensor κ^S that describes these diffusion processes parallel and perpendicular to the magnetic field.

2. ***Convection and Drift*** The charged particles are embedded into the solar wind which flows away from the sun at the velocity $\vec{u}_{sw}$. The proper motion of the particles can be influenced by gradient and/or curvature drifts and is represented by the velocity $\vec{v}_d$.

3. ***Adiabatic Energy Loss*** Since the magnetic field of the solar wind is radially diverging away from the sun and thus thins out, the particles are adiabatically cooled and the kinetic energy declines with:

$$\frac{1}{T}\frac{dT}{dt} = -\frac{1}{3}\frac{\partial v_i}{\partial x_i} = \frac{1}{p}\frac{\partial p}{\partial t} \tag{2.11}$$

With these considerations, Parker took (2.6) as a basis to derive the *Parker transport equation*:

$$\frac{\partial f}{\partial t} = \underbrace{\nabla \cdot \left(\kappa^S \cdot \nabla f\right)}_{\text{Diffusion}} - \underbrace{\left(\vec{u}_{sw} + \vec{v}_d\right) \cdot \nabla f}_{\text{Advection and Drift}} + \underbrace{\frac{1}{3}\left(\nabla \cdot \vec{u}_{sw}\right)\frac{\partial f}{\partial \ln p}}_{\text{Adiabatic Energy Loss}} + Q\left(\vec{r},p,t\right) \tag{2.12}$$

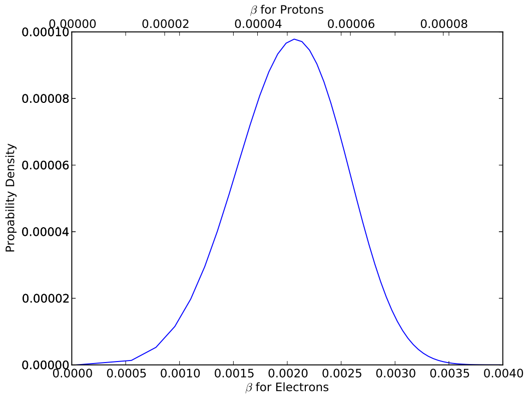

Figure 2.3.: The Maxwell-Boltzmann probability distribution of electrons (lower x-axis) and protons (upper x-axis) in the photosphere at a temperature of 6,000 Kelvin plotted over the relativistic factor $\beta = \frac{v}{c}$. The relativistic factors for protons are two orders of magnitudes lower than the factors for electrons.

2.3. Acceleration Processes

The particles that EPT is designed to measure are energetic in the way that their velocity is relativistic. An electron at 300 keV shows a relativistic factor $\beta = \frac{v}{c}$ of approximately 0.77. These particle energies are mostly of non-thermal nature since the kinetic energy of a free particle at the temperature of the photosphere ($\approx 6,000$ Kelvin) is about 0.8 eV and even in the high temperature corona at 10^6 Kelvin the energy of a particle at this temperature is only 130 eV.

Fig. 2.3 shows the Maxwell-Boltzmann probability distribution of the relativistic factors for electrons (lower x-axis) and for protons (upper x-axis). There, we can see that the likely relativistic factors are much lower than the factors we want to measure. As mentioned before, an electron traveling with a kinetic energy of 300 keV possesses a relativistic factor of 0.77 whereas a proton with 7 MeV travels with a relativistic factor of 0.12. The fig. 2.3 depicts that these factors are unlikely to be reached by either particle when driven by thermal motion. This means that other processes must accelerate the protons and electrons to reach relativistic velocities.

2.3.1. Acceleration by Varying Sunspots

Sunspots that grow or shrink in their sizes can accelerate charged particles (Grupen 2005). A sunspot is a cooler area on the surface of the sun that appears to be darker because of it's lower temperature compared to it's surrounding area. A sunspot is permeated by a high magnetic field $\vec{B}$ with the magnetic flux ϕ as shown in fig. 2.4:

$$\phi = \int \vec{B} \cdot d\vec{A} = B\pi R^2 \tag{2.13}$$

where B is the magnetic field permeating the spot, R is the radius of the spot and $\vec{A}$ is the normal vector of the spot's area.

When these sunspots build up and decay again their varying magnetic flux ϕ produces an electric field $\vec{E}$ that yields the potential U:

$$U = -\frac{d\phi}{dt} = \oint \vec{E} \cdot d\vec{s} \tag{2.14}$$

where $d\vec{s}$ is the infinitesimal distance along the particle's trajectory.

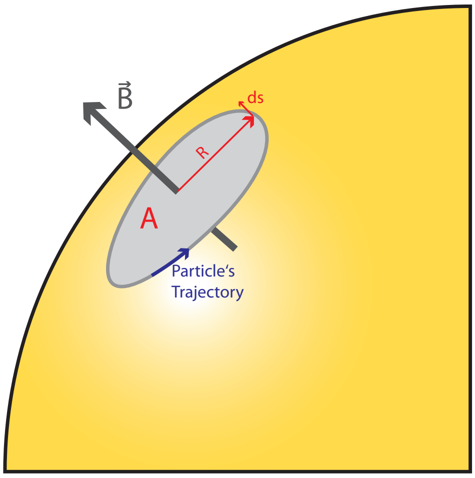

Figure 2.4.: A sunspot is permeated by a magnetic field $\vec{B}$. A growing or shrinking sunspot shows a varying magnetic field and thus also an electric field $\vec{E}$ in which charged particles can be accelerated. (after: Grupen (2005))

Charged particles like electrons and protons get accelerated when exposed to this electric field and when traveling through this potential and can gain energies of several hundreds of MeV (Grupen 2005).

2.3.2. Acceleration by Moving Sunspots

Sunspots are often observed in pairs that approach each other over time (see fig. 2.5). The polarities of the dipole moments $+\mu$ and $-\mu$ in the spots are contrary and annihilate each other when the sunspots merge. On their path the moving dipole moments produce an electric field that is perpendicular to the magnetic field and perpendicular to the spot's motion: $\vec{E} \parallel \vec{v} \times \vec{B}$ (Grupen 2005).

The energies gained by this process can reach the GeV range and with this is comparable to the acceleration by varying sunspots.

2.3.3. Magnetic Reconnection

Dynamic processes in the sun's interior and on the sun's surface can lead to magnetic stress where magnetic field lines are twisted, wound up and pushed around (Yamada et al. 2010). Magnetic stress occurs at three different occasions:

- The sun's dynamo produces magnetic flux in the lower regions of the convective zone that rises up tied to it's frozen-in plasma. The flux leaves the photosphere into the corona and encounters other pre-existing magnetic fields there.
- The differential rotation of the sun distorts magnetic loops whose two anchorage points lie on different latitudes.
- When the magnetic field that is associated with the plasma of the solar wind travels through interplanetary space it can hit a planet's magnetic field and deform and stress it.

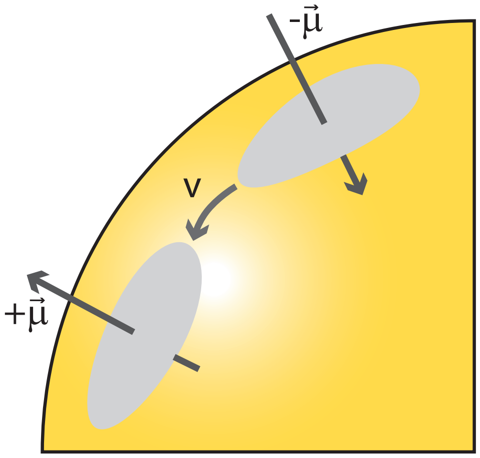

Figure 2.5.: Approaching sunspots produce electric fields due to the movement of the magnetic fields inside the spots. Charged particles inside this electric field can be accelerated to several GeV. (after: Grupen (2005))

When these stresses are high enough they can lead to restructuring processes in the magnetic fields that include the reconnection of adjacent field lines pointing in opposite directions.

When two of those magnetic field lines approach each other as shown in fig. 2.6(1) the field between them must drop to zero to fulfill steadiness – a field gradient is established between the two magnetic fields. When getting even closer, two field lines can reconnect with each other as shown in fig. 2.6(2). With ongoing approximation of the fields, more and more field lines reconnect as we can see in fig. 2.6(3) and 2.6(4).

Fig. 2.6(5) shows the plasma flows into the so-called diffusion region due to external forces that also drove the reconnection process at the beginning. In the middle of the diffusion zone the magnetic field is dropped to zero and the balance between the magnetic and the thermal pressure gives:

$$\frac{B_1^2}{2\mu_0} + p_1 = p_{\text{diff.}} = \frac{B_2^2}{2\mu_0} + p_2 \tag{2.15}$$

where B_1 and B_2 are the magnetic flux densities of the two undisturbed fields, p_1 and p_2 are the thermal pressures in the regions of the undisturbed fields and $p_{\text{diff.}}$ is the thermal pressure in the diffusion region. We see that $p_{\text{diff.}}$ is higher than p_1 and p_2 which leads to an accelerated outflow of plasma out of the diffusion region.

Magnetic reconnection can be found in solar flares, in the interaction of the solar wind with planetary magnetic fields and especially in coronal mass ejections (CMEs) as shown in fig.2.7. A deeper insight into magnetic reconnection and CMEs can be found in Yamada et al. 2010 and in Aschwanden 2006.

2.3.4. Second Order Fermi Acceleration

The former processes accelerated slow particles to higher energies partially to energies of a few GeV. The following two processes are called Fermi acceleration processes (Fermi 1949) and require an already relativistic particle to work.

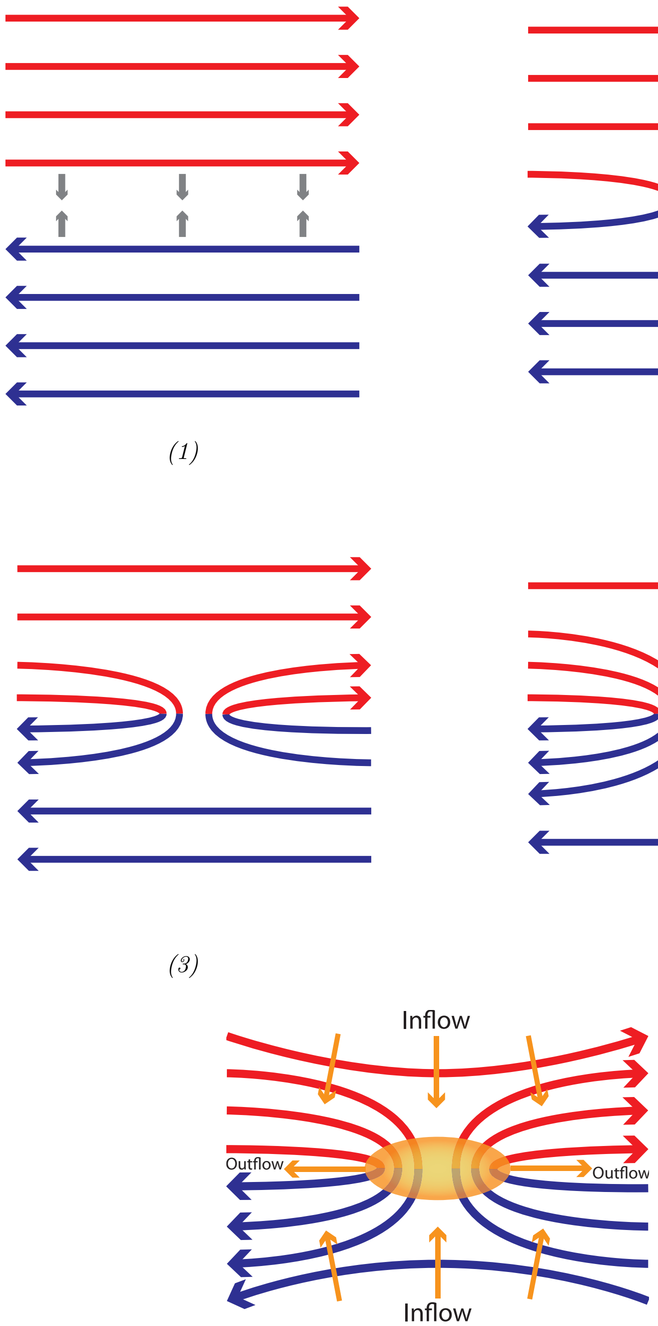
(1) (2)

(3) (4)

Figure 2.6.: When two areas carrying magnetic field in opposite directions their magnetic field lines can reconnect and establish a diffusion region (orange ellipse in lower picture) where charged particles can flow in and out (orange arrows).

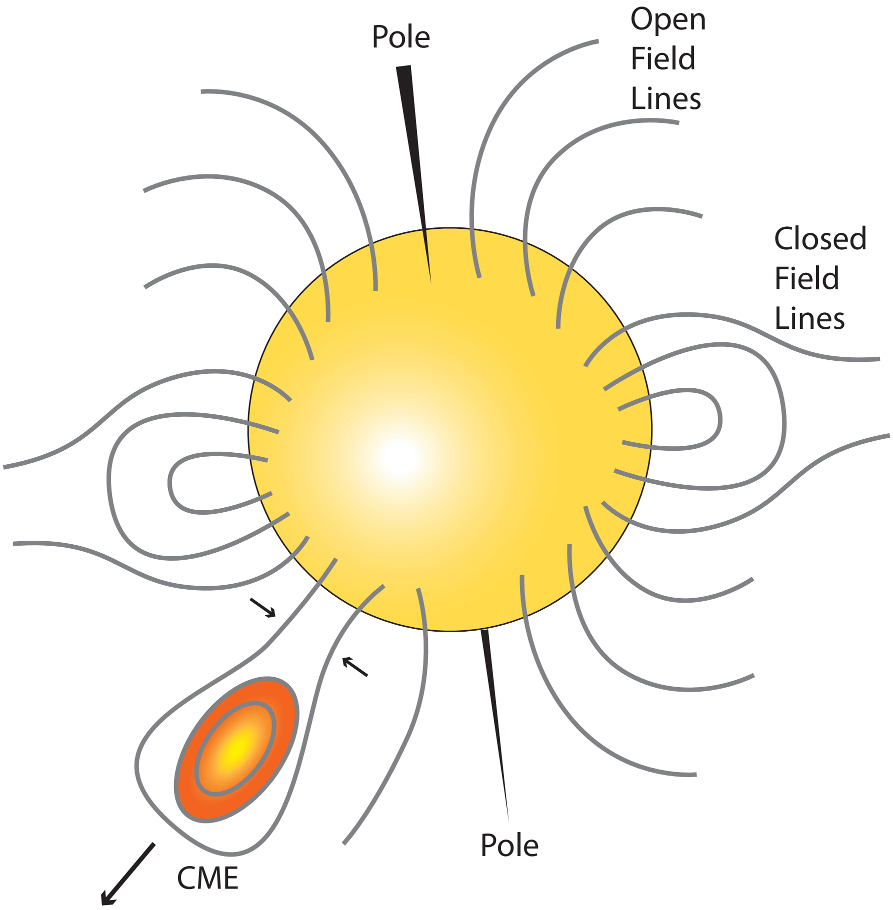

Figure 2.7.: A coronal mass ejection is flowing away from the sun at the lower left corner. As the lower parts of the closed field line of the CME draw near each other the top flows away from the sun. Enclosed in the cavity of the CME is the hot plasma from the solar wind (yellow/orange ellipse). Later, the opposing field lines at the base of the CME will reconnect (two arrows) and the CME will lose it's connection to the sun's surface and freely fly into the heliosphere.

As we saw in section 2.1, charged particles can drift in an area with magnetic turbulences and can also be trapped in that region when the pitch angle of the particle is high enough. These effects are considered in both Fermi acceleration processes. Fermi acceleration is based on the fact that energetic particles ($v \approx c$) gain energy by elastically scattering off magnetic turbulences and irregularities that move with a velocity $v \ll c$. Figure 2.8 shows the situation when such an energetic particle enters an area of magnetic turbulences – a so-called magnetic cloud . The particle travels with the velocity $v_{\text{part.}} \approx c$ and enters the cloud at the angle θ_1 with respect to the cloud's velocity $v_{\text{cloud}} \ll c$.

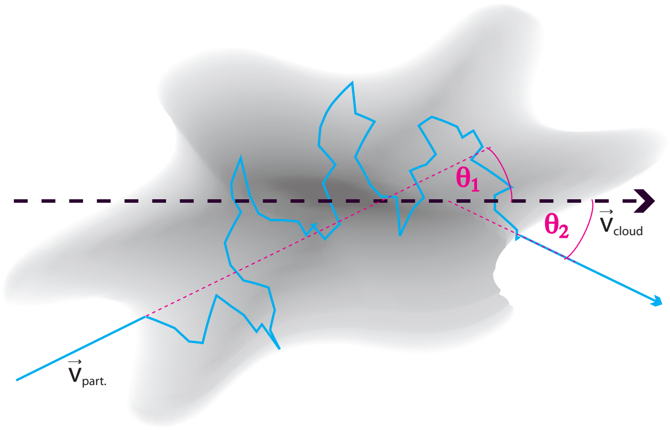

Figure 2.8.: An energetic particle gets accelerated by a region with magnetic turbulences – a so called magnetic cloud. It enters the cloud under the angle θ_1 related to the cloud's velocity $\vec{v}_{\text{cloud}}$, travels through the cloud following a random walk and leaves the region under the angle θ_2. (After: Régis Terrier, "Introduction to High Energy Astrophysics")

Because of the magnetic turbulences, the particle gets scattered and performs a random walk inside the cloud and only leaves the cloud at the angle θ_2 when the pitch angle is low enough to penetrate a possible magnetic mirror at the rim of the cloud.

The mean energy gain

$$\langle \xi \rangle = \frac{\Delta E}{E} = \frac{4}{3}\beta^2 \tag{2.16}$$

that the particles experience by scattering inside a magnetic cloud is proportional to the second power of the relativistic factor β of the magnetic cloud. (A detailed derivation of $\langle \xi \rangle$ can be found in appendix C.1.) This is why this acceleration process is called the **Second** Order Fermi Acceleration and is not so efficient as the First Order Fermi Acceleration. However, as fig. 2.9 illustrates, by multiple scattering in many magnetic clouds the charged energetic particles can repeatedly be accelerated to very high energies.

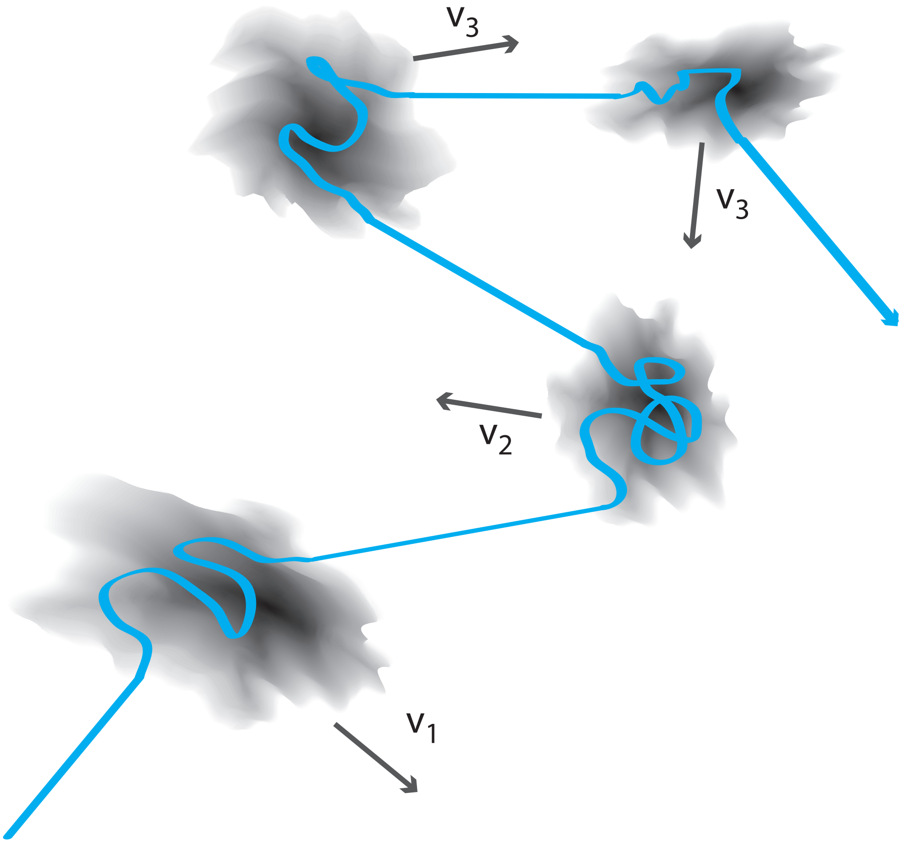

Figure 2.9.: An energetic particle can be accelerated to higher energies when traveling through multiple magnetic clouds with different velocities. (After: Régis Terrier, "Introduction to High Energy Astrophysics")

2.3.5. First Order Fermi Acceleration

In the second order Fermi acceleration process an energetic particle gets accelerated through an encounter with a magnetic cloud which is a compact and finite body. This circumstance yielded the mean values of the entry and the exit angle with which we calculated the mean energy gain (2.16). In the process of the first order Fermi acceleration an energetic particle is accelerated in the turbulent region behind a shock front (Jones et al. 1991; Lee 2000).

A shock forms when a fast flow of plasma meets a slower flow. Fig. 2.10 shows this situation in the shock's frame – this means, the observer is moving with the shock front at the velocity $v = v_u - v_d$. In this picture we see two flows of plasma traveling from the left to the right. The slow and dense flow escaping the shock with the velocity v_d is called the *downstream* while the *upstream* hits the shock front with the velocity v_u. Frozen into both streams is a magnetic field that is represented by the magenta lines.

Since the upstream is fast and thin, the magnetic field shows nearly no turbulence and the charged particles in the plasma follow their field lines on their helical paths as described in section 2.1, keeping their Larmor radii and pitch angles nearly constant. For this reason, there is hardly any particle drift taking place in the upstream region.

The situation changes when the particle travels through the shock front and gets into the region of the downstream. Because of the higher density and the lower velocity of the downstream plasma, we see significant magnetic turbulence here which is depicted by the more chaotic magnetic field lines behind the shock front.

As we can see in fig. 2.11, the higher magnetic turbulence in the downstream region leads to a higher particle drift which enables a charged particle to traverse the shock front back into the upstream region. There it can again cross the shock front from the left to the right. This can happen multiple times for one particle. the particle in the fig. 2.11 travels three times from the downstream to the upstream region and four times back again.

In appendix C.2 we derive the mean energy gain for first order Fermi acceleration:

$$\langle \xi \rangle = \frac{4}{3}\beta \tag{2.17}$$

with which we calculate the energy distribution of the accelerated particles behind the shock:

$$Z\left(E_N\right) = \left(\frac{E_N}{E_0}\right)^{3\frac{1}{\frac{v_u}{v_d}-1}} \tag{2.18}$$

This result shows that a measurement of the spectral profile of energetic particles with EPD will give us an insight into the thermal and kinetic condition before and after a shock front.

In the heliosphere, we can observe shocks at the front of CMEs as shown in fig. 2.7, at planetary magnetospheres where the supersonic solar wind gets decelerated by planetary magnetic fields and in co-rotating interaction regions at the junction between the fast and the slow solar wind as shown in fig. 2.12 (Jones et al. 1991).

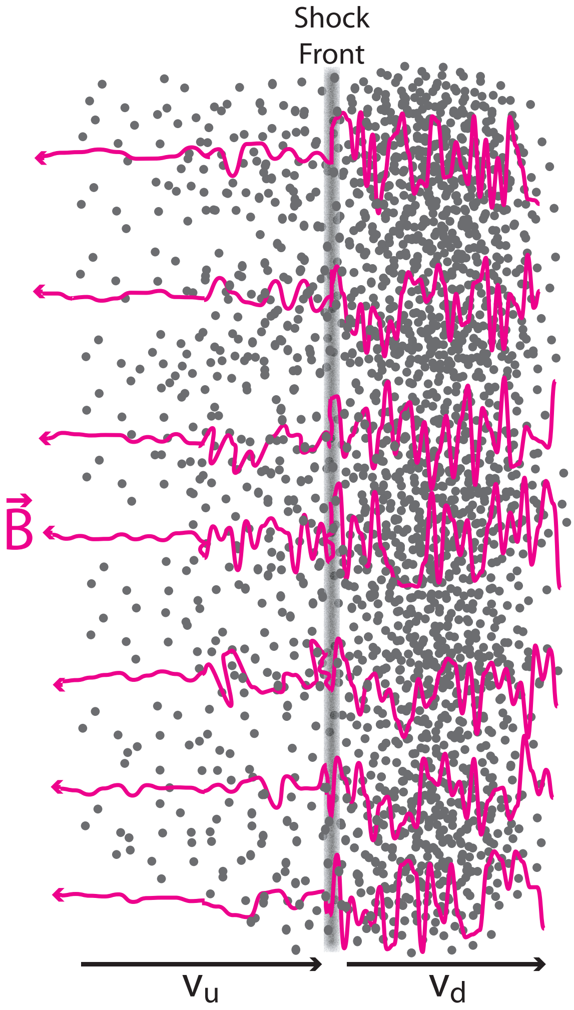

Figure 2.10.: This figure depicts the situation as seen in the shock front's frame. The particles in front of the shock approach the front with the velocity v_u (upstream) whilst the particles behind the shock flow away with the velocity v_d (downstream). The magnetic field in the upstream shows rather low variations whereas the turbulences grow in the vicinity of the shock front and are even much higher behind it. (After: Lee (2000))

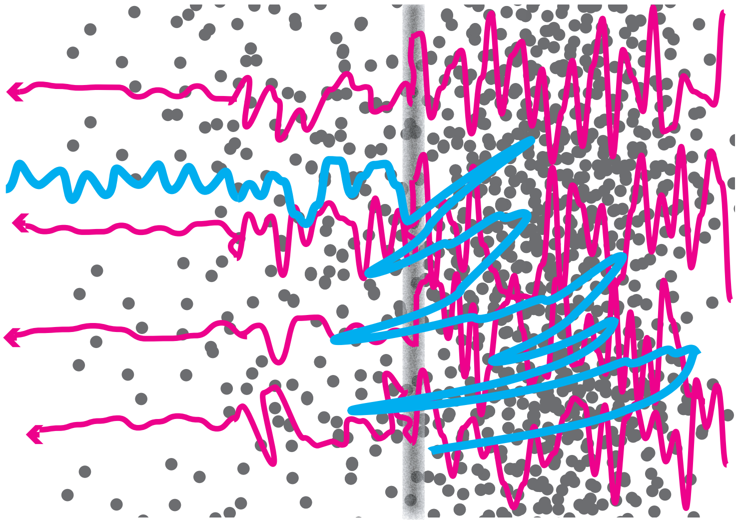

Figure 2.11.: Due to the high magnetic turbulences, it is possible for an energetic particle (blue line) to get scattered back into the upstream region and to get tossed back and forth multiple times gaining energy every time it passes the front. (After: Lee (2000))

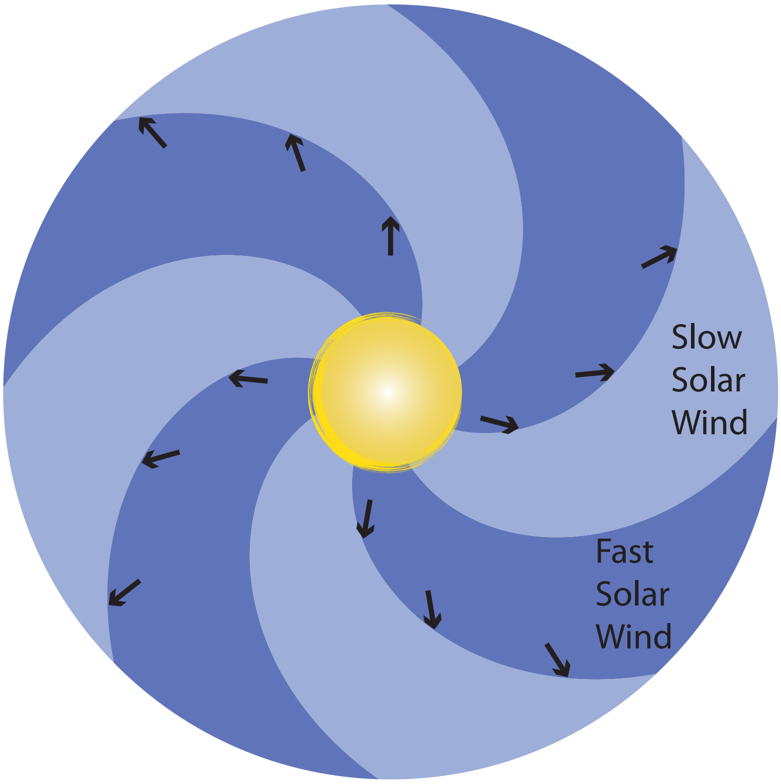

Figure 2.12.: The fast solar wind overtakes the slow solar wind at the front of it's Parker spiral (black arrows) and produces a shock there. Charged particles at the shock front can be accelerated by diffusive shock acceleration.

3. Introduction to EPT

As a successor of SEPT (fig. 3.1) onboard STEREO (Müller-Mellin et al. 2008), the EPT inherits the basic measurement concept from its predecessor. Just like SEPT, EPT is planned as an instrument duo in which each instrument consists of two paired double-ended telescopes. The two telescope-parts of one instrument point in antiparallel directions – this allows for a survey of the proton and electron fluxes in the forward and in the backward directions simultaneously. Onboard Solar Orbiter EPT shares an electronic box and hence the position together with its EPD partner HET (see fig. 3.2).

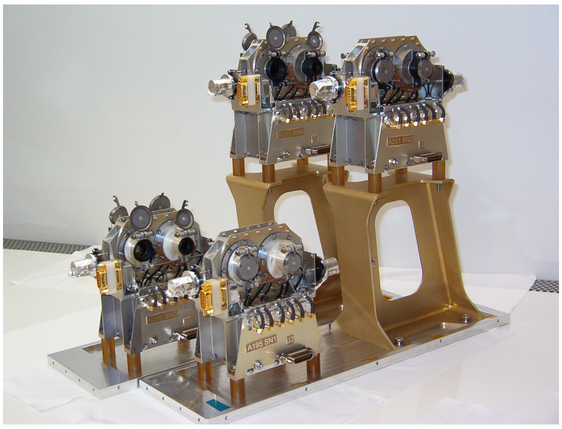

Figure 3.1.: Four of the SEPT instruments which are currently flying on STEREO-A and on STEREO-B. (Photo taken from Müller-Mellin et al., 2008)

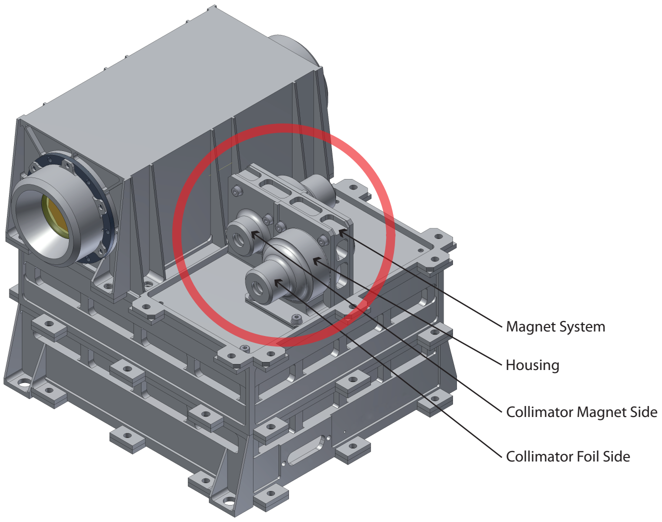

Figure 3.2.: A CAD view of the EPTHET-combination onboard Solar Orbiter. EPT is the instrument marked with the red circle. (Courtesy Lars Seimetz)

In the basic design EPT consists of 2 x 2 segmented solid state detectors surrounded by an aluminum housing and 2 x 2 aluminum collimators. Placed in front of the detectors is a magnet system that is shared by both sides of the instrument and two detectors are covered with a Kapton foil (see fig. 3.2 and fig. 3.3). The foils and the magnet system are used for the separation of electrons from protons which will later be described in more detail.

3.1. Detectors

The incident particles will be detected by two parallel 300 μm thick solid state detectors (SSD) named “A” and “C” made of passivated ion-implanted planar silicon (PIPS) (detector “B” existed in an earlier design but was rejected due to electronic limitations). These detectors are segmented into an inner part and an outer part and are operated in anti-coincidence mode. Figure 3.3 shows the detectors integrated inside the telescope. The distance between the detectors is 0.4 mm which will be discussed in section 5.4.

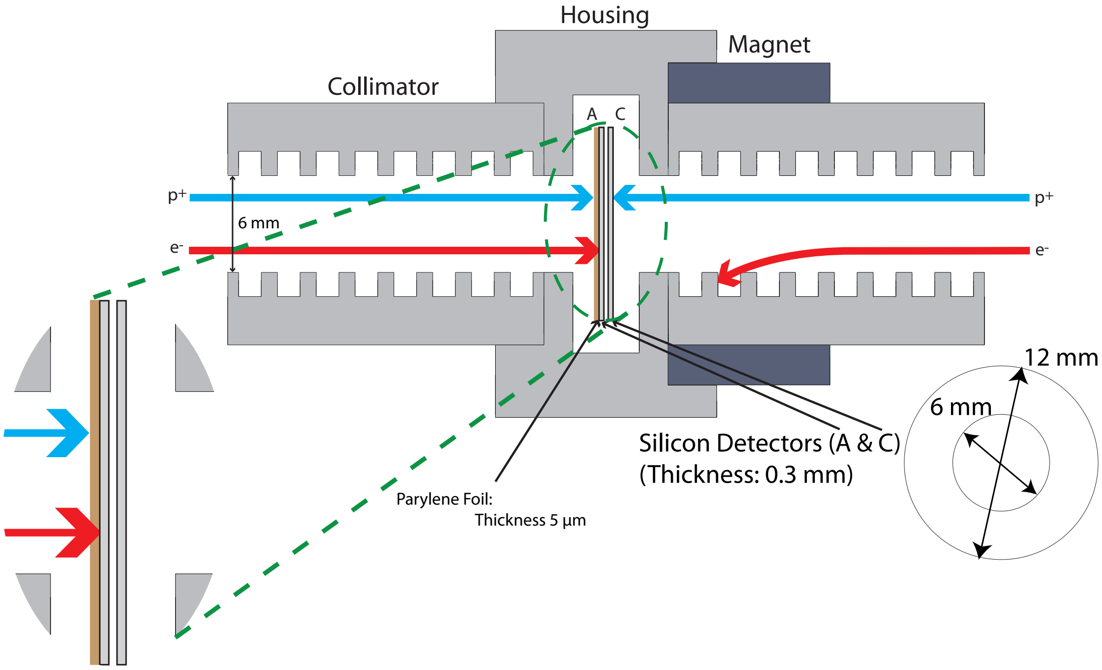

Figure 3.3.: The basic design of EPT including two collimators, a housing, a magnet system, a Kapton foil and two segmented silicon detectors.
EPT particle discrimination: Protons (blue) are stopped by the Kapton foil, whereas the electrons (red) can easily pass the foil and reach detector A (see zoomed in area). On the other side, the protons do not get deflected by the magnetic field due to their greater mass compared to the electrons which get deviated into the collimator.
(Note: All the dimensions given in this figure are a result of later discussions in this work and shall be anticipated here.)

The alignment and the segmentation of the detectors is used for the anti-coincidence mode that defines two trigger conditions.

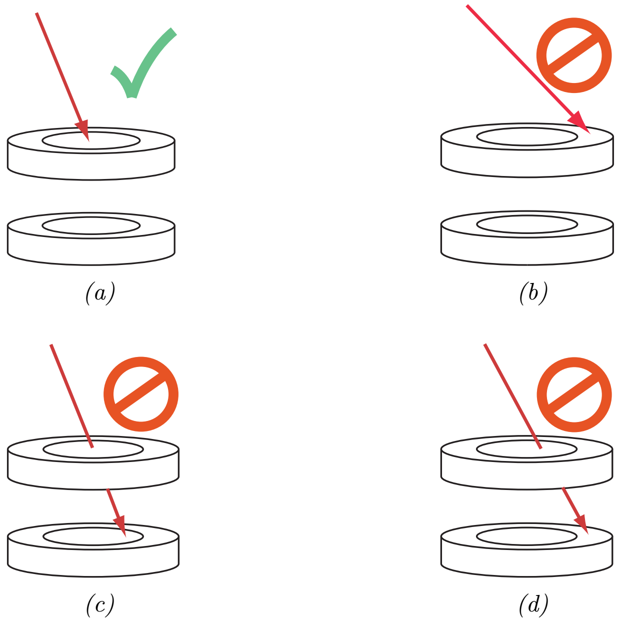

Figure 3.4.: A trigger condition is only fulfilled when a particle creates a signal only in the inner segment of the first detector it enters. These cases apply to both detectors A and C – i.e., the first detector hit by the particle can either be detector A or detector C. If the first detector is detector A then condition A is fulfilled otherwise trigger condition C is activated.

3.1.1. Trigger Conditions

When a particle reaches the inside detectors it can produce a signal in all the four segments depending on the particle type, the kinetic energy and the incident angle. To tell from which direction and angular range the particle came from, we define two trigger conditions “A” and “C”. Figure 3.4 demonstrates the principle of these conditions: In case (a) the incident particle reaches the inner segment of the first detector after traveling through the collimator and is stopped there. When the energy deposition is higher than a pre-defined threshold the concerning trigger condition is fulfilled. The particle in case (b) hits the first detector in the outer segment and ends its path there. This event will not be counted by the electronics. Case (c) shows the situation when a particle penetrates the inner segment of the first detector and reaches the inner segment of the second detector. Here, when the signal in the second detector exceeds the threshold, the anti-coincidence logic repels this event. Though, if the energy in the second detector is below the threshold this event will be counted as a trigger event. A similar situation is shown in case (d) – here the particle also penetrates the inner segment of the first detector but now reaches the outer segment of the second detector. Again, when the threshold level is reached in the outer segment the event is not counted. But if the threshold level is not exceeded the event will be registered as a trigger event.

To make it short: Depending on the name of the first detector hit (A or C) the trigger condition A or C are fulfilled only in case (a) .

3.2. Shielding

The detector stack is surrounded by an aluminum shielding that consists of a housing that contains the detectors and the Kapton foil (explained later in section 3.3) and a collimator in front of each detector.

The main purpose of the shielding is to prevent particles that come from outside the angular range defined by the collimator-detector-geometry from hitting for the inner segments of the detectors. In addition to that, the aluminum also protects the sensitive detectors from direct or reflected sunlight which would lead to an increased noise level.

But even the aluminum shielding can not hinder high energy particles to reach the detectors. To attenuate this disturbance the shielding and the detector setup will be discussed in section 5.4 and in section 5.2.

3.3. Particle Separation

Of course, electrons and protons both enter the collimators and would fulfill both trigger conditions. Without a separation technique we couldn't distinguish between the count rates of the electrons and the protons. EPT uses the same separation method as SEPT: a magnetic field is established before detector C to deflect electrons away and a 5 μm thin Kapton foil is deposited on detector A to stop incoming protons (see fig. 3.3). In earlier designs, a Parylene-C foil was spanned over the opening of the housing in front of detector A. But this was abandoned when the SSD manufacturer CANBERRA offered to apply the Kapton directly on the detector. This simplifies our construction procedure, because we don't need to span the Parylene foil in the collimator ourselves anymore. Also, the physical properties of Kapton are comparable to the properties of Parylene (see fig. 3.6).

Since the decision for the new detectors was made rather late during this work, all the simulations and calculations were made based on the Parylene instead of the Kapton foil. But as the two materials are very similar concerning their physical characteristics, we can keep the results from the Parylene simulations.

The protons with their much higher mass compared to the electrons are barely deflected from their path by the magnetic field and can still reach their assigned detector. On the other side, the protons must have a much higher kinetic energy than the electrons to pass through the Parylene foil (see fig. 3.5).

In some situations it can be possible for electrons to reach the inner segment of detector C despite the magnetic field. In section 6.2.6 we will make sure that these electrons will have such high kinetic energies that they penetrate detector C and reach detector A to produce a signal there that is higher than the threshold. Then the anti-coincidence logic will reject these events so that these electrons are not counted as “false” protons.

On the other side, we see in fig. 3.5 that protons with higher energies than approximately 230 keV can pass the foil and reach detector A. These protons produce false electron count rates because their energies lie in the range of he observed electron energies. But since EPT is designed as a bi-directional instrument, we can subtract the proton count rates gained from the other side of the instrument from the electron count rates. In this way we can zero this disturbances.

The design of the EPT instrument as a twin telescope also allows us to let two telescopes share one magnet system (see fig. 6.2 and 6.3b).

Now that we know that electrons trigger the trigger condition A and protons condition C, we will occasionally refer to the trigger conditions as the “electron channel” and the “proton channel” in this work.

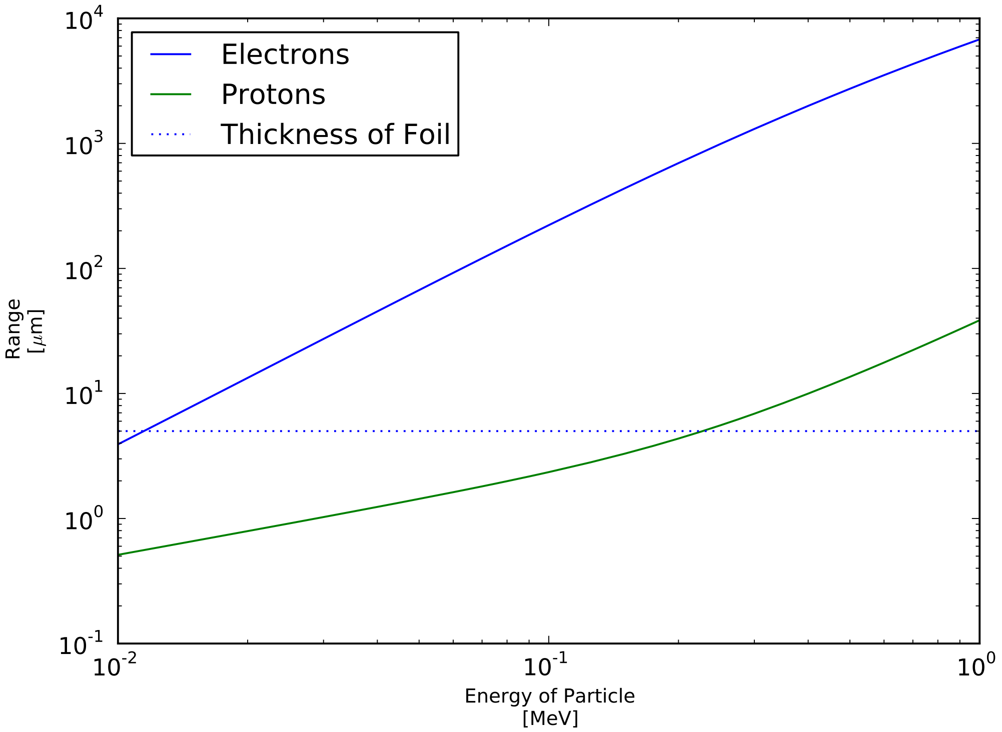

Figure 3.5.: The range of protons and electrons in Kapton. We see that protons must have a much higher energy to penetrate the foil in front of detector A. The data shown here was obtained from the National Institute of Standards and Technology (NIST website: `http://http://physics.nist.gov/PhysRefData/Star/Text/ESTAR.html`).

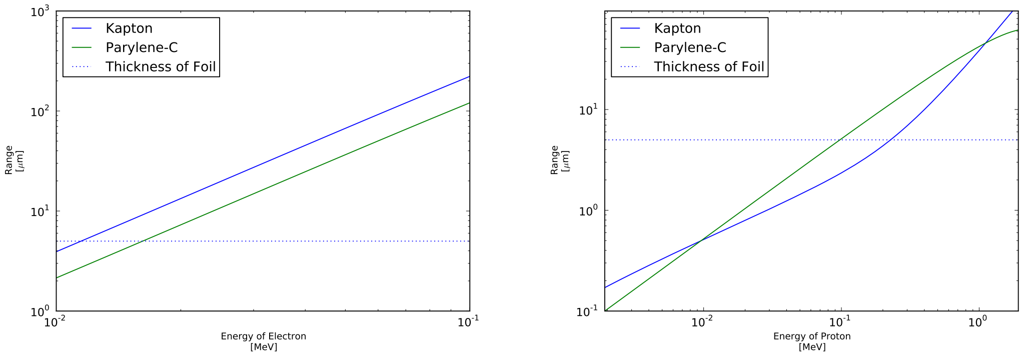

(a) Electrons

(b) Protons

Figure 3.6.: Passage of particles through the Parylene and the Kapton foil. While the electrons can pass the Kapton foil more easily than the Parylene foil, the protons need more energy to penetrate the Kapton than the Parylene. All data except the proton passage through Parylene was obtained from the National Institute of Standards and Technology. The passage of protons through Parylene was computed with the Bethe-Bloch-Formula (eqn. (5.19)) (NIST website: `http://http://physics.nist.gov/PhysRefData/Star/Text/ESTAR.html` (electron data) and `http://physics.nist.gov/PhysRefData/Star/Text/PSTAR.html` (proton data)).

4. Scope of This Work

Although the EPT design is based on the SEPT architecture, we still need to modify the new instrument to adapt it to the new environment at 0.28 AU. Since SEPT is measuring at 1 AU it is exposed to much lower flux densities than we expect for Solar Orbiter.

So at first we will calculate what count rates we will encounter at 0.28 AU. For this we will simulate the energetic spectra of electrons, protons and higher ions up to oxygen during an intense SEP event based on observational data obtained by an array of probes located at 1 AU. These intensities will then be extrapolated to 0.28 AU and compared to the maximum count rates that the onboard electronics can handle.

The point here is that the electronics that processes each single hit in the detectors is only capable to handle a limited amount of hits per second. To ensure that this limit will not be exceeded even at high intensity events we must shape the aperture and the detector sizes accordingly. The ratio of the manageable count rates to the expected count rates gives us the so-called nominal geometric factor that indicates how big the opening of the collimators and how big the diameters of the detectors can be designed to still gather enough particles but not to overload the electronics at the same time.

After we sized the aperture and the detectors, we will expose this design to the mentioned SEP event at 0.28 AU. This simulation will give us the information about the count rates in the single parts of the silicon detectors at such a strong event. These count rates must stay beneath the electronics limit otherwise we will need to reconsider our design.

With the adapted dimensions we can then determine the energy dependent geometric factor (short: geometric factor) for each trigger condition and for each particle type (electrons and protons). The geometric factor is energy dependent since the response of the silicon detectors to incident particles is not constant at every energy and the magnet/foil-technique only works in a defined energy range. Additionally to that, it is also possible that particles with high kinetic energy can penetrate the surrounding aluminum shielding and produce an unwanted signal in one of the detector segments. This effect will presumably raise the geometric factor at higher energies. Therefore, the determination of the geometric factor will give us evidence how the separation system works and how much noise we must expect from high energetic particles not coming through the collimators. We will gain these noise levels by relating the geometric factors for those kinds of particles with the expected spectra in these energy domains.

We determine the geometric factors by simulating the final EPT design in the Monte-Carlo framework GEANT4 (Agostinelli et al. 2003; Allison et al. 2006). In doing so, we must anticipate the later results concerning the shape of the design, the appearance of the collimator and the setup of the magnet system.

As indicated above, we must live with background noise that is made up of high energetic particles coming through the shielding and particles that get scattered back into a detector coming from the inside of the collimators after entering through the openings of the collimators. To reduce this noise will be a major issue of this work.

For this, we will first take a look at the aluminum shielding that encloses the silicon detectors. By introducing certain features that can strengthen the shielding ability in defined directions we use a so-called spot shielding method to minimize the noise from penetrating particles while keeping the overall weight of the shielding as low as possible at the same time. By combining the different features of the shielding in different sizes and shooting electrons at the instrument in GEANT4 we gain geometric factors for every test design which we can compare as a function of the starting direction of the primary particles. Based on this, we can choose the best design for reducing the background noise from penetrating electrons.

After that, we must improve the profile of the inside of the collimators to reduce the noise we get from scattering electrons. Together with the opening of the collimator the area of the inner segment of a detector forms an opening cone from which particles can reach the segment directly (neglecting the magnet/foil-separation for a while). All particles that enter the collimator through its opening and that do not come from inside of this cone should be stopped in the aluminum of the collimator. Due to the scattering ability of electrons, we must expect false signals produced by electrons that bounce from the inside of a collimator into a silicon detector. To reduce this noise, we will consider a number of profiles in GEANT4 that vary in shape and dimensions and see how these profiles can absorb electrons. The result of this comparison will be a profile that can be produced by our workshop and that significantly reduces the noise from scattered electrons.

Of course it is impractical to reduce the noise from penetrating particles to zero. Particles at relativistic velocities show a minimum of stopping power when penetrating matter. The only way we can reduce the background from these minimum ionizing particles (MIPs) is by using the trigger conditions and thus by aligning the detectors cleverly. We will vary the gap between the two silicon detectors and see how the geometric factors for these MIPs behave as a function of the gap's size. Unfortunately, we are restricted to a minimum distance between the detectors due to construction restraints. So we can gain a minimum geometric factor for the MIPs from a GEANT4 simulation with which we can estimate the background noise from relativistic particles.

When we are done with that, we will turn to the magnet system of EPT. Two requirements to the magnet system must be examined:

1. The magnetic field must deflect low energetic electrons that would cause false signals in the proton channel but can high energetic electrons that would also produce a signal in the second detector let pass.
2. The combined magnetic flux densities of both magnet systems from EPT1 and EPT2 must drop fast enough as a function of distance so that the measurements of the MAG instrument onboard Solar Orbiter are not disturbed.

One can clearly see that these two requirements are linked to each other: the raise of the deflection ability would also raise the disturbance of MAG. Our goal will be to find a balance between the two competing tasks.

To do this, we employ a three dimensional field calculating software called RADIA (Chubar et al. 1998) in which we can define our magnet systems and compute the resulting magnetic field. With this we will determine the minimum residual induction of the permanent magnets of the system by simulating the paths of the electrons inside the collimator. In RADIA we can also calculate the magnetic flux densities at the MAG location on the instrument boom to check whether we can fulfill the second requirement.

The manufactured magnet systems with the computed residual induction have to be measured concerning their ability to deflect electrons and concerning their stray field into the MAG directions.

For the first task we will use a Hall effect probe to determine the flux density in the middle of the two gaps of the magnet system. These flux densities can be compared to the calculated densities from RADIA. The measured densities should not be significantly lower than the calculated ones.

The stray field of the magnet systems will be measured using a magnetometer with the help of the self-designed iPhone App EMMA. As a result, we will see that we can not determine the magnetic flux densities at the MAG positions since the magnetic background field limits the distance to where we can still detect magnetic flux produced by our magnet systems.

For a worst case estimation, we will extrapolate the magnetic fields of the systems towards the MAG directions. For this, we must consider a dipole behavior of the field rather than a quadruple behavior although we still see a quadrupole decline of the field. The reason for this is that we will not be able to locate the turning point where the field turns from quadrupole to dipole gradient.

The magnet measurements will lead to a recommendation of a system combination for EPT1 and EPT2 that exposes MAG OBS to the lows field possible.

At the end of this work, we will show the first measurements of the EPT demo model with ^{207}Bi as a radioactive electron source that demonstrates the functioning magnet/foil-technique and the detecting ability of the silicon detectors.

5. Mechanical Design

In this chapter, we want to discuss the mechanical design of our instrument. This includes the shape of the aluminum shielding around the detectors, the profile of the collimators (both inside and outside), the size and alignment of the detectors and the detector/collimator arrangement.

Although we inherit the basic design of SEPT as a dual double-ended telescope with a magnet/foil combination for particle separation, the closer distance to the sun makes it necessary to adapt some features and dimensions to the more stressful environment.

At first, in section 5.1, we will examine what radiation intensities we can expect at the perihelion of Solar Orbiter and will then relate these count rates to the maximum count rates that our onboard electronics can handle. We will then choose the detector/aperture geometry accordingly in section 5.1.2 and verify this design with a Monte-Carlo simulation in section 5.1.3.

After that, we will take a look at the shielding of EPT in section 5.2. The higher intensities make it inevitable to build a smaller instrument but at the same time we also need to strengthen the shielding in order not to overload the electronics and to make a precise statement about the local particle fluxes.

This requirement also makes it necessary to adjust the inside profile of the collimator to minimize the background noise inflicted by scattering electrons. By introducing ribs and gaps inside the collimators in section 5.3, we will be able to reduce this noise by approximately 20%.

Finally, we will calculate the impact of relativistic protons from the galactic cosmic background on the count rates in the two trigger conditions A and C. These protons can easily penetrate any shielding and produce a signal in the detectors that lies in the observed energy regions of EPT. We will see in section 5.4 that a detector alignment as close as possible is the way to lower this background.

5.1. Expected Count Rates in the Single Detectors

EPT is designed to measure the electron and proton fluxes in the solar wind close to the sun up to a distance of 0.28 AU. But these fluxes can vary over several orders of magnitude in intensity – especially during Solar Energetic Particle events (SEP) and coronal mass ejections (CME) (Aschwanden 2006; Howard 2011; Schwenn et al. 1990). Since each particle that is hitting a detector produces a signal that has to be processed electronically for further analysis, we have to make sure that the instrument's electronic can handle even the highest cadences. For this, we will have to carefully choose the dimensions of the detectors and the aperture considering the limits of the electronics. Otherwise it could be possible that two successive event are counted as one event with higher energy for example.

After determining the size of the detectors and the aperture, we have to test the setup in a Monte-Carlo simulation using the framework Geant4 (Agostinelli et al. 2003;

Allison et al. 2006). An introduction to GEANT4 can be found in section B.1. After that, we will have the expected count rates in the single segments of the detectors and can verify that the electronics capabilities are sufficient for SEP events with high intensities at 0.28 AU.

5.1.1. Calculation of the Detector Dimensions

The work of Mewaldt et al. (2005) sums up data of SEP events delivered by ACE, SAMPEX and GOES-11 and processes it to overall spectra of the events and to count rates per second for the single particle types (electrons, protons, helium, oxygen) in a certain energy range. These three probes are located at 1 AU distance from the sun – this is why we will have to scale the results from the paper to represent the closer distance of 0.28 AU of Solar Orbiter to the sun.

To be able to even resolve the most intense events, we examine the solar particle event from Oct., 28th, 2003 which is the biggest event presented in the paper. To deduce the dimensions of the detectors and aperture, our plan is as follows:

- First, we will draw the particle intensities in the energy range observed by EPT for electrons and protons from the integrated spectra given in the paper by integrating these spectra over the concerning energies.
- Second, we will calculate the intensities per second by dividing the integrated intensities by the duration of the event.
- Then, we will scale these intensities from 1 AU to the perihelion of Solar Orbiter.
- Finally, we will relate these scaled intensities to the capabilities of our electronics and will determine the dimensions of the detectors and the aperture in this way.

In this estimation, we neglect the contributions of the other ions like helium and oxygen since they are by far less abundant that the hydrogen ions and the later Monte-Carlo simulations showed that the detected count rates in the detectors can be discarded here without any noteworthy impact.

Intensities in the Observed Energy Range

The shape of the integrated electron spectrum in fig. 5.1a is a broken power law of two different exponents (-1.9 and -4.3) witht the intersection at about 500 keV. The exact functionality given in the paper by Mewaldt et al. (2005) is as follows:

$$\frac{dJ_\mathrm{e}}{dE} = \begin{cases} 6.75 \cdot 10^8 E^{-1.9} \frac{\mathrm{electrons}}{\mathrm{cm^2\ srad\ MeV}} & : \quad E \leq 527\ \mathrm{keV} \\ 1.46 \cdot 10^8 E^{-4.29} \frac{\mathrm{electrons}}{\mathrm{cm^2\ srad\ MeV}} & : \quad E > 527\ \mathrm{keV} \end{cases}$$

where J_e is the intensity and E the kinetic energy of the electron in MeV.

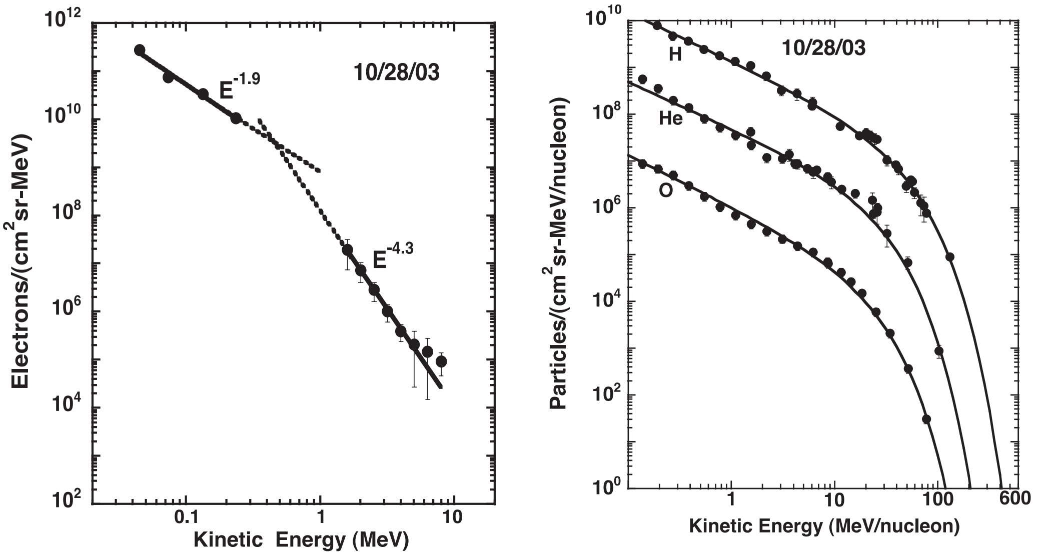

(a) Electron spectrum *(b)* Ions spectrum

Figure 5.1.: The particle spectra of the event from Oct., 28th, 2003 taken from Mewaldt et al.

Since the observed energies for electrons range from 20 keV to 400 keV, we only must integrate the first definition:

$$J_{\mathrm{e}} = \int_{20\ \mathrm{keV}}^{400\ \mathrm{keV}} 6.75 \cdot 10^{8} E^{-1.9} \frac{\mathrm{electrons}}{\mathrm{cm}^2\ \mathrm{srad\ MeV}} dE \approx 2.4 \cdot 10^{10} \frac{\mathrm{electrons}}{\mathrm{cm}^2\ \mathrm{srad}} \tag{5.1}$$

The proton spectrum on the other hand is described by Ellison et al. 1985 (see fig. 5.1b) using the form:

$$\frac{dJ_{\mathrm{p}}}{dE} = K E^{-\gamma} \exp\left(-\frac{E}{E_0}\right) \tag{5.2}$$

where J_{p} is the intensity, E the kinetic energy, K a normalization constant and E_0 is an energy constant.

The spectrum of our chosen event is represented as follows:

$$\frac{dJ_{\mathrm{p}}}{dE} = 1.35 \cdot 10^{9} E^{-1.05} \exp\left(-\frac{E}{28.2}\right) \frac{\mathrm{protons}}{\mathrm{cm}^2\ \mathrm{srad\ MeV}} \tag{5.3}$$

The integration of (5.3) from 20 keV to 7 MeV gives us the intensity in the observed energy range integrated during the whole event:

$$\begin{aligned} J_{\mathrm{p}} &= \int_{20\ \mathrm{keV}}^{7\ \mathrm{MeV}} 1.35 \cdot 10^{9} E^{-1.05} \exp\left(-\frac{E}{28.2}\right) \frac{\mathrm{protons}}{\mathrm{cm}^2\ \mathrm{srad\ MeV}} dE \\ &\approx 8 \cdot 10^{9} \frac{\mathrm{protons}}{\mathrm{cm}^2\ \mathrm{srad}} \end{aligned} \tag{5.4}$$

When we compare eqn. (5.1) with eqn. (5.4), we see that the intensity of the electrons exceeds that of the protons by nearly one magnitude – so, the driver for the geometry will be the electrons' intensity. To get the intensity per second I_{e} we divide the result from eqn. (5.1) by the duration of the measurement of the spectrum:

$$I_{\mathrm{e}} = \frac{J_{\mathrm{e}}}{118800 \text{ sec.}} = 202,020 \frac{\text{electrons}}{\text{cm}^2 \text{ srad sec.}} = I_{\mathrm{e}_{1 \text{ AU}}} \tag{5.5}$$

The last step shows that we are still at a distance of 1 AU away from the sun. To extrapolate the particle fluxes at the fronts of interplanetary shocks driven by CMEs from 1 AU to distances closer to the sun, Lario et al. 2006 showed that we have to use a functional form of $I \propto r^{-3}$. In order to get the expected count rates at the perihelion of the Solar Orbiter orbit at 0.28 AU, we multiply the count rates at 1 AU with a third scaling factor γ:

$$\gamma = \left(\frac{1 \text{ AU}}{0.28 \text{ AU}} \right)^3 \tag{5.6}$$

$$I_{\mathrm{e}_{0.28 \text{ AU}}} = \gamma I_{\mathrm{e}_{1 \text{ AU}}} \approx 9 \cdot 10^6 \frac{\text{electrons}}{\text{cm}^2 \text{ srad sec.}} \tag{5.7}$$

The digital-to-analog converters of the EPT electronics are working with a clock speed of 1 Mhz, i.e. theoretically we are able to resolve one million signals per second in each of the four detector-segments. But since the processing of one event needs several clock cycles, we are limited to a frequency of 100 kHz. Now, we must find a detector-setup that can handle the high intensity from eqn. (5.7) together with our electronics.

5.1.2. Geometric Factors

To push the maximum count rates that will be detected by EPT beneath the limit of the electronics of 10^5 events per second, we must find a detector/aperture geometry that opens to just a section of the environment. As shown in fig. 3.3, the two silicon detectors are surrounded by aluminum shielding with two collimators as the entrances for the particles. The solid angle that is covered by the inner segments and the opening of the collimator is called the geometric factor Γ. This factor Γ reflects the special geometry and detector alignment of our instrument with which we can directly extract the intensity I from the count rate C (Sullivan 1971):

$$C = \Gamma \cdot I \tag{5.8}$$

From eqn. (5.7) we got the maximum intensity of an SEP event and the maximum count rate that can be handled by the electronics is 10^5 events per second – this leads us to the following estimation for the needed geometric factor:

$$\Gamma = \frac{C_{\text{max.}}}{I_{\mathrm{e}_{0.28 \text{ AU}}}} = \frac{10^5 \frac{\text{electrons}}{\text{sec.}}}{9 \cdot 10^6 \frac{\text{electrons}}{\text{cm}^2 \text{ srad sec.}}} \approx 0.01 \text{ cm}^2 \text{ srad} \tag{5.9}$$

The above mentioned paper by Sullivan (1971) provides us with an analytic calculation of the geometric factor of an "ideal cylindrically symmetric telescope with two planar detectors" which EPT is:

$$\Gamma_{\text{analytic}} = \frac{1}{2}\pi^2 \left(R_1^2 + R_2^2 + l^2 - \sqrt{\left(R_1^2 + R_2^2 + l^2\right)^2 - 4R_1^2 R_2^2} \right) \tag{5.10}$$

where R_1 and R_2 are the radii of the two disk detectors and l is the distance between the two detectors. In line with the paper, we identify the first detector as the inner segment of one of the silicon detectors and the second “detector” as the opening of the collimator in front of that silicon detector.

One requirement for EPT that will be discussed in more detail later in section 5.3 is that the opening of the collimator together with the inner segments of the detectors must span a cone of 15°. When we choose the inner segments to have radii of 0.3 cm we must build the openings of the collimators to be 22.39 mm away from the detectors. This yields the following geometric factor for both trigger conditions A and B:

$$\Gamma_{\text{A/B}} = 0.0141 \text{ cm}^2 \text{ srad} \tag{5.11}$$

The assumptions we made up to here are that the detectors' sensitivity is constant for all particle types and at every particle energy and that every particle that aims for a detector also reaches it. In reality, we need to take into account that the protons get stopped in the foil up to a certain energy, that the electrons get deflected by the magnetic field, that the electrons get scattered in material and so on and so forth. To make it short: we must calculate the geometric factors for the single particle types by utilizing a Monte-Carlo-method in GEANT4.

According to the paper by Sullivan the gathering power of a telescope exposed to an isotropic intensity of radiation is given by:

$$G = \int_\Omega d\omega \int_S d\boldsymbol{\sigma} \cdot \hat{\boldsymbol{r}} \tag{5.12}$$

(equation (5) in the paper). Here G names the geometric factor of the telescope, Ω is the hemisphere from where incoming particles are detected, $d\omega = d\phi \, d\cos\theta$ is an element of solid angle on this hemisphere (θ polar angle, ϕ azimuth), S is the surface of the last detector in the telescope, $d\boldsymbol{\sigma}$ is the normal vector of an element of surface area on this detector and $\hat{\boldsymbol{r}}$ is the normal vector pointing from $d\sigma$ to $d\omega$ (see fig. 5.2).

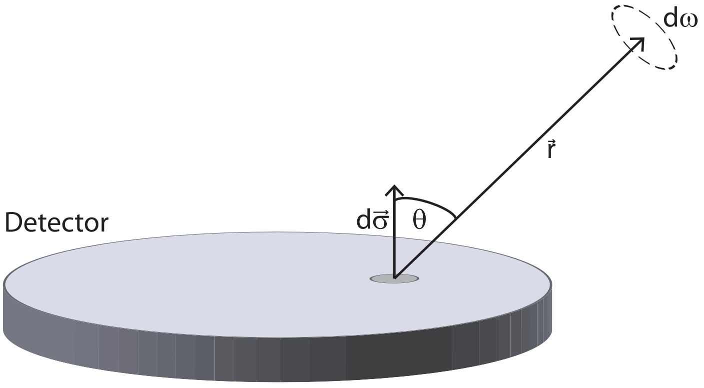

Figure 5.2.: This sketch illustrates the double integral from eqn. 5.12. We have to integrate $d\omega$ over the hemisphere above the detector for each element of surface area $d\boldsymbol{\sigma}$ on the detector surface.

For a telescope that consists of a single disk shaped planar detector the geometric factor can easily be calculated:

$$\begin{aligned} G &= \int_\Omega d\omega \int_S d\boldsymbol{\sigma} \cdot \hat{\boldsymbol{r}} = \int_\Omega \int_S \cos\theta \; d\sigma \; d\omega \\ &= 2\pi A \cdot \int_\Omega \cos\theta \; d\omega = 2\pi A \cdot \int_\Omega \cos\theta \; d\phi \; d\cos\theta \\ &= 2\pi A \cdot \int_0^{2\pi} d\theta \int_0^1 \cos\theta \; d\cos\theta \\ &= \pi A \end{aligned} \tag{5.13}$$

In the second step we utilized the definition of the scalar product, in the third we identified the integral over the surface with the surface area of the detector A and in the fourth step we used $d\omega = d\phi \; d\cos\theta$ to simplify the integral over the hemisphere.

In the fifth step we defined that only particles coming from one side of the telescope are considered. This is why we integrate rather over a hemisphere than over a full sphere. If we allowed the radiation to enter the telescope also from the backside the area A of the sensitive detector would have to be doubled.

The paper by Sullivan discusses a method how to obtain the geometric factor of an arbitrary particle detector. The procedure is to shoot particles from a randomly chosen starting point onto the instrument and see how many of these particles create a signal:

$$\Gamma_{\text{Geant4}} = \frac{\text{\# of detected particles}}{\text{\# of primary particles}} \cdot \text{gathering power of the opening aperture} \tag{5.14}$$

where the gathering power of the opening aperture is identified as the geometric factor of the collimator opening:

$$\begin{aligned} \text{gathering power of the opening aperture} &= G \\ &= \pi \cdot A = \pi \cdot \pi r^2 \\ &= \pi^2 \cdot (0.3\text{ cm})^2 \end{aligned}$$

Since we want to calculate the geometric factors of the two trigger conditions which reject particles coming from the back (see section 3.1.1), it is eligible to use the "one sided" equation 5.13.

We set up two Geant4 (Agostinelli et al. 2003; Allison et al. 2006) simulations with 10^7 events for electrons and protons from 20 keV to 1,000 MeV. The particles start from a random point on a sphere around the EPT and aim for an area in the middle of the instrument (see fig. 5.3). After the simulations, we apply equation (5.14) to discrete energy bins to get primary-energy-dependent geometric factors that represent the triggers' different sensitivities for different particle types at varying energies.

The model of EPT in this simulation is the latest design that reflects all the results of this work. This means that the torus around the foil collimator is included, the collimator design and the shielding follows the shape discussed in section 5.2 and in section 5.3, the distance between the detectors is 0.4 mm, detector A is covered with a Kapton foil and that the magnetic field implemented represents the field produced by the manufactured magnet systems.

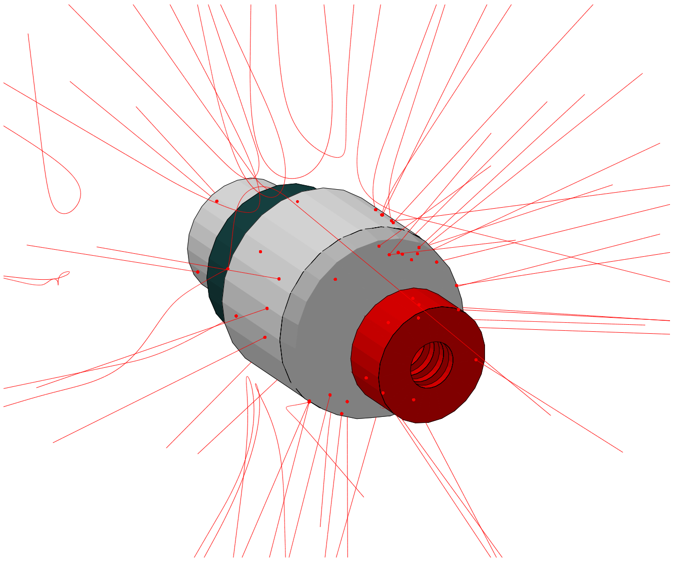

Figure 5.3.: A graphical view of the GEANT4 simulation for determining the geometric factors of EPT. The particles (here: electrons) are shot into the volume starting from a randomly chosen point on a sphere that surrounds the EPT head. The target points for each particle are also randomly chosen from the surface of a disk with radius 0.3 cm located in the middle of the volume and perpendicular facing the starting point of the particle. The magnetic field of the EPT agent system is imported in this simulation which leads to some curved trajectories of the electrons.

Discussion of the Geometric Factor for Trigger Condition A

The blue dotted line in fig. 5.4 represents the analytic calculation from equation (5.11). The factor for electrons gradually rises up close to the calculated value and stays nearly constant until it drops again when the electrons have enough energy to penetrate the first detector and to produce a signal in the second detector. Then the trigger condition is no longer fulfilled and the events are rejected by the anti-coincidence logic. Due to the scattering ability of electrons this does not happen abruptly but rather gradually – just as the rise at the lower energies also happened gradually. After reaching a minimum, the geometric factor increases again because of high energy electrons that pass through the aluminum shielding and end in the inner segment of detector A (see also fig. 5.6 and fig. 5.14). In fig. 5.6 we see that the total stopping power of electrons in aluminum rises again after going through a minimum at around 10^3 - 10^4 MeV. This explains the drop of the geometric factor at energies higher than 10^4 MeV. Fewer electrons can pass the shielding and reach the detectors since they lose more energy in the aluminum.

As predicted in section 3.3, the protons get stopped in the foil up to approx. 250 keV. After that, the geometric factor rises at once to the calculated value just as if the foil wasn't in the way. At higher energies the protons can penetrate the first detector and produce a signal in the second detector and thus get rejected by the anti-coincidence logic. This situation is reflected by a steep decline of the geometric factor at around 10^4 keV. When the protons reach relativistic velocities they can reach the detector through the shielding and raise the geometric factor again (see also section 5.4). At even higher energies, the energy loss of the protons in aluminum rises again and their ability to penetrate the shielding and with that the geometric factor decreases again (see also fig. 5.31(a)).

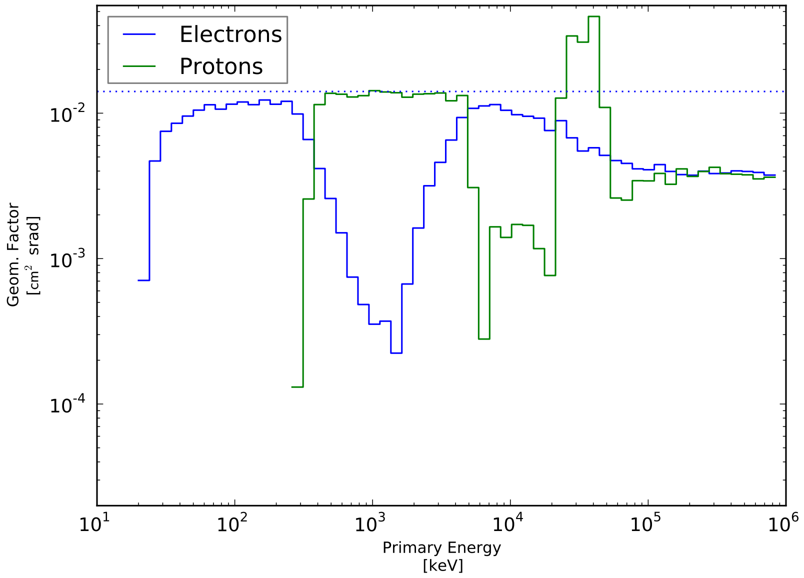

Figure 5.4.: Geometric factors of trigger condition A for electrons and protons.

Discussion of the Geometric Factor for Trigger Condition C

As before, the blue dotted line in fig. 5.5 also represents the analytic calculation from equation (5.11). The geometric factor for the electrons follows the course of the factor in fig. 5.4 except that low energy electrons can not reach detector C and get deflected away. Beginning at approx. 250 keV, the geometric factor for the electrons gradually rises first due to scattered electrons in the collimator, but then with higher energies ($\gtrsim 10^3$ keV) due to electrons passing through the shielding. Subsequent the geometric factor for electrons equals the factor from fig. 5.4.

The geometric factor for protons begins at a high level for low energies since there is no foil in the path of the particles that could stop them. Some protons with very low energy can get deflected by the magnetic field when their angle of entry is disadvantageous (similar to electrons – see section 6.2.6). But the influence of the field on the protons soon abates and the geometric factor for protons nearly reaches the calculated value until it suddenly drops drastically because the protons now penetrate the first detector and enter the second detector and get rejected by the anti-coincidence logic. From this point on, the geometric factor for protons follows the run of the respective factor in fig. 5.4.

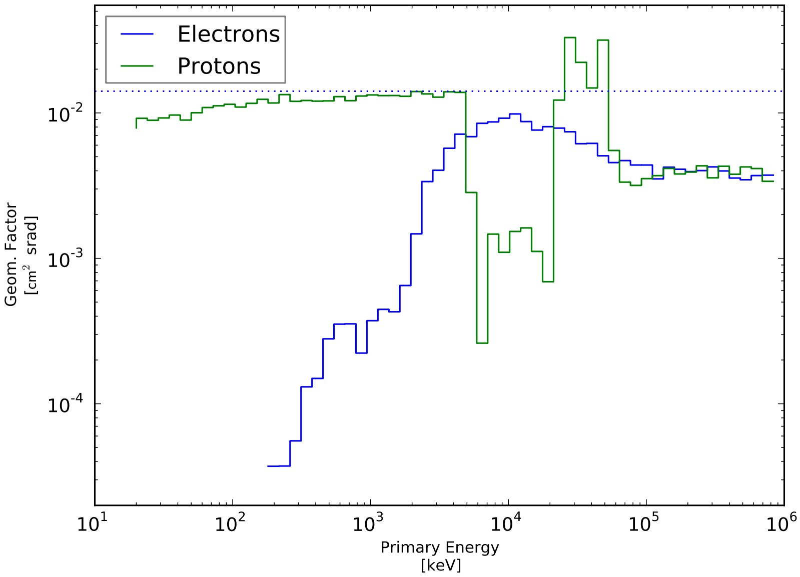

Figure 5.5.: Geometric factors of trigger condition C for electrons and protons.

Conclusion

The results of the Monte-Carlo-method in fig. 5.4 and in fig. 5.5 clearly show the magnet/foil-separation of the particles in the respective triggers and that the analytically calculated factor from eqn. (5.11) is nearly reached in the energy ranges of interest. One can also see that higher energetic particles seem to penetrate the shielding of EPT and produce a signal in both triggers.

In this simulation, we only considered one single telescope head and neglected not only the second part of the EPT instrument but also the adjacent HET and the underlying spacecraft which both will absorb a great portion of radiation that would instead hit our instrument. This additional “shielding” will certainly lower the impact of particles coming through the aluminum of EPT and thus reduce the geometric factors at higher energies in fig. 5.4 and in fig. 5.5. And since the spectra of electrons and protons more or less follow a power law (see section 5.1), in which the abundances of high energy particles rapidly decrease, the impact of this radiation on the count rates is very low and is acceptable as the noise of our measurements. To further lower this effect, we can strengthen the shielding of EPT. This will be the topic in section 5.2.

Note

In this chapter we used some results of the forthcoming sections without mentioning them explicitly – like the shape of the shielding and the alignment of the detectors. But since the principle of the geometric factor and the analytically gained geometric factor of EPT itself will frequently be used in all the parts of this work, it seemed reasonable to put this chapter at this early point.

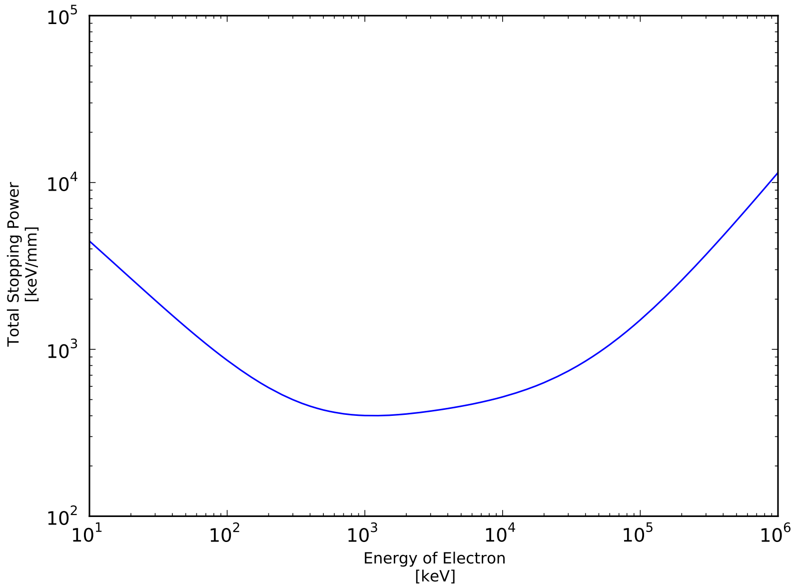

Figure 5.6.: The total stopping power of electrons in aluminum. Data obtained from the National Institute of Standards and Technology (NIST website: `http://physics.nist.gov/PhysRefData/Star/Text/ESTAR.html`).

5.1.3. Mote-Carlo Simulation for the Expected Count Rates

Now that we defined the detector setup and the geometry of the aperture, we can estimate the expected count rates in the four segments of the detectors neglecting the anti-coincidence logic by setting up a GEANT4 simulation (Agostinelli et al. 2003; Allison et al. 2006) of the mentioned solar particle event from Oct., 28th, 2003 (Mewaldt et al. 2005). The count rates we get from the simulation must then be scaled to represent the closer distance of 0.28 AU of Solar Orbiter to the sun.

As mentioned earlier, the shape of the electron spectrum in fig. 5.1a is a broken power law of two different exponents (-1.9 and -4.3) and the intersection at 527 keV. This can easily be patterned in GEANT4 by simply combining two separate simulation runs with two different energy distributions for the primary energy of the electrons. As also mentioned earlier, the proton spectrum is described by eqn. (5.2). We simulate this kind of distribution in GEANT4 by fitting three power law spectra with three different exponents to this shape (see fig. 5.7). The helium and oxygen spectra show the same behavior as the protons with the only difference that these ions are less abundant than hydrogen. We scale the count rates from helium and oxygen with the ratios given in the paper. The design we used in the simulations is the model #8 as in fig. 5.16, but the distance between the detectors is 1.5 mm and not 0.4 mm (as discussed in section 5.4). Since we turn off the anti-coincidence logic anyhow we can neglect this little difference.

Furthermore, this simulation still contains the Parylene foil spanned over the opening of the collimator instead of a Kapton foil applied onto detector A. But as we discussed earlier in section 3.3, the differences between Parylene and Kapton are not that big that we would expect essential different results from a simulation with Kapton.

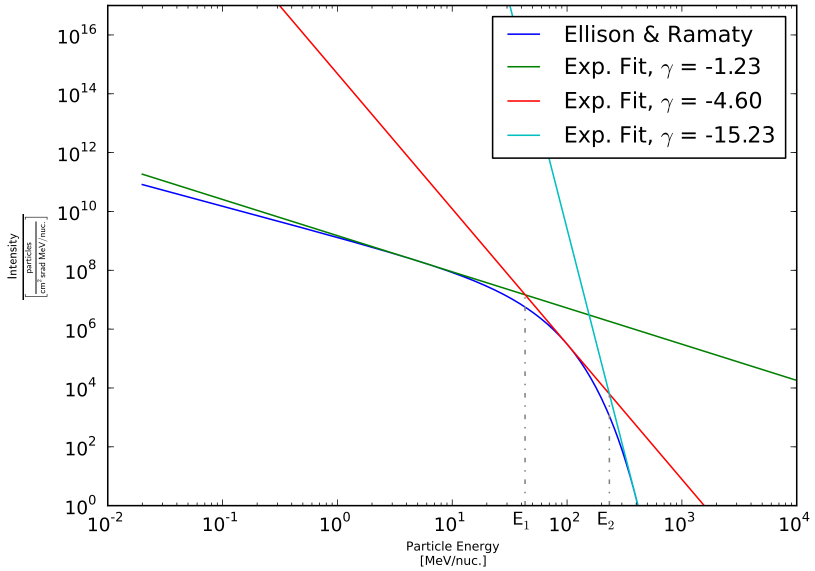

Figure 5.7.: We fit three exponential distributions to the proton spectrum that follows the shape given by Ellison et al. ($E_1 = 43$ MeV, $E_2 = 234$ MeV).

Fig. 5.8 illustrates the isotropic spatial distribution of the incident particles (here: electrons) in the GEANT4 simulation. The simulations contain $1 \cdot 10^7$ events per run with a minimum energy of 20 keV and a maximum energy of 10,000 MeV. To adjust two spectra with two different exponents we introduce a scaling factor α:

$$\alpha = \frac{\int_{E_1}^{E_2} \frac{dJ_2}{dE} dE}{\int_{E_0}^{E_1} \frac{dJ_1}{dE} dE} \tag{5.15}$$

with which we multiply the count rates induced by simulation 2.

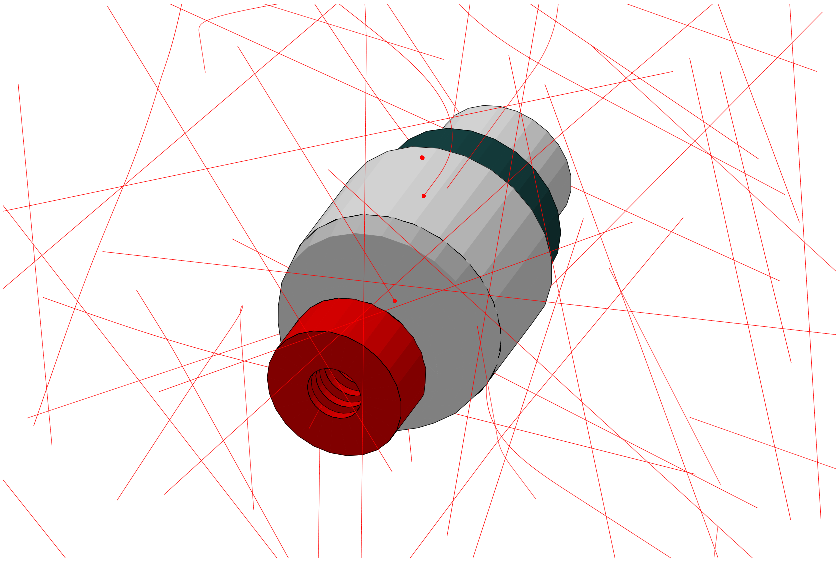

Figure 5.8.: Graphical view of the GEANT4-Simulation for the determination of the count rates in the single detectors. The particles are isotropically shot in into the simulated volume (here: electrons).

Since we want to give the expected count rates per second, we will have to find out how to scale the count rates from the GEANT4 simulations in order to represent the time of one second during the chosen event. From fig. 5.9 we read the intensities per second, cm^2, srad and MeV of electrons (7) and protons (30) in a given energy range. When we count the primary particles in this energy range in our GEANT4 simulations and compare this number with the intensities from the paper, we can derive an additional scaling factor β:

$$\beta_{\text{electrons}} = \frac{(\#\text{ of part. betw. 3 MeV and 15 MeV})_{\text{Mewaldt}}}{(\#\text{ of part. betw. 3 MeV and 15 MeV})_{\text{GEANT4}}} \tag{5.16}$$

$$\beta_{\text{protons}} = \frac{(\#\text{ of part. betw. 40 MeV and 80 MeV})_{\text{Mewaldt}}}{(\#\text{ of part. betw. 40 MeV and 80 MeV})_{\text{GEANT4}}} \tag{5.17}$$

with which we multiply the summed up count rates from the simulation parts to obtain count rates per second at 1 AU.

To extrapolate the particle fluxes at the fronts of interplanetary shocks driven by CMEs from 1 AU to distances closer to the sun, Lario et al. 2006 showed that we have to use a functional form of $J \propto r^{-3}$. In order to get the expected count rates at the perihelion of the Solar Orbiter orbit at 0.28 AU, we multiply the count rates at 1 AU with a third scaling factor γ:

$$\gamma = \left(\frac{1\text{ AU}}{0.28\text{ AU}}\right)^3 \tag{5.18}$$

Now we can plot the count rates in the single detector segments at 0.28 AU. In fig. 5.12 and in fig. 5.13 we show the integrated and the differential count rates in the segments of detector A and C separated by the particle types.

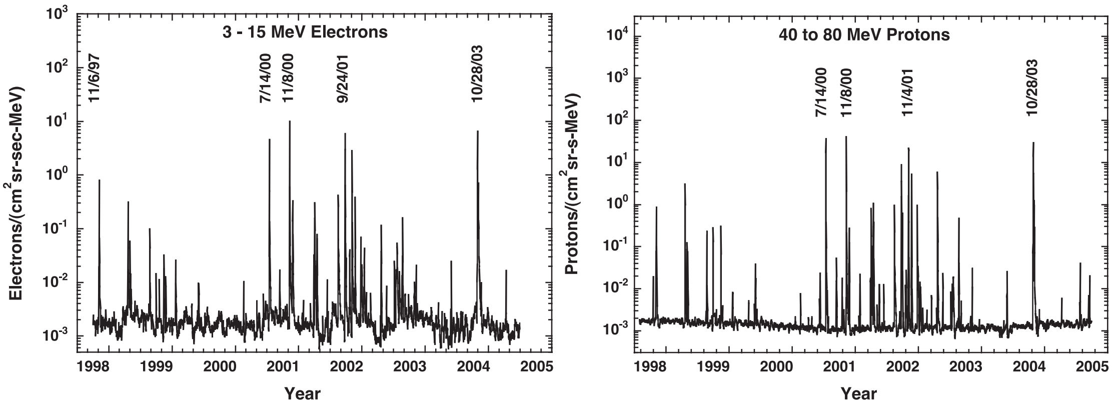

(a) Electrons *(b)* Protons

Figure 5.9.: The intensities of electrons (7 electrons $\left(\text{cm}^2 \text{ srad sec. MeV}\right)^{-1}$) and protons (30 protons $\left(\text{cm}^2 \text{ srad sec. MeV}\right)^{-1}$) of the event from Oct., 28th, 2003 (amongst other events) taken from Mewaldt et al.

In fig. 5.12, the upper two plots show the count rates against the detected energy in the inner and the outer segment of detector A, whereas the lower two show the count rates plotted against the primary energy of the incident particle. The red proton maxima at around $4 \cdot 10^4$ keV in the lower two plots show that the main proton contribution in both segments of detector A consists of relativistic particles that can penetrate the shielding but also the foil. The electrons' input to the count rates on the other hand consists of two parts: first at lower energies of electrons that come through or get scattered in the collimator and second at higher energies ($> 3 \cdot 10^2$ keV) of electrons that can penetrate the aluminum shielding (see also fig. 5.19).

In fig. 5.13, the upper two plots show the count rates against the detected energy in the inner and the outer segment of detector C, whereas the lower two show the count rates plotted against the primary energy of the incident particle. Just as in fig. 5.12, the red proton maxima at around $4 \cdot 10^4$ keV in the lower two plots represent the relativistic protons that come through the shielding and produce a signal in the segments of detector C. The inner segment of detector C also gets hit by some protons at lower enrages ($> 10^4$ MeV) coming through the aperture of the collimator. This contribution is almost missing in the outer part of the detector. The few signals detected at these low energies may be due to secondary radiation produced by Bremsstrahlung or ionization. The count rates for the electrons in the inner segment concerning the primary energy consist of three contributions: first of electrons that enter the collimator, get deflected by the magnetic field and then scatter into the detector, second of electrons at higher energies (> 750 keV) that enter the collimator and do not get deflected enough to hit the shielding but rather reach the detector directly, and third of high energy electrons ($> 3 \cdot 10^2$ keV) that can penetrate the aluminum shielding.

The results from fig. 5.10 to 5.13 show that the count rates in every detector-segment stays with 3,000 counts per second at the most far below the limit of the electronics of 10^5 counts per second. The geometric factor was chosen so that we can be sure to record even the strongest events at the closest orbit with no corruptions in the measured data. We are even prepared to measure higher intensities at this close distances to the sun where Solar Orbiter will travel.

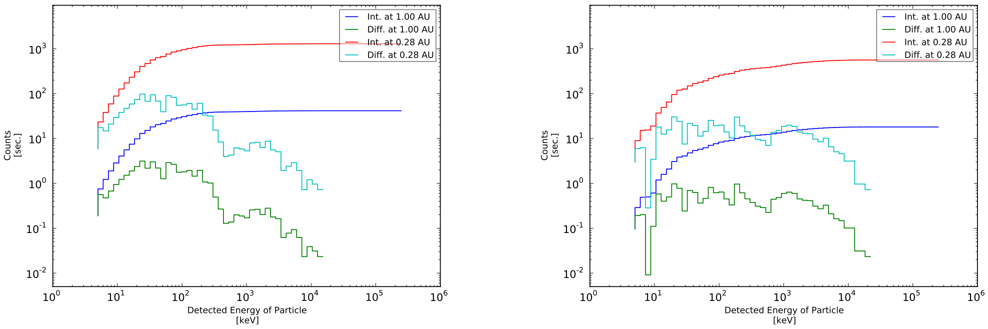

(a) Detector A, inner segment

(b) Detector A, outer segment

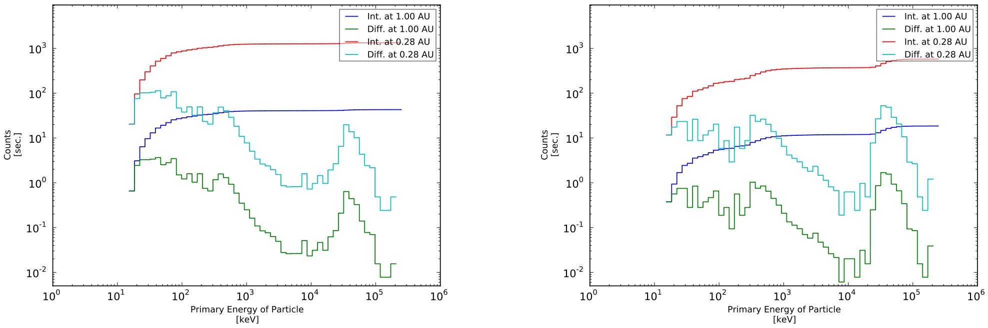

(c) Detector A, inner segment

(d) Detector A, outer segment

Figure 5.10.: The integrated and the differential count rates in the segments of detector A without any anti-confidence logic. The upper two plots show the count rates against the detected energy in the concerning segment, whereas the lower two show the count rates plotted against the primary energy of the incident particle.

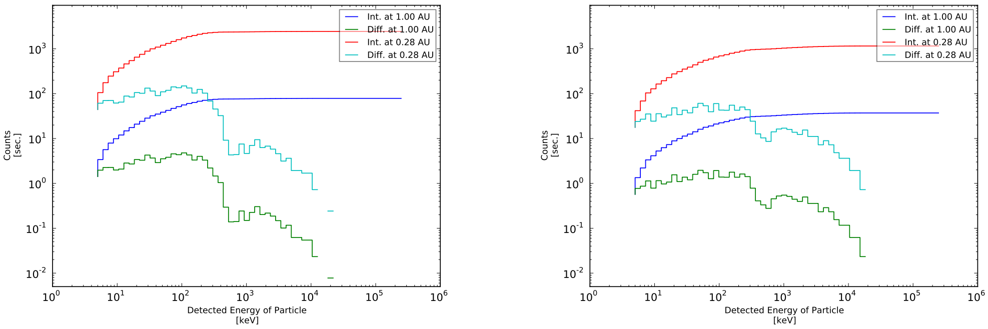

(a) Detector C, inner segment

(b) Detector C, outer segment

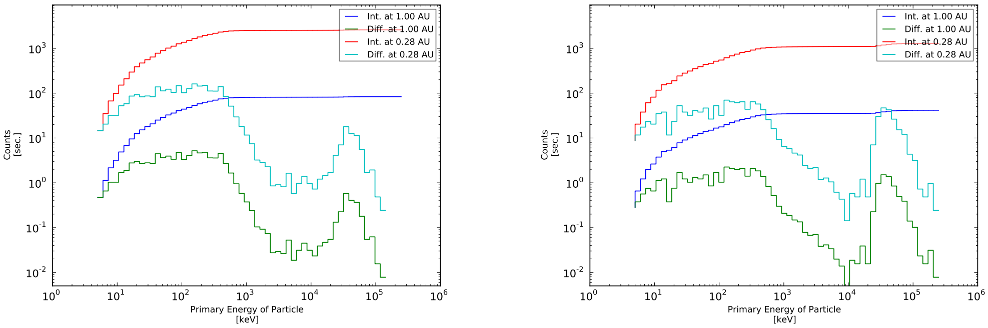

(c) Detector C, inner segment

(d) Detector C, outer segment

Figure 5.11.: The integrated and the differential count rates in the segments of detector C also without any anti-confidence logic. The upper two plots show the count rates against the detected energy in the concerning segment, whereas the lower two show the count rates plotted against the primary energy of the incident particle.

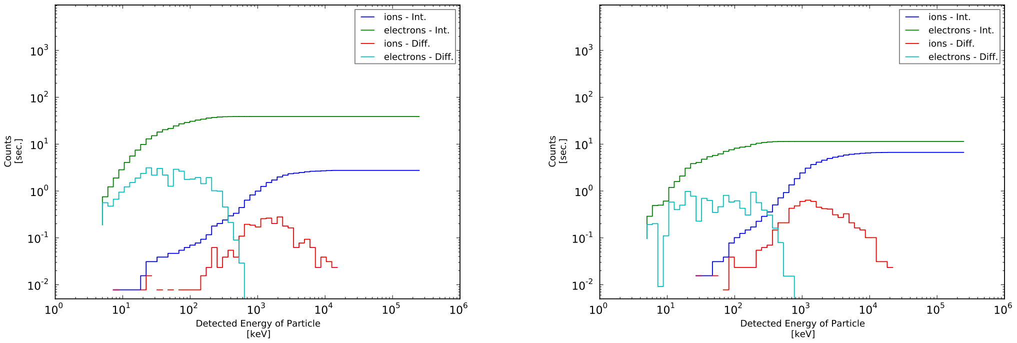

(a) Detector A, inner segment

(b) Detector A, outer segment

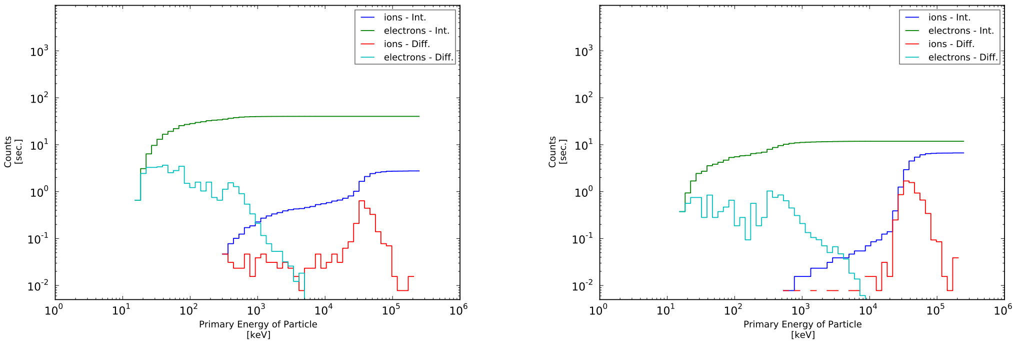

(c) Detector A, inner segment

(d) Detector A, outer segment

Figure 5.12.: The count rates in the single segments of detector A at 0.28 AU separated by the particle types.

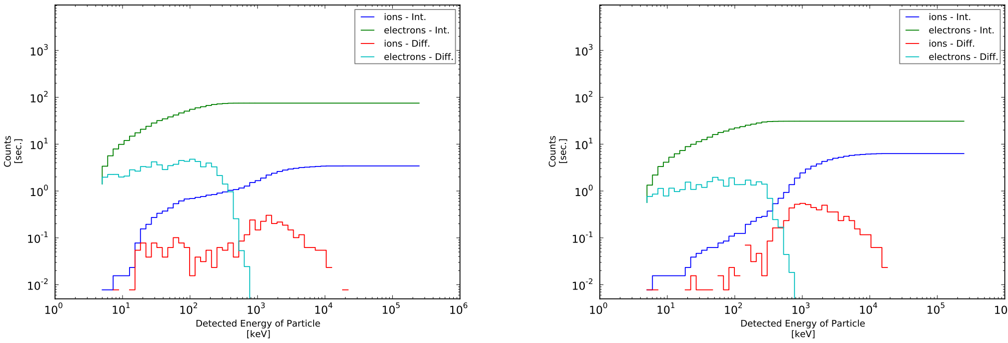

(a) Detector C, inner segment

(b) Detector C, outer segment

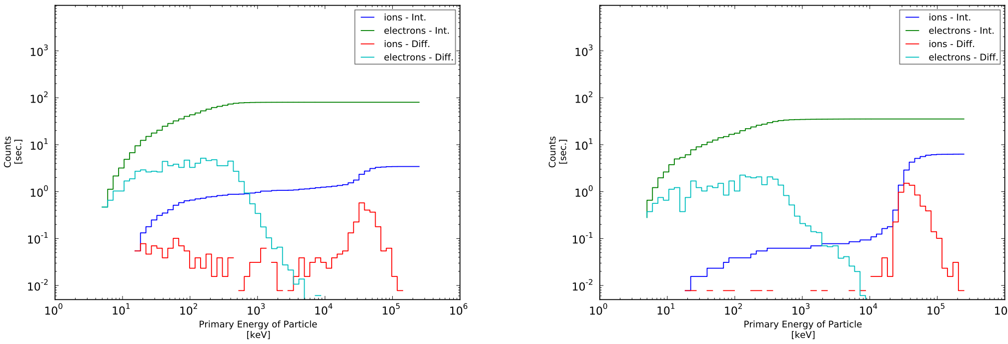

(c) Detector C, inner segment

(d) Detector C, outer segment

Figure 5.13.: The count rates in the single segments of detector C at 0.28 AU separated by the particle types.

5.2. Shape of the Shielding

The detectors of the EPT are closed off against the space environment by an aluminum housing with the collimators' apertures as the only opening to the outside. The purpose of this housing is to shield the detectors from incoming particles that did not come through the collimators. Unfortunately, it will not be possible to stop all particles in the aluminum (Evans 1955; Yao et al. 2006) – some high energetic particles will be able to pass through the housing and trigger a false signal in the electron or proton channel.

Especially scattered secondary high energy electrons produced by the relativistic galactic cosmic protons (Cucinotta et al. 1996) in the material of the spacecraft can produce a significant background noise in the silicon detectors (Ko et al. 2011).

Fig. 5.14 shows the range of electrons and protons in aluminum depending on the kinetic energy of the incoming particles. We see that the range of electrons is generally higher than the range of protons by an order of magnitude. The protons' range exceeds the electrons' range only for energies higher than approximately $3 \cdot 10^2$ MeV. But to stop particles at these energies we would have to shield the detectors with 10 cm of aluminum and this would make our instrument far too heavy.

Because of the much lower range of protons in aluminum and because they do not scatter in matter like the electrons do, we decide to just focus on the stopping of electrons in this discussion. When we can stop electrons we can also stop protons (regarding the energy range ($\leq 3 \cdot 10^2$ MeV) that is important for us).

Our task will now be to apply a "spot shielding" around the two silicon detectors in a way that we get a maximum protection from incoming relativistic electrons by simultaneously reducing the aluminum shielding and with this the weight of the instrument. This means, we need to strengthen the housing only at critical positions where passing-through particles could yield a signal for the trigger conditions and to keep the housing as thin as possible elsewhere.

This leads us to the main limitation to the design of our housing: we need to keep an eye on the overall weight of our instrument and this includes keeping the housing as lightweight as possible while making it thick enough to stop incoming particles. A simple solution to the problem would be to install the detectors in a big ball of aluminum that is thick enough to stop high energy electrons from all sides. But obviously this design would be very heavy and would thus waste a lot of our mass budget.

5.2.1. Features of the Shielding

Shielding of the EPT instrument is provided by:

- The housing that contains the detector stack.
- The two collimators.
- The magnet system that surrounds one collimator.
- The underlying electronic box.
- The adjacent HET.
- The spacecraft Solar Orbiter itself.

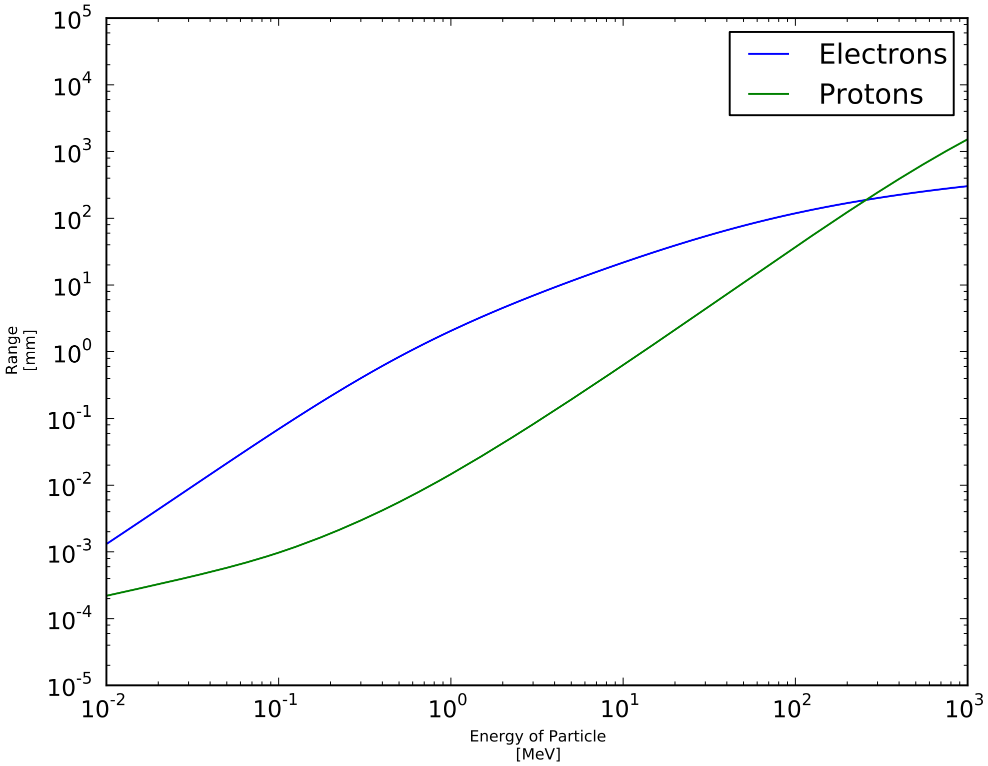

Figure 5.14.: The range of electrons and protons in aluminum. Data obtained from the National Institute of Standards and Technology. (NIST website: `http://physics.nist.gov/PhysRefData/Star/Text/ESTAR.html` (electron data) and
`http://physics.nist.gov/PhysRefData/Star/Text/PSTAR.html` (proton data))

The variation of the first two features will be discussed in this chapter, whereas the design of the magnet system will be the topic in chapter 6 and not be touched here. Nevertheless, we list the magnet system as a shielding part since it is mainly made of iron and thus plays a significant role for the shielding of particles.

The influences of the last three factors are not examined here and remain to be investigated in future works. Until this is done, this work has to be considered as a worst-case analysis in which the EPT is exposed to the space environment only protected by its own shielding.

Additional Features in the Shielding Design

Fig. 5.16(2) shows the basic design that shall be our starting point for the following optimization. It consists of a housing that surrounds the detector stack, two collimators attached to both sides of this housing (the collimator at the foil side is colored in red) and the magnet system (dark grey) around the collimator in front of detector C. As mentioned before, the magnet system shall remain untouched in this section.

To vary this basic design, we can thicken the housing as shown in fig. 5.16(3) and we can strengthen the collimators as seen in fig. 5.16(4). Additionally, to increase the aluminum shielding at the weak points of the design we introduce two additional features to the basic design:

- A torus at the interface of the housing and the collimator at the foil side (see fig. 5.16(6)).
- A dome around the housing (see fig. 5.16(1)).

Both features are round shaped to approximate a sphere of aluminum around the detectors. Especially the dome atop the housing reinforces the shielding more in an area from where incoming particles can avoid the anti-coincidence logic and trigger a signal in the inner segments of the detectors (see also section 5.4). The torus is installed at the interface of the collimator and the housing where we spot a weak point in the aluminum profile compared to the collimator. The two features are also easy to manufacture by our machine shop, which we also have to keep in mind in this discussion.

What these single features and variations mean to the profile of the shielding is shown in fig. 5.15. The figures 5.15(a)-(d) show the amount of aluminum that lies in the line of sight starting from the center of the gap between the two detectors and extending in varying directions. Here we can see the different contribution of each feature and variation compared to the basic design.

Now we combine these features and variations in eight different shielding designs (fig 5.16) that we want to test for their ability to stop high energy electrons. The aluminum profiles of these model are shown in fig. 5.17.

To test the models for their ability to attenuate the electron background we simulate $2 \cdot 10^6$ electrons in GEANT4 that aim for the inner segment of detector A starting from the half sphere 180° around the foil-collimator (see fig. 5.18). We then calculate the geometric factors for trigger A and the ratio of the detected events in trigger A to the initiated electrons in certain direction bins. The results are shown in fig. 5.19 and in fig. 5.20.

We see in fig. 5.19 that the choice of design really matters at higher energies starting from 700 keV. The model #8 reduces the electron background by nearly one magnitude

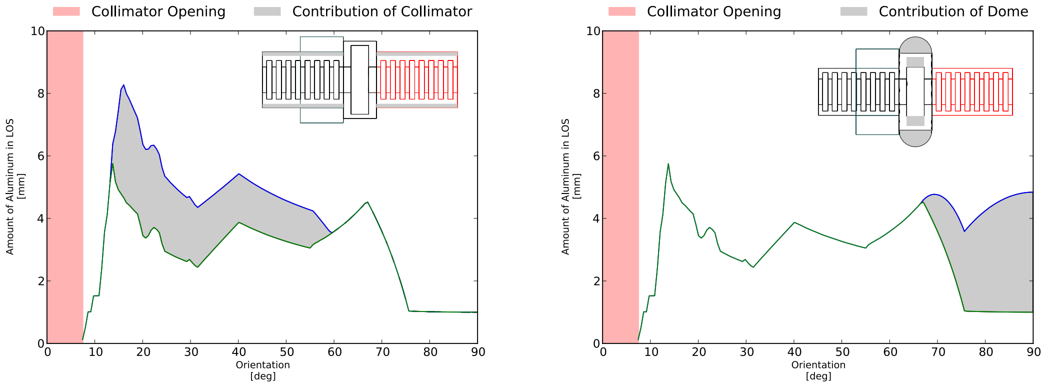

(a) Thickening the collimator *(b)* Adding a dome

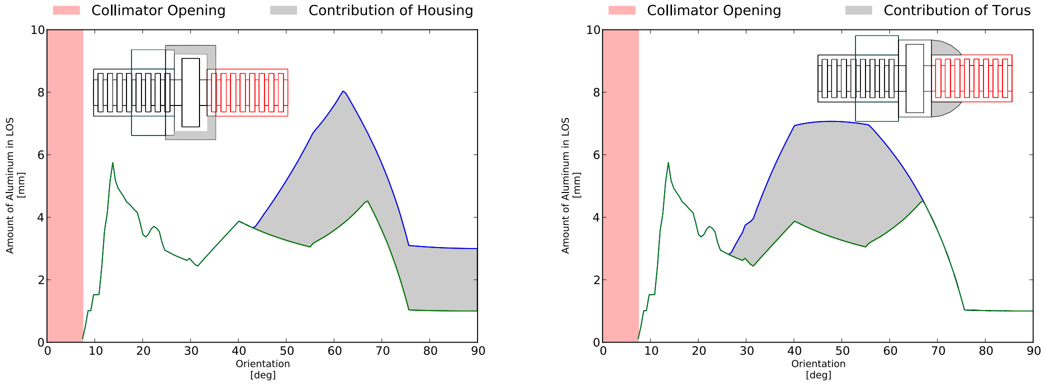

(c) Thickening the housing *(d)* Adding a torus

Figure 5.15.: The contributions (colored in light grey) of the different features of the shielding design compared to the basic design. Marked in red is the opening of the collimator at the foil side. The linked in sketches show which features are added (also colored in light grey) to the basic design. To avoid any confusions the magnets are not colored in dark grey anymore in these sketches. Plotted here is the amount of aluminum that lies in varying directions starting from the middle of the collimator at the foil side up to the “roof” of the housing (see also fig. 5.16 bottom). The green line represents the profile of the basic design as in fig. 5.16(2) and the area colored in a light shade of grey shows the amount of aluminum that is added to this basic shielding (also colored light grey in the linked in sketches).

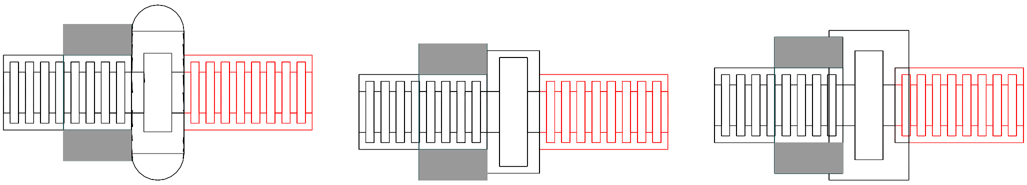

(1) Dome added *(2)* Basic *(3)* 2 mm thicker housing

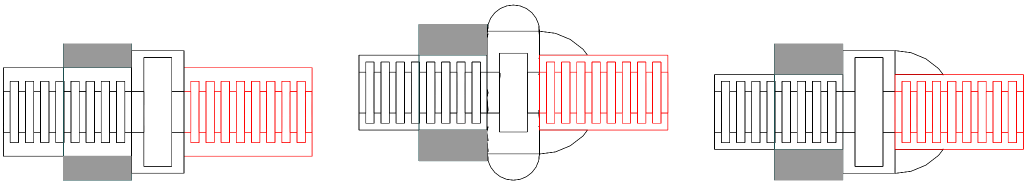

(4) 2 mm thicker collimator *(5)* Torus and Dome added *(6)* Torus added

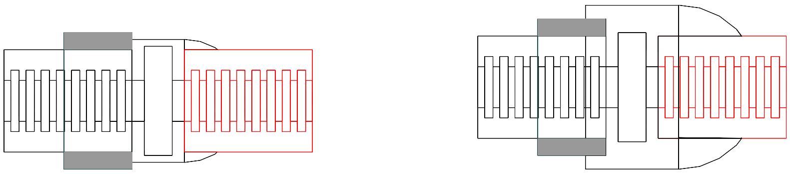

(7) Torus added, 2 mm thicker collimator

(8) Torus added, 2 mm thicker collimator, 2 mm thicker housing

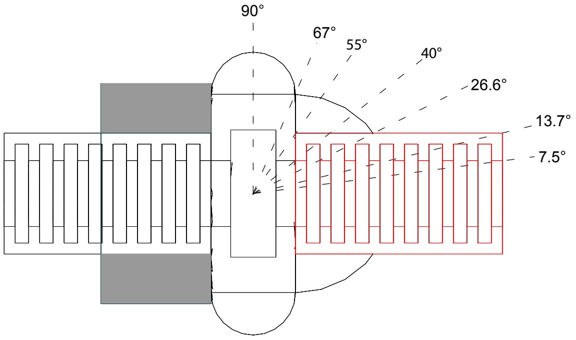

The dashed lines mark the beginnings and endings of the individual features such as the collimator, the torus, the housing, etc..

Figure 5.16.: The various possible designs of the EPT shielding. Colored in dark grey are the magnets of the magnet system. Note that the whole design is axially symmetric (see fig. 5.8).

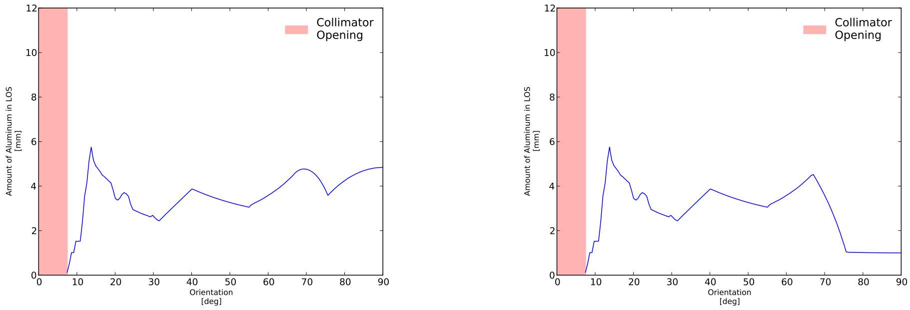

(1) Dome added

(2) Basic

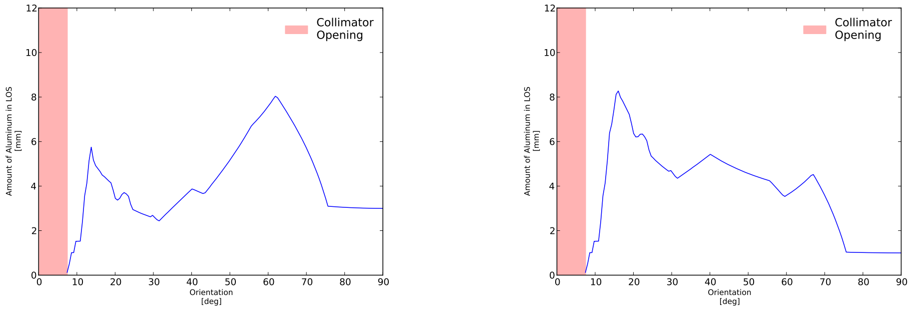

(3) 2 mm thicker housing

(4) 2 mm thicker collimator

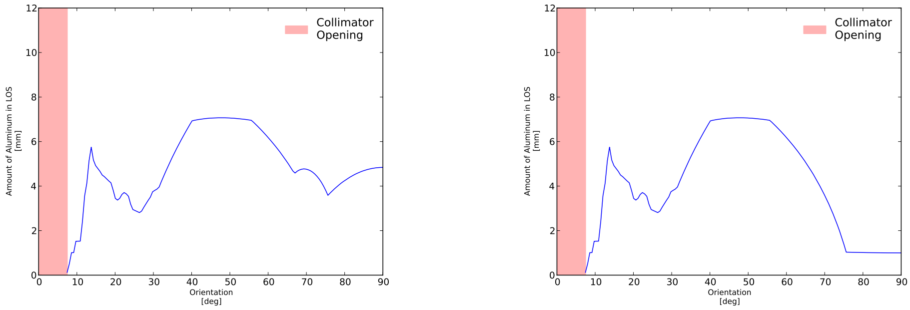

(5) Torus and Dome added

(6) Torus added

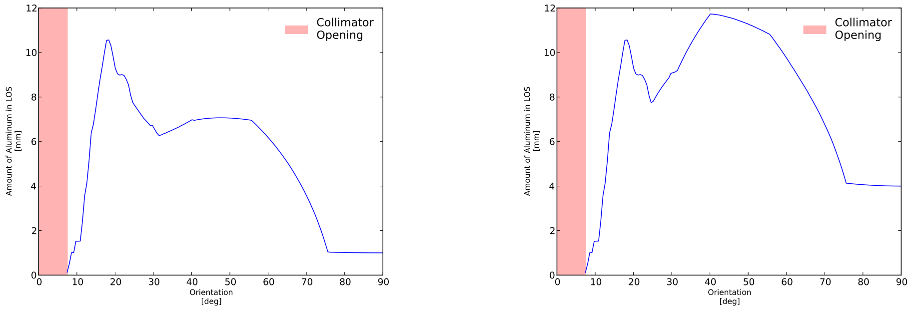

(7) Torus added,
2 mm thicker collimator

(8) Torus added,
2 mm thicker collimator,
2 mm thicker housing

Figure 5.17.: The aluminum profiles of the designs shown in fig. 5.16.

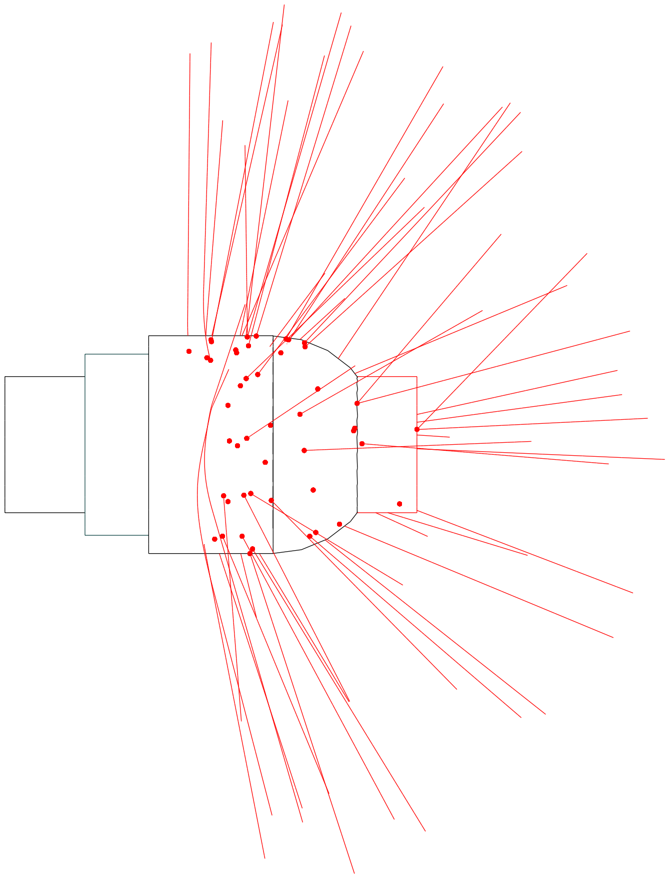

Figure 5.18.: Setup of the Geant4 simulation.

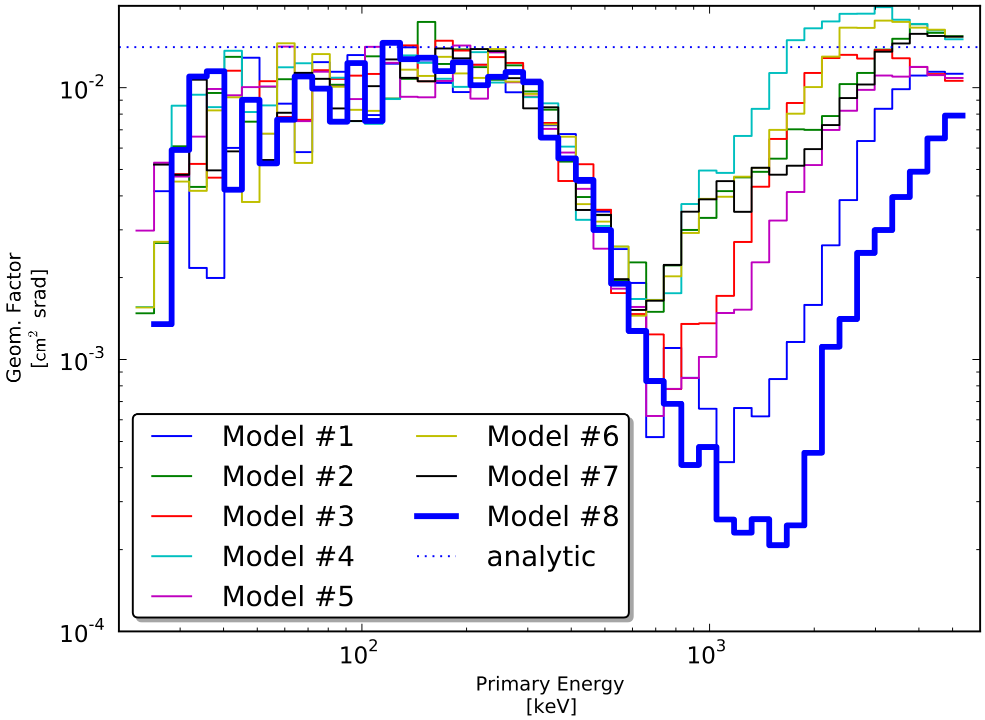

Figure 5.19.: Geometric Factors of the individual models. Model #8 (bold line) shows the least background at higher energies.

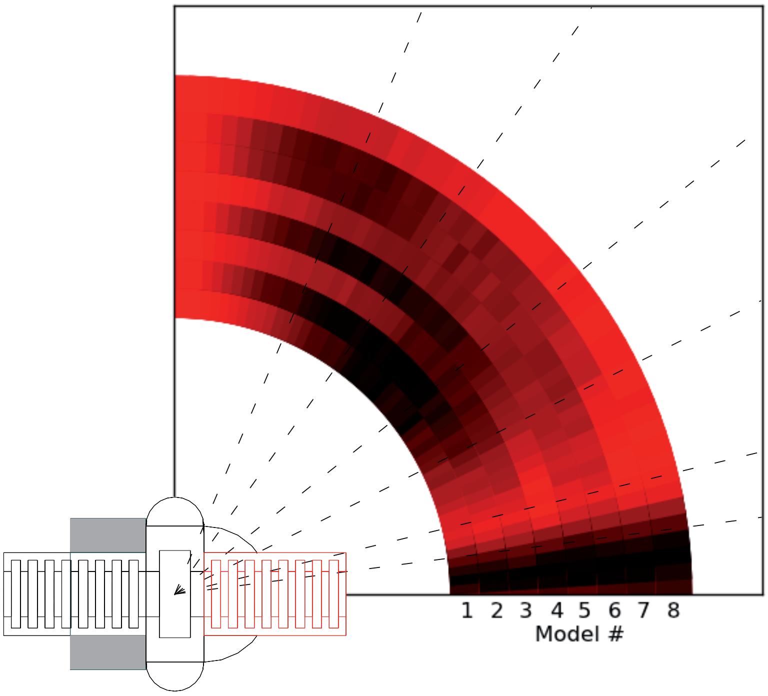

Figure 5.20.: The red arcs show from which directions the electrons in trigger A entered the shielding. The darker the arc the more electrons passed from that direction. The color scale of the arcs is normalized to one for each arc.

compared to the other designs. Fig. 5.20 shows that there is no weak point in model #8 – the design is able to shield the detectors equally in all directions. A look at the direction around 90° in fig. 5.20 shows that the amount of electrons scattering through the shielding there is almost the same for all models. This makes it possible to extend the cavity for the detector stack inside the housing (see section B.6). What really is important is the radius of the torus around the foil collimator – that's why the external dimension of the housing has to remain as stated in model #8.

But even with model #8 the geometric factor rises with higher energetic electrons up to and even exceeding the analytic calculated geometric factor from equation (5.10). This will be the background we must live with. The question which arises now is: How big is this background?

5.2.2. Background Electrons Entering Through the Shielding

As we saw in the figures 5.19 and 5.20, electrons with energies higher than 700 keV can penetrate the aluminum shielding and produce false signals in the silicon detectors. There are two different sources for these high energy electrons: the sun during SEP events and secondary electrons produced by primary protons from the galactic cosmic background (Ko et al. 2011).

In section 5.1.3, the figures 5.12 and 5.13 showed that the electrons above 700 keV during SEP events do not contribute much to the count rates in the single segments of the detectors. Especially fig. 5.12c reveals that we can not expect much background electrons in trigger A during SEP events.

To examine the second source, the secondary electrons produced by GCR protons in the aluminum shielding of EPT, we set up a GEANT4 simulation in which we shoot primary protons at an aluminum disk and see how many electrons are produced in the disk and with which energy they leave the disk (see fig. 5.21).

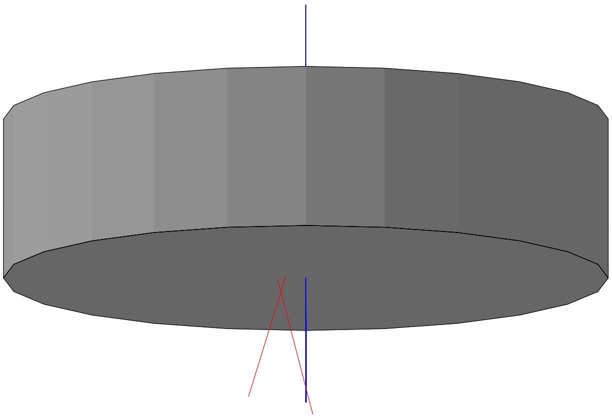

Figure 5.21.: Primary protons produce secondary electrons in aluminum: We shoot protons (blue) onto an aluminum disk and take stock of the produced secondary electrons (red).

The spectrum of the primary protons is drawn from the CREME96 project (Tylka et al. 1997) and represents the flux of GCRs during solar minimum when the GCR flux is highest (to make a worst-case assumption). Fig. 5.23 shows how the CREME96 spectrum is modeled in GEANT4.

The simulations are carried out with 10^6 protons per simulation distributed logarithmically flat over the energy range from 20 MeV to 10^5 MeV and with varying thicknesses of the aluminum disk from 1 mm to 16 mm in 0.5 mm steps.

At first, we count the secondary electrons and relate them to the number of primary protons. This production rate is plotted in fig 5.24. There, we see that the production of secondaries increases the more aluminum is in the way of the primary protons but reaches a limit of $\approx 1‰$ at about 12 mm aluminum.

Next, we plot the count rates of the electrons against the thicknesses of the disk and against the primary energy of the incident proton in fig. 5.25. The result of this plot is that only protons in a range from 10^6 to 10^7 keV produce a fair amount of secondary electrons. To know the energies of these electrons, we plot the count rates against the thicknesses and against the electrons' energy when leaving the target disk in fig. 5.26.

There we see that the electrons are narrowly distributed around an energy of about $5 \cdot 10^3$ keV and that the distributions broaden with increasing thicknesses. These secondary electrons all lie in an energy range where the geometric factor in fig. 5.19 nearly equals the analytical computed factor from equation (5.11).

For our worst-case analysis, we assume a constant geometric factor of the value from eqn. (5.11) for the secondary electrons and consider an aluminum shielding of 16 mm thickness in which the electrons are produced to get the highest production rate. By multiplying the geometric factor with the intensity at 16 mm in fig. 5.26 and summing up the resulting count rates per second and keV at all energies, we get a count rate of approximately $6.4 \cdot 10^{-7}$ electrons per second that can penetrate the EPT shielding during sun's quiet times.

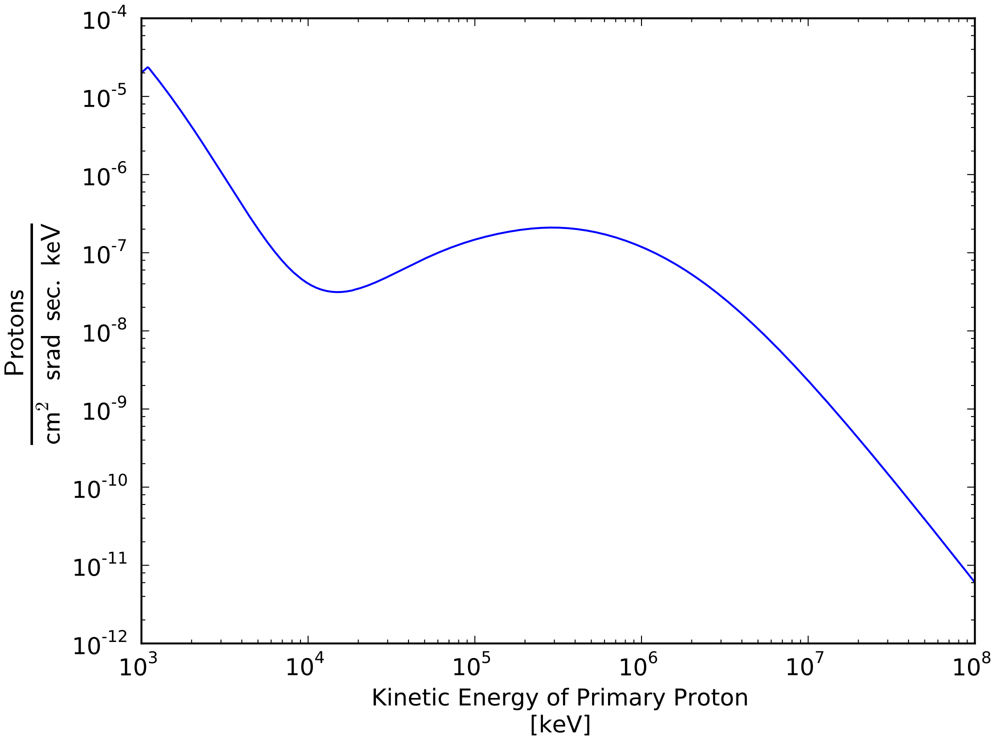

Figure 5.22.: The GCR proton spectrum as provided by the CREME96 website (`https://creme.isde.vanderbilt.edu`).

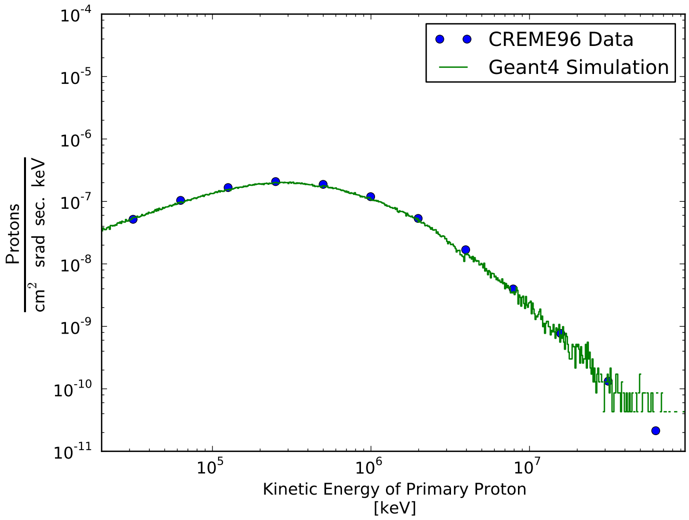

Figure 5.23.: The CREME96-spectrum from fig. 5.22 realized in the GEANT4 simulation.

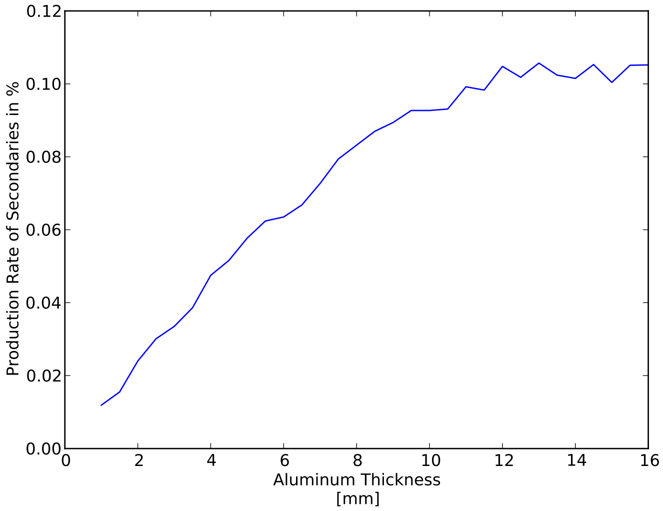

Figure 5.24.: The production rate of secondary electrons as a function of the thickness of the aluminum disk in fig. 5.21. We see that the production rates increases with growing thickness and reaches a limit of ≈ 1‰ at about 12 mm aluminum.

The electrons can be produced in any aluminum onboard the spacecraft – this must not necessarily happen inside the shielding of EPT. Since we took the general intensity of the GCR protons as our starting point for our valuation, the incident proton from fig. 5.21 can hit anywhere on Solar Orbiter and produce a secondary electron that reaches for EPT. The only time we needed an EPT specific value was the last step when we multiplied the secondary intensity with the EPT geometric factor. All the other steps were universal.

The result of $6.4 \cdot 10^{-7}$ electrons per second means that we can expect one false signal every 18 days which is negligible. In section 5.1 we saw that the aluminum shielding does its work during SEP events when the intensities are much higher than the GCR intensities.

5.3. Profile of the Collimator

Now that we have shaped the shielding around the detectors and the thickness of the collimators, it is time to take a look at the inside of the collimators. The profile of the collimator is especially important since particles can indirectly enter the detectors after hitting the inside of the aperture.

The collimators in front of the detectors have to fulfill two tasks:

- To keep away possible incoming direct sunlight when the spacecraft performs a 15° off-pointing maneuver at 0.28 AU (Solar Orbiter Team 2011) while still keeping track of the observed Parker-spiral.
  (**Note:** At the time of this work the off-pointing angle was defined to be 15°. However this value was lowered by the Solar Orbiter Team recently to 6.5°. Since

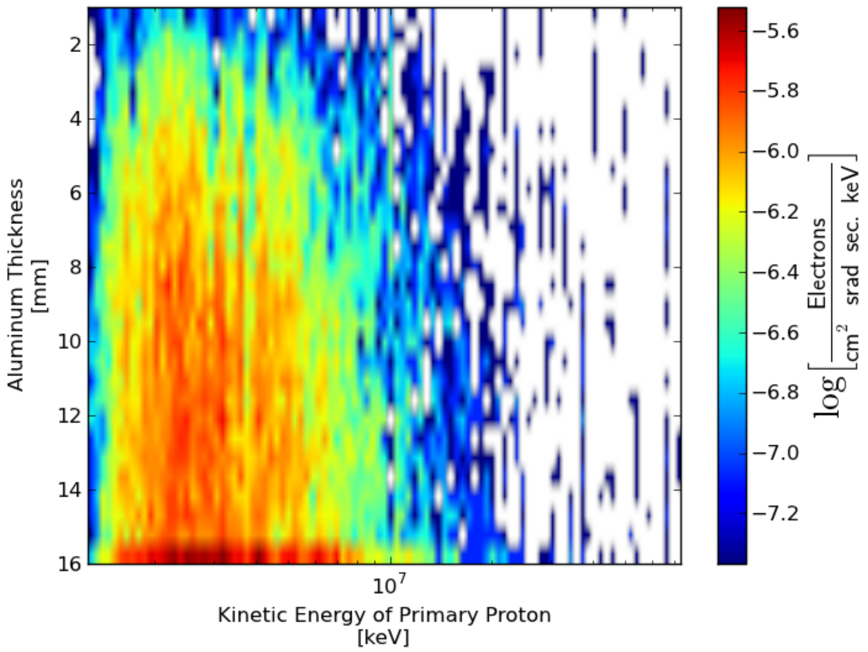

Figure 5.25.: The count rates of the secondary electrons plotted against the primary energy of the protons and against the thickness of the aluminum disk. One can see that almost only protons with a primary energy between 10^6 and 10^7 keV produce secondary electrons. We also see the result from fig. 5.24 verified that more secondaries are produced by a thicker aluminum disk.

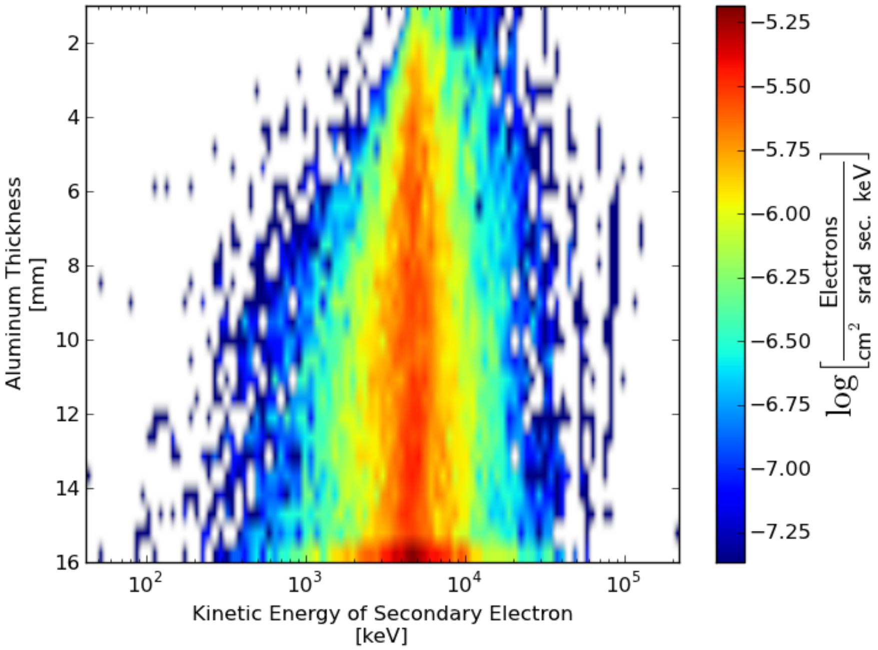

Figure 5.26.: The count rates of the secondary electrons plotted against the energy of these electrons when they leave the target disk and against the thickness of this disk. We see that the energy distributions of the electrons center at an energy level of about $5 \cdot 10^3$ keV and that the distributions broaden with increasing thicknesses.

our design based on the primary value still meets the requirements, we keep the geometry of the collimators as it is.)

- To hinder particles coming from outside of the cone around the middle axis of the telescope head to reach the detectors.

The first task can easily be dealt with by simply applying geometry. When the opening of the collimator is just as big as the inner segment of the detectors ($d = 6mm$), then the distance between the detector and the opening must be:

$$l = \frac{6 \text{ mm}}{\tan(15°)} \approx 22.39 \text{ mm}$$

The second task – to avoid detecting particles that head for the detectors from outside of a 15°-wide cone – would also be easily fulfilled, if it were only ions that must be kept away. Because of the greater mass compared to electrons, ions don't get scattered by the electrons of the aluminum shielding and quickly loose their energy by ionization processes in the aluminum until they are stopped (see fig. 5.14). So, when protons impinge the collimator under a greater angle than 15°, they enter the aluminum and stay in there and don't get scattered back into the detectors.

The path of electrons in matter on the other hand looks very erratic (Knoll 1989; Yao et al. 2006). Their low mass makes it easy for the electrons of the target material to scatter them into various directions – and possibly back into the detectors.

In order to attenuate this effect, we consider 10 different designs for the profile of the collimator and compare their ability to trap scattered electrons. In principle, the designs differ from each other in the shapes and thicknesses of ribs and in the depth and width of the gaps between those ribs.

We examine four different kinds of ribs:

- 1 mm thick ribs, rectangular shaped (named: thick ribs)
- 0.5 mm thick ribs, rectangular shaped (named: semi-thin ribs)
- 0.3 mm thick ribs, rectangular shaped (named: thin ribs)
- 0.3 mm thick ribs, sloped shape (named: thin cut ribs)

The width of the gap between the ribs is varied with the total number of ribs. Inside the collimator the ribs are arranged equally spaced. The depth of the gaps are chosen to be either 1.5 mm (named: normal) or 2.0 mm (named: deep). Additionally, we also consider a zig-zag shaped profile with 1.5 mm deep carvings. We refer these 9 models to a plain shaped interior of the collimator (named: "smooth" model) as a kind of basic design. The 10 different designs are shown in fig. 5.27 in profile and in fig. 5.28 three-dimensional.

Fig. 5.29 shows how we set up the GEANT4-simulation to test the collimator designs. We shoot 1,000,000 electrons with energies up to 10 MeV from the edge of the opening-cone onto the inner side of the collimator (spectral index 0). We then count the events detected in trigger A and compare this number to the number of events in trigger A from the "smooth" model. The results of these simulations can be seen in table 5.1 and in fig. 5.30.

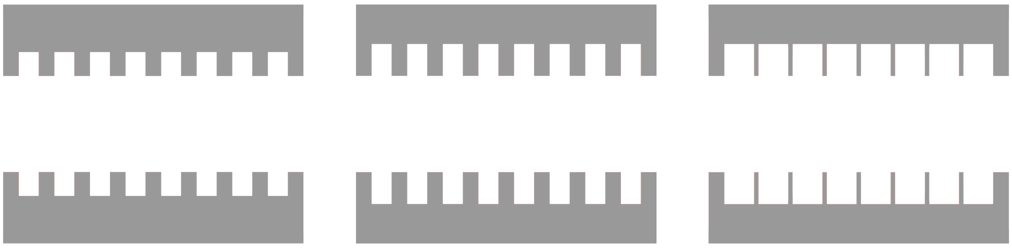

(1) 7 Thick Ribs, Normal Grooves

(2) 7 Thick Ribs, Deep Grooves

(3) 7 Thin Ribs, Deep Grooves

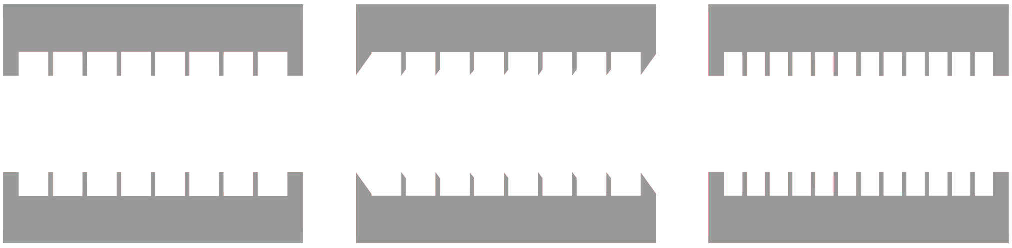

(4) 7 Thin Ribs, Normal Grooves

(5) 7 Thin Cut Ribs, Normal Grooves

(6) 11 Thin Ribs, Normal Grooves

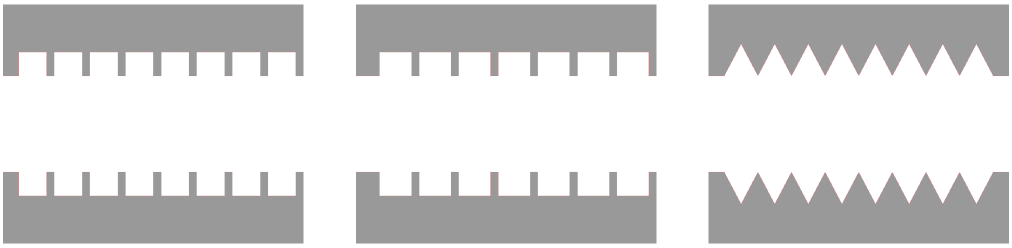

(7) 7 Semi-Thin Ribs, Normal Grooves

(8) 6 Semi-Thin Ribs, Normal Grooves

(9) Zig-Zag-Shaped, Normal Grooves

Smooth Collimator

Figure 5.27.: The various collimator-designs seen in profile. The particles enter the collimator from the right side. The current design for EPT is model 7.

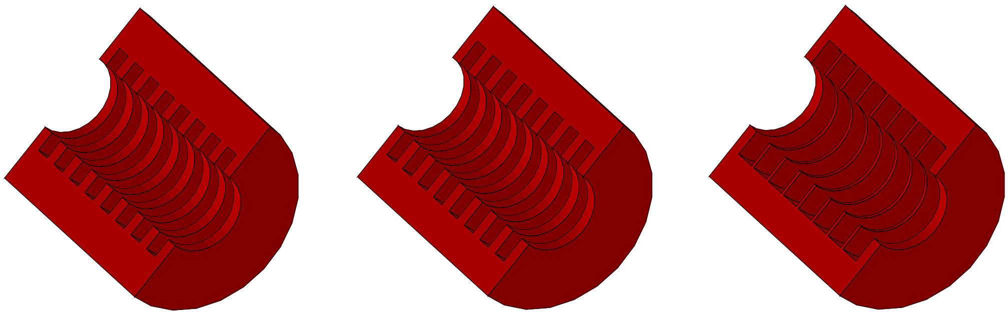

(1) 7 Thick Ribs, Normal Grooves

(2) 7 Thick Ribs, Deep Grooves

(3) 7 Thin Ribs, Deep Grooves

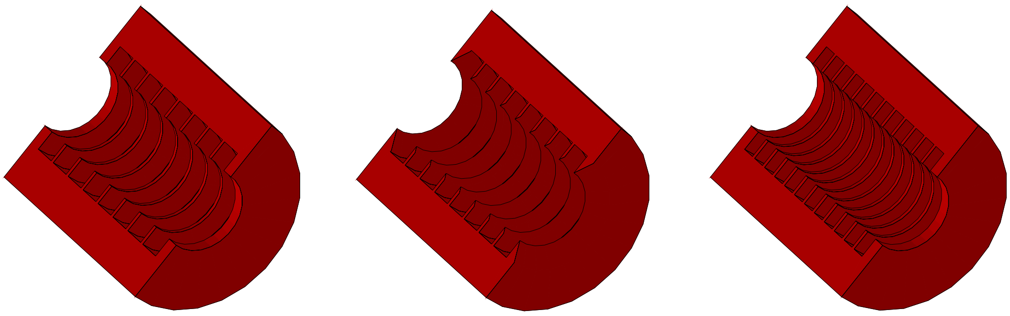

(4) 7 Thin Ribs, Normal Grooves

(5) 7 Thin Cut Ribs, Normal Grooves

(6) 11 Thin Ribs, Normal Grooves

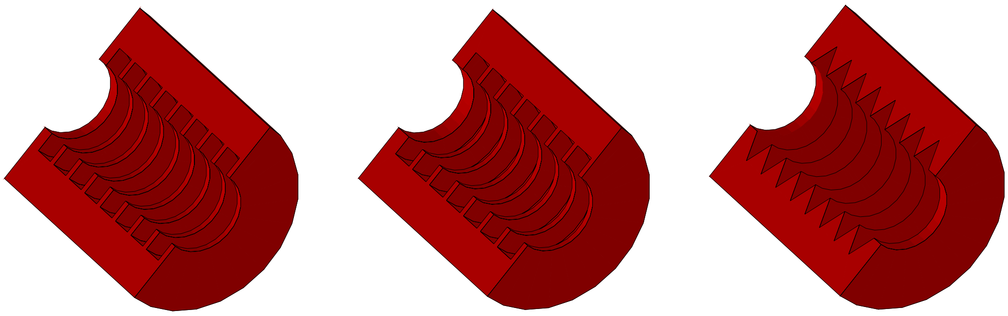

(7) 7 Semi-Thin Ribs, Normal Grooves

(8) 6 Semi-Thin Ribs, Normal Grooves

(9) Zig-Zag-Shaped, Normal Grooves

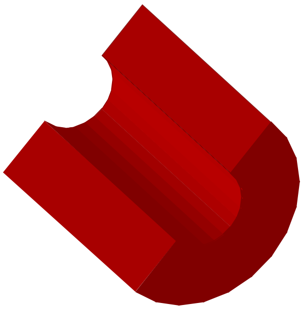

Smooth Collimator

Figure 5.28.: The various collimator-designs seen in 3D. The particles enter the collimator from the lower right. The current design for EPT is model 7.

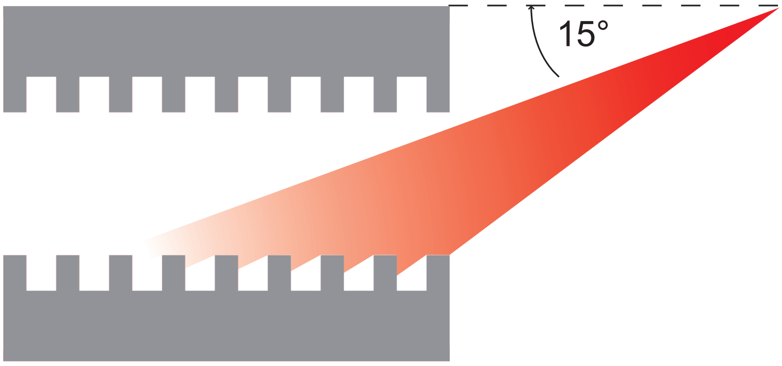

Figure 5.29.: We shoot in the electrons at an angle of 15° aiming at the entrance of the collimator.

#	Model	Counts in Trigger A	Counts reduced compared to "Smooth"
	Smooth Collimator	148202	
1	7 Thick Ribs, Normal Grooves	126114	-14.9 %
2	7 Thick Ribs, Deep Grooves	127638	-13.9 %
3	7 Thin Ribs, Deep Grooves	104517	**-29.5** %
4	7 Thin Ribs, Normal Grooves	107771	**-27.3** %
5	7 Thin Cut Ribs, Normal Grooves	108992	-26.5 %
6	11 Thin Ribs, Normal Grooves	121202	-18.2 %
7	7 Semi-Thin Ribs, Normal Grooves	117955	**-20.4** %
8	6 Semi-Thin Ribs, Normal Grooves	117963	**-20.4** %
9	Zig-Zag-Shaped, Normal Grooves	122240	-17.5 %

Table 5.1.: Statistics of the background reduction. Marked bold are the two models with the best background reduction and the two producible model with the best reduction.

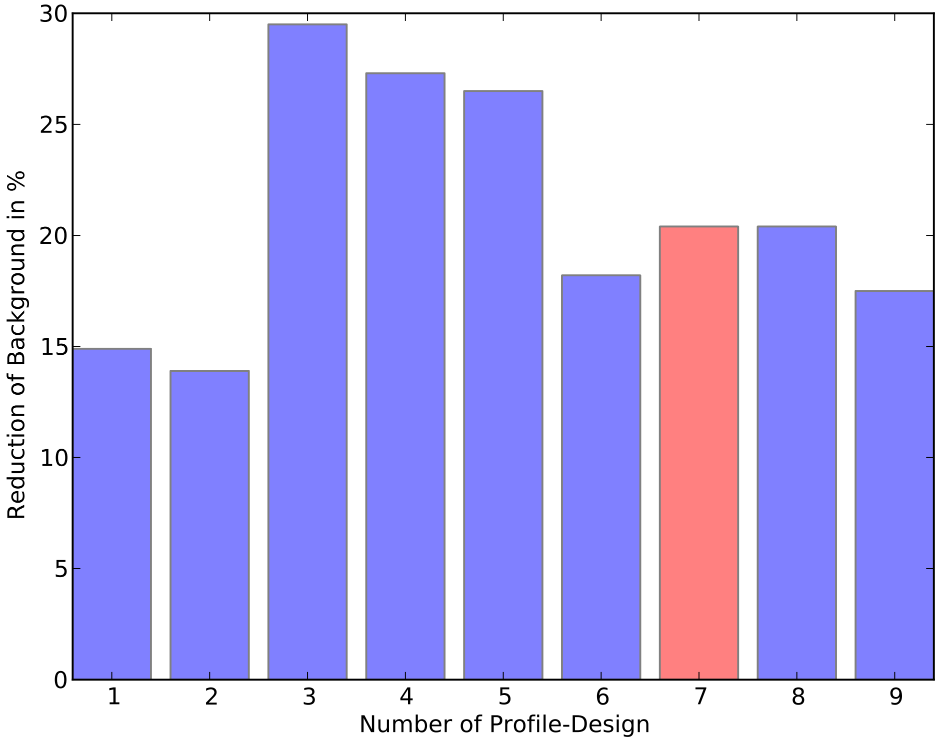

Figure 5.30.: Statistics of the background reduction. Marked in red is the model to be produced. Unfortunately, the models 3,4 and 5 can not be produced by our machine shop but would be better in terms of reducing the scattering.

The results show that it would be best to make the ribs as thin as possible and to cut the gaps between them deep and wide. Unfortunately, the models that reduce the background the most, model 3 and 4, can not be produced by our workshop. The thinnest ribs that can be manufactured are 0.5 mm thick. This is why we chose to utilize model 7 for EPT.

5.4. Minimum Ionizing Particles

Even with the collimator and the aluminum shielding around the detector stack we can not stop all particles at arbitrary energies before they reach the detectors. As explained in Yao et al. 2006 and in Knoll 1989, the Bethe-Bloch-Formula (Bethe 1930) describes the energy loss of ions traveling in matter:

$$-\frac{dE}{dx} = \frac{4\pi e^4 z^2}{m_0 v^2} \cdot NZ \left[\ln\left(\frac{2m_0 v^2}{I}\right) - \ln\left(1 - \frac{v^2}{c^2}\right) - \frac{v^2}{c^2} \right] \tag{5.19}$$

where v is the velocity of the primary particle, ze the charge of the primary particle, m_0 the electron rest mass, N the number density of the target matter, Z the atomic number of the target atoms and I is the average excitation and ionization potential of the absorber.

Fig. 5.31(a) shows this differential energy loss dE/dx for protons in aluminum calculated with equation (5.19). We see that the energy loss shows a local minimum at around $2 \cdot 10^3$ MeV where the proton loses only ≈0.05% of its energy per mm. In fig. 5.17(8) we see that the protons have to pass through 12 mm of aluminum at most. This means that they will only lose ≈0.6% of their energy and can easily penetrate the aluminum shielding and reach the detectors. Particles in this energy range are called minimum ionizing particles (or MIPS abbreviated) and can especially be found in the galactic cosmic background radiation (Barnett et al. 1996; Simpson 1983).

As illustrated in fig. 5.31(b), protons at the local ionizing minimum approximately lose 500 keV per mm which leads to a signal of 166 keV in the 300 μm thick silicon detectors. Since this signal is higher than the threshold of 20 keV, the incident proton could be counted as a trigger event depending on the angle of entry. Figure 5.32 demonstrates the situation how a particle can cause a false trigger signal: The geometry and alignment of the detectors span an angle α from which incoming protons can bypass the outer segments and the inner segment of the other detector. When the particles take this path they are able to invoke one of the trigger conditions A or C.

To compare this kind of opening with the aperture of the collimators, we calculate the solid angles of the two windows. The angles α_1 and α_2 from fig. 5.32 are determined by:

$$\tan(\alpha_1) = \frac{t}{d_{\text{inn}}} \tag{5.20}$$

$$\tan(\alpha_2) = \frac{d}{d_{\text{out}}} \tag{5.21}$$

where t is the thickness of the detectors, d_{inn} the diameter of the inner segments, d_{out} the size of the outer segments and d the distance between the two detectors.

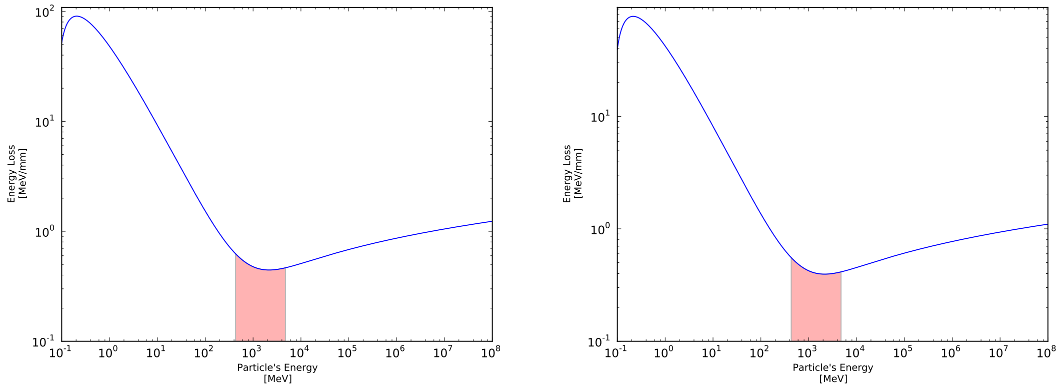

(a) Aluminum *(b)* Silicon

Figure 5.31.: The differential energy loss of protons in aluminum and silicon. Marked in red are the local minima.

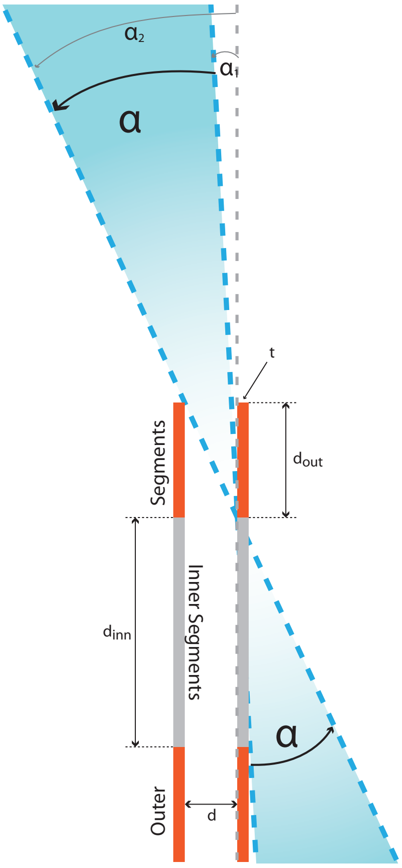

Figure 5.32.: The minimum ionizing particles can make a signal in the inner segment of a detector without triggering the anti-coincidence when they enter from both sides of the detector through the colored angles α.

With this we can calculate the solid angle for the minimum ionizing particles:

$$\Omega_{\mathrm{M}} = 2 \cdot \int_0^{2\pi} \int_{\alpha_1}^{\alpha_2} \sin\alpha \; d\alpha \; d\phi \tag{5.22}$$

The integrals are multiplied by 2 because the particles can enter the detector from both sides (the two ribbons in fig. 5.33). The solid angle of the collimator opening is estimated as follows:

$$\Omega_{\mathrm{C}} = 4\pi \sin^2\left(\frac{15^\circ}{2}\right) = 0.214094 \text{ srad} \tag{5.23}$$

To lower Ω_{M} α_2 must converge towards α_1. For this purpose, we can vary the four parameters t, d_{inn}, d_{out} and d. The thickness t of the detectors, however, is defined by the energy range of the particles that we want to observe and to thicken the detectors would diminish the ability to separate the particles (see fig. 5.4 and fig. 5.5). The detector geometry d_{inn} and d_{out} is determined by the geometric factor and the opening angle of 15° that we want to realize.

This leaves the distance d between the two collimators as the only parameter to change Ω_M. Fig. 5.33 illustrates how the solid angle of the MIPS changes for four different detector distances. Fig. 5.34 shows the solid angle for the MIPS, Ω_{M} exceeds Ω_{C} at detector distances of 0.6 mm and above. The figure shows the expected behavior of the solid angle: the smaller the gap between the detectors, the lower the background from the minimum ionizing particles.

To confirm this behavior we determine the geometric factors as described in section 5.1.2 for four different distances including the current detector distance of 0.4 mm. The results in fig. 5.35 are in good agreement with the analytic discussion. The geometric factor for the distance of 0.5 mm is comparable to the analytic calculated geometric factor from equation (5.10).

Since the geometric factor rapidly increases with the distance between the detectors the background of the galactic cosmic rays can interfere with the measurements of the lower energetic protons and electrons emitted by the sun. The high energetic MIPS may not be as abundant as the solar particles, but their much larger solid angle makes them not negligible. To lower this effect, it is important to decrease the detector distance as much as possible. The plan for the flight-models of EPT is to use detector stacks that are built as a sandwich-construction with 0.4 mm space between the two silicon detectors.

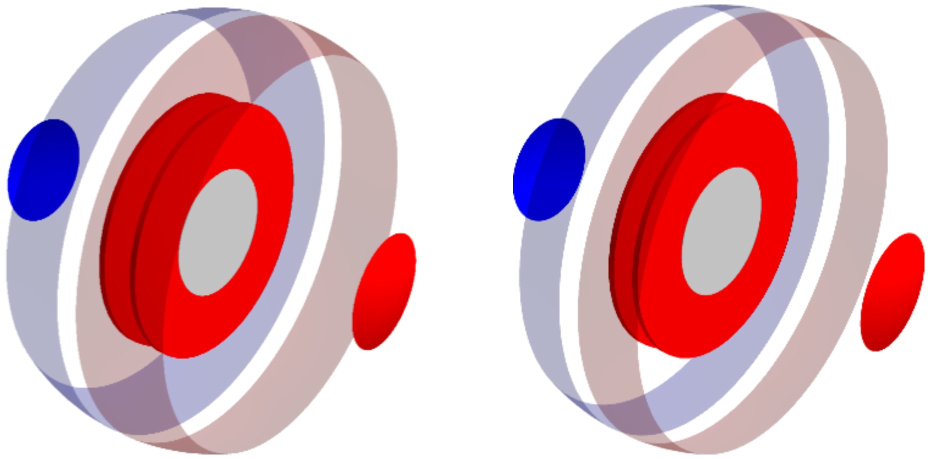

(a) 1.4 mm *(b)* 1.0 mm

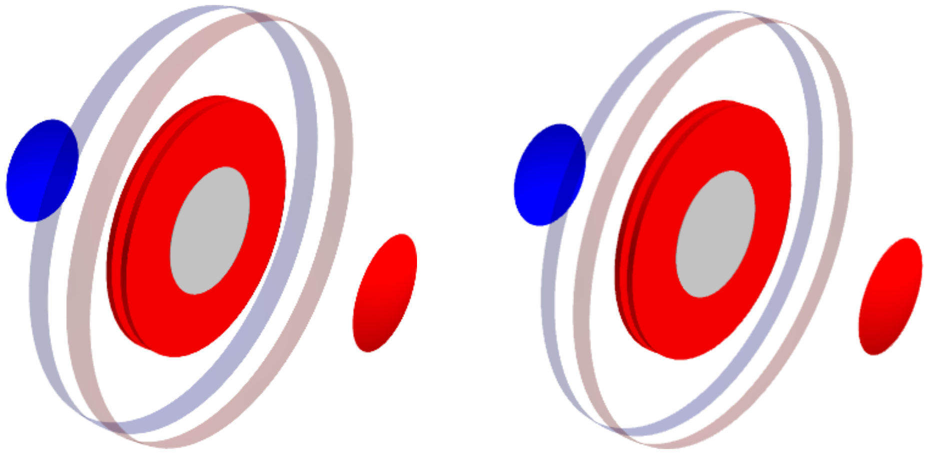

(c) 0.5 mm *(d)* 0.4 mm

Figure 5.33.: Three-dimensional view of the situation how minimum ionizing particles enter the detectors after passing through the shielding. Shown here are three different detector alignments with varying distances between them (1.4 mm, 1.0 mm, 0.5 mm, 0.4 mm). The blue and red disks behind and in front of the detectors represent the solid angles of the collimators. The red and blue ribbons around the detectors show the area from where the minimum ionizing particles must aim for the inner segments of the detectors to trigger a signal. The ribbons are located at the same radius as the collimator openings – i.e. the areas of the ribbons and the disks give an indication of the relation between the two solid angles.

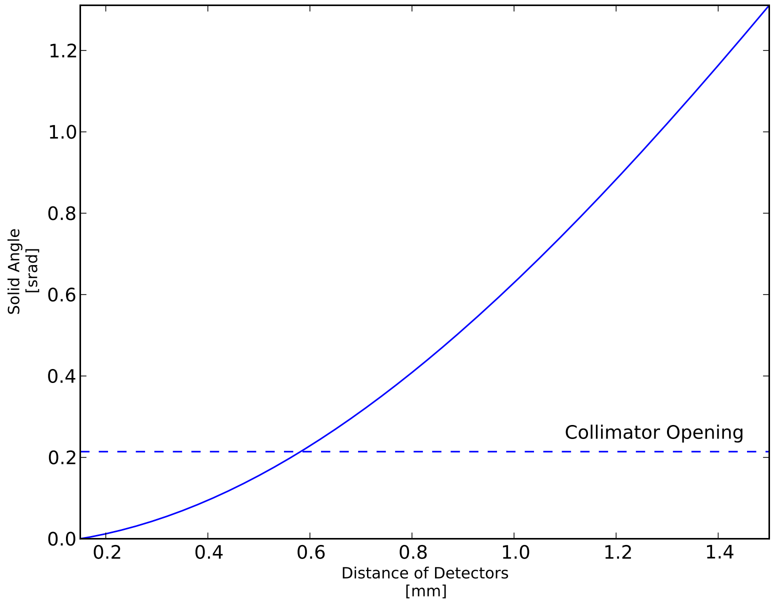

Figure 5.34.: The solid angles of the areas through which minimum ionizing particles can enter compared to the solid angle of one collimator calculated with eqn. (5.22) and (5.23).

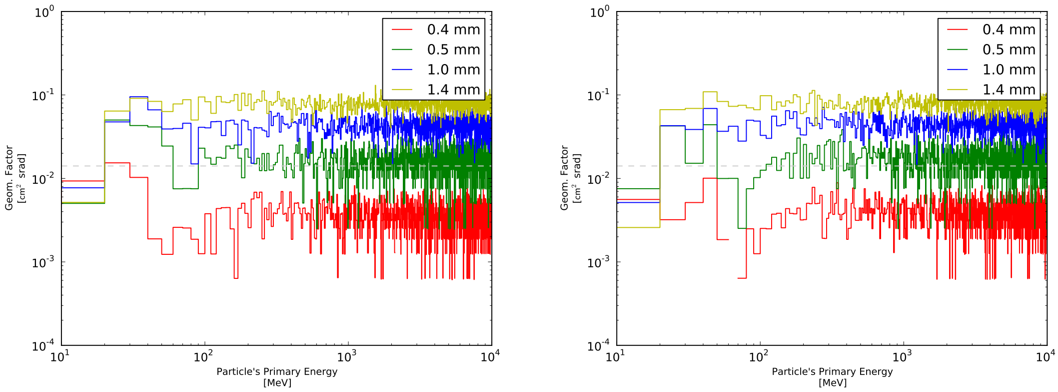

(a) Trigger A

(b) Trigger C

Figure 5.35.: Geometric factors for minimum ionizing protons. The dashed line shows the geometric factor of one trigger calculated with equation (5.10).

Of course, it would be favorable to further diminish this separator, but 0.4 mm is the smallest distance allowed by the manufacturer CANBERRA since wire bonding interconnection between the detectors and the electronics box is located in the gap between the detectors and this is the limiting factor of the distance d.

5.4.1. Expected Count Rates From the MIPS

The paper from Simpson gives a spectrum of the protons from the galactic cosmic background. The peak value that lies between 10^2 and 10^3 MeV indicates an intensity of:

$$I_\mathrm{p} = \frac{2}{\mathrm{m}^2\ \mathrm{srad\ sec.\ MeV}}$$

To gather the count rates we expect from the minimum ionizing protons, we use eqn. 5.8 and multiply the geometric factor from fig. 5.35 of about $4 \cdot 10^{-7}\ \mathrm{m}^2$ srad with this intensity:

$$\begin{aligned} C &= \Gamma \cdot I_p \\ &= \frac{8 \cdot 10^{-7}}{\mathrm{sec.\ MeV}} \end{aligned}$$

This means that we can expect approximately one such MIPS-event per MeV every 11 days. Taking a look at the hydrogen spectrum in the paper, we see that the differential flux drops to the fourth of the peak value at the energies of $5 \cdot 10^1$ MeV and $2 \cdot 10^3$ MeV. When we consider the peak value to be constant in this energy range we can make a raw estimation of the expected count rates in the trigger conditions induced by the MIPS:

$$\frac{\Delta N}{\Delta t} = C \cdot \left(2 \cdot 10^3\ \mathrm{MeV} - 5 \cdot 10^1\ \mathrm{MeV}\right) \approx \frac{8 \cdot 10^{-7}}{\mathrm{sec.\ MeV}} \cdot 2 \cdot 10^3\ \mathrm{MeV} = \frac{1.6 \cdot 10^{-3}}{\mathrm{sec.}} \tag{5.24}$$

This means that we can expect one false event in one of the trigger conditions produced by the MIPS every 10 minutes. This is a noise level with which we can live since it does not disturb the measurements of the solar fluxes very much.

6. Magnetic Field

6.1. Design of the EPT Magnet System

The EPT instrument onboard Solar Orbiter is a successor of the Solar Electron Proton Telescope – SEPT, which is a part of the SEP instrument suite onboard the NASA mission STEREO. As such, it also uses a magnetic field to deflect electrons away from the proton channel (Müller-Mellin et al. 2008; Russell 2008).

Just as SEPT, EPT is also designed to be a two-sided instrument with two telescope heads in one instruments. This allows us to let two telescopes share one magnet system (see fig. 6.2 and fig. 6.3b) and to inherit the quadrupole approach from SEPT.

The quadrupole, we will design, consist of two pairs of cubic rare-earth permanent magnets, which are each paired by a yoke made of an iron-cobalt alloy (see fig. 6.1). To separate the two magnet/yoke-assemblies, we use an aluminum separator in the middle of the magnet system. The permanent magnets are glued to the yokes by a special non-magnetic and heat resistant adhesive (VAC Magnetbonder 500). The two magnet/yoke-assemblies are held in place on the aluminum separator by the magnetic force, that the opposing magnets execute on each other and by notches, that are milled into the separator.

One big advantage of using a quadrupole magnet system instead of dipole setups is the behavior of the field around the systems. The magnetic flux density of a dipole declines with the cube of the distance:

$$B_{\text{dipole}} \propto r^{-3}$$

whereas the flux of a quadrupole decreases faster:

$$B_{\text{quadrupole}} \propto r^{-4}$$

We use this behavior to have a strong field within the collimator of the instrument whilst having a rather week field outside. This will later turn out to be a critical issue, when discussing the requirements we need to fulfill, in order not to disturb the measurements of the magnetometer MAG onboard Solar Orbiter.

6.1.1. The Manufacturer Vacuumschmelze

The VACUUMSCHMELZE GmbH & Co. KG in Hanau, Germany is one of the leading global manufacturers of magnetic materials and related products[1]. Our working group has already had a good co-operation with that company, when building and designing the magnet systems for SEPT. Back then, Vacuumschmelze constructed the permanent magnets and paired them together, so that they made up the best possible quadrupole

---

[1] VACUUMSCHMELZE-Website: `http://www.vacuumschmelze.com`

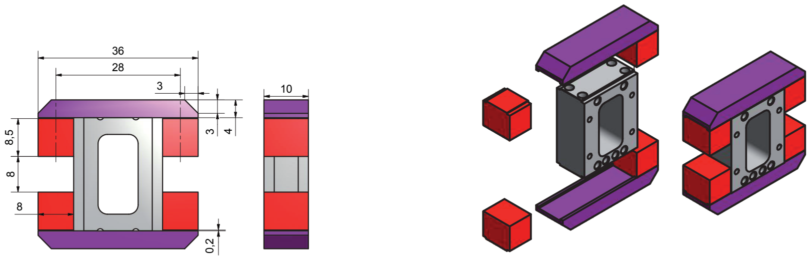

(a) Dimensions of the EPT magnet system (all in mm).

(b) Exploded view drawing of the EPT magnet system.

Figure 6.1.: Views of the CAD model of the EPT magnet system (by Lars Seimetz).

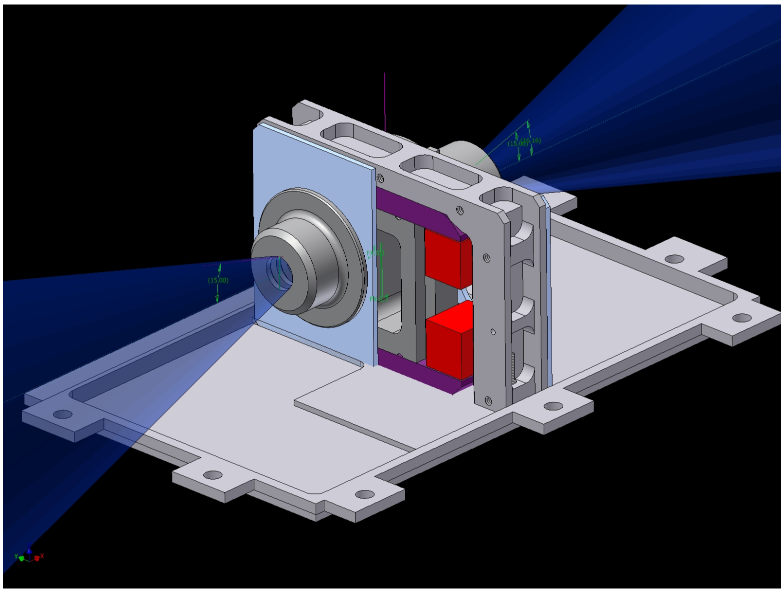

Figure 6.2.: This cutaway drawing of EPT reveals how two telescope heads share one magnet system (by Lars Seimetz).

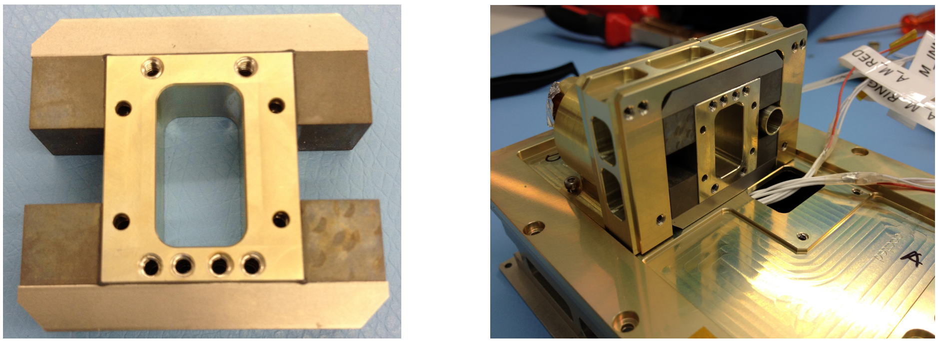

(a) A magnet system as delivered by Vacuumschmelze.

(b) A magnet system installed into the demo model of EPT.

Figure 6.3.: One of the actual magnet systems delivered by Vacuumschmelze.

setup. After that, they glued the magnets onto the yokes, plugged those magnet/yoke-combination on our separators and sent the magnet systems safely to Kiel. This procedure will now be carried out again for the manufacturing of the EPT systems.

The good experience that our group made with Vacuumschmelze during that whole process, makes this company our first choice for manufacturing our magnet systems.

In addition to that, later in section 6.2 it will turn out to be very convenient that the software we use for calculating the magnetic fields emitted by our systems already supports all the materials in the product line of VACUUMSCHMELZE.

6.2. Computing the Magnetic Field with RADIA

Although the EPT instrument inherits its design from SEPT onboard the STEREO spacecraft and with this also the magnet system to deflect electrons that enter the proton channel, EPT needs to be much smaller than SEPT, which makes it necessary to resize the magnet system while keeping the conceptual design as a quadrupole magnet.

Before ordering magnet systems from our component supplier VACUUMSCHMELZE in Hanau, we had to find out how the magnet systems had to be built.

Our chosen tool for this is a numerical software called “RADIA”, which we will introduce in the following.

6.2.1. About RADIA

RADIA is a three-dimensional magnetostatics computation software developed by Oleg Chubar, Pascal Elleaume and Joël Chavanne at the ESRF Synchrotron in Grenoble, France (Chubar et al. 1998; Elleaume et al. 1997). It was first released in April 1997 and is currently available in version 4.1 and can freely be downloaded from the ESRF website[2].

Designed to calculate the magnetic fields produced by accelerator magnets, RADIA enables us to determine the field generated by the magnet system inside EPT. In the following we will briefly present how RADIA works, what the benefits are and where the drawback or limitations of RADIA lie.

6.2.2. Computational Method

RADIA uses the boundary integral method as described in Chubar et al. 1998 and in Elleaume et al. 1997 and not a finite-element method. Whilst the finite-element method relies on a limited volume in which the computation takes place, the integral method can handle virtually infinite volumes. We benefit from that since we have to estimate magnetic field strengths in very small dimension inside the instrument (in front of the proton channel), but also in bigger dimensions further away from EPT close to the MAG instruments. This would require the redefinition of the limiting volume for each purpose and would also increase the computation time rapidly.

The calculations of the fields emerging from each single object are done with analytical solutions instead of numerical algorithms, as it is done with the finite-element method. This leads to a higher precision even at greater distances from the sources of the field.

---

[2] RADIA Website: `http://www.esrf.eu/Accelerators/Groups/InsertionDevices/Software/Radia`

The final computation in RADIA is handled by using a so called interaction matrix, which represents the mutual interactions between the objects in the simulation. For this, RADIA supposes a constant magnetic field in each object, which is not always desired. The field lines in a curved object for example follow this curved shape and will not point in the same direction in every point. This problem can be solved by segmenting the concerning objects into smaller subdivisions. Then each of these subdivisions can contain a field vector that points into a different direction than the field vectors of the other subdivisions.

6.2.3. Materials

RADIA can handle miscellaneous kinds of linear and nonlinear, isotropic and anisotropic magnetic materials. Especially supported are the materials sold by the german company VACUUMSCHMELZE including their hysteresis curves. Additionally, one can define any magnetic material by specifying its hysteresis curve.

6.2.4. Shapes

The physical parts of the magnet system can be represented in RADIA with various shaped volumes (e.g. parallelepipedic blocks, extruded polygons or polyhedrons). In principal, these volumes are shaped by limiting surfaces, that are taken as a starting-point for the computations of the magnetic field. In our case, we only need very simple kinds of volumes like cubes for the permanent magnets and cut cuboids for the yokes. More complex volumes would increase the number of interaction matrices in the calculation and with that would also increase the computing time.

6.2.5. The EPT Magnet System in RADIA

The modeling of the EPT magnet system in RADIA is rather simple (fig. 6.4). The magnet system is shaped mainly by using rectangular parallelepipedic blocks. The magnets are just cuboids, that are placed under the yoke (or above respectively) – but not directly. We leave a gap between the two components, where the glue is applied.

The yoke is built up by cutting a block by a plane at the left and right end of the yoke (see fig. 6.4) and segmented as described in section 6.2.2 to represent the various directions of the flux densities inside the yoke. The permanent magnets can not be segmented, since they are a magnetic "active" element in RADIA, that only hold one vector of magnetization.

We neglect the subtleties of the design like the notches in the yokes and the magnets, since these details are to complex to be reflected in RADIA and to small to be of great significance.

Initial Dimension of the Magnet System

To have a starting point in terms of dimensions for our magnet systems, we adopt the proportions from the CAD model of a first draft of the EPT, that already existed before the start of our work. If necessary, we can successively change these dimensions to fit the physical properties of the magnet systems to our needs and requirements (see fig. 6.1).

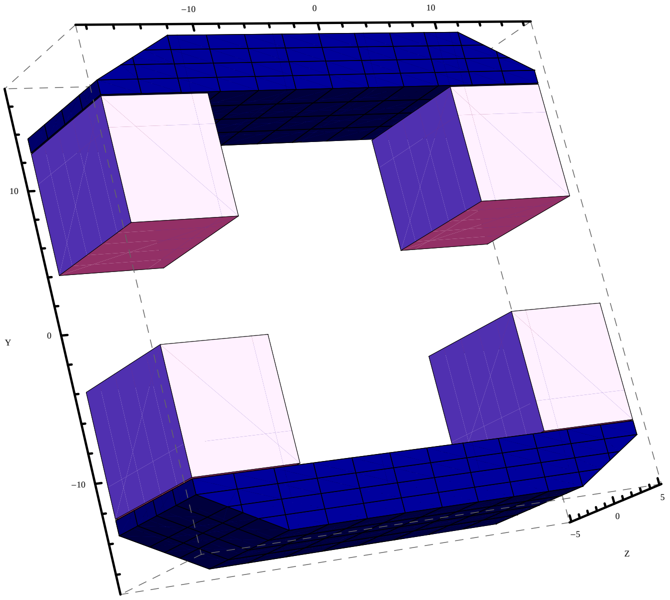

Figure 6.4.: The EPT magnet system as represented in RADIA.

Used Materials

Vacuumschmelze offers two main product lines of magnetic materials: VACODYM and VACOMAX (Data sheets describing both materials are available at the company's website: `http://www.vacuumschmelze.com`). VACODYM is a Neodymium Iron Boron (Nd2Fe14B) material with very high energy density, which makes it possible to produce compact magnets, that produce the same magnetic field as bigger magnets made of other alloys.

VACOMAX on the other hand consists of rare-earth materials and cobalt (SmCo – Samarium) and show high coercive field strength whilst having high saturation magnetic polarization. It is also very temperature-stable and corrosion-resistive.

Vacuumschmelze suggests to operate VACODYM up to temperatures ranging from 50°C to 230°C, whereas the maximum working-temperatures for VACOMAX range from 250°C to 350°C. The curie temperatures for VACODYM range from 310°C to 370°C, for VACOMAX from 800°C to 850°C.

Since the highest expected temperature that EPT is expected to be exposed to is +40°C (Rodriguez-Pacheco 2011), we want to benefit from the possibility to build a rather compact magnet system and choose VACODYM as the material for our permanent magnets, especially VACODYM 677 HR, which has a magnetic remanence of 1.18 Tesla and a suggested maximum working temperature of 190°C.

The requirement to the yokes is to connect the flux densities of the permanent magnets attached to the yokes. This leads to the demand of a material with high saturation polarization.

Again Vacuumschmelze offers two main product lines of magnetically soft cobalt-iron-alloys: VACOFLUX and VACODUR. The first material shows the highest saturation polarization of 2.35 Tesla, which makes it the material of our choice for the yokes.

6.2.6. Choosing the Right Residual Induction

The task of the magnet system in EPT is to deflect incoming electrons away from the proton channel. This leads to two driving requirements on the magnet system:

- The magnetic field in the collimator, where the electrons travel through, has to be high enough to deflect all electrons that could not make a signal in the second detector and thus would trigger the proton channel by mistake.
- The magnetic field outside the instrument must fall steeply with growing distance, so that it does not disturb the measurements of the two magnetometer instruments MAG onboard Solar Orbiter. The maximum overall DC magnetic field induced by the whole spacecraft allowed at MAG OBS is 10 nTesla (see also section 6.2.8).

These two requirements contradict each other in a way that the first asks for a high magnetic field in the gap between the permanent magnets, whereas the second requirement demands a magnetic field emitted by the whole system as low as possible. To harmonize these two extremes will be our task in the following.

As already mentioned before, we chose VACODYM 677 HR, the VACODYM alloy with the least magnetic remanence of 1.18 Tesla, as the material for our permanent magnets. Now we will check, if this material, together with the choice of VACOFLUX 50 for the yoke and with the dimension in fig. 6.1, will fulfill the two requirements. Otherwise we will have to choose a different material for the permanent magnets like VACODYM 655 HR with a magnetic remanence of 1.28 T or VACODYM 633 HR with a remanence of 1.35 T.

6.2.7. Deflection of Electrons

First, we will discuss whether the remanence of 1.18 T of the permanent magnets is sufficient for deflecting lower energetic electrons that could trigger a signal in the proton channel away from the detector. As seen in fig. 5.4, electrons with an energy of 400-500 keV and above can penetrate a silicon detector that is 0.3 mm thick and can produce a signal in the detector located behind and with this trigger the anti-coincidence logic. These electrons do not pose a threat to the measurement of protons, since they are neglected by the electronics. Electrons with a lower energy that are stopped in 0.3 mm silicon are more critical, for they will be counted as protons when they reach detector C despite the magnetic field. So we need to verify that the chosen remanence is high enough to deflect these electrons.

For this, we calculate a field in RADIA with an extent of 100 mm in the x-, y- and z-direction and with a resolution of 2 mm between two calculation points in each direction. We then import this field into a Python-class that returns a field vector for every point inside this 100 mm * 100 mm * 100 mm volume. If we ask the class for a field vector at a point which is located in a cube whose corner points are 8 points of calculation (i. e. we do not ask for a certain point of calculation directly, but rather for a point a little off), the class interpolates the field vector out of the 8 surrounding points from the RADIA-field.

Fig. 6.5 illustrates how we carry out the further simulation. Starting from the outer edge of the collimator, the electron gets shot into the telescope with varying kinetic energy and angles of entry. We then follow it's trajectory by solving the equation of motion

$$\vec{F} = \vec{F}_{mag} = -e\left(\frac{d\vec{s}}{dt} \times \vec{B}\right) = m_{e\text{-}}\frac{d^2\vec{s}}{dt^2}$$

until the electron either hits the collimator or the detector. In case of a detector hit, we record that event together with the angle of entry and the kinetic energy of the electron.

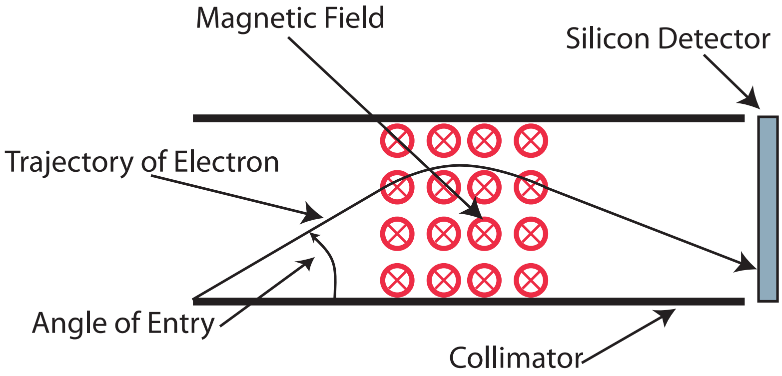

Figure 6.5.: We shoot in the electron from the edge of the collimator with varying angles and varying energies and see, whether it reaches the silicon detector.

The results of this simulation are shown in fig. 6.7. There we see that only electrons with a kinetic energy of at least 725 keV can reach the proton-detector and produce a signal there. But then, the electron is so energetic that it can penetrate the first detector and reach the second, to also produce a signal there. This would then trigger the anti-coincidence, so that this event would not be counted as a proton event (see fig. 5.5 in section 5.1.2).

In section 5.1.2 we calculated the geometric factors for the two trigger conditions A and C. There we shot electrons and protons in a sphere containing the instrument. These simulations included the latest design version of EPT including the magnetic field together with the stray field outside the collimator. Also, we simulated electron scattering in GEANT4 which we neglected in this consideration. The results in the figure 5.5 verify the conclusion drawn here that only electrons with an energy higher than approximately 1 MeV produce a serious number of signals in trigger C.

We come to the conclusion, that the remanence of the permanent magnets is sufficient to deflect electrons that could cause a fake signal in the proton-channel. Since 1.18 Tesla is the lowest remanence in the product line of VACODYM, there is no possibility to try out magnets with a lower magnetization that could as well deflect the low energy electrons.

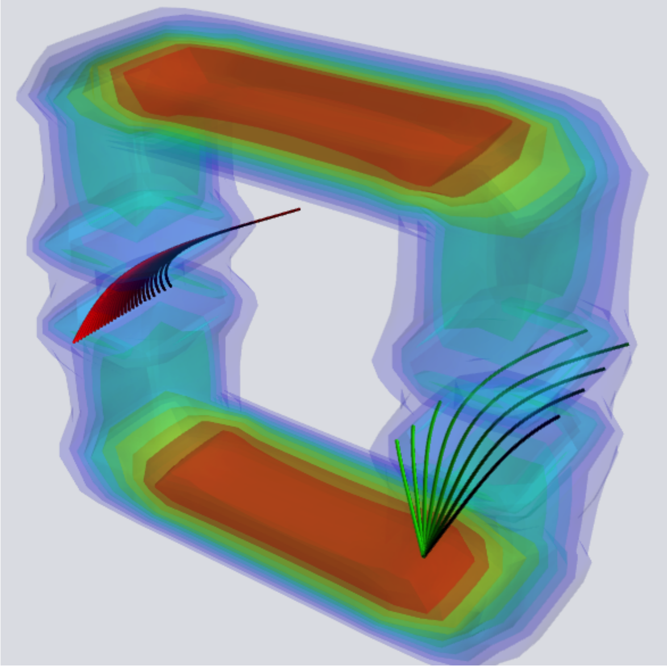

Figure 6.6.: A three-dimensional view at the paths of the electrons from the simulation in fig. 6.5 inside the magnetic field of the EPT magnet systems. The trajectories in green represent electrons at a certain energy, but with different angles of entry, whereas the red trajectories show the path of electrons starting into the collimator under the same angle but with different energies.

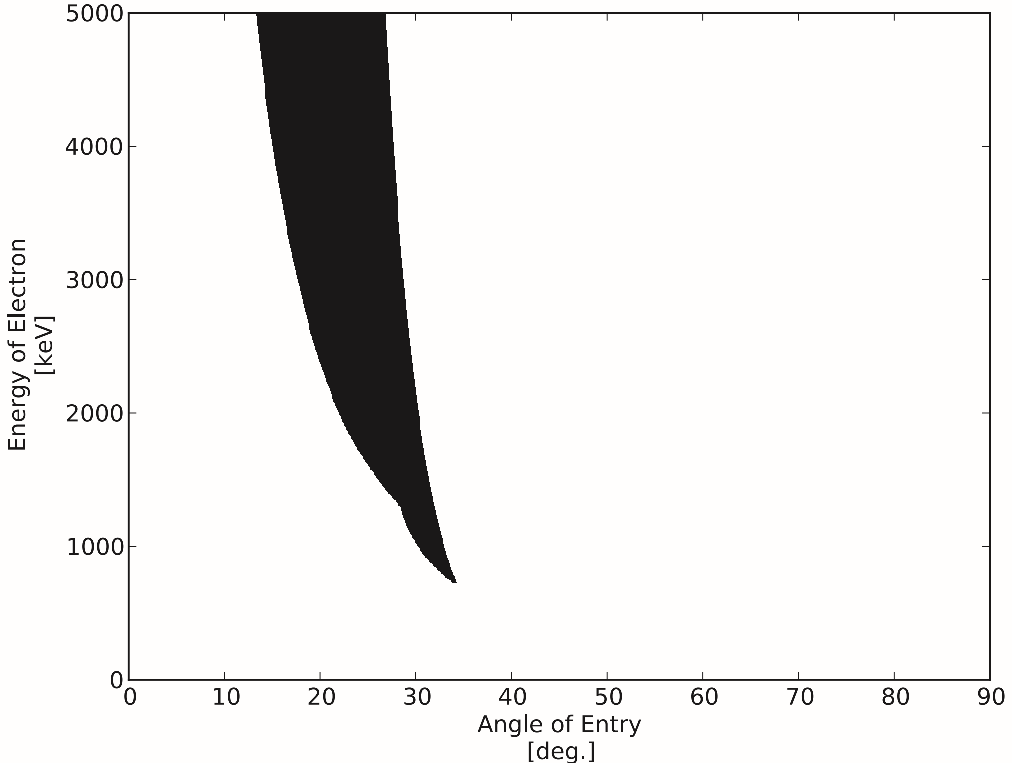

Figure 6.7.: The black area marks the configurations of electrons that can enter the proton channel despite the magnetic field. The lower apex of the area resides at the energy 725 keV and at the angle 34°. Such electrons will easily penetrate the first detector and also deposit sufficient energy in the second to trigger an anti-coincidence condition.

6.2.8. Calculation of the Field Towards MAG

The next issue we have to examine is, whether the field emitted by a magnet system equipped with these kinds of permanent magnets, disturbs the MAG instruments or not. MAG consists of two fluxgate magnetometers MAG IBS (in-board sensor) and MAG OBS (outboard sensor) located on the boom that extends behind Solar Orbiter (see fig. 6.8).

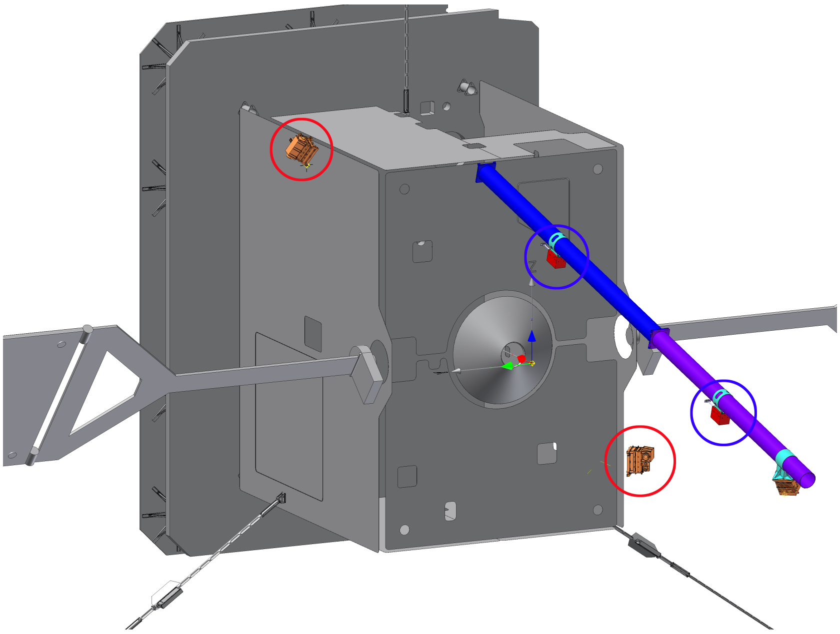

Figure 6.8.: The EPT/HET (red) and MAG (blue) instruments onboard Solar Orbiter. (by Lars Seimetz)

One of the requirements on the EPD instrument suite (of which EPT is a part of) is, that the overall DC magnetic field produced by the spacecraft and its onboard instruments at the position of MAG OBS should not exceed 10 nTesla (Solar Orbiter Team 2011). The sources of the field emitted by the spacecraft include the power supplies of the instruments and the spacecraft itself, electric currents flowing through cables inside the spacecraft and possible fields produced and emitted by instruments for scientific reasons like the field emitted by EPT.

Till today (December 18, 2012), it was not detailed, how much each single instrument of EPD is allowed to contribute to the limit of 10 nTesla. In this work, we assume that the 10 nTesla are equally shared among the 9 EPD sensor heads and that each EPT is allowed to contribute approximately 1 nTesla at the position of MAG OBS.

In order to calculate the fields in the directions of the magnetometers, we need to know the relative locations of them as seen from the center of the two magnet systems. We gain this information from the official CAD-model of Solar Orbiter and by using the transformation matrices from ESA, that allow us to transfer a vector in spacecraft-coordinates into the coordinate system of RADIA.

In RADIA, we calculate the magnetic flux densities along the connecting line originating in the center of the magnet systems and ending at the connection point of the magnetometers with the boom. The results can be seen in fig. 6.9. To get the overall

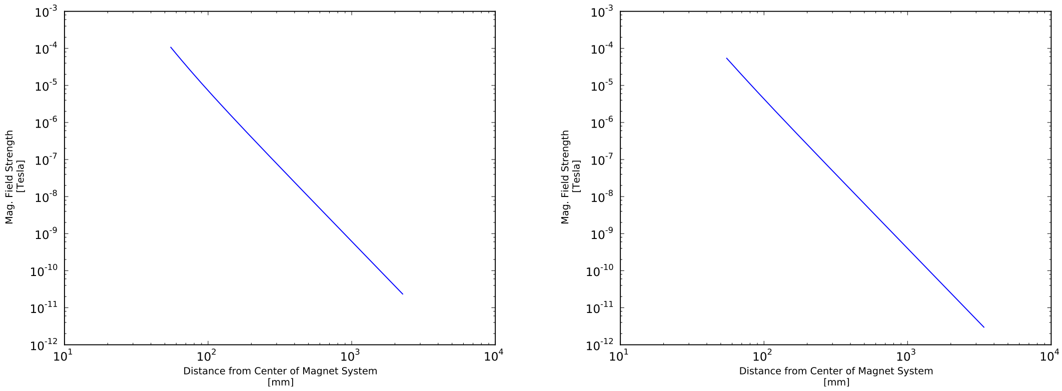

(a) EPT1→MAG IBS *(b)* EPT1→MAG OBS

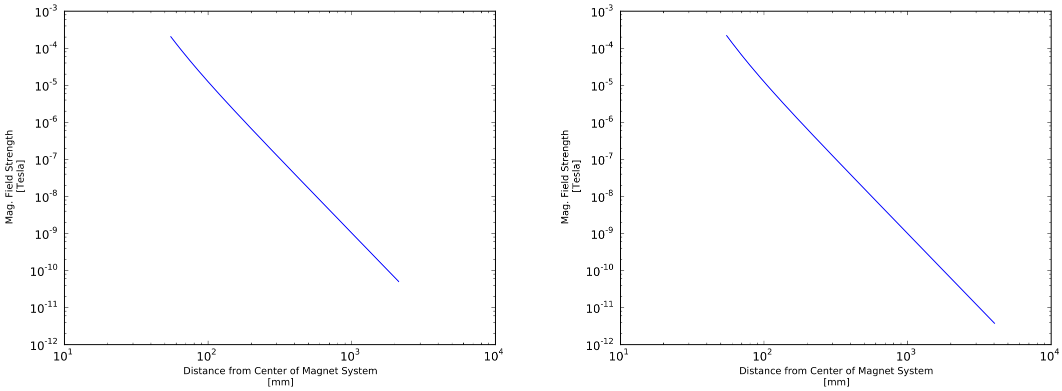

(c) EPT2→MAG IBS *(d)* EPT2→MAG OBS

Figure 6.9.: The various runs of the magnetic field towards the two MAG-instruments originating from the two EPT-instruments and ending at the two MAG-positions.

emission of both EPTs at the locations of the magnetometers, we need to add the field vectors component-by-component:

$$
\begin{aligned}
B_{\text{MAG IBS}} &= \sqrt{\left(B_{\text{x}_{\text{EPT1}\rightarrow\text{MAG IBS}}} + B_{\text{x}_{\text{EPT2}\rightarrow\text{MAG IBS}}}\right)^2 + \ldots} \\
B_{\text{MAG OBS}} &= \sqrt{\left(B_{\text{x}_{\text{EPT1}\rightarrow\text{MAG OBS}}} + B_{\text{x}_{\text{EPT2}\rightarrow\text{MAG OBS}}}\right)^2 + \ldots}
\end{aligned}
$$

The results from RADIA in table 6.1 show that our chosen magnet systems do not pose a threat to the measurements of the onboard magnetometers. The expected field at the MAG OBS-position of 0.0054 nTesla is far below the limit of 1 nTesla. But this is only a theoretical computation. We now actually need to measure the magnetic fields of the magnets systems we ordered from VACUUMSCHMELZE.

EPT1	→	MAG IBS	:	0.02320 nTesla
EPT1	→	MAG OBS	:	0.00298 nTesla
EPT2	→	MAG IBS	:	0.05010 nTesla
EPT2	→	MAG OBS	:	0.00376 nTesla
		MAG IBS total	:	0.0657 nTesla
		MAG OBS total	:	**0.0054 nTesla**

Table 6.1.: Results of the RADIA calculation of the magnetic field at the positions of the magnetometers.

6.3. The Magnet Systems Delivered by Vacuumschmelze

In the former section 6.2.6, we saw that the magnet system fulfills the requirements imposed to them. Therefore we ordered six systems at Vacuumschmelze for our various EPT models.

Right after the delivery of the systems, we made a first test of them and measured the maximum flux densities in the two gaps between the permanent magnets with a Hall-effect probe. The results shown in table 6.2 confirm the calculated value of 0.412443 Tesla from RADIA.

The serial numbers of the magnet systems (#02203, ...) are given by Vacuumschmelze and are hereby adopted by us. Occasionally they will be abbreviated for better reading (e.g. #03, #3, ...).

Magnet System	**Field, left** (in Tesla)	**Field, right** (in Tesla)	**Orientation of System**
#02203	0.4118	0.4096	70, 3, 75, 1
#02204	0.4078	0.4147	39, 15, 89, 8
#02205	0.4147	0.4085	18, 53, 17, 61
#02206	0.4095	0.4105	49, 9, 44, 36
#02207	0.4078	0.4123	45, 34, 43, 26
#02208	0.4107	0.4119	55, 13, 57, 7

Result from RADIA-calculation: 0.412443 Tesla

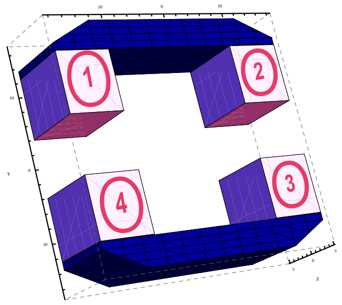

Table 6.2.: Measurement of the flux densities in the middle between the two pairs of permanent magnets. The column "Orientation of System" gives the information, which permanent magnet is on which position in the system. For example: In system #02203 magnet #70 is found in the upper left position, magnet #3 in the upper right, #75 in the lower right and #1 in the lower left position.

The field in the gap, which will later deflect the electrons, seems to be strong enough to do its job. The question now is, whether the outside field declines quickly enough, so that MAG is not disturbed. But before we can answer this question, we need to take a look at the environment, in which our measurements will be carried out.

6.4. Variations of Earth's Magnetic Field

Since all our measurements will take place in a non-insulated environment on earth, we need to take the behavior of the geomagnetic field into account. A constant background field would not pose a big handicap to our experiments, since we could subtract this from our measured values, but since the geomagnetic field (as well as man-made magnetic fields) is undergoing various fluctuations on different timescales, it is worth taking a closer look at it.

The Earth's magnetic field varies on various time scales from milliseconds to millions of years. The causes of these variances can be divided in two groups: internal and external sources (Kane 1976).

Variations of longer than a couple of decades are likely to be induced by variations of the interior of the earth, since the conditions in the inner core and the earth crust also change on these time scales. On the other hand, the variances in the geomagnetic field on the shorter time scales originate in interactions between the solar wind and the Earth's magnetosphere and in changes in the current systems in the upper atmosphere.

The variations caused by internal sources range from a few tens to hundreds of nT, but this causes no problem to our measurements as they do not last that long. On the other hand, the geomagnetic field shows a distinct diurnal variation with a variance of a few tens nT and a minimum at around local noon (see fig. 6.10) (Gauss 1838; Okeke et al. 2000). This oscillation is caused by the heating and cooling of the electrically conductive ionosphere, whose ionization among others is a function of temperature and sun irradiation.

This shift is of more significance to us, since we want to reach an accuracy of 10 nT, which is the given precision of our magnetometer. We will compensate this by recording the background without a magnet in the vicinity of the magnetometer directly before and after the measurement with the magnet.

6.5. The Magnetometer

All the measurements of the magnetic flux densities emitted by the EPT magnet systems are carried out using a 3 axes milligauss meter manufactured by *AlphaLab Inc.* in Salt Lake City, USA[3]. In the following we will take a closer look at this instrument by introducing the principle of measurement and describing the features of the measurement device.

6.5.1. Principle of Measurement

The Anisotropic Magnetoresistance

The magnetometer utilizes the anisotropic magnetoresistance (AMR), that was discovered 1857 by William Thompson, 1$^{\text{st}}$ Baron Kelvin (Thomson 1856). The AMR is an effect observed in some ferromagnetic metals below the Curie temperature when they are exposed to an external magnetic field. When an electric current flows through an AMR-sensitive metal or alloy, the electric resistance depends on the angle between the magnetic field lines and the direction of the current and also on the strength of the magnetic field. The metal shows maximum resistance when current and field are parallel

---

[3] AlphaLab Inc. Website: `http://www.trifield.com/content/dc-milligauss-meter-3-axis/`

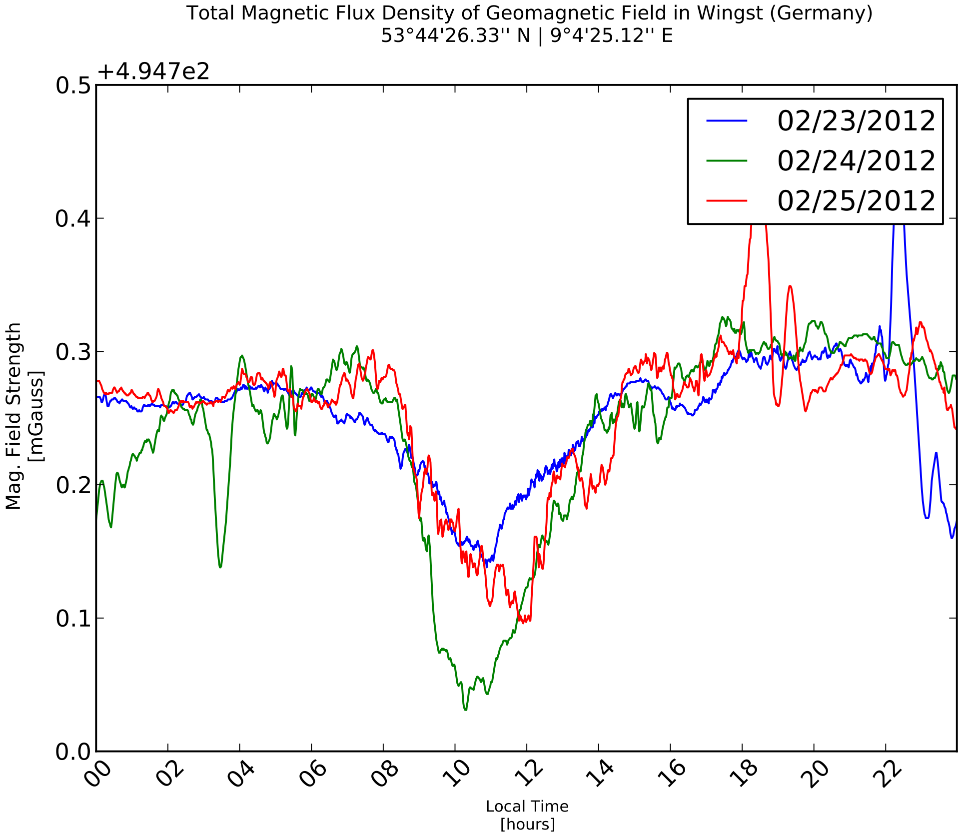

Figure 6.10.: The total magnetic flux density in Wingst measured at three successional days (Kerridge 2010). Data obtained from INTERMAGNET database. (INTERMAGNET website: `http://ottawa.intermagnet.org/apps/dl_data_prel_e.php`)

and minimum resistance, when perpendicular. This is due to the anisotropic scattering cross section of the core electrons. The reason for this behavior is the spin-orbit coupling, which turns the charge distribution of the atom non-spherical-symmetric. A more detailed discussion of this phenomenon can be found in Ebert et al. 1996 and an overview of various magnetic field sensors in Lenz et al. 2006.

The valence electrons more or less run freely in the metal, whereas the core electrons are retained by their atom and can only gyrate around the magnetic field lines. Now, when these lines run parallel to the current, the plane of rotation of the core electrons is perpendicular to the path of the electrons that make up the electric current. This increases the chance of electron scattering and so increases the specific resistance in the metal.

The sensors are built of a thin, prolate film of AMR-sensitive material (Genish et al. 2004), through which an electric current flows. The magnetic field in the plane of the foil and perpendicular to the current direction is detected by measuring the electric resistance of the foil.

Advantages of the AMR-Technology

Using AMR-sensors brings some advantages over other principles of measurement as for example fluxgate-sensors, hall-effect-sensors or proton magnetometers (Mapps 1997):

- ***High Precision*** The high linearity and low hysteresis of the AMR-sensitive sensors make it possible to measure very low field strengths.
- ***High Resolution*** Due to a very good signal-to-noise ratio one can detect very small differences in the flux, which leads to a very high resolution of measurement.
- ***Robustness*** AMR-sensors are very rugged and almost immune against mechanical stress. Furthermore, the principle of measurement is also not very susceptible to interference from dirt, radiation or extreme temperatures.
- ***Insensibility*** A sophisticated configuration of the AMR-sensors make them insensitive against homogeneous noise fields.

6.5.2. Description of the Magnetometer From AlphaLab Inc.

The milligauss meter from AlphaLab is designed to measure the DC magnetic flux density in the three cartesian axes with a scaling accuracy of ±0.5 % in the dynamic range from 0 to ±1999.9 mGauss and in the temperature range from -1.1°C to 43.3°C . The magnetometer consists of a control box and a probe with the shape of a box with the dimensions 2.3 cm * 3.9 cm * 2.6 cm (see fig. 6.11). The control box and the probe are connected by a 3.21 m long ribbon cable, so that any magnetic field emitted by the control box does not disturb the measurements.

The magnetometer probe contains three AMR-sensors for measuring the magnetic flux densities in direction of the three cartesian axes. The exact positions of the sensors in the probe were given by AlphaLab. The magnetometer provides three analog output channels for reading out the measured values of the DC magnetic flux density in the three Cartesian axes.

It turned out that the measurements of the magnetometer tend to drift in the first 20 to 30 minutes due to changing temperature of the instrument. So we turn on the magnetometer at least three hours before the measurements and don't turn it off anymore unless we need to move it to a different laboratory.

Analog Outputs

In fig. 6.11 we can see three analog BNC outputs on the right side of the control box of the magnetometer. These outputs allow us to tap voltages that are proportional to the measured flux densities in the three axes over the full dynamic range (1 Volt ≡ 1 Gauss ±0.5%). As later described (see section 6.6.2), we will use this interface for semi-automatically measuring and analyzing the magnetic field values. The update rate of the voltages on the output is 3 Hz.

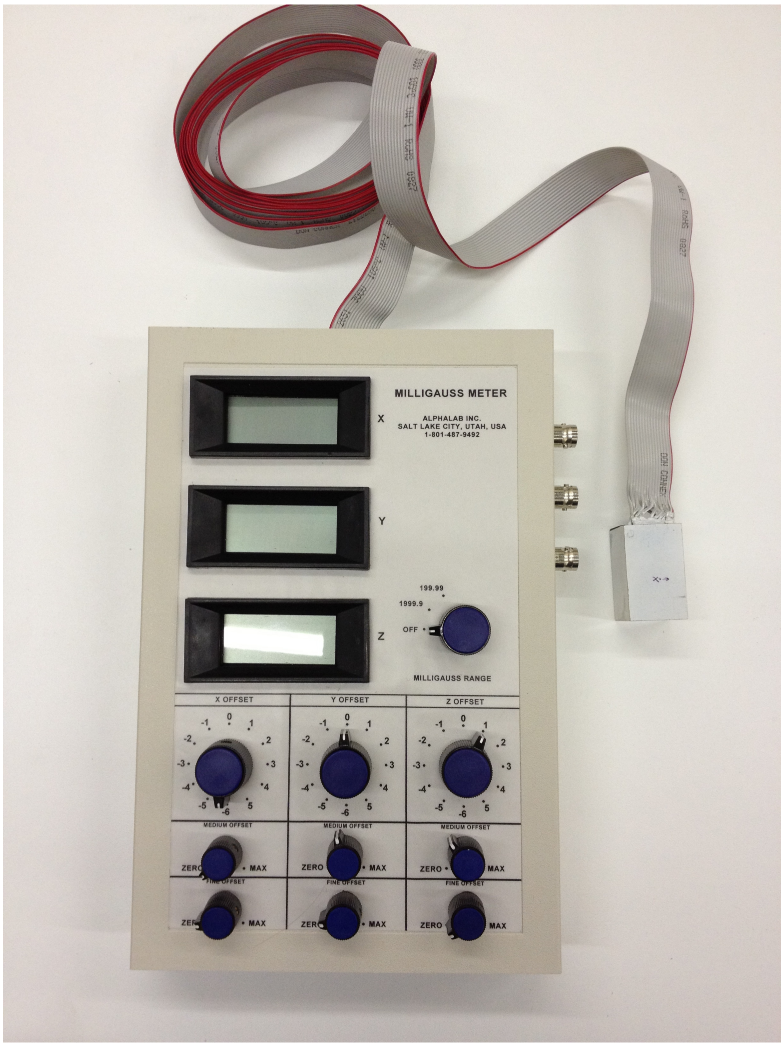

Figure 6.11.: Magnetometer with measuring probe. Located in the upper left of the control box are the three displays for the measured values in the three cartesian axes. To the right of the displays is the on/off switch. Installed in the lower part are three times three control dials, with which one can tune different offsets for the flux densities.

Positions of the Individual Sensors Inside the Probe

On the surface of the probe in fig 6.11 one can see a black dot and an arrow marked with a little "x". This dot serves as an indication for the location of the single sensor for the x-axis inside the probe. ALPHALAB gives the following information for the three sensors:

- ***X-Sensor***: 5 mm directly below the dot.
- ***Y-Sensor***: 5 mm directly below the dot.
- ***Z-Sensor***: 8 mm directly below the dot.

Due to this kind of construction of the probe, it is not possible to measure the magnetic flux densities in all three directions in one single point, but rather in three separate points. We must factor in this circumstance, when it comes to the measurements of the EPT fields and the comparisons with the calculated RADIA flux densities.

To have a single reference point for our location measurements later, we calculate the barycenter of the three sensors by constituting a coordinate system in the middle of the probe and calculating the center of the sensor-triangle (see fig 6.12). The results are shown in table 6.3.

	x-sensor	**y-sensor**	**z-sensor**
x	0.15	0.65	-0.77
y	0.27	0.00	1.15
z	-0.80	0.79	0.87

Table 6.3.: Coordinates of the three sensors inside the magnetometer probe (all in cm).

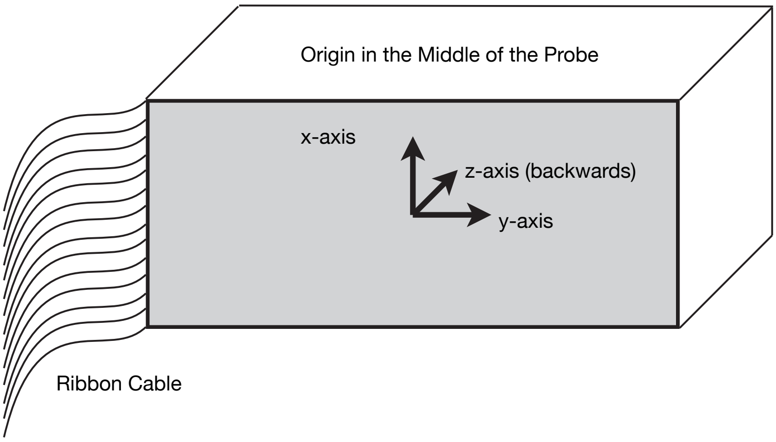

Figure 6.12.: We define a coordinate system with the origin in the middle of the probe.

6.6. The iPhone-App EMMA

In this chapter we will introduce the iPhone-App **EMMA** (**E**PT **M**agnetic Field **M**apping **A**pp), with which we will measure the magnetic fields emitted by the magnet systems for EPT.

At first, we will point out, why we use a smart phone and especially an iPhone for recording and evaluating our measurements. After that we will give an overlook and an introduction to the features and functions of EMMA. A manual of how to use EMMA can be found in appendix A.

6.6.1. The iPhone as the Measurement Instrument

To explain, why we use an iPhone for the measurements of the magnetic fields, one must consider the requirements for the measurement process and conditions under which this process must be carried out:

- A great number of data has to be stored and evaluated.
- The measurements must be carried out rapidly.
- The instrument must not disturb the measurement by emitting a non negligible amount of DC magnetic field.
- The whole assembly of measurement has to be portable to test different locations in respect of EM cleanliness.
- The stored data has to be easily accessible for further analysis.

We will now discuss these bullet points in more detail.

A Great Number of Data has to be Stored and Evaluated

We'll have to take the measurements of six magnet systems, which can be installed into two EPT with two different sides pointing into two different directions towards the MAG instruments. This sums up to at least 48 series of measurements, that consist of approximately 50 data points for three values for the magnetic flux density in three directions of the cartesian axes.

Altogether we have 7200 values to be noted on paper and typed in again into a database, which would be too time-consuming if it is done by hand. So we definitely need an half automated way to do this. This means that we need a device which we can use to automatically record the flux values delivered by the magnetometer by pressing a button for example.

Technically the iPhone is nothing but a computer with phoning ability. As such a computer it also contains a serial port to receive and send data from and to the world. We can use this port to connect to the magnetometer to read the measured values. And also as a computer, the iPhone comes with enough flash memory to store our data persistently (the model we used offers 32 GByte of storage space). And finally, the A5 CPU of the iPhone delivers enough computing power to evaluate the measured data.

The Measurements Must be Carried out Rapidly

Since we lack a laboratory that is insulated from the earth's magnetic field, we have to take the variance of this background field into account during our measurements. As described in section 6.4, the geomagnetic field shows a daily variation of approx. 0.3 mGauss with a distinct minimum around local noon. Our measurements take place in the morning or in the afternoon, thus in a time with a steep decline or incline. We will later compensate for this by defining a kind of "mean" background field, that is calculated by taking the mean value of two background measurements before and after the real measurement with the magnet systems:

$$\vec{B}_{\mathrm{back}_{\mathrm{mean}}}(t) = \frac{\vec{B}_{\mathrm{back}_{\mathrm{before}}}(t_1) + \vec{B}_{\mathrm{back}_{\mathrm{after}}}(t_2)}{2}$$

where t is the time, at which the magnet measurement takes place, whereas t_1 and t_2 are the times at which the background measurements before and after this measurement are carried out:

$$t_1 < t < t_2$$

The drawback of this method is, that this value for the background field does not exactly represent the background field at the time t when the field of the magnet system is measured. As long as the geomagnetic field varies, there will always be a deviation between the assumed background and the real background.

To keep these deviations as small as possible, we need to shorten the time between the measurements of the background fields and with that to shorten the time of the magnet measurement itself. This is difficult to achieve just by hand. An automated way to measure and store data saves us time, we would otherwise spend on writing down the data and determining the measured values.

The Instrument Must not Disturb the Measurement by Emitting a non Negligible Amount of DC Magnetic Field

It is obvious, that we only want to determine the magnetic field emitted by the EPT magnet systems and not additionally a field possibly emitted by the measurement setup itself. That is the reason why the cable, that connects the magnetometer probe with the control unit, is 3.21 m long – to keep the control unit far away from the probe, so that disturbances caused by magnetic fields emitted by the inside electronics are kept as low as possible.

At first glance, this could also be a solution for our recording device. But unfortunately we will need to input and check data on the device too. We do not need to interact with the magnetometer's control unit during the measurements, but with the recording device we will. This makes it difficult to have the recording device to be placed 3 meters away from us while measuring – we will have the device to be positioned within the experimenter's reach.

But then, the appliance shouldn't emit a magnetic field that's strong enough to disturb the measurements. A device with a connection with the power grid contains a transformer with a ferromagnetic core, that would definitely afflict the measurement.

As a mobile device, the iPhone rather relies on a built-in battery than on a connection to the power grid via a transformer. Also it consumes very low electric currents to save energy. As a consequence the iPhone produces a very low magnetic field around itself when in airplane mode. We noticed a significant effect in the magnetometer when holding the iPhone directly adjacent to the magnetometer probe. But already approximately at a distance of 5 cm away from the probe we don't see any influence of the iPhone at all.

The Whole Assembly of Measurement has to be Portable to Test Different Locations in Respect of EM Cleanliness

In the course of the field measurements we will want to figure out, which location is best for us in respect of EM cleanliness. Electric installations, running machines or even driving cars can emit a non negligible amount of magnetic noise field. Before executing a long series of measurements in a laboratory, we will first test this location for those kind of disturbances.

It would not be very convenient to carry our whole equipment, if our measurement setup would be bulky and heavy. The magnetometer itself is not very big and rather lightweight. With a whole computer including a monitor we would lose this portability. A notebook would be more portable, but the limited battery power restricts the time, in which we can use it without connecting it to a power adapter, that again includes a transformer, which is not an option as we pointed out before.

As a mobile phone, the iPhone fits into the palm of a hand and draws its power from a battery with enough capacity to use it for approximately 8 hours for measurements (airplane mode switched on). So, the mobile phone is portable and persistent enough to meet our requirements.

The Stored Data has to be Easily Accessible for Further Analysis

The values for the magnetic flux densities of the different EPT magnet systems need to be analyzed and visualized for further treatment. Also, the data has to be shared with and be made accessible to the whole EPD consortium. Using a computer or notebook would make this task an easy one, just by storing the results on a network or USB drive.

Data stored on an iOS device can be read out using iTunes, when the device is connected via USB cable to a computer. But this excludes computers, for which there are no versions of iTunes available, like machines that run under the Linux OS. To be able to store the data on those clients, we use the cloud service Dropbox. With that we are able to push the results via an internet connection onto a dedicated directory on these computers for further treatment.

Conclusion

The iPhone is small, persistent, powerful and capable enough to serve as a measurement device for our special needs at determining the EPT magnetic field. The data is easily accessible, whilst the device itself emits so little own magnetic field, that the measurements are not disturbed in any ways. The mobile phone will serve as a replacement for pen and paper to record the measured values in a half-automated way. Otherwise the amount of data would be to much to handle by hand.

Of course, any other smart phone with a different OS, would also do the trick. But the solution with the iOS device is the easier way, since there is already a serial cable and a special SDK (Software Development Kit) for programming the serial port available for purchase. With an Android phone the task would be far more difficult, because there is no officially supported SDK or even serial cable available. All the solutions we found are more complex and more time-consuming.

6.6.2. How EMMA works

In appendix A we discuss how to measure a data point or measure a time series or "empty" series, but never explain in detail, how the App does this exactly. In this chapter we will now make up for this.

Digitization of the Magnetic Flux Densities

The magnetometer produced by *AlphaLab* provides us with three analog outputs, where we can tap electric voltages, that are proportional to the measured flux densities. To further process these signals with EMMA, we need to digitize them using an AD-converter.

As mentioned in section 6.5.2, the magnetometer has a dynamic range from 0.0 mGauss to ±1999.9 mGauss with a precision of 0.1 mGauss. This leads to a dynamic range with 39998 different values. Since in binary 39998 is a 16-bit number ("1001 1100 0011 1110"), we choose to implement the 16 bit AD-converters "AD7706" from *Analog Devices* on our ADC-board [4]. Each of these chips contains two AD-converter circuits, that can be addressed by a micro-controller via the **S**erial **P**eripherial **I**nterface (**SPI**). So in sum, we have four AD-converter circuits from which we connect three to the magnetometer.

Every 0.03 seconds the micro-controller asks the three ADCs in sequence for the results of their digitalization processes and prints out the values every 0.2 seconds to the serial port. The serial interface of our converter box is connected to the iOS device by a serial-to-Dock-Connector cable produced by *Redpark*[5].

The circuit diagram of the AD-converter and the program that is running on the micro-controller can be looked up in appendix B.3. Fig. 6.13 shows the converter box connected to the magnetometer and the iOS device.

Processing of the Serial Data Provided by the Converter Box

Now that we have delivered the digitized data from the converter box, we need to treat them in our App. With the help of the SDK (Software Development Kit), that got shipped together with the serial cable from *Redpark*, we developed three methods to process the measured data:

1. Recording a value every 0.1 seconds by reading out the serial buffer of the iOS device. This method is the basic procedure of EMMA to gather data from the magnetometer. The following two methods rely on this one.

2. Gathering the values provided by method 1 (above) for 5 seconds and calculating the mean of these values. This method is invoked every time the user asks EMMA for a value of the magnetic flux density. The following method relies on this one.

3. Gathering the results from method 2 (above) every 6 seconds and storing them during an estimated time. This method is used when taking "empty" series. The

---

[4] AD7706 Datasheets: `http://www.analog.com/static/imported-files/data_sheets/AD7705_7706.pdf`

[5] Redpark Website: `http://www.redpark.com`

Figure 6.13.: The box, that contains the AD-converter for EMMA. On the left the box is connected to the iOS device and to the power adapter (black), and on the right to the three outputs of the magnetometer.

former method is performed in the background by EMMA itself. It turned out, that we needed to give EMMA one second time to store the results from the former method instead of gathering the results every 5 seconds.

We use method 1 for plotting our time series as described in section A.1.4, in order to see in detail any disturbances that can occur in our laboratory. Method 2 is used with measuring the location series from section A.1.5 to consider the gaussian distribution of the measurement. We considered 5 seconds to be long enough to gather enough data to get a meaningful mean value and short enough to avoid variations of the geomagnetic field as explained in section 6.4.

6.7. Survey of the EPT Magnet Systems

We now come to the practical measurements of the magnetic flux densities using the EMMA/magnetometer-combination. But before we turn to the measurements of the actual fields produced by the EPT magnet systems, we want to get more acquainted with the magnetometer and the laboratory conditions.

6.7.1. Determination of the Background-Field

Since we do not posses a background-free laboratory, all our measurements are exposed to the geomagnetic field mentioned in section 6.4. To just measure the magnetic fields emitted by the magnet systems, we determine the background field twice: the first time before the actual measurement and the second time after the measurement. As already described in section 6.6.1, we then subtract the mean of these two backgrounds from the actual measurement.

But even with this workaround, we can not totally get rid of fluctuations that originate in the surrounding noise. During the actual measurements, we are still exposed not only to the geomagnetic field, but also to fields produced by other sources like air conditioning units, running machines, electric currents in the wall, elevators, etc..

These disturbances pose a limit to the precision of our measurements. For a thorough analysis of the EPT magnetic field, we need to take into account these disturbances as an error to the values we get from the EMMA/magnetometer-combination.

Fluctuation of the Background Field

As described in section A.2 and in section 6.6.2, EMMA provides us with the ability to record an "empty" time series. We use this function to analyze the environments of different locations in terms of magnetic stability. Of course, we don't need a magnet system for this test, but to represent the conditions when measuring the actual location series with a magnet, we wait 15 minutes between the two series, which is about the amount of time it takes to measure the field of a magnet system.

In the following, we will take "empty" series at two different locations. After turning on the magnetometer, we adjusted the three offsets to zero (see description of the magnetometer on page 110) and waited before the first measurement, to allow the drift of the instrument to calm down. This waiting time took approx. 20 to 30 minutes. The differences of the values of the average background field between the different test-locations are due to the differing waiting times between the tuning of the offsets and the beginning of the measurement, since the background field changed during that time and due to inaccuracies in manually tuning the offsets.

At first we take a series in the laboratory in LS11/012 – a laboratory in the basement of the *Institute for Experimental and Applied Physics, Kiel.* The room normally serves as a kind of storage room and contains diverse scientific equipment, but no working machines, switched on computers or electrical consumers, that could emit non-constant magnetic fields. Possible constant fields that originate in the room add to the overall background field, but don't contribute to the fluctuations. Yet, the room LS11/12 lies in the vicinity of a cleanroom, which is constantly air-conditioned and equipped with a variety of electric hardware, that is in long-term use. Additionally, automatic doors (moved by an electric motor) located approximately 15 meters away from the laboratory could also pose a threat to the precision of our measurements.

At the time we take the "empty" series, the magnetometer and the AC-converter box have been turned on in the room for days and the room itself is kept at a constant temperature. So, the instruments are working at a constant temperature and under a constant average relative humidity of approximately 50%.

Fig. 6.14 shows the time series of the measurements. The two series show standard deviations of 0.31 mGauss and 0.27 mGauss, leading to a mean deviation of 0.29 mGauss.

The second "empty" series are taken outdoors on a lawn behind the tower of LS19. We power the EMMA/magnetometer-combination via a 50 meter extension cable. This enables us to build our testing site 30 meters away from the building and with that also 30 meters away from any possible source of disturbance other than the geomagnetic field. The day on which we take the measurement was a partly clouded day with temperatures of around 13°C and a relative humidity of approximately 40%. We switch on the EMMA/magnetometer-combination one hour before the measurements to allow the instruments to adapt itself to the surrounding conditions.

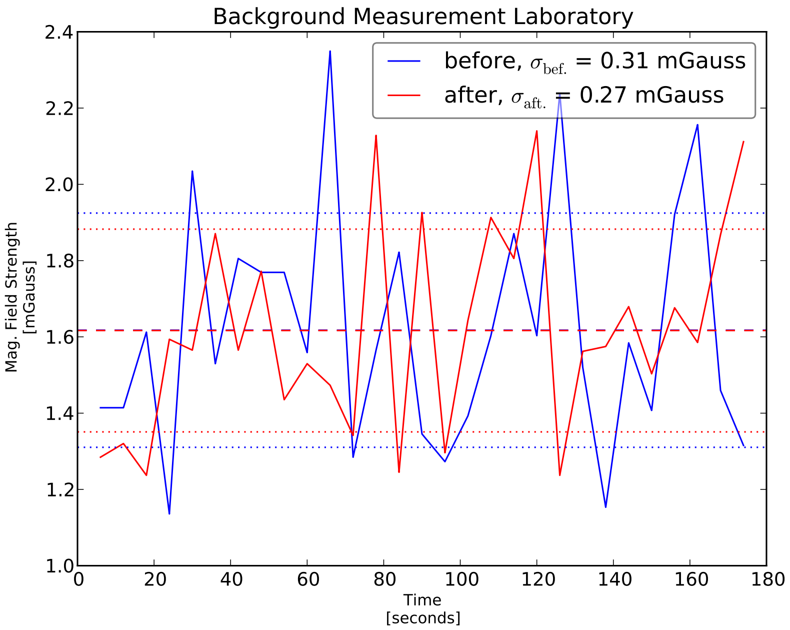

Figure 6.14.: Background field in the laboratory.

The results in fig. 6.15 show standard deviations of 0.21 mGauss and 0.29 mGauss, leading to a mean deviation of 0.25 mGauss. This is approximately 14% less fluctuation than in the laboratory.

This result sounds convincing to carry out our measurements completely outdoors. But unfortunately, Kiel is a very windy place – and wind hampers the experiment, since we have to pack the EPT magnet systems in two nitrogen flooded plastic bags, when carrying them outside. And this combination (wind plus two big plastic bags serving as a sail) nearly makes it impossible for the experimenter to place the plastic pedestals (see fig. 6.22) properly on the wooden plate (see fig. 6.25). As a result of that, the errors of measurement outdoors is likely to be much higher than the 0.25 mGauss, which the “empty” series suggests.

Error-Estimation of the Background Field

We will later need to quantify the fluctuations of the magnetic background. For this purpose, we consider two kinds of variations in the field:

- Changes in the field during one recording of an “empty” series.
- Change of the mean value of the background field between two “empty” series.

In fig. 6.14 we see that the mean values of the two series are identical, whereas the standard deviations are slightly different – the deviation of the “before” series is a bit higher than the one of the “after” series. The second kind of variation can clearly be seen in fig 6.15: the mean value of the background field drifted to a higher value during the measurement of the location series.

Consequently, we determine the fluctuation of the background field by summing up the half the difference of the mean values with the maximum of the two standard deviations:

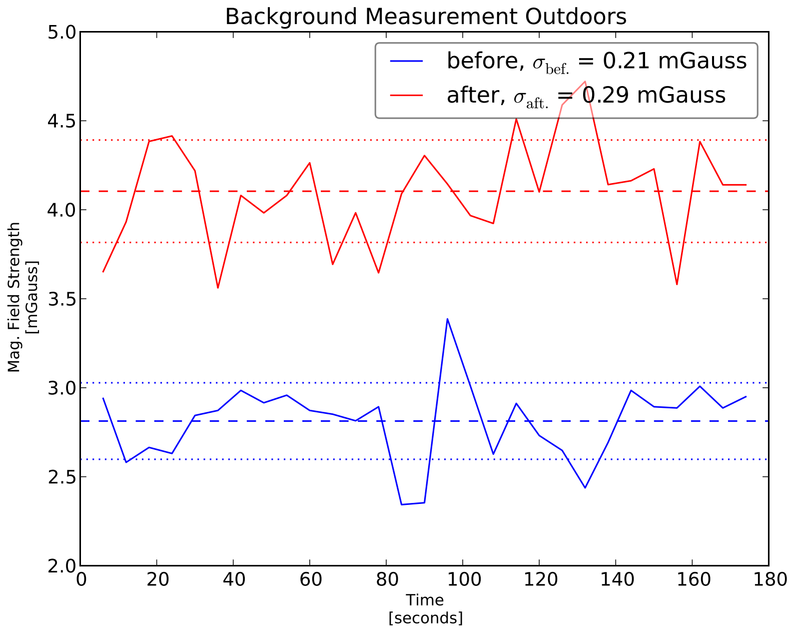

Figure 6.15.: Background field outdoors.

$$\Delta B_0 = \left| \frac{\overline{B_0}_{\text{before}} - \overline{B_0}_{\text{after}}}{2} \right| + \max\left(\sigma_{\text{before}},\ \sigma_{\text{after}}\right) \tag{6.1}$$

Long-Term Measurement of the Magnetic Background

A look at fig. 6.15 shows that the mean value of the background field increased between the two measurements by approximately 1 mGauss. To examine this behavior in more detail we carry out a long-term measurement of the background field in the laboratory LS11/12 for three days. Here, we do not use EMMA together with an iPhone for recording the field values, but rather a desktop computer with the desktop version of EMMA called “MacEMMA”. MacEMMA also relies on the AD-converter box and can be set up to record for up to three days. We tell MacEMMA to record the mean value of the measurements that the converter box delivered during the last 5 seconds – i.e. the computer gathers the information from the magnetometer every 0.1 seconds for 5 seconds and stores the mean of these data into a data base. The results of the measurement can be seen in the figures 6.16, 6.17 and 6.18.

We see that the background field fluctuates a lot more during the weekdays between 4:30 am and 7:00 pm than during the whole weekend. We observe sudden leaps in the measurements a lot more often from Thursday to Friday than on Saturday. A closer look in fig. 6.18 reveals that the flux densities remain nearly on the same level between two leaps and that the time between two leaps can vary from seconds to almost 30 minutes. Between the two background measurements outdoors from fig. 6.15, there must have occurred at least one such leap, which explains the difference of the mean values of nearly 1 mGauss.

A hint to the source of these fluctuations can be found by a fourier-analysis of the long-term data. But unfortunately fig 6.19 shows no sign of a periodically appearing

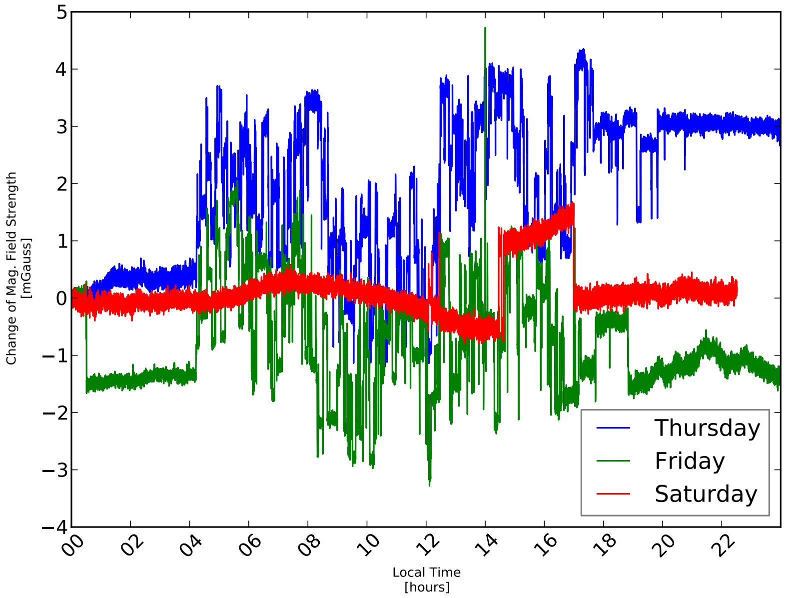

Figure 6.16.: Long-term measurement of the magnetic background in LS11/12. The values give the change of the magnetic flux densities in respect of the first values measured on the beginning of the respective day.

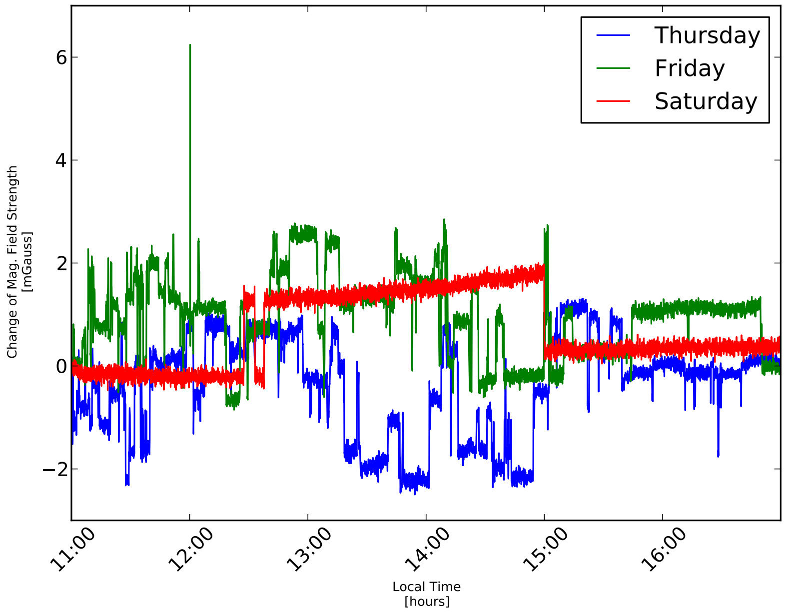

Figure 6.17.: Zoom into the long-term measurement from fig. 6.16. The measurements of the EPT fields mainly took place during this time.

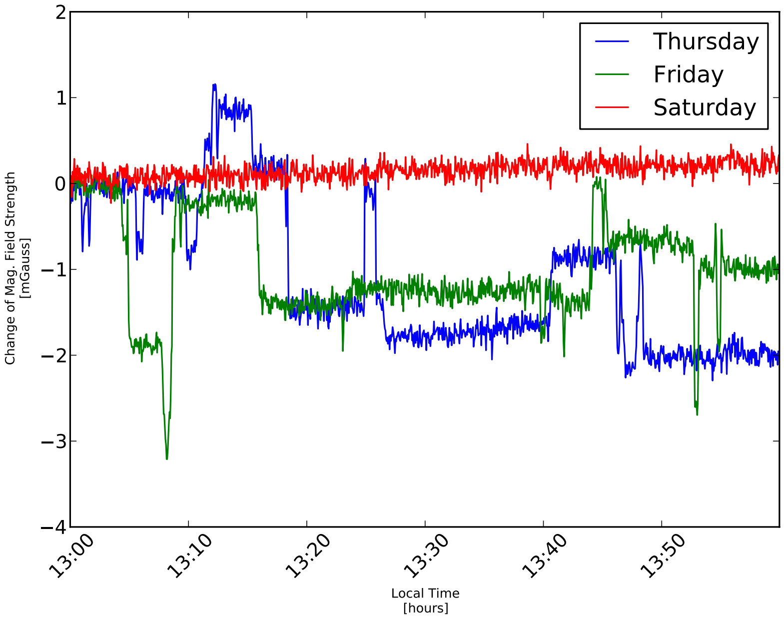

Figure 6.18.: One hour zoom into the long-term measurement from fig. 6.17.

disturbance. Till today we have no clue what the reason for the fluctuations might be. We can exclude the following suspects:

- Air conditioning system: This would also show up at the weekends.
- Circulating pumps of the heating installation: Were completely shut down at the time of our long-term measurement.
- Running experiments in the vicinity of LS11/12: A survey amongst the colleagues showed that there are no running experiments carried out that are switched on so early in the mornings.

As seen in section 6.4, the geomagnetic field varies about 0.3 mGauss, but on longer timescales as our 3 minutes for our background measurement. Fig. 6.10 suggests, that the geomagnetic field also fluctuates on shorter timescales, but much less than we have seen. This divergence can have its cause in the various high voltage experiments, that are carried out in the whole center of physics in the Leibnizstrasse, Kiel. The overall result of the background determination is, that we rather carry out our measurements during the night or the weekend. We chose to measure during the nights.

One solution to lower the influences of the geomagnetic field and the noise fields in the building could be the use of permalloy (also called Mu-metal) to deflect the annoying fields from our experimental setup. But unfortunately, our budget does not allow for this, since we would need a box of at least 1 m * 1 m * 1 m to contain all our instruments, which would cost about 2,000 €. To have a decent magnetic clean environment we would probably have to plank the whole laboratory with Mu-metall – and this would be disproportional expensive. On the other hand, Mu-metall is a “soft” magnetic material with very high magnetic permeability,t which not only manipulates the outer magnetic

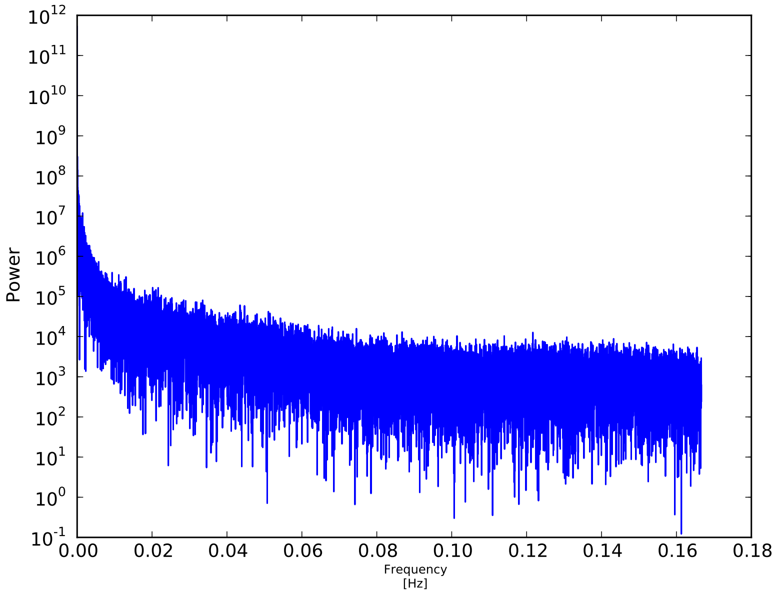

Figure 6.19.: Fourier transformation of the measured data from fig. 6.16.

field, but also the field inside. If we carried out our measurements inside a Mu-metallic box, the field from our magnet systems would also be diverted and thus be falsified. This could only be avoided, if the box was much bigger, so that the falsifications would be lower. But this would increase the price of the box significantly.

Precision of the AD-Converter Box

A source of imprecision could as well be the EMMA/magnetometer-combination itself. To test for this, we ground all the inputs of the AD-converter box to get a constant input-signal and take an "empty" series of 6 minutes. The result in fig. 6.20 is a standard deviation of 0.11 mGauss, which adds to the overall fluctuation as a base error caused by the inaccuracies in the electronic of the AD-converter box.

The AD-converter box digitizes the incoming voltage in the following way:

$$\text{AD-Value} = \frac{U + 2.5\text{V}}{5\text{V}} \cdot 65535$$

where "AD-Value" is the unit-less result of the AD-conversion, U is the input voltage and "65536" represents the full 16-bit-resolution of the AD-circuits.

EMMA calculates the flux densities with a linear relation, whose coefficients we got from a calibrating measurement (see section A.2.2). For example, the value for the y-axis is calculated with:

$$B_y \approx 5000 \text{ mGauss} - 0.152 \text{ mGauss} \cdot \text{AD-Value}$$

(for simplification reasons, we use an approximation. This is admissible, since our goal is only a rough estimation of the inaccuracies of the converter-box).

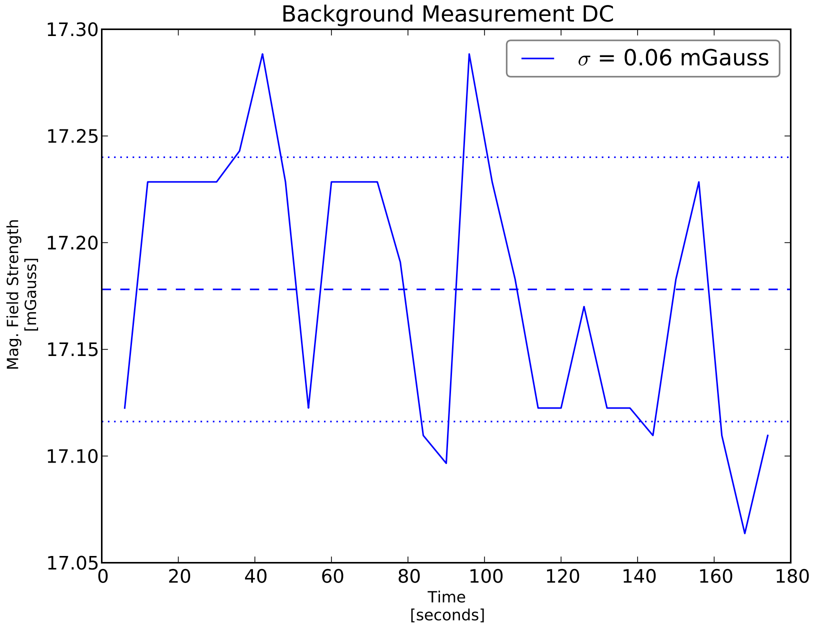

Figure 6.20.: "Fake" Background field, measured from a DC-source.

This leads to the following error estimation:

$$\begin{aligned} \triangle B_y &= 0.152 \text{ mGauss} \cdot \triangle \text{AD-Value} \\ &\Downarrow \\ \triangle \text{AD-Value} &= \frac{\triangle B_y}{0.152 \text{ mGauss}} = \frac{0.06 \text{ mGauss}}{0.152 \text{ mGauss}} \lesssim 0.4 \end{aligned}$$

This means that the conversion result varies with less than half a digit in average, which is exactly the error that is stated in the data sheets from *Analog Devices* mentioned in section 6.6.2. Since the inaccuracies of the AD-converters are approximately the same size as the errors of the magnetometer (see section 6.5.2), it would have been better to use 24 bit AD-converters instead of 16 bit converters. Then we would be able to also digitize the noise of the magnetometer. But using 24 bit converters would need a new design of the converter-board and a different micro-controller to control the converters. Unfortunately, we had not enough time to realize this improvement to the readout electronics. This could be a task for future works on the magnet systems.

Consequences of the Background Noise

The precision of our measurements are limited by the fluctuations of the background field and by the noise of our instrumentation. Now, that we know these limits, we can estimate the capabilities of our experimental setup in terms of how far away from the magnet systems we can detect their fields. Later in section 6.7.3 we will designate a distance, from which on we can not differ the background field from the EPT field.

6.7.2. Measurement of the Field

We will now come to the mapping of the EPT magnet systems. We start by describing in detail the experimental setup and the procedure, how to carry out the measurements.

Experimental Setup

The experimental setup consists of several auxiliary installations, that allow us to position and align the magnet systems according to the condition onboard Solar Orbiter. Special attention was laid on the requirement, that the whole setup must not contain any magnetic materials, that could influence the original fields of the magnet systems.

Wooden stand with Plastic Mounting and Wooden Plate The probe of the magnetometer is clamped into a plastic mounting that is held by a wooden stand that allows us to change the height and the position of the probe in the laboratory (see fig. 6.21). Both, the stand and the mounting, contain no metallic material at all and thus do not disturb the measurements.

The stand is positioned on a white wooden plate on which we can draw marks for our measurements (e.g. the perpendicular point of the barycenter of the three sensors inside the probe (see fig. 6.24)).

Plastic Pedestals To represent the relative orientation of the magnet systems onboard Solar Orbiter towards the MAG instruments, we designed four plastic cylinders with different slopes, onto which we place the magnet systems (see fig. 6.22). Each of these pedestals reproduce a different orientation of EPT1/EPT2 with respect to MAG IBS/MAG OBS. Carved into each slope is a deepening where we can place the magnet systems (see fig. 6.23). At the side of the deepening a piece of adhesive tape marks where to place the upper yoke side of the magnet system. The upper yoke is the one, where the separator of the magnet system contains four drill holes instead of two. To fix the systems we use Kapton tape.

The pedestals are marked with four carvings that are arranged at 90 distances around the bottom of the cylinder. We use these markings to keep the orientation of the magnet systems constant. One of these markings is labeled as the mark that has to point towards the magnetometer probe.

Measurement Setup The magnetometer has to be switched on for at least three hours before the measurements. The wooden plate is laid down on the floor of the laboratory. Onto the plate, the wooden stand containing the magnetometer probe is placed and not to be moved during the whole following measurements. We note the perpendicular point of the centroid of the three sensors in the magnetometer probe. Starting from that point on, we draw a line perpendicular to the wooden stand on which we mark the distances from the centroid. One of the plastic pedestals is then placed on that line at a distance where we want to measure the field. The accordingly labeled mark has to point towards the magnetometer probe (see fig. 6.24, 6.25 and 6.26).

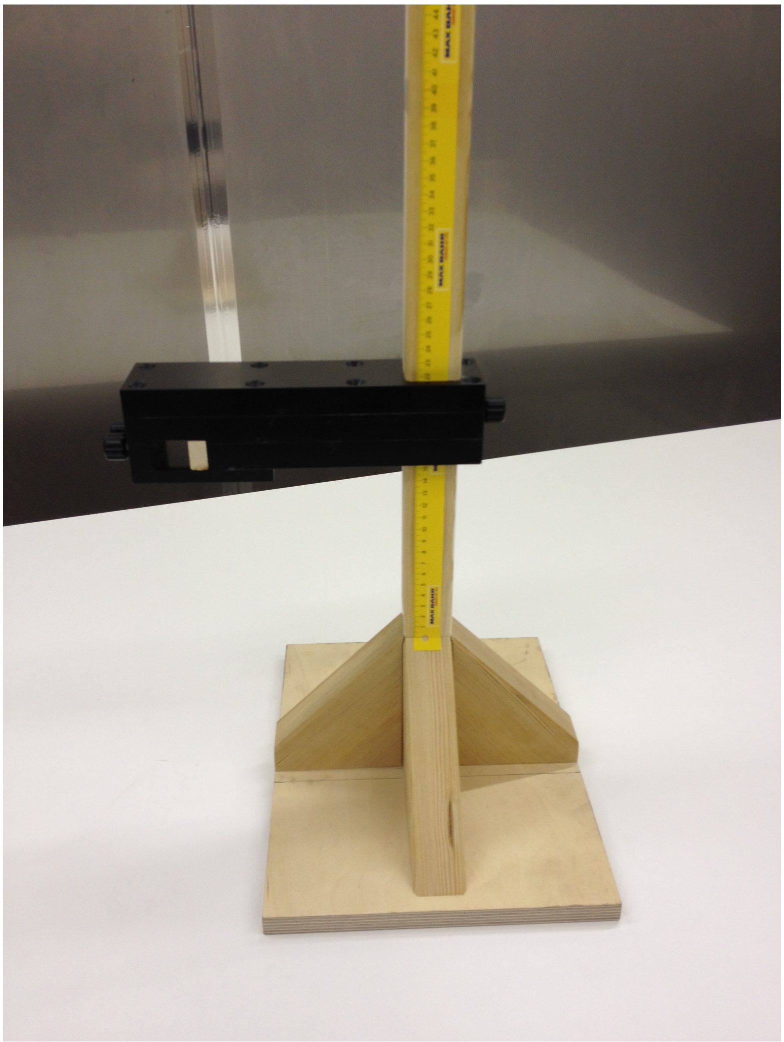

Figure 6.21.: Wooden Stand with plastic mounting (black) on wooden plate. Stuck on the stand one can see a yellow measuring paper tape for measuring the height of the probe.

Figure 6.22.: Four plastic pedestals to hold the magnet systems.

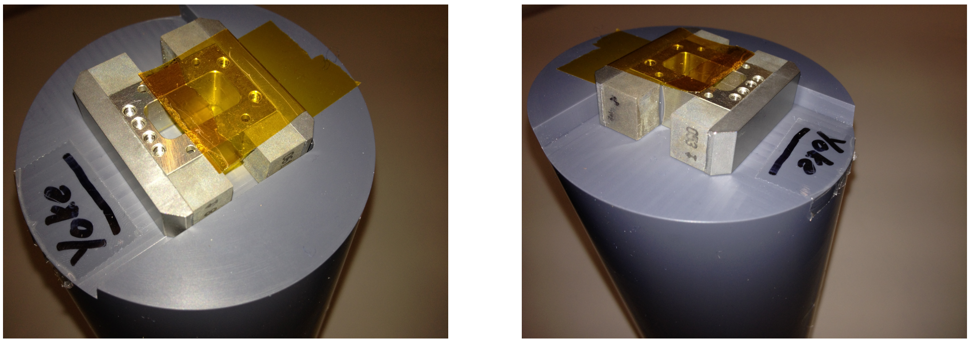

Figure 6.23.: Example of how the magnet systems are placed on the pedestals. Seen in both pictures is system *#2205*. The yoke with the four drill holes is placed at the side of the tape-marking. The side of the system in this configuration is called side 1, since the magnet at the yoke, that lies at the plastic edge, has a lower number (*18*) than the other magnet (*53*).

Figure 6.24.: Placement of the pedestal EPT1 →MAG IBS. The pedestal holds a dummy of a magnet system and is covered with a plastic bag. On the wooden plate one can see the drawings of the perpendicular point of the barycenter of the three sensors and the yellow measurement tape.

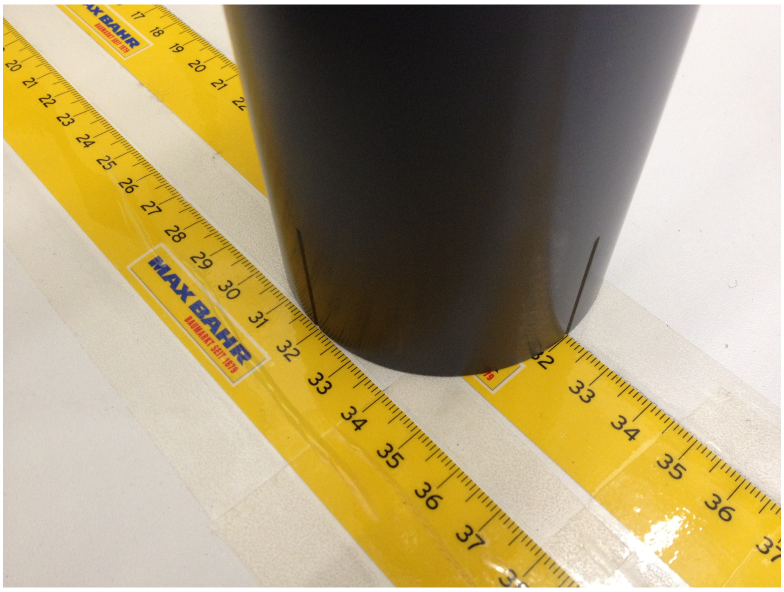

Figure 6.25.: In this picture the pedestal is positioned in a way, that the centre of the magnet system is 32 cm away from the centroid of the magnetometer probe and the orientation of the system towards the probe represents the orientation of the EPT toward the MAG instrument.

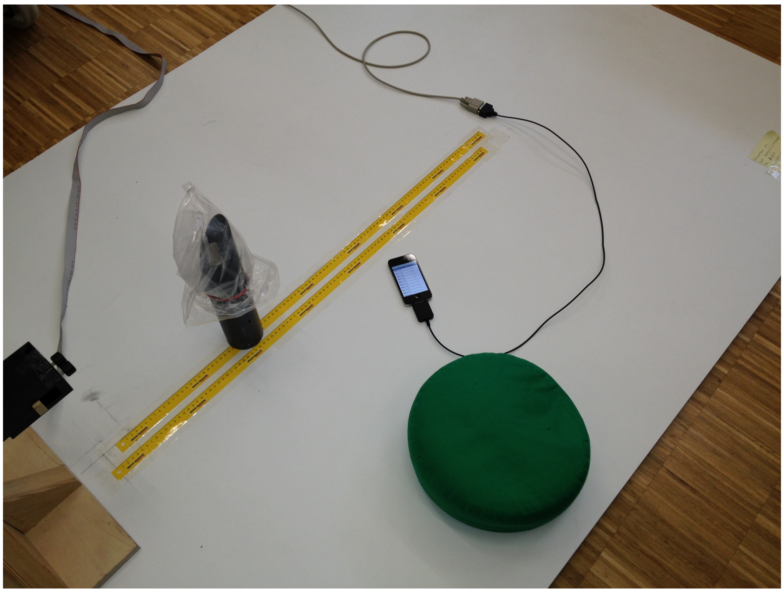

Figure 6.26.: Wooden plate on the floor of the laboratory with wooden stand, pedestal, and iPhone connected to AD-converter via serial cable. The round green cushion is for the experimenter to sit on and is filled with spelt.

Measurement-Procedure for a Location Series

We will now list in detail the steps to measure a location series for a magnet system as described in appendix A.2 :

1. We turn on the "Airplane Mode" of the iPhone/iPad/iPod.
2. At first, we take a measurement of the background field without the magnet system on the pedestal for three minutes. When already brought into the laboratory, the magnet system has to be located as far away from the magnetometer probe as possible.
3. After that, wearing gloves, we place the magnet system in the deepening of the pedestal and note which side points towards the probe.
4. We fix the magnet system with Kapton tape.
5. To keep the magnet system from dust, we cover it with a plastic bag.
6. We take a measurement at each point we want to measure. For EPT1-directions, we begin at a distance of 6.5 cm and continue with 0.5 cm steps up to the desired distance. For EPT2-directions we do the same, but starting at 8.5 cm.
7. After reaching the desired distance, we stow away the magnet system in its storage box (again wearing gloves) and take an additional "empty" measurement.
   Again: In the laboratory, the magnet system has to be located as far away from the magnetometer probe as possible.
8. We repeat the steps 2-7 (measurement without magnet, with magnet, without magnet again) for each combination of EPT1/EPT2, MAG IBS/ MAG OBS, Side 1/Side2.

6.7.3. Range of the Magnetometer

Before carrying out all the location measurements for all the EPT magnet systems, it is necessary to know the range of the magnetometer. As mentioned before in section 6.7.1, we need to designate a distance, from which on we can not differ the background field from the EPT field.

To determine this distance, we choose an arbitrary magnet system (#02204) and take its location series for the direction EPT 2 → MAG OBS up to 50 cm away from the center of the system. The results in fig. 6.27 show the magnetic flux densities in the three cartesian axes with the average background field in the respective directions already subtracted. Also plotted in fig 6.27 are the standard deviations σ_x, σ_y and σ_z of the background field in the x-, y- and z-axis.

We can see, that the x-value of the flux density drops into the order of magnitude of the corresponding standard deviation at a distance of approximately 200 mm, whereas the other two values reach their standard deviation later at around 330 mm and 380 mm. At about 250 mm the y- and z-values arrive at about twice their standard deviations.

We chose 40 cm as our measuring length, since at this distance all three components of the magnetic flux density we measure are dominated by the background noise. We will later in section 6.7.6 compare the measured data with the noise-level of the background (determined as described in section 6.7.1) to gain the last point from which we can tell that it shows a measurement of the EPT magnetic field.

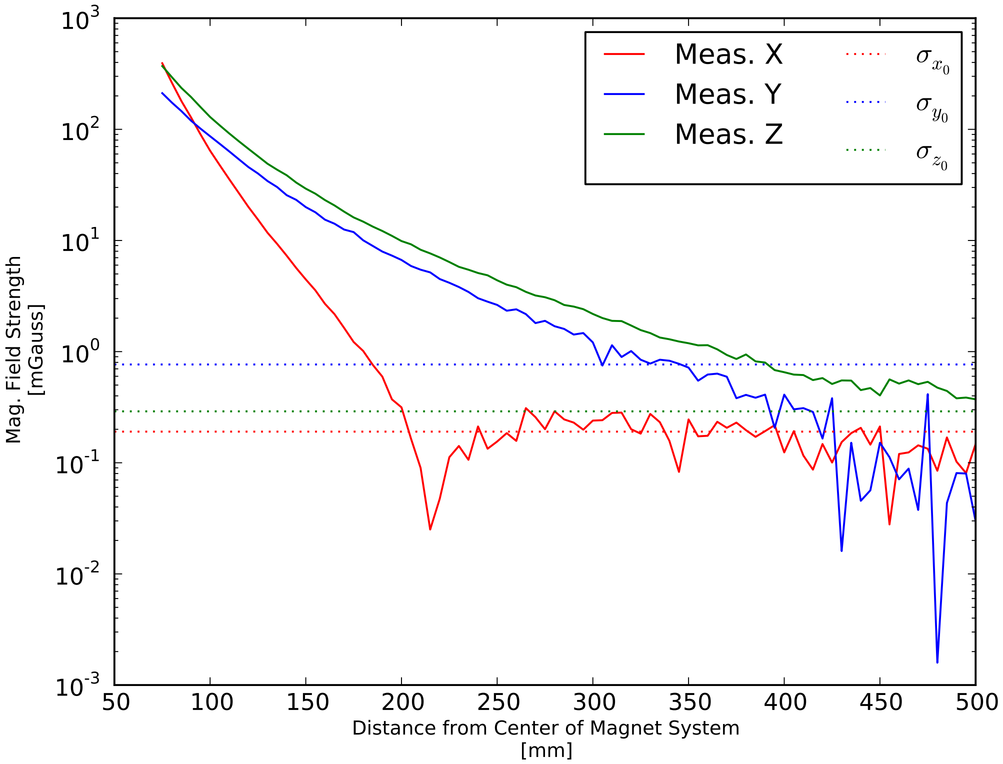

Figure 6.27.: Measurement plot of an arbitrary magnet system up to a distance of 50 cm.

6.7.4. Results of the Location Series of the EPT Magnet Systems

Following the procedure as described in section 6.7.2, we carry out the location series measurements for all the EPT-MAG-System-Side-combinations. Assigned to each of these combinations are three data files:

1. The first measurement of the background with no magnet system around.
2. The location series up to 40 cm with a magnet system on the plastic pedestal.
3. The second measurement of the background.

These three files have to be processed further to extract the pure magnetic field emitted by the magnet systems. At first, we will describe, how to deduct the background field from the EPT-field.

Processing of the Measured Data

The files containing the "empty" measurements consist of four comma separated columns that hold the time in seconds from the start of the measurement and the mean flux densities in the three cartesian axes at that time. We calculate mean values for each direction and for each data file:

$$\begin{array}{rclrcl} B_{x0_{\text{before}}} & = & \frac{1}{n}\sum_{i=1}^{n} B_{x0_{i_{\text{before}}}} & B_{x0_{\text{after}}} & = & \frac{1}{n}\sum_{i=1}^{n} B_{x0_{i_{\text{after}}}} \\ B_{y0_{\text{before}}} & = & \frac{1}{n}\sum_{i=1}^{n} B_{y0_{i_{\text{before}}}} & B_{y0_{\text{after}}} & = & \frac{1}{n}\sum_{i=1}^{n} B_{y0_{i_{\text{after}}}} \\ B_{z0_{\text{before}}} & = & \frac{1}{n}\sum_{i=1}^{n} B_{z0_{i_{\text{before}}}} & B_{z0_{\text{after}}} & = & \frac{1}{n}\sum_{i=1}^{n} B_{z0_{i_{\text{after}}}} \end{array}$$

And of course we calculate the overall mean values:

$$B_{x_0} = \frac{B_{x0_{\text{before}}} + B_{x0_{\text{after}}}}{2};\ B_{y_0} = \frac{B_{y0_{\text{before}}} + B_{y0_{\text{after}}}}{2};\ B_{z_0} = \frac{B_{z0_{\text{before}}} + B_{z0_{\text{after}}}}{2}$$

The data file from the location series measurement contains the values for the distance of the magnet systems from the magnetometer probe d_i and the mean flux densities in the three cartesian axes in this distance $B_{x_{\text{meas.}_\text{i}}}$, $B_{y_{\text{meas.}_\text{i}}}$ and $B_{z_{\text{meas.}_\text{i}}}$. From these flux densities we subtract the overall mean values of the background field to get the flux densities of the EPT magnet system:

$$\begin{array}{rcl} B_x(d_i) & = & B_{x_{\text{meas.}_\text{i}}} - B_{x_0} \\ B_y(d_i) & = & B_{y_{\text{meas.}_\text{i}}} - B_{y_0} \\ B_z(d_i) & = & B_{z_{\text{meas.}_\text{i}}} - B_{z_0} \end{array}$$

From this we calculate the norm as the total flux density:

$$B(d_i) = \sqrt{B_x^2(d_i) + B_y^2(d_i) + B_z^2(d_i)}$$

Figure 6.28 shows the results of the location measurements. We can see, that all magnet systems behave more or less equally – there is no outlier. We can also see, that the relative fluctuations increase with growing distance from the center of the magnet system.

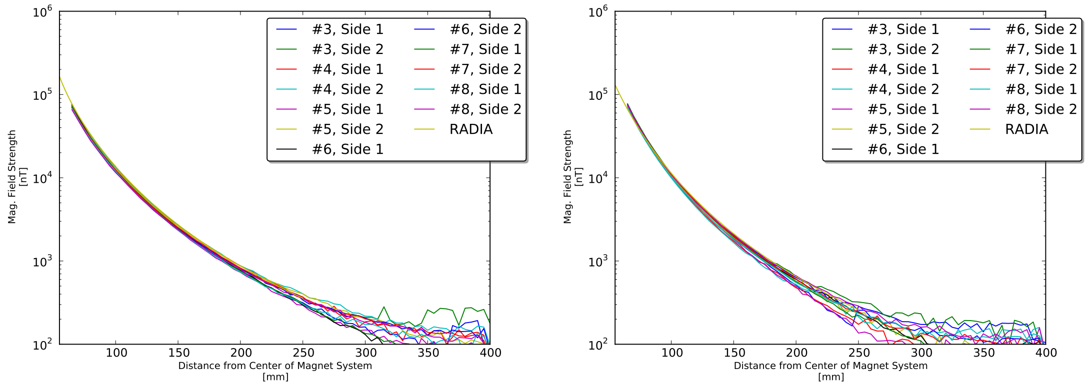

(a) EPT1 → MAG IBS *(b)* EPT1 → MAG OBS

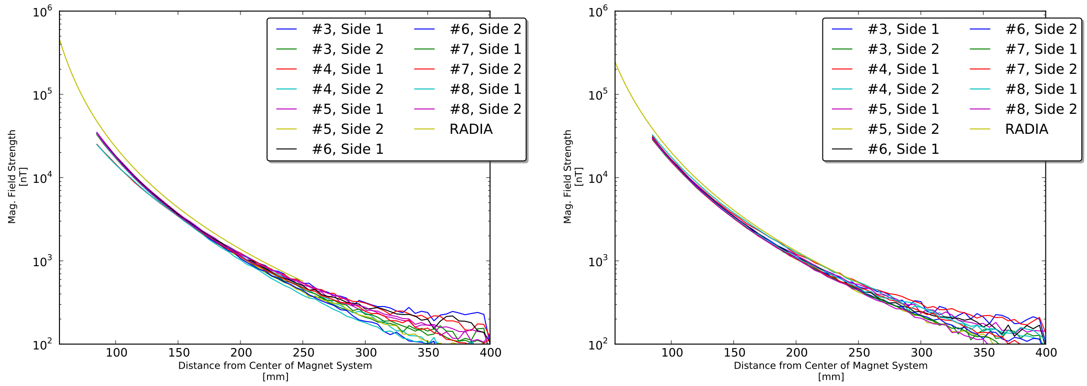

(c) EPT2 → MAG IBS *(d)* EPT2 → MAG OBS

Figure 6.28.: Measurements of the magnetic fields emitted by the EPT magnet systems compared to the RADIA simulations. We abbreviated the identifications of the magnet systems for better readability. Due to design constraints of the experimental setup, the location series for the directions EPT2 → MAG IBS and EPT2 → MAG OBS start later at 85 mm.

Together with the measurements, we also plotted the calculated behavior of the magnetic field with RADIA. In this calculation, we regarded the fact that the sensors inside the magnetometer probe are not joined into one single point and calculated the field as we would measure them with separate sensors. It shows that our measurements follow the predicted course and do not exceed the calculated values of the flux densities.

6.7.5. The Limits of the Dipole-Range

Now that we know the behavior of the near fields, we need to derive the far-field from that, in order to deduce the field values at the MAG-positions. The magnetic field of our magnet systems consist of a dipole and a quadrupole ratio:

$$B = B_{\text{dip.}} + B_{\text{quad.}}$$

where $B_{\text{dip.}} \propto r^{-3}$ and $B_{\text{quad.}} \propto r^{-4}$.

Near the magnet system, the quadrupole ratio outweighs the dipole ratio and we expect a decline of the field with r^{-4}. But with growing distance, the dipole term exceeds the quadrupole term and the field drops slower with r^{-3}.

Running Exponents

Our task now will be to make a worst-case assumption with regard to the MAG-limits, by determining the point, where the fields of the magnet systems begin to behave like a dipole rather than a quadrupole field and to extrapolate the field values from that point to MAG.

To achieve this, we use MATHEMATICA to fit the measured flux densities to an exponential model:

$$B = a \cdot x^b \tag{6.2}$$

where B and x are the measured field values and the distances from the magnet system, and a and b are the coefficients we get from the fit to the data points. In order to detect the desired turn-off-point to the dipole regime, we don't fit the model to the whole sample of data at once – we rather calculate a running fit to up to 10 points equally distributed around a chosen distance. ("Up to" means, that at the start and at the end of the data set, we fit the model to 5 points instead to 10 points for example, since there is no data available before the start respectively after the end.) This assigns an exponent to each distance and with that, we can then see where the field begins to switch from quadrupole to dipole.

Since fig. 6.28 shows, that all magnet systems practically behave the same way, we begin by examining one sample system – the results are shown in fig. 6.29. There we see that the exponent of the system reaches the noise level before the exponent raises from -4 to -3. It seems that the precision of our measurements is insufficient to detect the beginning of the far-field. To verify this assumption, we apply the mentioned running-fit-method to data calculated with RADIA.

The figures 6.30 and 6.31 show, that the far-field is expected to begin at a distance of about 70 cm and a minimum precision of 0.1 mGauss is needed. In section 6.7.1, we saw that the minimum fluctuation of the background field is at about 0.25 mGauss. This leads to the conclusion, that we are not able to measure the far-field of our magnet systems with our experimental setup and that we need to use a different approach to extrapolating the field values at MAG-positions.

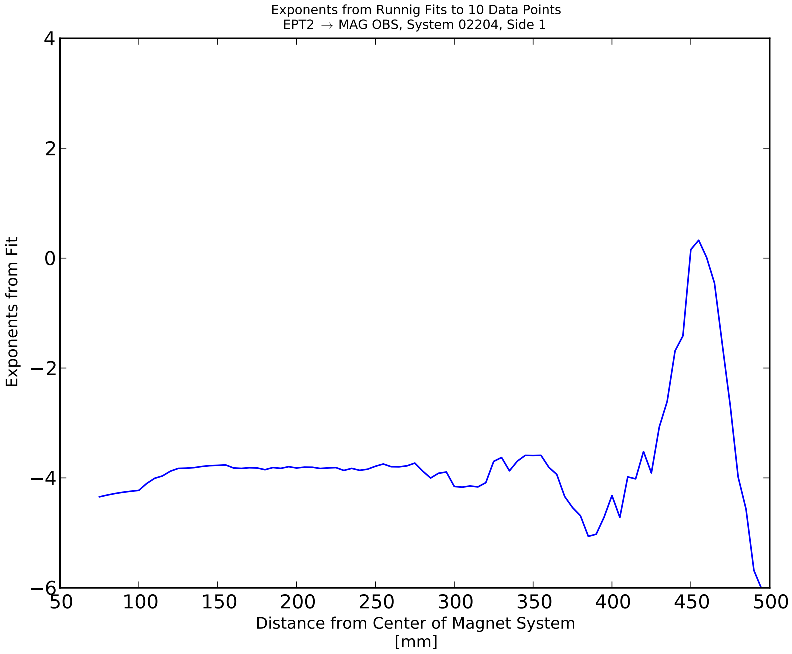

Figure 6.29.: Exponents from running fits to 10 data points for magnet system #02204, side 1, direction EPT2→MAG OBS.

Split Running Exponents

Another approach to finding the transition from the quadrupole- to the dipole-region is to split the location series

$$\text{location series} = \left\{ \left(r_0, \vec{B}_0\right), \left(r_1, \vec{B}_1\right), ..., \left(r_\mathrm{n}, \vec{B}_\mathrm{n}\right) \right\}$$

in two halves (the "near" series closer to the magnet system and the "far" series further away)

$$\left.\begin{aligned} \text{“near''}\ \text{series}\,(r_x) &= \left\{ \left(r_0, \vec{B}_0\right), \left(r_1, \vec{B}_1\right), ..., \left(r_\mathrm{x}, \vec{B}_\mathrm{x}\right) \right\} \\ \text{“far''}\ \text{series}\,(r_x) &= \left\{ \left(r_x, \vec{B}_x\right), \left(r_{x+1}, \vec{B}_{x+1}\right), ..., \left(r_\mathrm{n}, \vec{B}_\mathrm{n}\right) \right\} \end{aligned}\right\} 1 \leq \mathrm{x} \leq \mathrm{n}$$

and to determine the two exponents $\gamma_\mathrm{near}(r_x)$, $\gamma_\mathrm{far}(r_x)$ of the fits to the two parts.

To get an idea of how this would look like, we artificially calculated a magnetic field with defined transition points from the quadrupole- to the dipole-region at 13 cm and from the dipole- to the background-region at 36 cm. In fig. 6.32 we can see the flat dipole gradient of the "far" series starting at 13 cm. If the real turning point from quadrupole to dipole would lie above the background level of our measurements we would see a behavior that looks similar to the one shown in fig. 6.32.

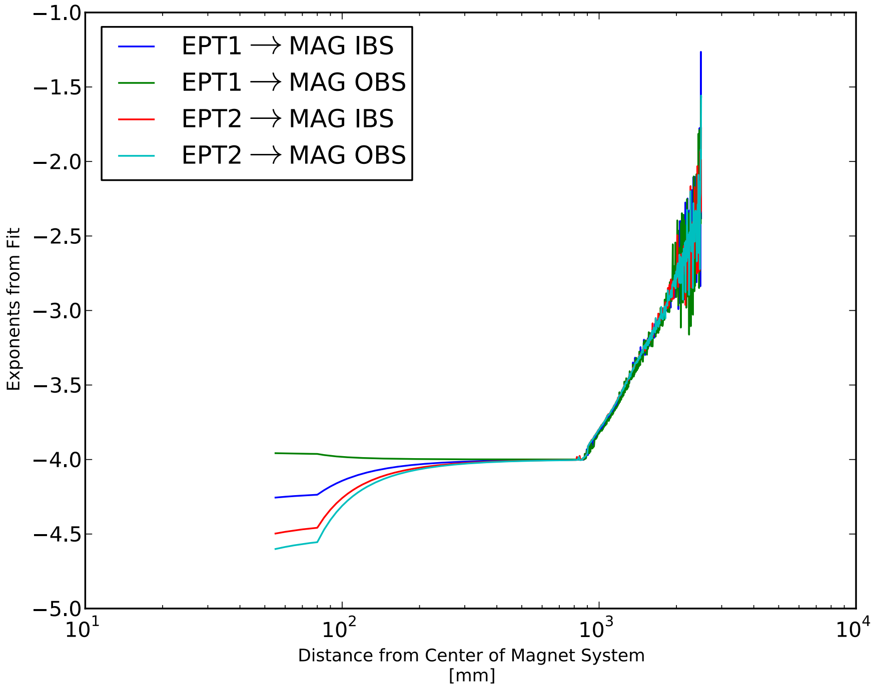

Figure 6.30.: Running exponents from RADIA calculation plotted over the distance from the center of the magnet system for the four different directions towards MAG.

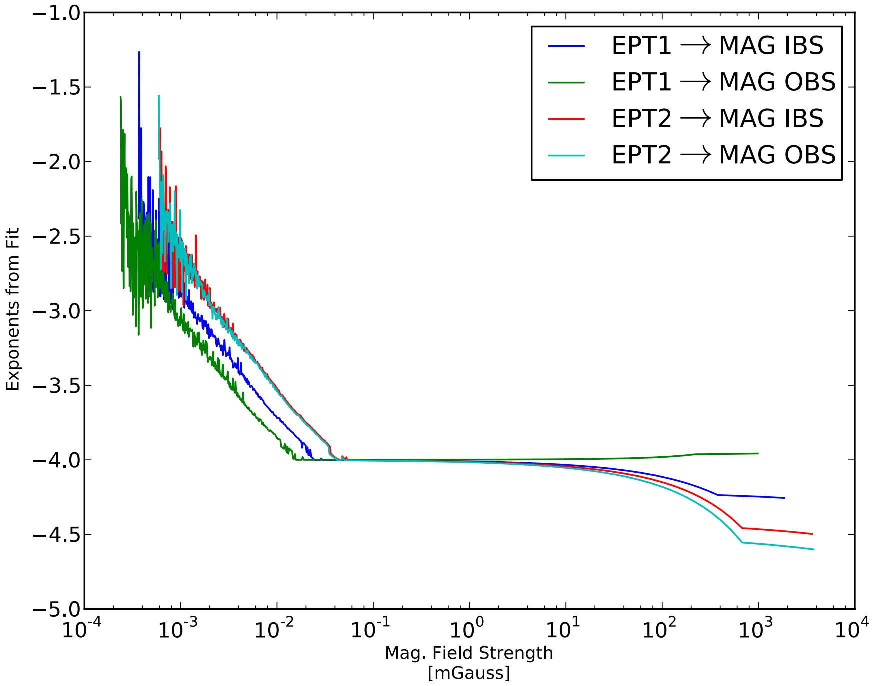

Figure 6.31.: Running exponents from RADIA calculation plotted over the field strength at the distance where the exponent was derived for the four different directions towards MAG.

A look at fig. 6.33 shows, that the exponents of the "far" series almost immediately and steadily rise from the quadrupole exponent of -4 and do not remain at the dipole value of -3, but instead rather show the behavior of the background noise at greater distances. So again, the result of this analysis is that the dipole-region of the EPT magnets can not be detected with our equipment and is concealed in the background magnetic field.

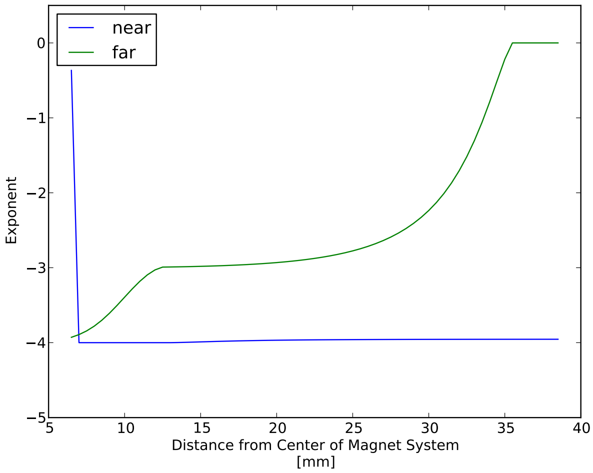

Figure 6.32.: Simulated gradients of the two exponents from the "far" and the "near" parts of the location series. The dipole domain is set to start at 13 cm. One can clearly see how the exponents from the far series start at the quadrupole value but steadily increase to the dipole value of -3 and remain there for more than 10 cm before they rise again to the background value of 0.

6.7.6. Extrapolation to the MAG Positions

Unfortunately, the former discussion showed that we neither can measure the magnetic flux densities at the MAG positions directly nor can we exactly tell where the fields begin to behave like a magnetic dipole. Our only possibility to make an assumption of the fields inflicted from EPT on MAG is to assume the worst case that the dipole-region starts right there where the measurements end and where the background starts and to extrapolate the field from that point on to the MAG positions.

We fit the model from equation (6.2) to 10 points around the middle of the relevant data set. The relevant data set is the range of the declining values up to the point, where the field reaches the value of the variation of the background field as determined in equation (6.1). The distances of these last relevant points of measurement from the center of the magnet systems are illustrated in fig. 6.34. We then use the fitted exponential relation to calculate the field value at that last relevant distance and extrapolate this field value with

$$B = a_{\text{dip.}} \cdot x^{-3}$$

to the respective distances to MAG.

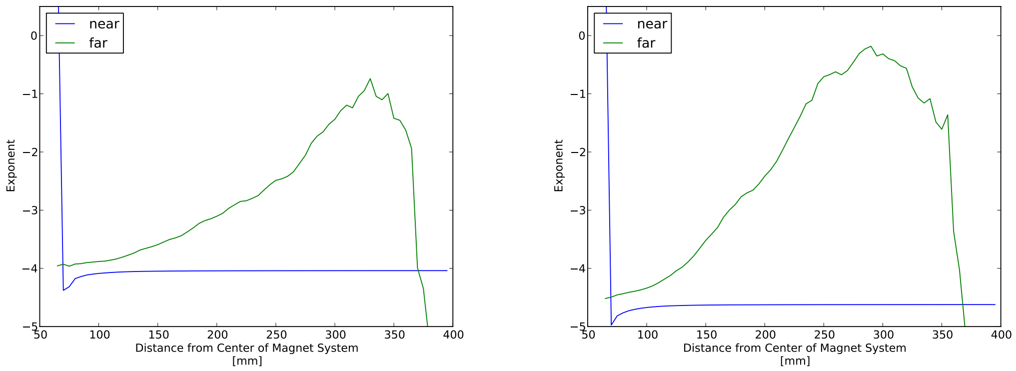

(a) EPT 1→MAG IBS
System #02204, Side 2

(b) EPT 1→MAG OBS
System #02204, Side 2

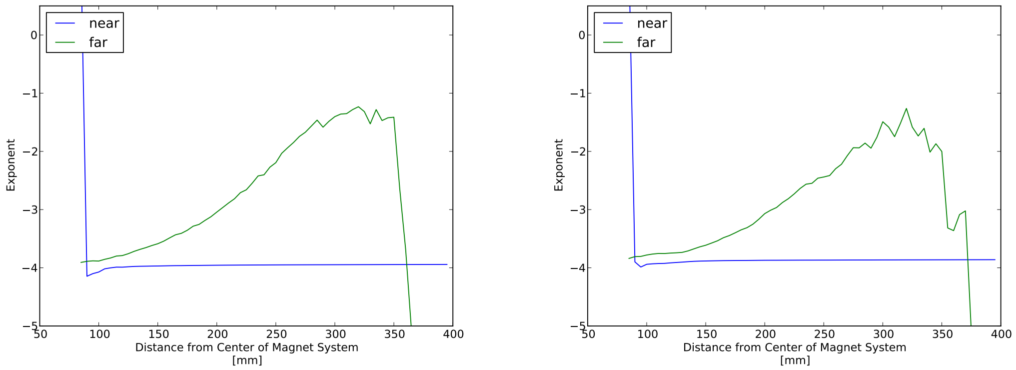

(c) EPT 2→MAG IBS
System #02202, Side 1

(d) EPT 2→MAG OBS
System #02202, Side 1

Figure 6.33.: The gradients of the two exponents from the “far” and the “near” parts of the location series. These four examples were chosen because of the low level of background disturbances (see section 6.7.6 fig. 6.34). All the remaining plots for the other EPT-MAG-system-side-combinations look similar to those shown here, except that the rise of the far exponents are partly steeper and begin sooner due to the higher background levels.

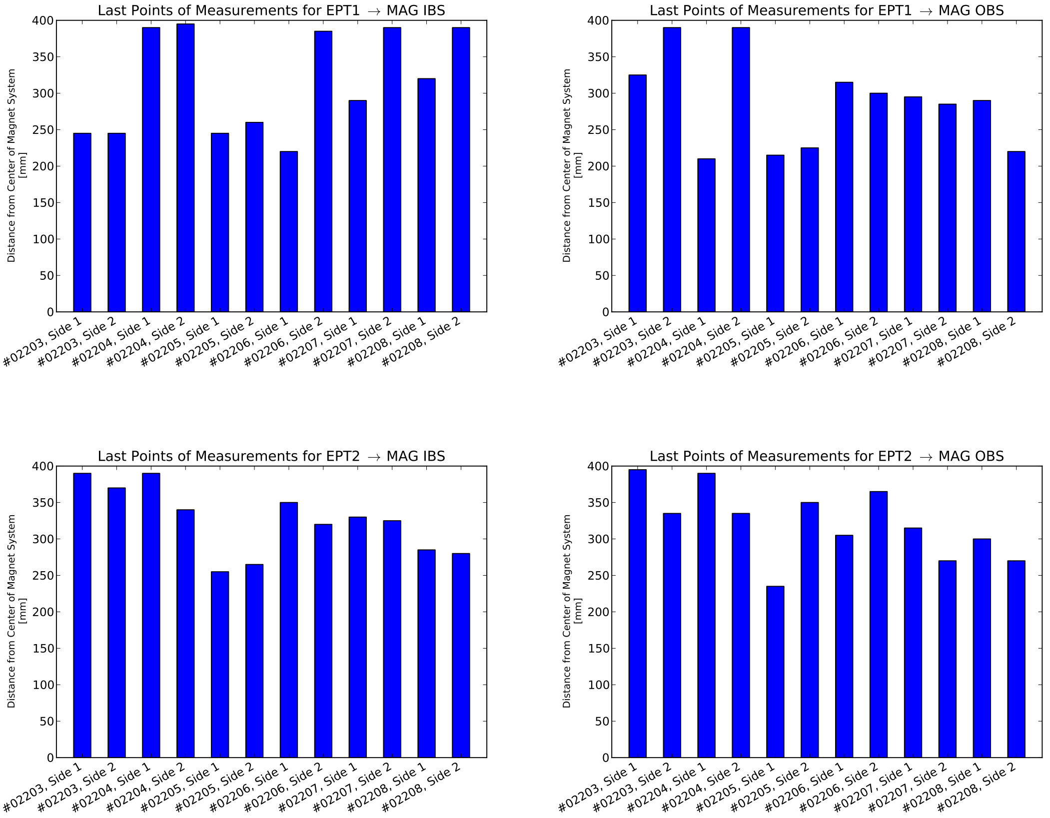

Figure 6.34.: Lengths of the location series until the background noise is reached grouped by the four different directions.

The coefficient $a_{\text{dip.}}$ is gained by solving

$$a_{\text{quad.}} \cdot x_{\text{last}}^{b} = a_{\text{dip.}} \cdot x_{\text{last}}^{-3}$$

for $a_{\text{dip.}}$.

After doing this for every measurement, we have got an extrapolated field value for every combination of magnet system, system side and EPT→MAG direction. The results for each direction are shown in fig. 6.35 and in table 6.4.

Now we “install” the magnet systems into the EPTs by combining two different systems into the two telescopes leaving out impossible combinations like:

- EPT1: System #02204, Side 1
- EPT2: System #02204, Side 2

We then add up the extrapolated field values of all the possible combinations and get the results shown in the figures 6.36 and 6.37.

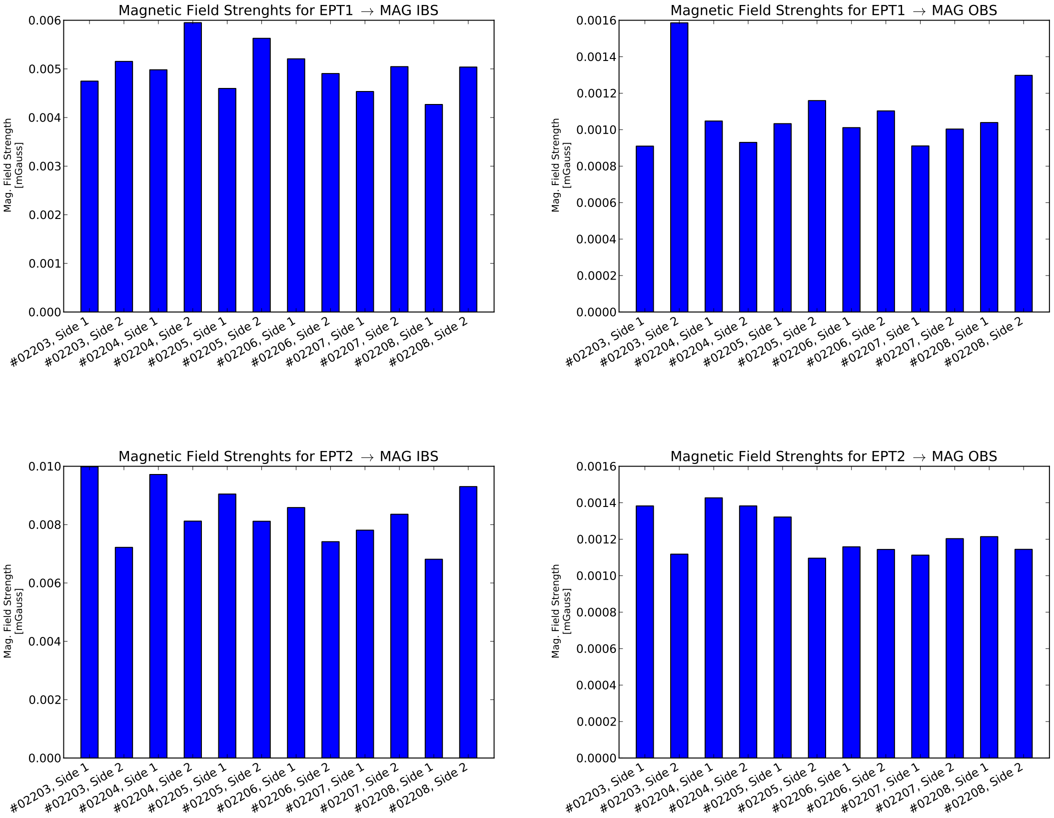

Figure 6.35.: The single distributions of each magnet system to the fields at the MAG positions grouped by the four different directions.

Magnet System #		**EPT1** **Field at MAG IBS (in T)**	**EPT1** **Field at MAG OBS (in T)**	**EPT2** **Field at MAG IBS (in T)**	**EPT2** **Field at MAG OBS (in T)**
02203	Side 1:	0.004749	0.000910	0.009985	0.001383
	Side 2:	0.005154	0.001586	0.007221	0.001118
02204	Side 1:	0.004982	0.001047	0.009719	0.001427
	Side 2:	0.005951	0.000930	0.008120	0.001383
02205	Side 1:	0.004598	0.001033	0.009048	0.001322
	Side 2:	0.005629	0.001160	0.008116	0.001096
02206	Side 1:	0.005207	0.001011	0.008585	0.001158
	Side 2:	0.004904	0.001103	0.007416	0.001144
02207	Side 1:	0.004535	0.000911	0.007810	0.001113
	Side 2:	0.005047	0.001003	0.008356	0.001203
02208	Side 1:	0.004268	0.001039	0.006813	0.001214
	Side 2:	0.005038	0.001298	0.009304	0.001144

Table 6.4.: The extrapolated field values of the magnet systems at the two MAGs.

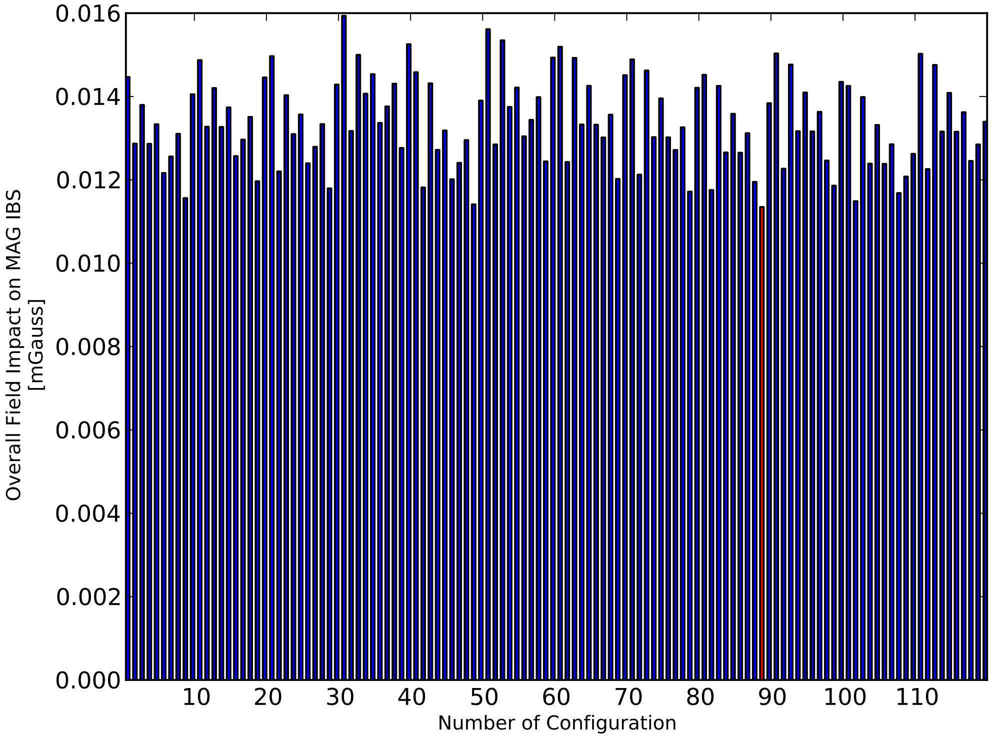

Figure 6.36.: Overall impact of the magnet systems on MAG IBS for every possible system configuration. Marked in red is the configuration with the least emission to MAG IBS: EPT1: System #02207, Side 1 – EPT2: System #02208, Side 1.The code for the configuration numbers can be found in table 6.5.

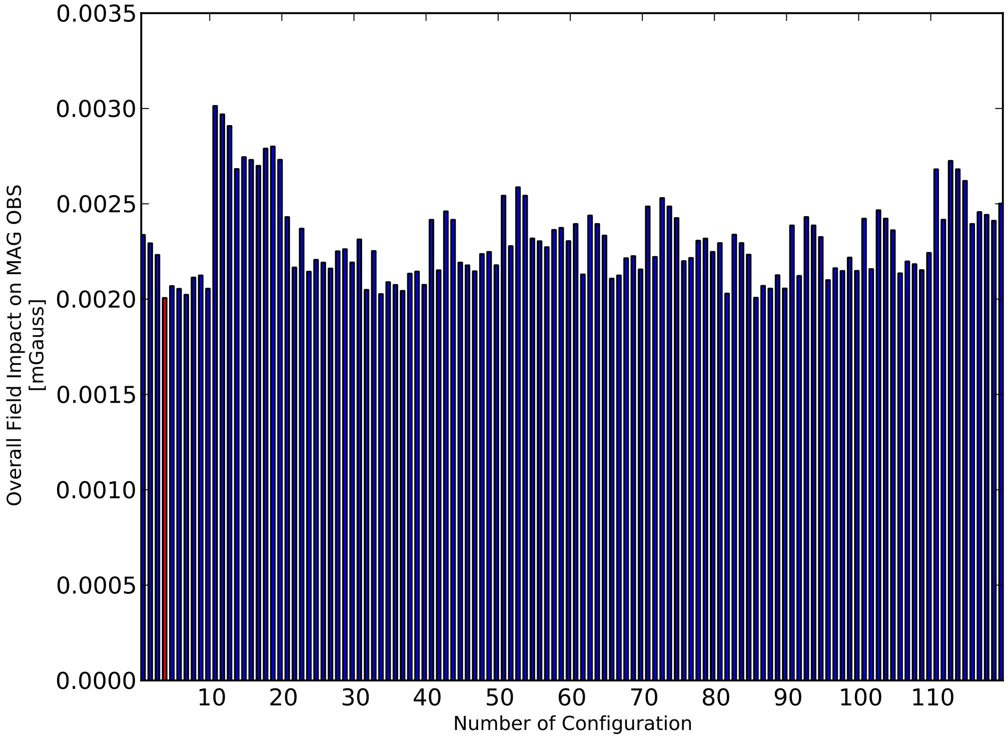

Figure 6.37.: Overall impact of the magnet systems on MAG OBS for every possible system configuration. Marked in red is the configuration with the least emission to MAG OBS: EPT1: System #02203, Side 1 – EPT2: System #02205, Side 2.The code for the configuration numbers can be found in table 6.5.

	EPT1		**EPT2**			**EPT1**		**EPT2**			**EPT1**		**EPT2**	
Config.	**System #**	**Side**	**System #**	**Side**	**Config.**	**System #**	**Side**	**System #**	**Side**	**Config.**	**System #**	**Side**	**System #**	**Side**
1	02203	1	02204	1	*41*	02205	1	02203	1	*81*	02207	1	02203	1
2	02203	1	02204	2	*42*	02205	1	02203	2	*82*	02207	1	02203	2
3	02203	1	02205	1	*43*	02205	1	02204	1	*83*	02207	1	02204	1
4	02203	1	02205	2	*44*	02205	1	02204	2	*84*	02207	1	02204	2
5	02203	1	02206	1	*45*	02205	1	02206	1	*85*	02207	1	02205	1
6	02203	1	02206	2	*46*	02205	1	02206	2	*86*	02207	1	02205	2
7	02203	1	02207	1	*47*	02205	1	02207	1	*87*	02207	1	02206	1
8	02203	1	02207	2	*48*	02205	1	02207	2	*88*	02207	1	02206	2
9	02203	1	02208	1	*49*	02205	1	02208	1	*89*	02207	1	02208	1
10	02203	1	02208	2	*50*	02205	1	02208	2	*90*	02207	1	02208	2
11	02203	2	02204	1	*51*	02205	2	02203	1	*91*	02207	2	02203	1
12	02203	2	02204	2	*52*	02205	2	02203	2	*92*	02207	2	02203	2
13	02203	2	02205	1	*53*	02205	2	02204	1	*93*	02207	2	02204	1
14	02203	2	02205	2	*54*	02205	2	02204	2	*94*	02207	2	02204	2
15	02203	2	02206	1	*55*	02205	2	02206	1	*95*	02207	2	02205	1
16	02203	2	02206	2	*56*	02205	2	02206	2	*96*	02207	2	02205	2
17	02203	2	02207	1	*57*	02205	2	02207	1	*97*	02207	2	02206	1
18	02203	2	02207	2	*58*	02205	2	02207	2	*98*	02207	2	02206	2
19	02203	2	02208	1	*59*	02205	2	02208	1	*99*	02207	2	02208	1
20	02203	2	02208	2	*60*	02205	2	02208	2	*100*	02207	2	02208	2
21	02204	1	02203	1	*61*	02206	1	02203	1	*101*	02208	1	02203	1
22	02204	1	02203	2	*62*	02206	1	02203	2	*102*	02208	1	02203	2
23	02204	1	02205	1	*63*	02206	1	02204	1	*103*	02208	1	02204	1
24	02204	1	02205	2	*64*	02206	1	02204	2	*104*	02208	1	02204	2
25	02204	1	02206	1	*65*	02206	1	02205	1	*105*	02208	1	02205	1
26	02204	1	02206	2	*66*	02206	1	02205	2	*106*	02208	1	02205	2
27	02204	1	02207	1	*67*	02206	1	02207	1	*107*	02208	1	02206	1
28	02204	1	02207	2	*68*	02206	1	02207	2	*108*	02208	1	02206	2
29	02204	1	02208	1	*69*	02206	1	02208	1	*109*	02208	1	02207	1
30	02204	1	02208	2	*70*	02206	1	02208	2	*110*	02208	1	02207	2
31	02204	2	02203	1	*71*	02206	2	02203	1	*111*	02208	2	02203	1
32	02204	2	02203	2	*72*	02206	2	02203	2	*112*	02208	2	02203	2
33	02204	2	02205	1	*73*	02206	2	02204	1	*113*	02208	2	02204	1
34	02204	2	02205	2	*74*	02206	2	02204	2	*114*	02208	2	02204	2
35	02204	2	02206	1	*75*	02206	2	02205	1	*115*	02208	2	02205	1
36	02204	2	02206	2	*76*	02206	2	02205	2	*116*	02208	2	02205	2
37	02204	2	02207	1	*77*	02206	2	02207	1	*117*	02208	2	02206	1
38	02204	2	02207	2	*78*	02206	2	02207	2	*118*	02208	2	02206	2
39	02204	2	02208	1	*79*	02206	2	02208	1	*119*	02208	2	02207	1
40	02204	2	02208	2	*80*	02206	2	02208	2	*120*	02208	2	02207	2

Table 6.5.: Codes of the magnet system/sides configurations in EPT1 and EPT2.

Note: Here we first calculated the norms of the magnetic field, then extrapolated them to the MAG-positions and summed up the results in the end. Whereas in section 6.2.8, we first summed up the field vectors component-by-component and then calculated the norm of the result. This implies, that the results of our extrapolated measurements have to be looked at as upper limits of the real values of the magnetic field at the MAG-positions, which is feasible, since our goal was to make a worst-case analysis for our impact on MAG.

The result from the analysis is, that the combination:

- EPT1: System #02207, Side 1
- EPT2: System #02208, Side 1

emits the least overall field to both MAGs, whereas the combination:

- EPT1: System #02203, Side 1
- EPT2: System #02205, Side 2

results in an overall field that is slightly higher for both MAGs, but with 0.2006 nTesla shows the least magnetic field at the MAG OBS position. All these mentioned values are far below the limit of 2 nTesla at MAG OBS for both EPTs together. A further survey of all the possible combinations showed that the best choice for the flight-spare model of EPT would be magnet system #02206 considering that we must be able to replace either of both EPTs.

A final measurement of the magnetic far-field at the Imperial College in London by the MAG group is pending and will clear the impact of the EPT magnet systems on the magnetometers onboard Solar Orbiter.

7. First Measurements

7.1. EPT Demo Model

With the most important theoretical preliminary work finished, we started building a demo model of EPT (Burmeister 2011) to prove the basic functionality and to verify the measuring capabilities (Sie 2011) (see fig. 7.1). For that we used remaining detectors of SEPT, which have the same dimensions as the planned EPT detectors. Some of these detectors are covered with a Parylene foil, which we also wanted to apply to our detectors at first, but instead replaced the Parylene with Kapton. In section 5.4 we saw that the Parylene and the Kapton foil are quite similar concerning their physical properties. For this reason we are able to safely use these detectors for our demo model.

Another difference to the planned detector system is the space between the two detectors: The design of the old detectors only allow for 4 mm as the closest distance, but since this gap is only crucial in terms of minimum ionizing particles coming through the shielding, we can neglect this detail for demonstration purposes.

In other respects, the demo model was designed and built just as discussed in this work, including the collimator, the shielding and the magnet system. Thus, it represents the later flight models in detail and can demonstrate the functionality of the instrument.

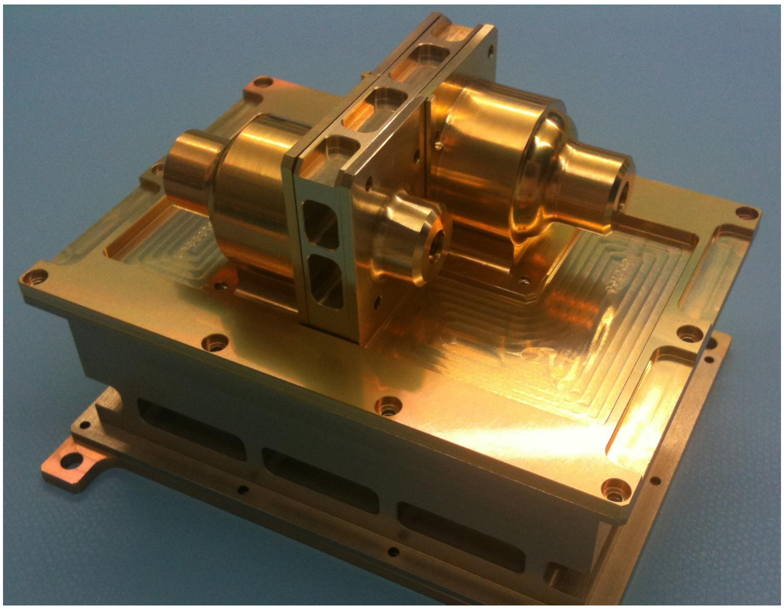

Figure 7.1.: The demo model of EPT.

7.2. Measurements with Bi-207

Following the test procedure worked out by Sie (2011), the first tests on the demo model were carried out by using a radioactive ^{207}Bi source that can be placed in front of the two collimator openings of a telescope. ^{207}Bi is, inter alia, a source of energetic electrons that originate mainly from internal conversions of the excited nucleus. The prominent e^- emission lines are listed in table **??**.

With this source, we can test the setup for the ability to deflect electrons away from the detector on the magnet side and for the concept of anti-coincidence when the electrons pass through the detector on the foil side and produce a signal in the second detector.

These tests were carried out by the colleague Dennis Sie. He placed the ^{207}Bi source in front of the foil side of the telescope and measured the count rates in the four single segments of the detectors for 24 hours. After that he repeated this measurement but now with the source in front of the magnet side.

Magnetic Deflection The comparison of the count rates in the inner segments of the two detectors from the two measurements is shown in fig. 7.2. There we can see that the magnetic field can deflect the conversion electrons at 482 keV and at 554 keV. When we remember fig. 6.7 we recall that electrons above 725 keV can reach the detector despite the magnetic field. The detection of the electron at 976 keV in detector C approves this result.

(**Note**: According to fig. 5.14, the range of electrons at 976 keV is much longer than the 0.3 mm thickness of the detectors, but the ability of electrons to scatter in matter and to travel a longer path than the straight line makes it possible for them to deposit all their energy in one detector.)

Anti-Coincidence Logic When we take a look at the count rates in the inner segments of the two detectors from the measurement with the source in front of the foil side we see in fig. 7.3 the peaks of the K-, L- and K-conversion electrons at 481.7 keV, 553.8 keV and at 975.7 keV in detector A but also shifted towards lower energies in detector C. This means that the electrons pass through the first detector and trigger the anti-coincidence logic in the second detector.

These results show that the tests were successful and that the deflection of electrons by the magnetic field and the anti-coincidence principle work as predicted.

Process	Energy in keV	Intensity in %
Auger L	7.97	54.4 ± 14
Auger K	56.7	2.9 ± 3
CE K	240.10 ± 12	$1.88{\cdot}10^{-4}$ ± 17
CE L	312.24 ± 12	$3.2{\cdot}10^{-5}$ ± 3
CE M	324.25 ± 12	$7.5{\cdot}10^{-6}$ ± 7
CE K	481.6935 ± 21	1.537 ± 22
CE L	553.8372 ± 21	0.442 ± 6
CE M	565.8473 ± 21	0.111 ± 5
CE K	809.77 ± 12	0.00246 ± 10
CE L	881.91 ± 12	$4.07{\cdot}10^{-4}$ ± 17

Table 7.1.: Prominent e^- emission lines of ^{207}Bi. Data obtained from NuDat2. (NuDat2 website: `http://www.nndc.bnl.gov/nudat2/`)

Process	**Energy in keV**	**Intensity in %**
CE M	893.92 ± 12	$9.5 \cdot 10^{-5} \pm 4$
CE K	975.651 ± 3	7.08 ± 17
CE L	1047.795 ± 3	1.84 ± 5
CE M	1059.805 ± 3	0.44 ± 3
CE K	1354.20 ± 20	$3.55 \cdot 10^{-4} \pm 8$
CE L	1426.34 ± 20	$6.13 \cdot 10^{-5} \pm 13$
CE M	1438.35 ± 20	$1.44 \cdot 10^{-5} \pm 3$
CE K	1682.224 ± 9	0.0238 ± 12
CE L	1754.367 ± 9	0.0034 ± 5

Table 7.1.: Prominent e$^-$ emission lines of ^{207}Bi. *(continued)*

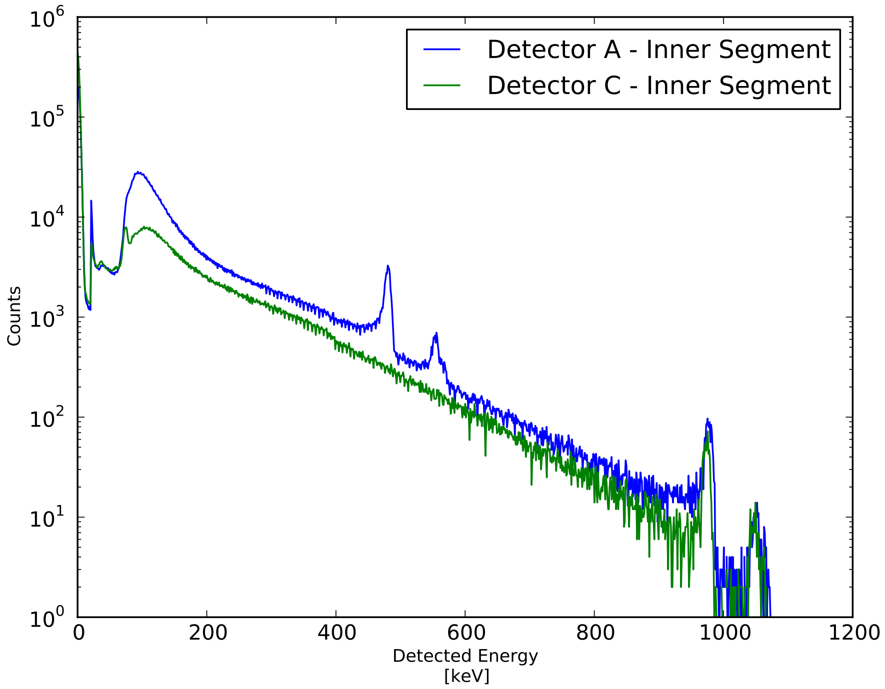

Figure 7.2.: Result of two 24 hours measurements with a Bi-207 radioactive source. The source was placed before the collimator opening of the magnet side (green) and in front of the opening of the foil side (blue) of one telescope head. One can clearly see that the two peaks from conversion electron K and L at 482 keV and at 554 keV are missing in the spectrum of the magnet side, whereas the higher energetic peak of the conversion electron K at 976 keV is still visible – the magnet deflection of the electrons works as predicted.

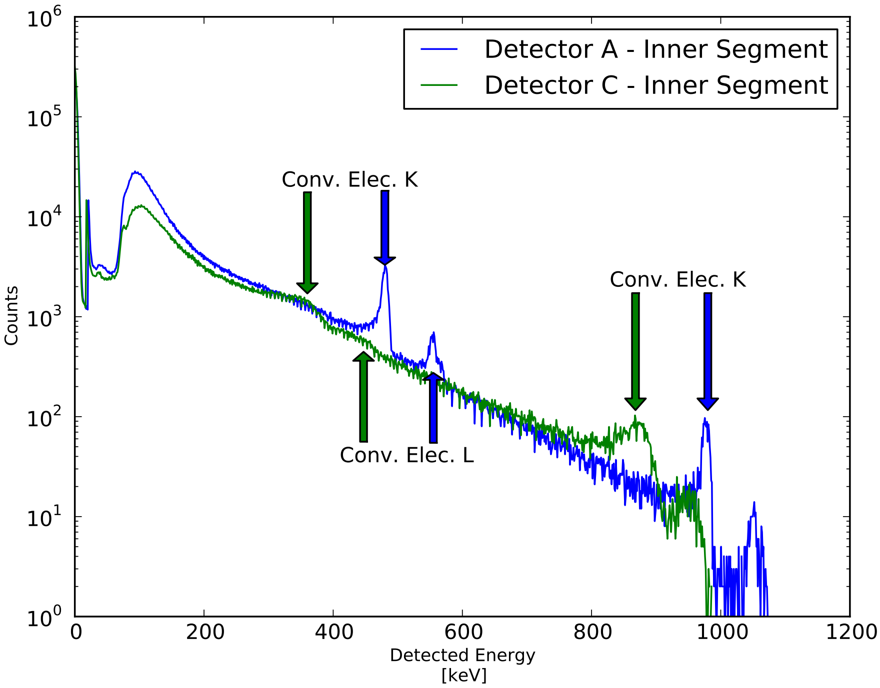

Figure 7.3.: During this 24 hour measurement the Bi-207 source was placed in front of the foil side. We can easily see the peaks of the K-, L- and K-conversion electrons at 481.7 keV, 553.8 keV and at 975.7 keV in the first detector at the foil side (blue arrows). These peaks also appear in the second detector at the magnet side (green) but shifted towards lower energies (green arrows), since the electrons lost some energy while passing the first detector. This behavior is utilized by the anti-coincidence logic.

8. Conclusions

Now it is time to look back and see if we could reach our goals from section 4, but also to take a look into the future and see what we can do to build a successful instrument onboard Solar Orbiter.

8.1. Summary and Assessment

Based on a measurement of a big SEP event at 1 AU, we estimated the proton and electron intensities at 0.28 AU and derived a needed geometric factor of ≈ 0.01 cm^2 srad considering the maximum cadence of the read-out electronics of 10^5 events per second. We implemented this geometric factor by choosing the opening of the collimators and the size of the silicon detectors to be of 6 mm in diameter where the openings are located 22.39 mm away from the detector surfaces. This gave us a nominal geometric factor of 0.0141 cm^2 srad.

Equipped with this geometry, we exposed the EPT model in GEANT4 to the mentioned SEP event with the same spectral shape as measured but with higher intensities to represent the closer distance of 0.28 AU of Solar Orbiter to the sun. The result of this simulation was that the count rates in the single segments of the detectors do not exceed the electronics' limit which means that EPT will be able to fully observe even such high events so close to the sun.

Anticipating following results concerning the mechanical design and the magnet system, we determined the energy dependent geometric factors for the two trigger conditions for electrons and protons. The GEANT4 simulation showed two results:

1. The energy dependent geometric factors are similar to the nominal factor for electrons and protons over the designated energy range of the particle types.
2. The particle separation technique works as desired – also with the stray field of the magnet system reaching out far outside of the instrument considered in the GEANT4 simulation.

To minimize the background noise produced by scattering electrons penetrating the shielding or bouncing from the inside of the collimators or by relativistic particles, we had to improve the mechanical design of the aluminum shielding and the profile of the collimator. Furthermore, we had to consider the dependence of the noise level from the distance between the detectors.

For the first issue, we applied the spot-shielding method to strengthen the aluminum shielding where necessary. We found out that a shape with a torus around the interface of the housing and the foil-collimator, a 2 mm thicker collimator and a 2 mm thicker housing reduces the noise from penetrating electrons enough that these false signals do not influence our measurements much. We could also show that we don't need a dome shaped fortification around the housing that contains the detectors.

With this defined shape of the shielding, we were able to determine the noise we still must expect from penetrating electrons. For this purpose, we examined how the primary protons from the galactic cosmic background produce secondary electrons in aluminum. We did this by shooting cosmic protons onto an aluminum disk with varying thickness in GEANT4 and gathering the resulting spectrum of secondary electrons. The accumulated intensities of the secondary electrons were then multiplied by the geometric factor of the resulting EPT model. This gave us the result that we can expect one false event in 18 days ($6.4 \cdot 10^{-7}$ events per second), which is low enough that it doesn't falsify the EPT measurements severely.

The problem with scattered electrons inside the collimators could be lowered by approximately 20% by choosing a collimator profile with 7 ribs that are 0.5 mm thick, 1.5 mm high and equally aligned over the collimator length. This model is not the one that reduces the scattering the most, but the other two models that could adsorb more electrons can not be manufactured by our workshop.

The background from relativistic particles that can always penetrate nearly any shielding can only be minimized by utilizing the trigger conditions together with a close detector alignment. We saw that the minimum distance between the two detectors of 0.4 mm reduces the geometric factor for those minimum ionizing particles significantly. An estimation of the expected count rates from GCRs yielded the result of one event to be expected in 10 minutes ($1.6 \cdot 10^{-3}$ counts per second), which is also acceptably low.

After improving the mechanical design of EPT, we turned towards the setup of the magnet system of the instrument.

Calculations showed that 1.18 Tesla is the right residual induction for the permanent magnets of the magnet system. With this setup we computed that we could deflect electrons up to 725 keV entering the collimator under the angle of 34°. We could also show that the far field at the MAG OBS position would be 0.0054 nT which is far below the maximum allowed field of 1 nT.

Measurements with a Hall effect probe of the magnetic field in the gaps of the ordered and manufactured systems showed similar values as the simulations. We therefore concluded that the systems are able to deflect electrons that would otherwise produce a false signal in the proton channel. The measurements of the near fields showed a very close accordance with the field computations in RADIA.

The determination of the far field at the MAG OBS location however was not this easy. The high background from the geomagnetic field prevented us to directly measure the magnetic flux density this far away from the center of the magnet systems. We were also not able to discover the point where the behavior of the field turns from a quadrupole to a dipole regime. Therefore, we were compelled to extrapolate the field to the MAG OBS position using a dipole decline beginning at the last point where we were able to detect a significant magnetic field produced by a magnet system.

This procedure gave us an extrapolated field value at MAG OBS for every EPT/system/side/direction combination. from this data we obtained a combination that exposes MAG OBS to the lowest magnetic field:

- EPT1: System #02203, Side 1
- EPT2: System #02205, Side 2

The extrapolated field at the MAG OBS position sums up to approximately 0.2 nT and is far below the 1 nT limit.

The first measurements with the ^{207}Bi source showed that the particle separation technique works as desired and that electrons with high energies can penetrate the first detector to produce a signal in the second detector which is necessary for the trigger condition logic. These first tests also showed the high energy resolution of the instrument.

8.2. Outlook

Although a lot of work has been done, there still remain some open issues and topics that are worth to be treated in the future:

- The magnet systems now have been tested for their ability to deflect electrons and their outside fields have been measured. All this happened at room temperature and under the normal atmospheric pressure. Now it would be interesting to know how the magnets behave in a space environment – i.e. examinations and simulations have to be carried out at higher and lower temperatures and under vacuum conditions.
- The new detectors from CANBERRA have to be analyzed concerning their parylene coating and their reliability in space.
- The whole setup has to be calibrated using electron and ion beams from accelerator sites.
- The shielding has to be tested if it withstands high energetic particles.
- The shielding and the production of high energy particles by the spacecraft, the electronic box and the adjacent HET has to be investigated in order to give a more exact approximation of the background noise produced by galactic cosmic rays.
- The absorption of electrons in the collimators has to be verified with an electron source.

Appendix

A. Introduction to EMMA

This section is meant to be a short manual for the EMMA-user to give a quick look into the functions and features the App provides.

At the end of this section we show the calibration data of the EMMA/magnetometer-combination.

A.1. Using EMMA

After installing, EMMA is launched by tapping the icon as shown in fig. A.1. At first, EMMA greets us with her main tasks (see fig. A.2):

- Location Series
- Time Series
- Histogram
- Dropbox Synchronization
- Link Dropbox

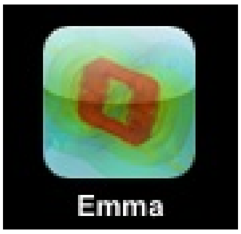

Figure A.1.: EMMA-Icon

The language, that EMMA talks, is dependent on the system language of the iOS device. In the first version, EMMA supports english and german. In the following, we will keep to the english version. The german version differs from the english one only in the used language and not in any functionality.

With the start of the App, EMMA checks whether the serial cable is plugged in or not and tells the user about this (see fig. A.3).

What happens, when an entry in the table from fig. A.2 is tapped, is described in the following.

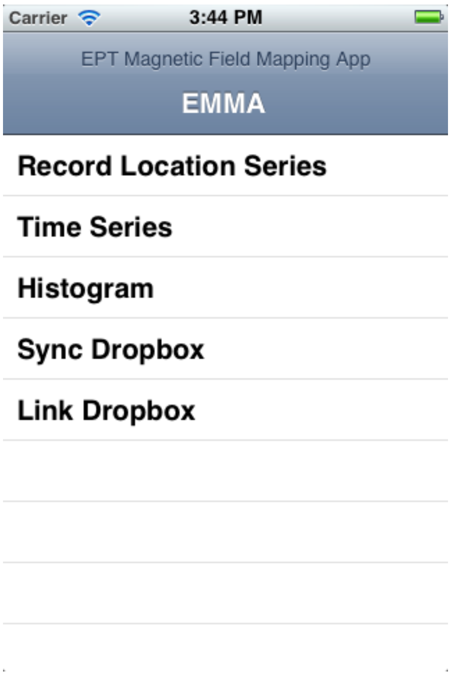

Figure A.2.: EMMA Start-Screen

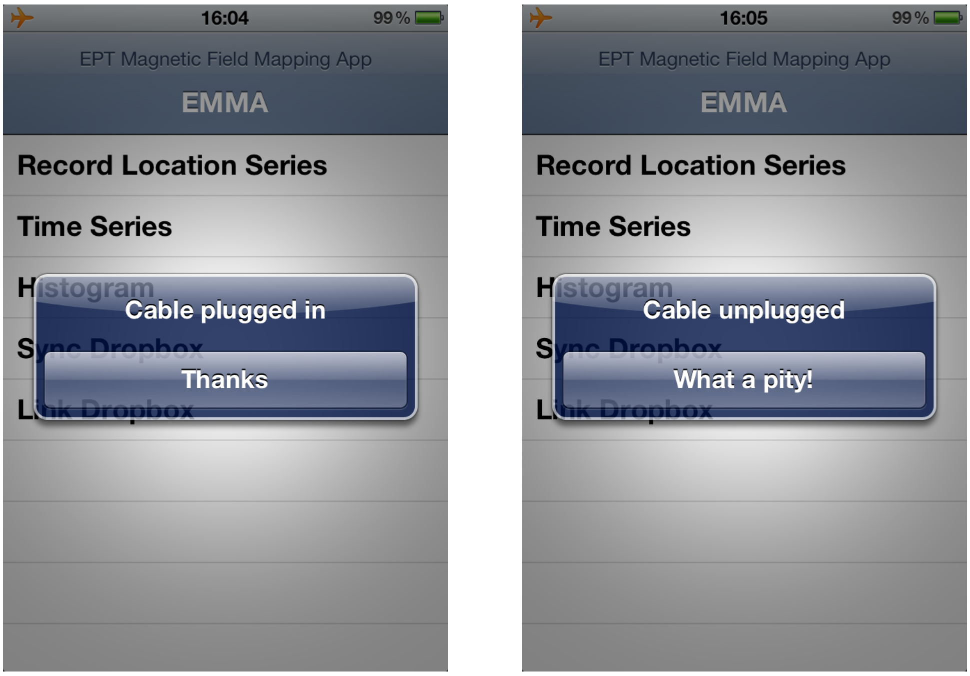

Cable plugged in

Cable unplugged

(a) Plugged In *(b)* Plugged Off

Figure A.3.: EMMA notifies the user, that the serial cable is plugged in (a), or that the serial cable is not plugged in (b).

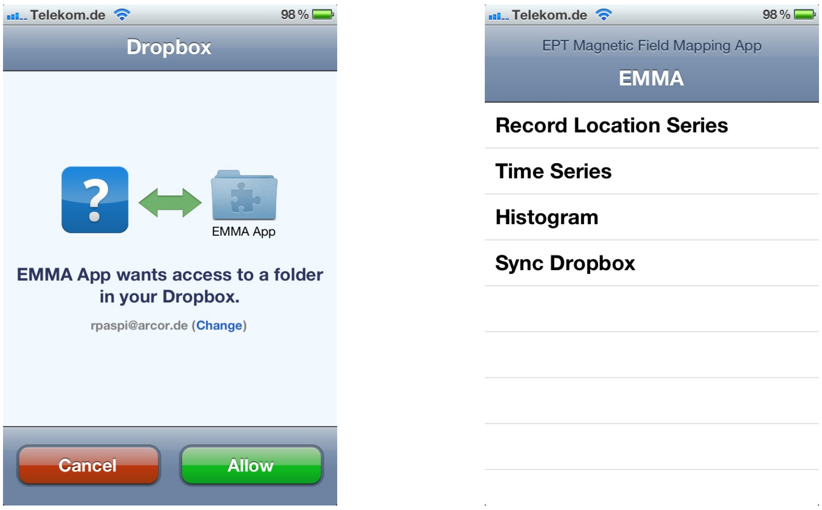

EMMA App wants access to a folder in your Dropbox.

rpaspi@arcor.de (Change)

(a) (b)

Figure A.4.: *(a)*: EMMA requests access to the Dropbox.
(b): EMMA Start-Screen after successful link with Dropbox. The last entry "Link Dropbox" vanished, since it is no longer needed.

A.1.1. Link Dropbox

As mentioned before, we use the cloud service Dropbox to upload data to a computer for further analysis. But before EMMA can do this, we need to link the App with an existing Dropbox account. When tapping "Link Dropbox", we will be redirected to the Dropbox website, where we must log in and verify that EMMA is granted access to our Dropbox storage.

Once this is done, there is no need to link EMMA with the Dropbox account again and so the "Link Dropbox" entry on the start-screen disappears and is not shown anymore (see fig A.4).

A.1.2. Dropbox Synchronization

After a successful link with the Dropbox account, EMMA is able to push the measured and stored data to the dedicated Dropbox folder. After tapping "Dropbox Synchronization" the successful upload is indicated by a chime. The airplane mode has to be switched off for this.

A.1.3. Histogram

In this function EMMA continuously gathers data delivered by the magnetometer and displays a histogram of this data. This feature can be used to verify a gaussian shape of the measured value at a constant distance away from the magnet system.

A.1.4. Time Series

As mentioned in section 6.6.1, we want to check the laboratories for possible noise fields. To quickly check the environment, we included this function into EMMA. Here, the magnetic flux densities in the directions of the three cartesian axes are shown over the last 60 seconds. New values are gathered every 0.1 seconds, which is faster than the update rate of the magnetometer – so, no measurement gets lost. A sample measurement is shown in fig. A.5.

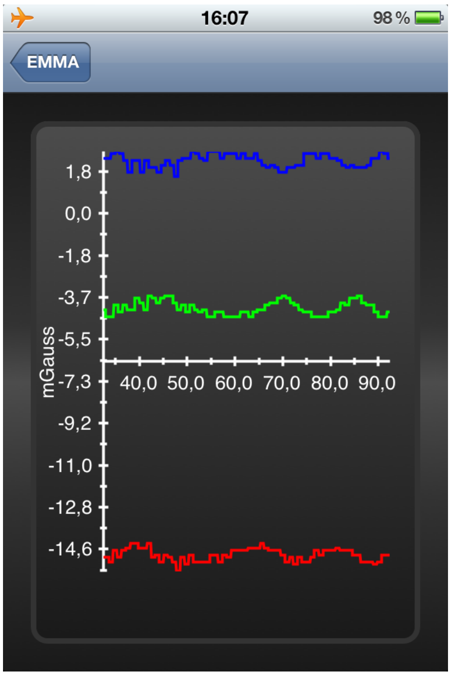

Figure A.5.: Example of a time series. We can see the magnetic flux densities in the X-direction (red), Y-direction (green) and Z-direction (blue) of the last 60 seconds.

A.1.5. Location Series

By far the most important task of EMMA is to perform a series of measurements at different distances away from the center of the magnet systems (subsequently termed "location series"). As explained in more detail in section 6.7.2, we place the magnet systems on plastic pedestals, that represent the orientation of the systems towards the MAG instruments, and vary the distance between the pedestals and the magnetometer probe. Thus, we are able to determine the slope of the magnetic flux densities and to extrapolate them up to the distances of the MAG instruments.

Due to the importance of this function, we will discuss this topic in more detail in the following chapter.

A.2. Measuring Location Series with EMMA

Fig. A.6 shows the option-screen of the location series function. The four different directions from the two EPT instruments to the two MAG instruments can be tuned in by repeatedly pressing the buttons ① and ②. The slider ③ represents the distance up to which we want to measure. The slider ④ below that slider is used to vary the distance of the single measurement points between each other. In fig. A.6 we chose a measurement length of 80 cm with 0.5 cm space between two measurement points –

which leads to a total of 160 measurement points. By tapping the button ⑤, we can quickly choose default values for the measurement length and the distance between two measurement points. These default values can be edited in the separate settings section of the App.

Meas. Len.: 0.80 Meter

Distance of Meas. Points: 5 mm

Figure A.6.: EMMA's option-screen of the location series function.

The selector ⑥ determines the side of the magnet system, that we want to measure. How the numbers of the sides of the magnet systems are defined, is explained in fig 6.23.

When we want to carry out a measurement of the magnetic background (a so called "empty" measurement), we can state this by turning on the switch ⑦. Then selector ⑧ determines, whether this measurement takes place before or after the measurement of the magnet system.

The picker view ⑨ at the bottom allows us to choose between the six magnet system, we can use for EPT.

When everything is set up correctly, we can start the measurement by pressing the record button ⑩. If we changed a former configuration, we are first asked, whether we want to keep the old configuration, or if we want to continue with the new one. When we intended to do an "empty" series, EMMA now records this background field every 6 seconds for a given time. This time can be selected in the settings section of the App. the measurement of the background field can be cancelled by tapping the "Stop!" button in fig. A.7. The successful end of the "empty" series is announced by a chime.

In the case of a magnet system measurement instead of a background measurement, a table containing the points to be measured is pushed into view (see fig. A.8). If this special measurement with this dedicated setup has been measured ever before, this data is loaded and shown in the table. On the other hand, if the setup is completely new, every data point is filled with the three default values 0.0 mGauss for the magnetic fluxes. Each cell, that shows these default values is marked in yellow, whereas all the

Meas. Len.: 0.50 Meter

Distance of Meas. Points: 5 mm

Figure A.7.: EMMA is recording the background field.

0005.50 cm
+0000.00 +0000.00 +0000.00 +0000.00
0006.00 cm
+0000.00 +0000.00 +0000.00 +0000.00
0006.50 cm
+0000.00 +0000.00 +0000.00 +0000.00
0007.00 cm
+0000.00 +0000.00 +0000.00 +0000.00
0007.50 cm
+0000.00 +0000.00 +0000.00 +0000.00
0008.00 cm
+0000.00 +0000.00 +0000.00 +0000.00
0008.50 cm
+0000.00 +0000.00 +0000.00 +0000.00
0009.00 cm
+0000.00 +0000.00 +0000.00 +0000.00
0009.50 cm
+0000.00 +0000.00 +0000.00 +0000.00
0010.00 cm

Figure A.8.: EMMA location series measurement table. No measurements have been taken yet. The offset of 5.5 cm can be set in the settings section of the App. The bold line in a table row gives the distance to the center of the magnet system and the four values below that line represent the measured values in the three cartesian axes and the norm of these three values.

other cells are marked white. This gimmick makes it easier for the experimenter to keep track of the data points he already measured.

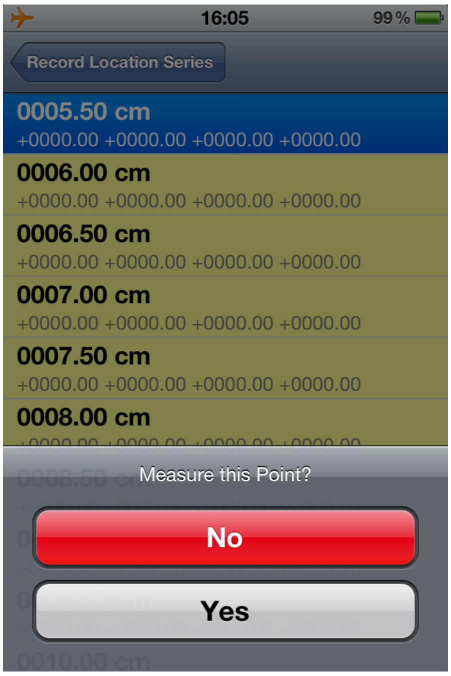

Figure A.9.: EMMA asks, whether we really want to measure the tapped data point.

By tapping a table cell, we trigger the confirmative question, whether this data point is to be measured or not (fig. A.9). When tapping “No”, nothing will happen. When tapping “Yes”, EMMA starts measuring the magnetic flux densities delivered by the magnetometer (in case the magnetometer is plugged in (see fig. A.11) – if not, EMMA will remind the use to do so (see fig. A.10)). How the App does this is explained in section 6.6.2. The ongoing measurement is indicated in the concerning cell by a spinning indicator (see fig A.11). During the measurement, EMMA accepts no tap inputs by the user. Again, a successful measurement is announced by a chime. We can always overwrite a measurement by a renewed tap on the concerning cell. After each successful measurement, the data is automatically stored on the device’s flash memory.

A.2.1. EMMA’s Settings

As we mentioned at some points before, EMMA can be configured in some aspects by the user. This is done by starting the “Setting” App of the iOS device and choosing the “EMMA” entry in the Apps section. Here we can change the way, the values delivered by the AD-converter are interpreted, the offset of the magnetometer probe, the duration of the “empty” measurement and the default values for the location series.

The AD-converter outputs integer values between 0 and 65535 for the converted magnetometer voltages via the serial cable. These values are proportional to the measured flux densities. The intercepts of the regression lines and the slopes can be changed corresponding to a calibrating measurement (see fig. A.12a).

0005.50 cm
+0000.00 +0000.00 +0000.00 +0000.00
0006.00 cm
+0000.00 +0000.00 +0000.00 +0000.00
0006.50 cm
+0000.00 +0000.00 +0000.00 +0000.00
0007.00 cm
+0000.00 +0000.00 +0000.00 +0000.00
0007.50 cm
+0000.00 +0000.00 +0000.00 +0000.00
0008.00 cm
+0000.00 +0000.00 +0000.00 +0000.00
0008.50 cm
+0000.00 +0000.00 +0000.00 +0000.00
0009.00 cm
0010.00 cm

Plug in Magnetometer!

Figure A.10.: EMMA warns, that the magnetometer is not plugged in.

0005.50 cm
+0000.00 +0000.00 +0000.00 +0000.00
0006.00 cm
+0000.00 +0000.00 +0000.00 +0000.00
0006.50 cm
+0000.00 +0000.00 +0000.00 +0000.00
0007.00 cm
+0000.00 +0000.00 +0000.00 +0000.00
0007.50 cm
+0000.00 +0000.00 +0000.00 +0000.00
0008.00 cm
+0000.00 +0000.00 +0000.00 +0000.00
0008.50 cm
+0000.00 +0000.00 +0000.00 +0000.00
0009.00 cm
+0000.00 +0000.00 +0000.00 +0000.00
0009.50 cm
+0000.00 +0000.00 +0000.00 +0000.00
0010.00 cm

Figure A.11.: Recording of a data point of a location series in progress.

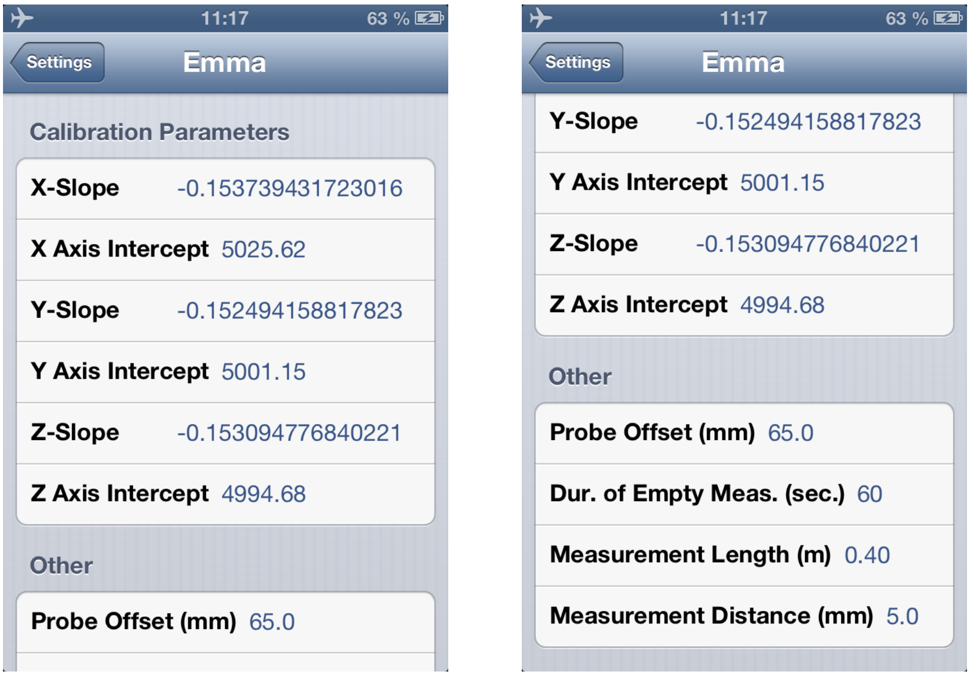

Calibration Parameters

X-Slope -0.153739431723016

X Axis Intercept 5025.62

Y-Slope -0.152494158817823

Y Axis Intercept 5001.15

Z-Slope -0.153094776840221

Z Axis Intercept 4994.68

Other

Probe Offset (mm) 65.0

(a)

Y-Slope -0.152494158817823

Y Axis Intercept 5001.15

Z-Slope -0.153094776840221

Z Axis Intercept 4994.68

Other

Probe Offset (mm) 65.0

Dur. of Empty Meas. (sec.) 60

Measurement Length (m) 0.40

Measurement Distance (mm) 5.0

(b)

Figure A.12.: *(a)*: The proportionality factors of the AD-value-to-flux-density conversion can be changed in the “Settings” App.
(b): The lower part of the EMMA settings section. Here, the probe offset, the duration of the “empty” measurement and the default values for the location series can be changed.

The probe offset is the closest distance that we can place the plastic pedestals in front of the magnetometer probe. The construction of the pedestals does not allow to place the middle of the magnet systems closer than this value (5.5 cm for EPT1, 7.7 cm for EPT2). In the location series function the list of measurement points will start at this value (see fig. A.12b).

Finally, the duration of the “empty” measurement and the default values for the location series can be changed. The effects of all changes take place immediately. I.E. EMMA has not to be quit and started again.

A.2.2. Calibrating EMMA

To convert the values that the AD-converter delivers, into magnetic flux densities, we carry out calibration measurements for each of the three sensors of the magnetometer and fit the data to a linear model. The results can be seen in fig. A.13 and table A.1.

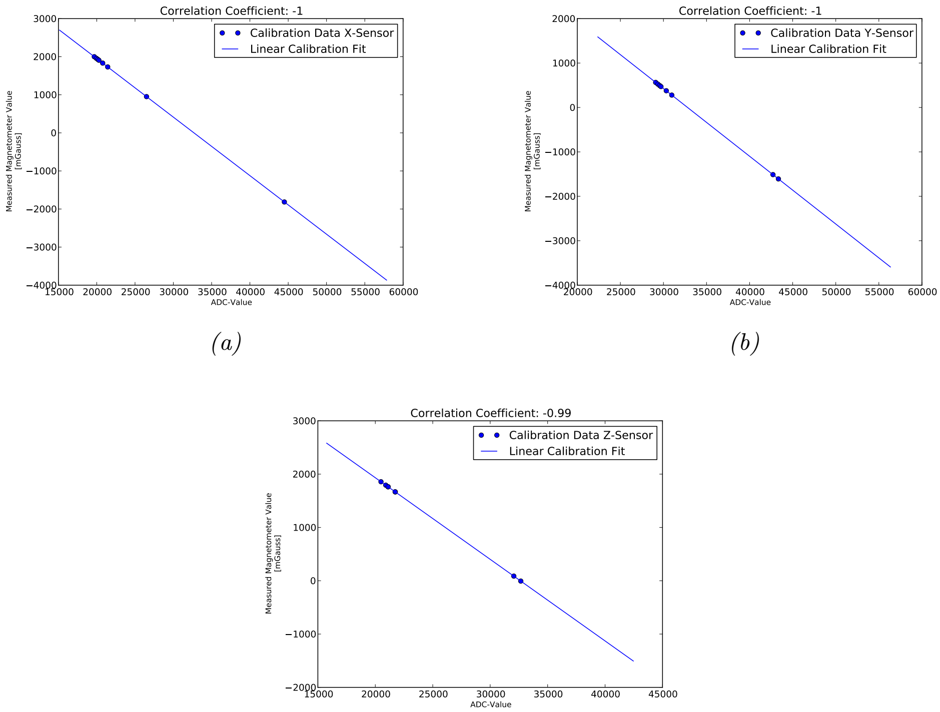

(a) *(b)*

(c)

Figure A.13.: Linear fits to the calibration data for EMMA.

	X-Sensor	Y-Sensor	Z-Sensor
Slope (in mGauss)	-0.154	-0.152	-0.153
Intercept (in mGauss)	5025.62	5001.15	4994.68
Corr. Coeff.	-1	-1	-0.99

Table A.1.: Results of the calibration measurements for EMMA.

A.2.3. EMMA's File Formats

We will now explain how to interpret the files that EMMA pushes into the Dropbox.

Empty Series

The data file containing the measurements of an empty series contains comma separated values (ASCII coded) where each line consists of four entries: the first entry gives the time in seconds when a measurement is stored and the next three entries give the measured flux densities in the three cartesian axes.

```
6,-71.3,27.1,-70.59999999999999
12,-71.5,26.9,-71.09999999999999
18,-71.5,27.2,-71.09999999999999
24,-70.8,27.1,-71.5
30,-71.5,26.9,-71.2
36,-71.8,26.8,-70.90000000000001
42,-70.2,27.2,-70.59999999999999
48,-69.8,26.5,-70.90000000000001
54,-70.7,26.3,-70.5
60,-71.16274509803922,26,-70.59999999999999
66,-71.3,26,-70.5
72,-71.5,26,-70
78,-71,26.6,-70.2
84,-70.40000000000001,26.9,-70
90,-71.3,27.9,-70.59999999999999
96,-71.09999999999999,26.8,-70.59999999999999
102,-71.59999999999999,26.6,-70.59999999999999
108,-71.59999999999999,27.1,-71.09999999999999
114,-71.3,26.9,-71.09999999999999
120,-71.5,27.6,-70.5
126,-70.40000000000001,27.9,-71.5
132,-71.5,27.1,-71.09999999999999
138,-70.40000000000001,27.6,-71.40000000000001
144,-71,28,-70.5
150,-71.09999999999999,26.9,-70.90000000000001
156,-70.5,27.6,-71.40000000000001
162,-71.59999999999999,27.6,-70.3
168,-70.7,27.6,-71.2
174,-71,26.9,-71.2
```

Listing A.1: Example of an empty series data file.

Location Series

The files for the location series are also ASCII coded and also contain comma separated values. The files consist of 7 columns where the first three columns give the distance from the center of the magnet system, the next three give the measured values in the three cartesian axes and the last column gives the norm of these three values.

```
55,55,55,-193.935294117647,-734.843137254902,21.45490196078433,760.3062853174843
60,60,60,-205.2941176470589,-533.9372549019607,6.299999999999997,572.0789778629571
65,65,65,-185.0235294117647,-399.8588235294119,-9.947058823529408,440.7036750125307
70,70,70,-184.9803921568629,-302.7941176470588,-16.37254901960783,355.2042842162339
75,75,75,-170.2450980392156,-231.9058823529412,-24.28235294117647,288.7098272325315
80,80,80,-151.9725490196079,-176.7176470588236,-31.97450980392156,235.2597537079497
85,85,85,-132.0921568627451,-136.4627450980392,-41.31176470588233,194.3632696973857
90,90,90,-120.6431372549019,-106.4000000000001,-46.53529411764703,167.4552482465719
95,95,95,-113.5156862745099,-82.22549019607838,-49.40000000000003,148.6176378104508
100,100,100,-105.2941176470588,-64.25882352941177,-53.24509803921568,134.3543377701756
```

Listing A.2: Extract of an example location series data file.

B. Listings

In this section we show some listings that are crucial for the simulations and calculations in this work. We begin with the presentation of GEANT4 and the definition of the EPT instrument in the framework. Then we take a look at the part of EMMA where the data from the converter box is received and processed. Afterwards, we show the programm that is running on the micro-controller of the converter box connected to EMMA. The following MATHEMATICA listing defines the magnet systems and computes the field gradients from EPT to MAG. Finally, we present the PYTHON method to extract a magnetic flux density vector from a RADIA-field file.

B.1. Geant4-Introduction and Listings

B.1.1. The Geant4 Framework

A good portion of the simulations in this work are based on the GEANT4 (**Ge**ometry **an**d **T**racking) framework written and maintained by the GEANT4 Collaboration (Agostinelli et al. 2003; Allison et al. 2006).

With the GEANT4 toolkit one can examine the impact and behavior of particles and radiation as they move through matter and electromagnetic fields. For that, the software uses Monte-Carlo methods to simulate the interactions of the particular particle or radiation with the surrounding environment.

GEANT4 enables the user to model his detector design using object-oriented techniques programmed in C++. The software supports the user at this work with a series of predefined methods for building geometries like tubes, disks, cubes or rotational solids for example.

The materials from which these geometries are made of can either be chosen from a list of materials from the framework or be user-defined by declaring the atomic composition. When the setup is complete, the user starts the simulation by shooting particles and radiation onto the experiment. The software then keeps track of the possible interactions and decay- or production-processes in the observed volumes. The response of the detectors to the incident radiation can be recorded for further analysis.

GEANT4 also offers various output channels for the graphical visualization of the modeled detectors and the incident particles and radiations (as we saw in fig. 5.8 and fig. 5.18).

B.1.2. Simulated Processes and Particles

GEANT4 allows the user to implement and simulate particles and physical processes as he likes by defining a so called physics list. In all our GEANT4 simulations we used the same physics list that contains the following particles:

- Gamma rays
- Mesons:
  - Pions +
  - Pions -
  - Pions 0
  - Eta mesons
  - Kaons +
  - Kaons -
  - Kaons 0
  - Antikaons -
  - Antikaons long
  - Antikaons short
- Leptons:
  - Electrons
  - Positron
  - Muons+
  - Muons-
  - Electron neutrinos
  - Electron antineutrinos
  - Muon neutrinos
  - Muon antineutrinos
- Baryons:
  - Protons
  - Antiprotons
  - Neutrons
  - Antineutrons

and the following processes:

- Compton scattering
- Gamma conversion
- Photoelectric effect
- Multiple scattering
- Ionization
- Bremsstrahlung
- Annihilation
- Pair production
- Decay processes

B.1.3. Detector Definition

Implementation of Detector-Class

The following listing is the implementation file of the Detector-class in GEANT4. In row 117 we import the magnetic field that was computed in RADIA before.

In row 56 we import the definition file that describes the profile of the collimator.

```
 1 #include "detector.h"
 2
 3 #include "G4MagneticField.hh"
 4
 5 #include "G4Material.hh"
 6 #include "G4NistManager.hh"
 7 #include "G4PVPlacement.hh"
 8 #include "G4TransportationManager.hh"
 9 #include "G4FieldManager.hh"
10 #include "G4UniformMagField.hh"
11 #include "G4PropagatorInField.hh"
12 #include "G4UserLimits.hh"
13 #include "G4Transform3D.hh"
14 #include "EPTMagField.h"
15 #include "EPTROGeometry.h"
```

```
#include "EPTSensitiveDetector.h"
#include "EPTDigi.h"
#include "EPTDigitizer.h"
#include "G4SDManager.hh"
#include "G4DigiManager.hh"
#include "G4VisAttributes.hh"
#include "G4Colour.hh"
#include "G4Region.hh"
#include "RadiaMagField.h"
#include "math.h"



Detector::Detector(G4double kT, G4String p, G4bool torus, G4bool bulge, G4double add, G4bool smoothRibs, G4int start, G4double detectorDistance) :
  solid_World(0), logic_World(0), physical_World(0),
//  spaceCraftDummy_solid(0), spaceCraftDummy_logic(0), spaceCraftDummy_physical(0),
  solid_foil(0), logic_foil(0), physical_foil(0),
  solid_detector_A(0), solid_detector_C(0),
  logic_detector_A(0), logic_detector_C(0),
  physical_detector_A(0), physical_detector_C(0),
  solid_housing(0), logic_housing(0), physical_housing(0),
  solid_EPT(0), logic_EPT(0), physical_EPT(0),
  solid_magnet(0),logic_magnet(0), physical_magnet(0),
  seal_solid(0), seal_logic(0), seal_physical(0),
//  tritest(0), bsptest(0), logic_bsp(0), phys_bsp(0),
  fWorldLength(0.),
  kollimatorThickness(kT),
  path(p),
  torusBool(torus), bulgeBool(bulge), additional(add), ribs(smoothRibs),
  startEvent(start), dAC(detectorDistance)
{

}

Detector::~Detector()
{}

G4VPhysicalVolume* Detector::Construct()
{

  #include "detectorParameters.h"

  G4bool   withTorus  = torusBool;
  G4bool   withDome   = bulgeBool;
  G4double housingThickness = additional;
  G4double domeHeight = (3.84*mm+housingThickness) + 9.*mm+housingThickness;
  G4double RMax = domeHeight;

  G4String name, symbol;  // a=mass of a mole;
  G4double a, z;
    G4double density;

  G4Material* Vacuum =
    new G4Material("Interplanetar",   //  name
```

```
  1.0,                      //  Atomic number
  1.008 * g/mole,           //  mass of mole
  1.1e-25 * g/cm3,           //  density
  kStateGas,                //  state
  2.73 * kelvin,            //  Temperature
  2.e-18 * pascal);         //  pressure

//Detektormaterial
G4Material* Silicon =
  new G4Material("Silicon",
  z = 14.,
  a = 28.0855 *g/mole,
  density= 2.33 * g/cm3);

G4NistManager* man = G4NistManager::Instance();
G4Material* Al = man->FindOrBuildMaterial("G4_Al");
G4Material* Pb = man->FindOrBuildMaterial("G4_Pb");
G4Material* Niob = man->FindOrBuildMaterial("G4_Nb");

  G4int ncomponents, natoms;

// define Elements
a = 1.01*g/mole;
G4Element* elH = new G4Element(name="Hydrogen",symbol="H" , z= 1., a);

a = 12.01*g/mole;
G4Element* elC = new G4Element(name="Carbon" ,symbol="C" , z= 6., a);

a = 35.453*g/mole;
G4Element* elCl = new G4Element(name="Chlor", symbol="Cl", z = 17, a);

a=14.01*g/mole;
G4Element* elN = new G4Element(name="Nitrogen",symbol="N2",z=7.,a);

a=16.*g/mole;
G4Element* elO = new G4Element(name="Oxygen",symbol="O2",z=8.,a);

// Parylene
density = 1.298*g/cm3;
G4Material* Parylene_C= new G4Material(name="Parylene-C", density,
    ncomponents=3);
Parylene_C->AddElement(elH , natoms=7);
Parylene_C->AddElement(elC , natoms=8);
Parylene_C->AddElement(elCl, natoms=1);

// Kapton
density = 1.42*g/cm3;
G4Material* Kapton = new G4Material(name="Kapton",density, ncomponents
    =4);
Kapton->AddElement(elO,5);
  Kapton->AddElement(elC,22);
  Kapton->AddElement(elN,2);
  Kapton->AddElement(elH,10);

  fWorldLength = 10.*cm;
G4double HalfWorldLength = 0.5*fWorldLength;

G4RotationMatrix* rot = new G4RotationMatrix;
```

```
  rot->rotateY(90.*deg);

  // Magnetic Field
  static G4bool fieldIsInitialized = false;
  if(!fieldIsInitialized)
  {
    RadiaMagField* myField = new RadiaMagField(14.*mm, 0.*mm, 8.84*mm, 202, 202, 202);  // Zweite Zeile im Magnetfeld-File
    G4FieldManager* fieldMgr = G4TransportationManager::GetTransportationManager()->GetFieldManager();
      fieldMgr->SetDetectorField(myField);
      fieldMgr->CreateChordFinder(myField);
      fieldMgr->SetDeltaOneStep(0.1*mm);
      G4TransportationManager* tmanager = G4TransportationManager::GetTransportationManager();
    tmanager->GetPropagatorInField()->SetLargestAcceptableStep(.05*mm);

    fieldIsInitialized = true;
  }

  solid_World = new G4Orb("R0world", HalfWorldLength);
    logic_World = new G4LogicalVolume( solid_World, Vacuum, "World");
    physical_World = new G4PVPlacement(0, G4ThreeVector(), logic_World, "World", 0, false, 0);

//   spaceCraftDummy_solid = new G4Box("SC_dummy", 3.1*cm, .7*cm, 22.*cm);
//   spaceCraftDummy_logic = new G4LogicalVolume(spaceCraftDummy_solid, Al, "SC_logic");
//   spaceCraftDummy_physical = new G4PVPlacement(0, G4ThreeVector(0., -2.*cm, 0.), spaceCraftDummy_logic, "SC_dummy", logic_World, false, 0);

    solid_EPT = new G4Tubs("EPT", 0., domeHeight, 3.84*mm+2*cL, 0.*deg, 360.*deg);
    logic_EPT = new G4LogicalVolume(solid_EPT, Vacuum, "EPT");
    physical_EPT = new G4PVPlacement(0, G4ThreeVector(0., 0., 0.), logic_EPT, "EPT", logic_World, false, 1);

  solid_foil = new G4Tubs("foil",0.,R_out, foil_thickness/2.0, 0.*deg, 360.*deg);
  logic_foil = new G4LogicalVolume(solid_foil , Kapton, "foil");
  // physical_foil = new G4PVPlacement(0, G4ThreeVector(0., 0., -2.05*mm), logic_foil, "foil", logic_EPT, false, 2);
  physical_foil = new G4PVPlacement(0, G4ThreeVector(0., 0., positionA-Thickness-(foil_thickness/2.0)), logic_foil, "foil", logic_EPT, false, 2);

  solid_detector_A = new G4Tubs("Detektor_A", 0., R_out, Thickness, 0.*deg, 360.*deg);
  logic_detector_A = new G4LogicalVolume(solid_detector_A, Silicon, "Silicon_ABC");
  physical_detector_A = new G4PVPlacement(0, G4ThreeVector(0., 0., positionA), logic_detector_A, "Detektor_A", logic_EPT, false, 8);

  solid_detector_C = new G4Tubs("Detektor_C", 0., R_out, Thickness, 0.*deg, 360.*deg);
  logic_detector_C = new G4LogicalVolume(solid_detector_C, Silicon, "
```

```
Silicon_ABC");
physical_detector_C = new G4PVPlacement(0, G4ThreeVector(0., 0., positionC), logic_detector_C, "Detektor_C", logic_EPT, false, 9);

solid_smooth_collimator = new G4Tubs("glatter_Kollimator", c0, cR, cL, 0.*deg, 360.*deg);
logic_smooth_collimator = new G4LogicalVolume(solid_smooth_collimator, Al, "latter_Kollimator_Aluminium");

solid_collimator_foil = new G4Polycone("Kollimator_foil", 0.*deg, 360.*deg, numperOfPoints, r_points, z_points);
logic_collimator_foil = new G4LogicalVolume(solid_collimator_foil, Al, "Kollimator_foil");

if (ribs)
  physical_collimator_foil = new G4PVPlacement(0, G4ThreeVector(0., 0., (-1.0)*cL-3.84*mm), logic_collimator_foil, "Kollimator_foil", logic_EPT, false, 4);
else
  physical_collimator_foil = new G4PVPlacement(0, G4ThreeVector(0., 0., (-1.0)*cL-3.84*mm), logic_smooth_collimator, "Kollimator_foil", logic_EPT, false, 4);

solid_collimator_magnet = new G4Polycone("Kollimator_magnet", 0.*deg, 360.*deg, numperOfPoints, r_points, z_points_magnet);
logic_collimator_magnet = new G4LogicalVolume(solid_collimator_magnet, Al, "Kollimator_magnet");
physical_collimator_magnet = new G4PVPlacement(0, G4ThreeVector(0., 0., cL+3.84*mm), logic_collimator_magnet, "Kollimator_magnet", logic_EPT, false, 5);


G4double r_points_housing[] = {CollimatorOpening, grooves+kollimatorThickness, grooves+kollimatorThickness, 9.0*mm+housingThickness, 9.0*mm+housingThickness,MagnetOuterRadius, MagnetOuterRadius, CollimatorOpening, CollimatorOpening, 8.0*mm, 8.0*mm, CollimatorOpening};
G4double z_points_housing[]  = {-3.84*mm, -3.84*mm, -3.84*mm-housingThickness, -3.84*mm-housingThickness, 3.84*mm+housingThickness, 3.84*mm+housingThickness, 3.84*mm, 3.84*mm, 2.05*mm, 2.05*mm, -2.05*mm, -2.05*mm};

solid_housing = new G4Polycone("Housing", 0.*deg, 360.*deg, 12, r_points_housing, z_points_housing);
logic_housing = new G4LogicalVolume(solid_housing, Al, "Housing");
//  physical_housing = new G4PVPlacement(0, G4ThreeVector(0., 0., 0.), logic_housing, "Housing", logic_EPT, false, 24);

solid_magnet = new G4Tubs("Magnet", grooves+kollimatorThickness, MagnetOuterRadius, MagnetLength, 0.*deg, 360.*deg);
logic_magnet = new G4LogicalVolume(solid_magnet, Niob, "Magnet");
physical_magnet = new G4PVPlacement(0, G4ThreeVector(0., 0., 3.84*mm+MagnetLength), logic_magnet, "Magnet", logic_EPT, false, 3);

G4double r_torus = grooves+kollimatorThickness;
G4double rMax = 9.0*mm+housingThickness-r_torus;
G4double RSphere = 9.*mm + housingThickness;
//G4double offset = -3.84*mm;
```

```
  G4double offset = 0.*mm;
//  G4double r_points_seal[] = {0., r_torus, r_torus, r_torus+rMax, r_torus+rMax, 0.};
//  G4double z_points_seal[] = {-rMax, -rMax, 0., 0., rMax, rMax};
//  G4Torus* seal_torus = new G4Torus("Seal_Torus", 0.0*mm, rMax, r_torus, 0.*deg, 360.*deg);
  G4double dr = 0.1*mm;
  G4double r_points_seal[] = {0., r_torus, r_torus, RSphere+dr, RSphere+dr, 0.};
  G4double z_points_seal[] = {-RSphere-dr, -RSphere-dr, 0., 0., RSphere+dr, RSphere+dr};
  G4Orb* seal_torus = new G4Orb("Seal_Torus", RSphere);
  G4Polycone* seal_polycone = new G4Polycone("Seal_Polycone", 0.*deg, 360.*deg, 6, r_points_seal, z_points_seal);
  seal_solid = new G4SubtractionSolid("Seal", seal_torus, seal_polycone);
  seal_logic = new G4LogicalVolume(seal_solid, Al, "Seal");
  if (withTorus)
    seal_physical = new G4PVPlacement(0, G4ThreeVector(0., 0., -3.84*mm-housingThickness), seal_logic, "Seal", logic_EPT, false, 6);

  G4Torus* sub_torus = new G4Torus("dome", 0.0*mm, (3.84*mm+housingThickness), 9.*mm+housingThickness, 0.*deg, 360.*deg);
  G4Tubs* sub_tub = new G4Tubs("sub_tub", (9.*mm+housingThickness) - (3.84*mm+housingThickness), 9.*mm+housingThickness, (3.84*mm+housingThickness), 0.*deg, 360.*deg);
  dome_solid = new G4SubtractionSolid("dome", sub_torus, sub_tub);
  dome_logic = new G4LogicalVolume(dome_solid, Al, "Dome");
//  dome_physical = new G4PVPlacement(0, G4ThreeVector(0., 0., 25.), dome_logic, "Dome", logic_EPT, false, 24);

  G4UnionSolid* shielding_solid = new G4UnionSolid("shielding", solid_housing, dome_solid);
  if (withDome)
    shielding_logic = new G4LogicalVolume(shielding_solid, Al, "shielding");
  else
    shielding_logic = new G4LogicalVolume(solid_housing, Al, "shielding");
  G4VPhysicalVolume* shielding_physical = new G4PVPlacement(0, G4ThreeVector(0., 0., 0.), shielding_logic, "shielding", logic_EPT, false, 7);
  rot->rotateY(90.*deg);

//  tritest = new ligel::TriStore("/home/et152/paspir/workspace/EPT/collimator.bsp");
//  bsptest = new BSPSolid("collimator.bsp", tritest);
//  logic_bsp = new G4LogicalVolume(bsptest, Niob, "Niob_BSP");
//  phys_bsp = new G4PVPlacement(0, G4ThreeVector(10.*cm, 10.*cm, 10.*cm), logic_bsp, "BSP", logic_World, false, 1);

  //-------------------------------------------------
  // Sensitive detectors
  //-------------------------------------------------
  G4VReadOutGeometry* eptRO = new EPTROGeometry(kollimatorThickness, withTorus, withDome, additional, 10+2, dAC);
  eptRO->BuildROGeometry();
  G4SDManager* SDman = G4SDManager::GetSDMpointer();
  EPTSensitiveDetector* detectorSD = new EPTSensitiveDetector("detectorSD
```

```
      ", path, 10, startEvent);
  detectorSD->SetROgeometry(eptRO);
  SDman->AddNewDetector(detectorSD);


  //--------------------------------------------------
  // Regions
  //--------------------------------------------------

  G4Region* detectorRegion = new G4Region("Detector_Region");
  detectorRegion->AddRootLogicalVolume(logic_EPT);

//  logic_EPT->SetSensitiveDetector(detectorSD);

  logic_detector_A->SetSensitiveDetector( detectorSD );
  logic_detector_C->SetSensitiveDetector( detectorSD );

  logic_collimator_foil->SetSensitiveDetector(detectorSD);
  logic_collimator_magnet->SetSensitiveDetector(detectorSD);
  if (withTorus)
    {
      seal_logic->SetSensitiveDetector(detectorSD);
    }

  shielding_logic->SetSensitiveDetector(detectorSD);

  logic_foil->SetSensitiveDetector(detectorSD);
  logic_magnet->SetSensitiveDetector(detectorSD);


  logic_detector_A->SetVisAttributes(G4Colour(1.,0.,0.));
  logic_detector_C->SetVisAttributes(G4Colour(1.,1.,0.));
  logic_foil->SetVisAttributes(G4Colour(0.,1.,1.));
  logic_magnet->SetVisAttributes(G4Colour(0.1,0.3,0.3));
  logic_collimator_foil->SetVisAttributes(G4Colour(1.,0.,0.));
  logic_housing->SetVisAttributes(G4Colour(0.,0.,1.));

  //logic_detector_A->SetVisAttributes(G4VisAttributes::GetInvisible());
  //logic_detector_C->SetVisAttributes(G4VisAttributes::GetInvisible());
  //logic_foil->SetVisAttributes(G4VisAttributes::GetInvisible());
  //logic_collimator_magnet->SetVisAttributes(G4VisAttributes::
      GetInvisible());
  //logic_collimator_foil->SetVisAttributes(G4VisAttributes::GetInvisible
      ());
  //logic_housing->SetVisAttributes(G4VisAttributes::GetInvisible());
  //logic_magnet->SetVisAttributes(G4VisAttributes::GetInvisible());
  //shielding_logic->SetVisAttributes(G4VisAttributes::GetInvisible());
  //seal_logic->SetVisAttributes(G4VisAttributes::GetInvisible());
  logic_EPT->SetVisAttributes(G4VisAttributes::GetInvisible());
  logic_World->SetVisAttributes(G4VisAttributes::GetInvisible());

//  G4DigiManager * fDM = G4DigiManager::GetDMpointer();
//  EPTDigitizer* myDM = new EPTDigitizer( "EPTDigi" );
//  fDM->AddNewModule(myDM);

  G4double maxStep = 0.001*mm;
  logic_World->SetUserLimits(new G4UserLimits(maxStep));

```

```
  return physical_World;
}

G4double Detector::GetCollimatorThickness()
{
  return kollimatorThickness;
}
```

Definition of Detector Parameters

This is the listing of the definition file that describes the profile of the collimator. The number of ribs is given in row 21 and the thickness of these ribs in row 20.

```
 1 /*
 2  * detectorParameters_ribs.h
 3  *
 4  *  Created on: 12.11.2010
 5  *      Author: privat
 6  */
 7
 8 #ifndef DETECTORPARAMETERS_H_
 9 #define DETECTORPARAMETERS_H_
10
11   G4bool   old_Design = false;
12   G4double Thickness = .15*mm;
13   G4double foil_thickness = 0.005*mm;
14
15   G4double R_inn = 3.0*mm;
16   G4double R_out = 6.0*mm;
17 //  G4double gap = 1.4*mm;
18 //  G4double rib = 1.0*mm;
19 //  G4double gap = 2.0125*mm;
20   G4double rib = 1.0*mm;
21   G4double n = 8.0; // Anzahl der Rippen + 1
22   G4double MagnetOuterRadius = 10.*mm;
23   G4double MagnetLength = 5.*mm;
24   G4double positionA = -((dAC/2.) + Thickness);
25   G4double positionC = ((dAC/2.) + Thickness);
26   G4double CollimatorOpening = R_inn;
27   G4double cO = CollimatorOpening;
28   G4double collimatorOffset = 3.84*mm;
29   G4double grooves = CollimatorOpening + 1.5*mm;
30   G4double cR = grooves + kollimatorThickness;
31   G4double cL = ((2. * CollimatorOpening) / tan(15.0*pi/180.0) - (
       collimatorOffset - (dAC/2.))) / 2.0;
32   G4double d = 1.*mm;
33   G4double gap = (2.*cL - (n-1.)*rib - 2.*d) / n;
34   G4double off = cL - d;
35
36   G4int numperOfPoints = (G4int)n * 4 + 4;
37
38   G4double z_points[] = {(-1.0)*cL, (-1.0)*cL, cL, cL,
39       off-0.0*gap-0.0*rib, off-0.0*gap-0.0*rib,
40       off-1.0*gap-0.0*rib, off-1.0*gap-0.0*rib,
41       off-1.0*gap-1.0*rib, off-1.0*gap-1.0*rib,
42       off-2.0*gap-1.0*rib, off-2.0*gap-1.0*rib,
43       off-2.0*gap-2.0*rib, off-2.0*gap-2.0*rib,
44       off-3.0*gap-2.0*rib, off-3.0*gap-2.0*rib,
```

```
      off-3.0*gap-3.0*rib, off-3.0*gap-3.0*rib,
      off-4.0*gap-3.0*rib, off-4.0*gap-3.0*rib,
      off-4.0*gap-4.0*rib, off-4.0*gap-4.0*rib,
      off-5.0*gap-4.0*rib, off-5.0*gap-4.0*rib,
      off-5.0*gap-5.0*rib, off-5.0*gap-5.0*rib,
      off-6.0*gap-5.0*rib, off-6.0*gap-5.0*rib,
      off-6.0*gap-6.0*rib, off-6.0*gap-6.0*rib,
      off-7.0*gap-6.0*rib, off-7.0*gap-6.0*rib,
      off-7.0*gap-7.0*rib, off-7.0*gap-7.0*rib,
      off-8.0*gap-7.0*rib, off-8.0*gap-7.0*rib};

  G4double r_points[] = {c0, cR, cR, c0,
      c0, grooves, grooves, c0,
      c0, grooves, grooves, c0,
      c0, grooves, grooves, c0,
      c0, grooves, grooves, c0,
      c0, grooves, grooves, c0,
      c0, grooves, grooves, c0,
      c0, grooves, grooves, c0,
      c0, grooves, grooves, c0}; // n+1 Zeilen

  G4double *z_points_magnet = z_points;


#endif /* DETECTORPARAMETERS_H_ */
```

B.2. EMMA Listings

The following listing is an extract of the EMMA-project and shows how the data delivered by the converter box is treated by the iPhone.

```
- (void) readBytesAvailable:(UInt32)numBytes
{
  int bytesRead;
  UInt8 buffer[numBytes];
  self.error = NO;
    double tempX = 1.0;
    double tempY = 2.0;
    double tempZ = 3.0;
  // Read the data out
  bytesRead = [rsc read:buffer Length:numBytes];
    if (TEST) {
        if (self.callingView) {
            ((AufnahmeController *)self.callingView).messwertX = [
                NSNumber numberWithInt:1];
            ((AufnahmeController *)self.callingView).messwertY = [
                NSNumber numberWithInt:2];
            ((AufnahmeController *)self.callingView).messwertZ = [
                NSNumber numberWithInt:3];
        }

    } else {
        @try {
            if ((int)bytesRead == 6)
            {
                if (buffer[0]=='X') {
```

```
                NSString *tempString = [NSString stringWithFormat:@"%c%c%c%c%c", buffer[1], buffer[2], buffer[3], buffer[4], buffer[5]];
                tempX = [tempString doubleValue];
                tempX = runde((self.x_achsenabschnitt - self.x_steigung * tempX), 1);
                self.messwertX = [NSNumber numberWithDouble:tempX];
                if ((self.callingView) && ([[self.callingView class] instancesRespondToSelector:@selector(setMesswertX:)])) {
                    ((AufnahmeController *)self.callingView).messwertX = [NSNumber numberWithDouble:tempX];
                }
            } else if (buffer[0]=='Y') {
                NSString *tempString = [NSString stringWithFormat:@"%c%c%c%c%c", buffer[1], buffer[2], buffer[3], buffer[4], buffer[5]];
                tempY = [tempString doubleValue];
                tempY = runde((self.y_achsenabschnitt - self.y_steigung * tempY), 1);
                self.messwertY = [NSNumber numberWithDouble:tempY];
                if ((self.callingView) && ([[self.callingView class] instancesRespondToSelector:@selector(setMesswertY:)])) {
                    ((AufnahmeController *)self.callingView).messwertY = [NSNumber numberWithDouble:tempY];
                }
            } else if (buffer[0]=='Z') {
                NSString *tempString = [NSString stringWithFormat:@"%c%c%c%c%c", buffer[1], buffer[2], buffer[3], buffer[4], buffer[5]];
                tempZ = [tempString doubleValue];
                tempZ = runde((self.z_achsenabschnitt - self.z_steigung * tempZ), 1);
                self.messwertZ = [NSNumber numberWithDouble:tempZ];
                if ((self.callingView) && ([[self.callingView class] instancesRespondToSelector:@selector(setMesswertZ:)])) {
                    ((AufnahmeController *)self.callingView).messwertZ = [NSNumber numberWithDouble:tempZ];
                }
            }
        }
        else {
            self.error = YES;
        }
    }
    @catch (NSException *exception) {
        NSLog(@"Error: %@", [exception reason]);
        self.error = YES;
    }
    if ([[self.callingView class] instancesRespondToSelector:@selector(playTone:)]) {
        [(ToneDetector *)self.callingView playTone:[NSArray arrayWithObjects:self.messwertX, self.messwertY, self.messwertZ, nil]];
    }

```

```
    }
}
```

The following methods handle the measurement processes in EMMA:

```
- (void)zeitlichesMittelMessen {
    self.measurementInProgess = true;
    if (!leer) {
        activity = [[UIActivityIndicatorView alloc]
            initWithActivityIndicatorStyle:
            UIActivityIndicatorViewStyleGray];
        activity.hidesWhenStopped = YES;
        UITableViewCell *cell = [self.tableView cellForRowAtIndexPath:
            self.cellToChange];
        [cell setAccessoryView:activity];
    }

    self.mittelWertArray = [[NSMutableArray alloc] initWithCapacity:10];
    self.elapsedTime = [NSNumber numberWithInt:0];
    myTimer = [NSTimer scheduledTimerWithTimeInterval:0.1 target:self
        selector:@selector(tick:) userInfo:nil repeats:YES];
    if (!leer) {
        [activity startAnimating];
    }
    [myTimer fire];
}

- (void) recordEmpty {
    self.measurementInProgess = true;
    leer = true;
    self.leerArray = [[NSMutableArray alloc] initWithCapacity:100];
    myTimerLeer = [[NSTimer alloc] init];
    self.elapsedTimeLeer = [NSNumber numberWithInt:0];
    myTimerLeer = [NSTimer scheduledTimerWithTimeInterval:6.0 target:self
         selector:@selector(tickLeer:) userInfo:nil repeats:YES];
    leerAlert = [[UIAlertView alloc] initWithTitle:NSLocalizedString(@"
        Leerreihe wird aufgenommen ...", @"Leerreihe wird aufgenommen ..."
        ) message:nil delegate:self cancelButtonTitle:NSLocalizedString(@"
        Aufh ren!", @"Aufh ren!") otherButtonTitles:nil];
    [leerAlert show];
    [myTimerLeer fire];
}

- (void)stoppeZeitreihe {
    [myTimer invalidate];
    int anzahlWerte = [self.mittelWertArray count];
    double summeX = 0.0;
    double summeY = 0.0;
    double summeZ = 0.0;
    double mittelWertX = 0.0;
    double mittelWertY = 0.0;
    double mittelWertZ = 0.0;

    for (NSMutableArray *tempArray in self.mittelWertArray) {
        summeX = summeX + [[tempArray objectAtIndex:0] doubleValue];
        summeY = summeY + [[tempArray objectAtIndex:1] doubleValue];
        summeZ = summeZ + [[tempArray objectAtIndex:2] doubleValue];
    }

```

```
    if (anzahlWerte > 0) {
        mittelWertX = summeX / (double)anzahlWerte;
        mittelWertY = summeY / (double)anzahlWerte;
        mittelWertZ = summeZ / (double)anzahlWerte;
    }

    self.messwertX = [NSNumber numberWithDouble:mittelWertX];
    self.messwertY = [NSNumber numberWithDouble:mittelWertY];
    self.messwertZ = [NSNumber numberWithDouble:mittelWertZ];

    [mittelWertArray release];
    if (!leer) {
        [activity stopAnimating];

        SystemSoundID pmph;
        id sndpath = [[NSBundle mainBundle]
                      pathForResource:@"measurementFinished"
                      ofType:@"aif"
                      inDirectory:@"/"];
        CFURLRef baseURL = (CFURLRef) [[NSURL alloc] initFileURLWithPath:
           sndpath];
        AudioServicesCreateSystemSoundID (baseURL, &pmph);
        AudioServicesPlaySystemSound(pmph);
        [(id)baseURL release];

        [self messen];
    }

    if (leer) {
        self.elapsedTimeLeer = [NSNumber numberWithDouble:([self.
           elapsedTimeLeer doubleValue] + 6.0)];
        if ([self.elapsedTimeLeer doubleValue] >= (double)self.leer_dauer
           ) {
            [self stoppeZeitreiheLeer];
        }
        NSLog(@"Tick Leer. --> %@\t%@\t%@\t%@\n", self.elapsedTimeLeer,
           self.messwertX, self.messwertY, self.messwertZ);
    }

    self.measurementInProgess = false;
    if (!leer) {
        [self speichern];
    }
}

- (void)stoppeZeitreiheLeer {
    if ([myTimerLeer isValid]) {
        [myTimerLeer invalidate];
    }
    if ([myTimer isValid]) {
        [myTimer invalidate];
    }

    SystemSoundID pmph;
    id sndpath = [[NSBundle mainBundle]
                  pathForResource:@"measurementFinished"
                  ofType:@"aif"
                  inDirectory:@"/"];
```

```
    CFURLRef baseURL = (CFURLRef) [[NSURL alloc] initFileURLWithPath:
        sndpath];
    AudioServicesCreateSystemSoundID (baseURL, &pmph);
    AudioServicesPlaySystemSound(pmph);
    [(id)baseURL release];

    self.measurementInProgess = false;
    [leerAlert dismissWithClickedButtonIndex:0 animated:YES];
}

- (void)tick:(NSTimer *)theTimer
{
    if (TEST) {
        [self.mittelWertArray addObject:[NSMutableArray arrayWithObjects
            :[NSNumber numberWithInt:1], [NSNumber numberWithInt:2], [
            NSNumber numberWithInt:3], nil]];
    } else {
        [self.mittelWertArray addObject:[NSMutableArray arrayWithObjects:
            self.messwertX, self.messwertY, self.messwertZ, nil]];
    }
    self.elapsedTime = [NSNumber numberWithDouble:([self.elapsedTime
        doubleValue] + 0.1)];
    if ([self.elapsedTime doubleValue] >= 5.0) {
        [self stoppeZeitreihe];
    }
}

- (void)tickLeer:(NSTimer *)theTimer
{
    [self zeitlichesMittelMessen];
    if ([self.elapsedTimeLeer doubleValue] > 0.0) {
        [self.leerArray addObject:[NSMutableArray arrayWithObjects:self.
            elapsedTimeLeer, self.messwertX, self.messwertY, self.
            messwertZ, nil]];
    }
}
```

B.3. Converter Box Listing and Circuit Diagramm

This program is running on the micro-controller that is built in into the EMMA-converter box.

The subsequent circuit diagram shows the add-on board for a ATmega128 micro-controller inside the EMMA converter box. The scheme was made by Bjoern Schuster.

```
int main(void)
{
  char S[80] = "\0";
  unsigned int result1 = 0, result2 = 0, result3 = 0;

  _delay_ms(10);
  avr_init();
  spi_init();
  ad7706_init(1);
  ad7706_init(2);
  ad7706_init(3);

```

```
  UART_WriteString(UART1, "\r\n\r\n\r\n\r\nSTART\r\n");

  while(1)
  {
    //readThreeValues();
    for(int t=0; t<WAIT_TIME; t++)
    {
      _delay_ms(1);
    }
    result1 = readChannel(1);
    for(int t=0; t<WAIT_TIME; t++)
    {
      _delay_ms(1);
    }
    result2 = readChannel(2);
    for(int t=0; t<WAIT_TIME; t++)
    {
      _delay_ms(1);
    }
    result3 = readChannel(3);

    sprintf(S, "X%05u", result2);
    UART_WriteString(UART1, S);
    for(int t=0; t<200; t++)
    {
      _delay_ms(1);
    }
    sprintf(S, "Y%05u", result3);
    UART_WriteString(UART1, S);
    for(int t=0; t<200; t++)
    {
      _delay_ms(1);
    }
    sprintf(S, "Z%05u", result1);
    UART_WriteString(UART1, S);
    for(int t=0; t<200; t++)
    {
      _delay_ms(1);
    }
  }

  return 0;
}
```

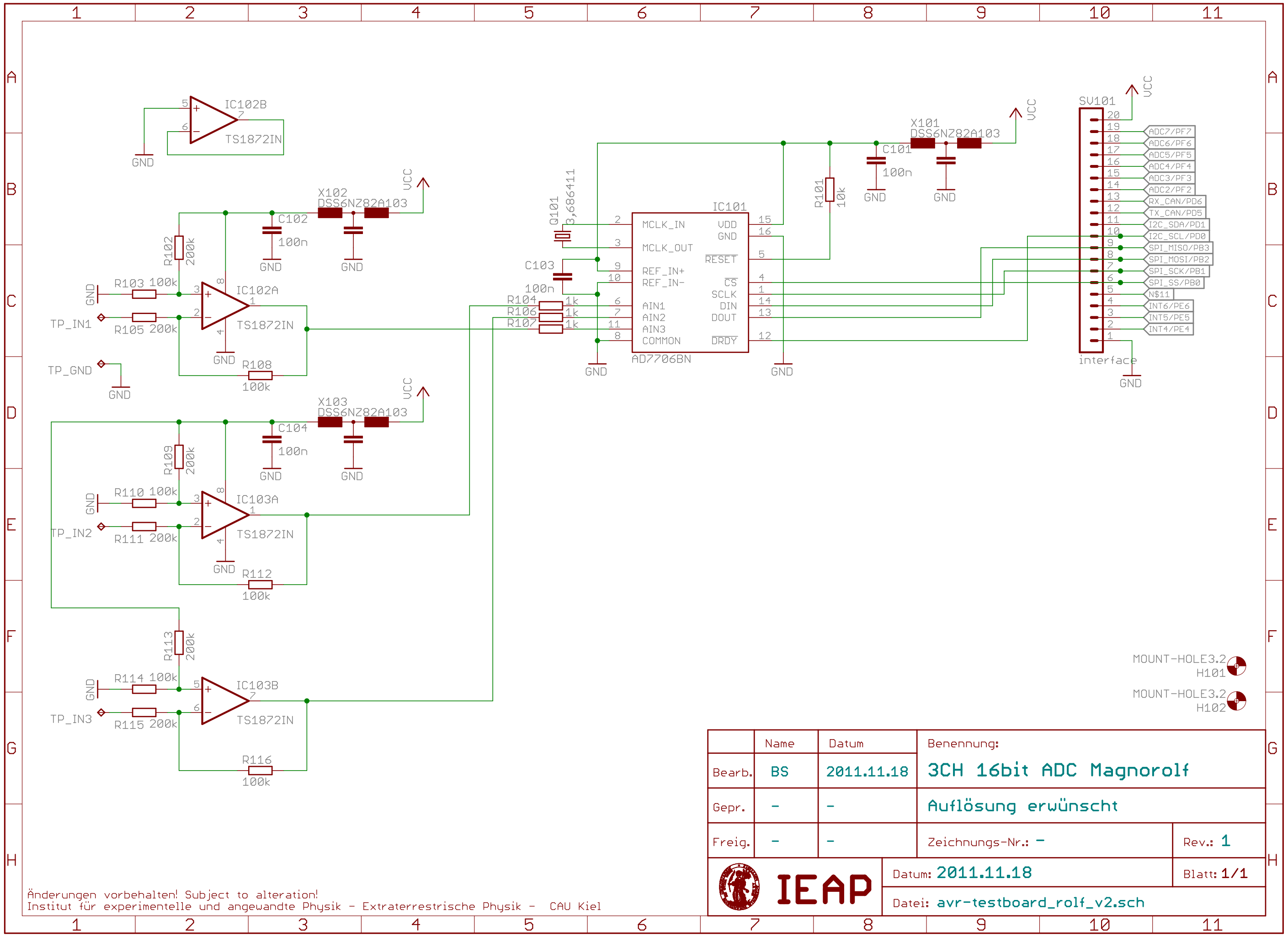
IC102B
TS1872IN
IC102A
IC103A
IC103B
TS1872IN
X101
X102
X103
DSS6NZ82A103
VCC
GND
C101
C102
C103
C104
100n
R101
10k
R102
R109
R113
200k
R103 100k
R105 200k
R110 100k
R111 200k
R114 100k
R115 200k
R108
R112
R116
100k
R104
R106
R107
1k
TP_IN1
TP_GND
TP_IN2
TP_IN3
Q101
3,686411
IC101
MCLK_IN
MCLK_OUT
REF_IN+
REF_IN-
AIN1
AIN2
AIN3
COMMON
VDD
GND
RESET
CS
SCLK
DIN
DOUT
DRDY
AD7706BN
SV101
interface
ADC7/PF7
ADC6/PF6
ADC5/PF5
ADC4/PF4
ADC3/PF3
ADC2/PF2
RX_CAN/PD6
TX_CAN/PD5
I2C_SDA/PD1
I2C_SCL/PD0
SPI_MISO/PB3
SPI_MOSI/PB2
SPI_SCK/PB1
SPI_SS/PB0
N$11
INT6/PE6
INT5/PE5
INT4/PE4
MOUNT-HOLE3.2
H101
H102
Name
Datum
Benennung:
Bearb.
BS
2011.11.18
3CH 16bit ADC Magnorolf
Gepr.
Auflösung erwünscht
Freig.
Zeichnungs-Nr.: -
Rev.: 1
IEAP
Datum: 2011.11.18
Blatt: 1/1
Datei: avr-testboard_rolf_v2.sch
Änderungen vorbehalten! Subject to alteration!
Institut für experimentelle und angewandte Physik - Extraterrestrische Physik - CAU Kiel

B.4. Mathematica Listings

This listing contains the definition of the magnet systems in RADIA and the data output into a file:

```
Clear["Global‘*"]
vEPT1IBS:={1556.8000000000002‘,-205.31825788719675‘,-1638.6210321477658‘} (* EPT1 - MAG IBS *);
vEPT1OBS:={1019.8700000000001‘,972.2108113782634‘,-3094.880171559004‘} (* EPT1 - MAG OBS *);
vEPT2IBS:={1874.8208674651648‘,-750.8592594160762‘,-670.7287569851076‘} (* EPT2 - MAG IBS *);
vEPT2OBS:={3776.594057273381‘,-1131.301995830799‘,-855.3294366129367‘} (* EPT2 - MAG OBS *);
Row[{PopupMenu[Dynamic[Instrument],{"EPT1","EPT2"}],"->",PopupMenu[Dynamic[MAGInstrument],{"MAG IBS", "MAG OBS"}]}]

MagnetToleranzZ=0.025;
dZMagnet1A=0.0;
dZMagnet1B=0.0;
dZMagnet2A=0.0;
dZMagnet2B=0.0;
{Control[{dZMagnet1A,-MagnetToleranzZ,MagnetToleranzZ}],"Abweichung f r Magnet 1A"}
{Control[{dZMagnet1B,-MagnetToleranzZ,MagnetToleranzZ}],"Abweichung f r Magnet 1B"}
{Control[{dZMagnet2A,-MagnetToleranzZ,MagnetToleranzZ}],"Abweichung f r Magnet 2A"}
{Control[{dZMagnet2B,-MagnetToleranzZ,MagnetToleranzZ}],"Abweichung f r Magnet 2B"}

JochToleranzX=0.1;
JochToleranzZ=0.1;
dXJoch1=0.0;
dXJoch2=0.0;
dZJoch1=0.0;
dZJoch2=0.0;

If[Instrument =="EPT1",If[MAGInstrument=="MAG IBS",v:=vEPT1IBS,v:=vEPT1OBS],If[MAGInstrument=="MAG IBS",v:=vEPT2IBS,v:=vEPT2OBS]];
If[v==vEPT1IBS, SaveFile="MAGEbene_EPT1-IBS.csv",If[v==vEPT1OBS, SaveFile="MAGEbene_EPT1-OBS.csv",If[v==vEPT2IBS, SaveFile="MAGEbene_EPT2-IBS.csv",If[v==vEPT2OBS, SaveFile="MAGEbene_EPT2-OBS.csv",]]]];
If[$OperatingSystem=="MacOSX",SavePath="/Users/"<>$UserName<>"/Desktop/",SavePath="/data/etph/paspir/Radia-Fields/"];
Subscript[v, x]:=v[[1]]
Subscript[v, y]:=v[[2]]
Subscript[v, z]:=v[[3]]
Subscript[u, x]:=0.3;
solutionu:=Solve[{Subscript[v, x]*Subscript[u, x]+Subscript[v, y]*Subscript[u, y]+Subscript[v, z]*Subscript[u, z]==0,Subscript[u, x]^2+Subscript[u, y]^2+Subscript[u, z]^2==1},{Subscript[u, y],Subscript[u, z]}];
{Subscript[s, y],Subscript[s, z]}={Subscript[u, y],Subscript[u, z]}/.solutionu[[1]];
solw:=Solve[{Subscript[v, x]*Subscript[w, x]+Subscript[v, y]*Subscript[w, y]+Subscript[v, z]*Subscript[w, z]==0,Subscript[u, x]*Subscript[w, x]+Subscript[s, y]*Subscript[w, y]+Subscript[s, z]*Subscript[w, z]==0,
```

```
    Subscript[w, x]^2+Subscript[w, y]^2+Subscript[w, z]^2==1},{Subscript[w
    , x],Subscript[w, y],Subscript[w, z]}];
{Subscript[t, x],Subscript[t, y],Subscript[t, z]}={Subscript[w, x],
    Subscript[w, y],Subscript[w, z]}/.solw[[1]];
a:=N[{Subscript[u, x],Subscript[s, y],Subscript[s, z]}]
b:=N[{Subscript[t, x],Subscript[t, y],Subscript[t, z]}]
getPoint[j_,k_]:=v+j*a+k*b;
da:=2.50;
db:=2.50;
extendA:=150;
extendB:=150;
eV:=v/Norm[v];

<<Radia`;
Off[General::spell]
(* Ma e des Permanentmagneten*)
xMagnet := 8;
yMagnet := 8.5;
zMagnet := 10;
(* Ma e der Jochs *)
xJoch := 36;
yJoch := 4; (* Originaldicke: 4 mm *)
zJoch := zMagnet;
SegX:=10;                                                       (* Segmentierung des
    Jochs in X-Richtung *)
SegY:=16;                                                       (* Segmentierung des
    Jochs in Y-Richtung *)
SegZ:=2;                                                       (* Segmentierung des
    Jochs in Z-Richtung *)
Gap:=8;                                                          (* Luecke zwischen
    den Magneten *)
deltaX:=20;                                                 (* Abstand zweier Magnete
     am Joch *)
klebeluecke:=0.09;                                    (* Klebeluecke zwischen Magnet
    und Joch *)

Magnet1A=radObjRecMag[{-(xMagnet+deltaX)/2,(yMagnet+Gap)/2,0},{xMagnet,
    yMagnet,zMagnet},{0,1,0}];
Magnet1B=radObjRecMag[{(xMagnet+deltaX)/2,(yMagnet+Gap)/2,0},{xMagnet,
    yMagnet,zMagnet},{0,-1,0}];
Magnet2A=radObjRecMag[{-(xMagnet+deltaX)/2,-(yMagnet+Gap)/2,0},{xMagnet,
    yMagnet,zMagnet},{0,1,0}];
Magnet2B=radObjRecMag[{(xMagnet+deltaX)/2,-(yMagnet+Gap)/2,0},{xMagnet,
    yMagnet,zMagnet},{0,-1,0}];
radTrfOrnt[Magnet1A,radTrfTrsl[10.0*{0,0,dZMagnet1A}]];
radTrfOrnt[Magnet1B,radTrfTrsl[10.0*{0,0,dZMagnet1B}]];
radTrfOrnt[Magnet2A,radTrfTrsl[10.0*{0,0,dZMagnet2A}]];
radTrfOrnt[Magnet2B,radTrfTrsl[10.0*{0,0,dZMagnet2B}]];
SeptJoch=radObjCnt[{}];
JochMaterial=RadMatAFK502[];
Joch1=RadObjFullMag[{0,(yJoch+Gap+2*yMagnet)/2+klebeluecke,0},{xJoch,
    yJoch,zJoch},{0,0,0},{SegX,SegY,SegZ},SeptJoch,JochMaterial
    ,{0,0,0.6}];
Joch2=RadObjFullMag[{0,-(yJoch+Gap+2*yMagnet)/2-klebeluecke,0},{xJoch,
    yJoch,zJoch},{0,0,0},{SegX,SegY,SegZ},SeptJoch,JochMaterial
    ,{0,0,0.6}];
radTrfOrnt[Joch1,radTrfTrsl[10.0*{dXJoch1,0,dZJoch1}]];
radTrfOrnt[Joch2,radTrfTrsl[10.0*{dXJoch2,0,dZJoch2}]];
```

```
cutDicke:=1;
JochSchmal:=xJoch-2*3;
aufpunkt1rechts:={xJoch/2,yMagnet+Gap/2 + cutDicke+klebeluecke ,0};
aufpunkt1links:={-xJoch/2,yMagnet+Gap/2 + cutDicke+klebeluecke ,0};
aufpunkt2rechts:={xJoch/2,-(yMagnet+Gap/2 +cutDicke+klebeluecke),0};
aufpunkt2links:={-xJoch/2,-(yMagnet+Gap/2 + cutDicke+klebeluecke),0};
?:=ArcTan[(xJoch-JochSchmal)/(yJoch-cutDicke)];
vektor1rechts:={Cos[?],Sin[?],0};
vektor1links:={-Cos[?],Sin[?],0};
vektor2rechts:={Cos[?],-Sin[?],0};
vektor2links:={-Cos[?],-Sin[?],0};
JochCut1rechts=radObjCutMag[Joch1,aufpunkt1rechts,vektor1rechts];
JochCut1links=radObjCutMag[JochCut1rechts[[1]],aufpunkt1links,
    vektor1links];
JochCut2rechts=radObjCutMag[Joch2,aufpunkt2rechts,vektor2rechts];
JochCut2links=radObjCutMag[JochCut2rechts[[1]],aufpunkt2links,
    vektor2links];
MagnetSystem=radObjCnt[{}];
(* Definition der Remanenzmagnetisierung in den Permanentmagneten *)
Remanenz:=1.18;
MagnetMaterial1A=RadMatNdFeB[Remanenz];
MagnetMaterial1B=RadMatNdFeB[Remanenz];
MagnetMaterial2A=RadMatNdFeB[Remanenz];
MagnetMaterial2B=RadMatNdFeB[Remanenz];
radMatApl[Magnet1A,MagnetMaterial1A];
radMatApl[Magnet1B,MagnetMaterial1B];
radMatApl[Magnet2A,MagnetMaterial2A];
radMatApl[Magnet2B,MagnetMaterial2B];
radMatApl[Joch1,JochMaterial];
radMatApl[Joch2,JochMaterial];
radObjAddToCnt[MagnetSystem,{Magnet1A}];
radObjAddToCnt[MagnetSystem,{Magnet1B}];
radObjAddToCnt[MagnetSystem,{Magnet2A}];
radObjAddToCnt[MagnetSystem,{Magnet2B}];
radObjAddToCnt[MagnetSystem,{JochCut1links[[1]]}];
radObjAddToCnt[MagnetSystem,{JochCut2links[[1]]}];;

RadSolve[MagnetSystem,10^-8,7000,4];
MagneticFieldStrength[x_,y_,z_]:=Sqrt[radFld[MagnetSystem,"Bx",{x,y,z
    }]^2+radFld[MagnetSystem,"By",{x,y,z}]^2+radFld[MagnetSystem,"Bz",{x,y
    ,z}]^2];
eX={1,0,0};
eY={0,1,0};
eZ={0,0,1};
MagneticFieldStrengthShifted[x_,y_,z_]:=Sqrt[radFld[MagnetSystem,"Bx",{x
    +1.4,y-2.03,z-10.87}]^2+radFld[MagnetSystem,"By",{x+6.4,y-4.73,z
    +5.03}]^2+radFld[MagnetSystem,"Bz",{x-7.8,y+6.77,z+5.83}]^2];
eX={1,0,0};
eY={0,1,0};
eZ={0,0,1};

Liste=Table[{},{0}];
For[t=55,t<=Norm[v],t+=5,
feldbetragShifted:=MagneticFieldStrengthShifted[t*eV[[1]],t*eV[[2]],t*eV
    [[3]]];
feldbetrag:=MagneticFieldStrength[t*eV[[1]],t*eV[[2]],t*eV[[3]]];
Liste=Append[Liste,Flatten[{t,t,t,radFld[MagnetSystem,"B",{t*eV[[1]],t*eV
    [[2]],t*eV[[3]]}],feldbetragShifted,feldbetrag}]]
```

```
];
Export[SavePath<>"Feld_Richtung_"<>SaveFile, Liste, "CSV"];
Quit[];
```

B.5. Python-Listings

This listing is an extract from a Python that is written to represent a magnetic field. This method returns the extrapolated magnetic flux densities at a given point in space relying on a field-file written by RADIA.

```
def getFieldValue(self, x, y, z):
    Punkt_null = numpy.array([math.floor(x), math.floor(y), math.floor(z)])
    Punkt_1 = Punkt_null + numpy.array([1.0*self.dx, 0.0*self.dy, 0.0*self.dz])
    Punkt_2 = Punkt_null + numpy.array([1.0*self.dx, 0.0*self.dy, 1.0*self.dz])
    Punkt_3 = Punkt_null + numpy.array([0.0*self.dx, 0.0*self.dy, 1.0*self.dz])
    Punkt_4 = Punkt_null + numpy.array([0.0*self.dx, 1.0*self.dy, 0.0*self.dz])
    Punkt_5 = Punkt_null + numpy.array([1.0*self.dx, 1.0*self.dy, 0.0*self.dz])
    Punkt_6 = Punkt_null + numpy.array([1.0*self.dx, 1.0*self.dy, 1.0*self.dz])
    Punkt_7 = Punkt_null + numpy.array([0.0*self.dx, 1.0*self.dy, 1.0*self.dz])

    Feld_nullpunkt = self.getRadField(Punkt_null)
    Feld_punkt_1 = self.getRadField(Punkt_1)
    Feld_punkt_2 = self.getRadField(Punkt_2)
    Feld_punkt_3 = self.getRadField(Punkt_3)
    Feld_punkt_4 = self.getRadField(Punkt_4)
    Feld_punkt_5 = self.getRadField(Punkt_5)
    Feld_punkt_6 = self.getRadField(Punkt_6)
    Feld_punkt_7 = self.getRadField(Punkt_7)

    mitte = numpy.array([x, y, z])

    distance_null = numpy.linalg.norm(mitte - Punkt_null)
    distance_1 = numpy.linalg.norm(mitte - Punkt_1)
    distance_2 = numpy.linalg.norm(mitte - Punkt_2)
    distance_3 = numpy.linalg.norm(mitte - Punkt_3)
    distance_4 = numpy.linalg.norm(mitte - Punkt_4)
    distance_5 = numpy.linalg.norm(mitte - Punkt_5)
    distance_6 = numpy.linalg.norm(mitte - Punkt_6)
    distance_7 = numpy.linalg.norm(mitte - Punkt_7)

    d0 = distance_null
    d1 = distance_1
    d2 = distance_2
    d3 = distance_3
    d4 = distance_4
    d5 = distance_5
    d6 = distance_6
    d7 = distance_7

```

```
    zaehler0 = d1*d2*d3*d4*d5*d6*d7
    zaehler1 = d0*d2*d3*d4*d5*d6*d7
    zaehler2 = d0*d1*d3*d4*d5*d6*d7
    zaehler3 = d0*d1*d2*d4*d5*d6*d7
    zaehler4 = d0*d1*d2*d3*d5*d6*d7
    zaehler5 = d0*d1*d2*d3*d4*d6*d7
    zaehler6 = d0*d1*d2*d3*d4*d5*d7
    zaehler7 = d0*d1*d2*d3*d4*d5*d6

    zaehler_sum = zaehler0 + zaehler1 + zaehler2 + zaehler3 + zaehler4 +
        zaehler5 + zaehler6 + zaehler7

    faktor0 = zaehler0 / zaehler_sum
    faktor1 = zaehler1 / zaehler_sum
    faktor2 = zaehler2 / zaehler_sum
    faktor3 = zaehler3 / zaehler_sum
    faktor4 = zaehler4 / zaehler_sum
    faktor5 = zaehler5 / zaehler_sum
    faktor6 = zaehler6 / zaehler_sum
    faktor7 = zaehler7 / zaehler_sum


    feld = (Feld_nullpunkt*faktor0) + (Feld_punkt_1*faktor1) + (
        Feld_punkt_2*faktor2) + (Feld_punkt_3*faktor3) + (Feld_punkt_4*
        faktor4) + (Feld_punkt_5*faktor5) + (Feld_punkt_6*faktor6) + (
        Feld_punkt_7*faktor7)

    return feld
```

B.6. CAD Drawing of EPT

The following figure shows a CAD drawing of the EPT including the magnet system.

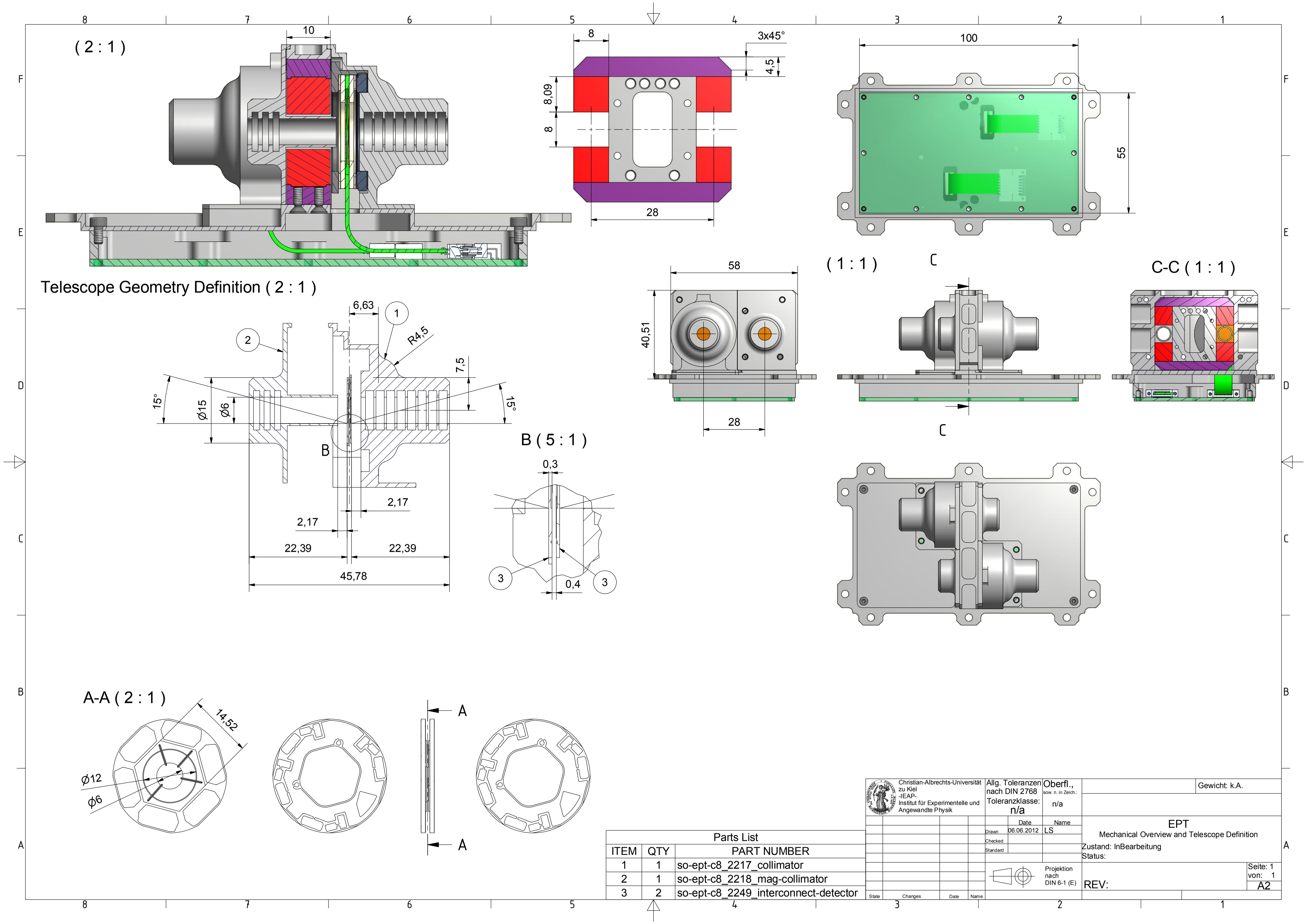

Figure B.1.: CAD-drawing of one EPT instrument (by Lars Seimetz).

C. Derivations for the Fermi Acceleration Processes

C.1. Second Order Fermi Acceleration

We will now derive the relation for the middle energy gain $\langle\xi\rangle$ during the process of second order Fermi acceleration (Fermi 1949) as presented in section 2.3.4 following the derivations from Terrier (2011). We consider the situation as described there and depicted in fig. 2.8: an energetic particle enters a region of magnetic turbulence (a so-called magnetic cloud) under the angle θ_1 relative to the cloud's motion $\vec{v}_{\mathrm{cloud}}$, gets scattered inside this region and finally leaves the cloud under the angle θ_2.

To express the energy of the entering particle in the cloud's coordinate system we perform a Lorentz transformation from the lab system (S) to the cloud system ($S^{'}$):

$$E_1^{'} = \gamma E_1 \left(1 - \beta \cos\theta_1\right) \tag{C.1}$$

where $\beta = v_{\mathrm{cloud}}/c$ and $\gamma = 1/\sqrt{1-\beta^2}$. Variables in the cloud's system are marked with a prime.

A second Lorentz transformation from the cloud system back to the lab system for the exit energy gives:

$$E_2 = \gamma E_2^{'} \left(1 + \beta \cos\theta_2^{'}\right) \tag{C.2}$$

We assume the density in the cloud to be so low that we can neglect direct particle-particle collisions and the mass of the cloud to be so high that the momentum transfer from particle to cloud can also be neglected. These considerations lead to the conservation of the particle's energy in the cloud's frame:

$$E_2^{'} = E_1^{'} \tag{C.3}$$

With eqn. (C.3) we can eliminate $E_2^{'}$ in (C.2) and with that together with (C.1) we can calculate the relative energy gain:

$$\begin{aligned}
\xi &= \frac{E_2 - E_1}{E_1} = \frac{\gamma E_1^{'}\left(1 + \beta\cos\theta_2^{'}\right) - \frac{E_1^{'}}{\gamma(1-\beta\cos\theta_1)}}{\frac{E_1^{'}}{\gamma(1-\beta\cos\theta_1)}} \\
&= \left(\gamma\left(1 + \beta\cos\theta_2^{'}\right) - \frac{1}{\gamma\left(1 - \beta\cos\theta_1\right)}\right)\gamma\left(1 - \beta\cos\theta_1\right) \\
&= \gamma^2\left(1 + \beta\cos\theta_2^{'}\right)\left(1 - \beta\cos\theta_1\right) - 1
\end{aligned} \tag{C.4}$$

To get a general physical statement we rather need to ask for the mean value $< \xi >$ for which we need the corresponding values $< \cos\theta_1 >$ and $< \cos\theta_2^{'} >$. The outgoing direction is randomized, therefore:

$$\left\langle \cos\theta_2^{'} \right\rangle = 0 \tag{C.5}$$

The cloud is hit by

$$dN \propto (v_{\text{part.}} - v_{\text{cloud}} \cos\theta_1)\, \delta t \tag{C.6}$$

particles from the direction θ_1 in the time δt.

We gain the average of the cosine of the incident angle by integrating over all possible directions weighing with the collision rate $dN/\delta t$ and relating that to the total amount of particles hitting the cloud:

$$\begin{aligned}
\langle \cos\theta_1 \rangle &= \frac{\int_{-1}^{+1} \cos\theta_1 \,(v_{\text{part.}} - v_{\text{cloud}} \cos\theta_1)\, d\cos\theta_1}{\int_{-1}^{+1} (v_{\text{part.}} - v_{\text{cloud}} \cos\theta_1)\, d\cos\theta_1} \\
&= \frac{\int_{-1}^{+1} x\,(v_{\text{part.}} - v_{\text{cloud}} x)\, dx}{\int_{-1}^{+1} v_{\text{part.}} dx - \int_{-1}^{+1} v_{\text{cloud}} x dx} \\
&= \frac{\int_{-1}^{+1} x v_{\text{part.}} dx - \int_{-1}^{+1} x^2 v_{\text{cloud}} dx}{2v_{\text{part.}} - \frac{v_{\text{cloud}}}{2}\left[x^2\right]_{-1}^{+1}} \\
&= \frac{\frac{v_{\text{part.}}}{2}\left[x^2\right]_{-1}^{+1} - \frac{v_{\text{cloud}}}{3}\left[x^3\right]_{-1}^{+1}}{2v_{\text{part.}} - 0} \\
&= \frac{0 - \frac{v_{\text{cloud}}}{3} \cdot 2}{2v_{\text{part.}}} \\
&= -\frac{1}{3}\frac{v_{\text{cloud}}}{v_{\text{part.}}} \\
&\overset{v_{\text{part.}} \approx c}{\approx} -\frac{1}{3}\frac{v_{\text{cloud}}}{c} \\
&= -\frac{\beta}{3}
\end{aligned} \tag{C.7}$$

Inserting (C.7) into (C.4) together with $\left\langle \cos\theta_2^{'} \right\rangle = 0$ yields:

$$\begin{aligned}
\langle \xi \rangle &= \gamma^2 \left(1 + \beta \left\langle \cos\theta_2^{'} \right\rangle\right) \left(1 - \beta \left\langle \cos\theta_1 \right\rangle\right) - 1 \\
&= \frac{\left(1 + \beta \left\langle \cos\theta_2^{'} \right\rangle\right) \left(1 - \beta \left\langle \cos\theta_1 \right\rangle\right)}{1-\beta^2} - 1 \\
&= \frac{1 + \frac{\beta^2}{3}}{1-\beta^2} - 1 \\
&= \frac{1 + \frac{\beta^2}{3} - 1 + \beta^2}{1-\beta^2} \\
&= \frac{\frac{4}{3}\beta^2}{1-\beta^2} \\
&\approx \frac{4}{3}\beta^2 \qquad \text{(C.8)}
\end{aligned}$$

In the last step, we used that the velocity of the cloud is non-relativistic: $v_{\text{cloud}} \ll c$.

C.2. First Order Fermi Acceleration

As we saw in section 2.3.4, a charged particle can gain energy when it travels through a region of high magnetic turbulence. The mean energy gain at the second order Fermi acceleration was calculated with eqn. (C.8) using the mean values of the cosine of the entry angle (eqn. (C.7)) and the exit angles (eqn. (C.5)).

Following the derivations from Jones et al. (1991) and Terrier (2011), we will now derive the mean energy gain of the first order Fermi acceleration as described in section 2.3.5 and depicted in the figures 2.10 and 2.11. We start with eqn. (C.4) and determine $< \cos\theta_1 >$ and $< \cos\theta_2^{'} >=< \cos\theta_2 >$. For this purpose, we first need to define the probabilities $P(\cos\theta_1)$ and $P(\cos\theta_2)$ that a particle traverses the shock front under the angle θ_1 coming from the upstream and θ_2 from the downstream.

In both regimes we assume an isotropic radiation distribution in θ which means that the probability distribution is constant in $\cos\theta$:

$$\frac{dP(\cos\theta)}{d\cos\theta} = \text{const.} \qquad \text{(C.9)}$$

Furthermore, we consider that the probability $P(\cos\theta)$ is proportional to the particle's velocity $v_{\|} = v \cdot \cos\theta$ parallel to the shock movement:

$$P(\cos\theta) \propto v \cdot \cos\theta \qquad \text{(C.10)}$$

Finally, we need to normalize the probability distribution in a way that a particle in the upstream coming from the left crosses the front to the right under an angle θ_1 for which $\cos\theta_1$ lies between -1 and 0. A similar consideration gives the range from 0 to $+1$ for the cosine of the angle θ_2 of a particle from the downstream:

$$\text{upstream}: \quad \textstyle\int_{-1}^{0} P\left(\cos\theta_1\right)\ d\cos\theta_1 := 1 \tag{C.11}$$

$$\text{downstream}: \quad \textstyle\int_{0}^{+1} P\left(\cos\theta_2\right)\ d\cos\theta_2 := 1 \tag{C.12}$$

These three considerations lead to the following conclusions for the probability distributions:

$$P\left(\cos\theta_1\right) = \left\{ \begin{array}{ccrl} 2\cos\left(\theta_1\right) & : & -1 & \leq \cos\theta_1 \leq 0 \\ 0 & : & 0 & \leq \cos\theta_1 \leq +1 \end{array} \right.$$

$$P\left(\cos\theta_2\right) = \left\{ \begin{array}{ccrl} 2\cos\left(\theta_2\right) & : & 0 & \leq \cos\theta_2 \leq +1 \\ 0 & : & -1 & \leq \cos\theta_2 \leq 0 \end{array} \right.$$

With these two probability distributions we can calculate the expected values of $\cos\theta_1$ and $\cos\theta_2$ (deriving the integrals I_1 and I_2 in the numerator and denominator separately):

$$\langle\cos\theta_1\rangle = \frac{\int_{-1}^{+1} \cos\theta_1 P\left(\cos\theta_1\right)\ d\cos\theta_1}{\int_{-1}^{+1} P\left(\cos\theta_1\right)\ d\cos\theta_1} = \frac{I_1}{I_2} \tag{C.13}$$

$$\begin{aligned} I_1 &= \int_{-1}^{+1} \cos\theta_1 P\left(\cos\theta_1\right)\ d\cos\theta_1 \\ &= \int_{-1}^{0} \cos\theta_1 2\cos\theta_1\ d\cos\theta_1 \\ &= \int_{-1}^{0} 2x^2 dx \\ &= \frac{2}{3}\left[x^3\right]_{-1}^{0} \\ &= \frac{2}{3} \end{aligned} \tag{C.14}$$

$$\begin{aligned} I_2 &= 2\int_{-1}^{0} \cos\theta_1\ d\cos\theta_1 \\ &= 2\int_{-1}^{0} x dx = -1 \end{aligned} \tag{C.15}$$

$$\langle\cos\theta_1\rangle = \frac{I_1}{I_2} = -\frac{2}{3} \tag{C.16}$$

$$\langle\cos\theta_2\rangle = \frac{\int_{-1}^{+1} \cos\theta_2 P\left(\cos\theta_2\right)\ d\cos\theta_2}{\int_{-1}^{+1} P\left(\cos\theta_2\right)\ d\cos\theta_2} = \frac{I_1}{I_2} \tag{C.17}$$

$$\begin{aligned} I_1 &= \int_0^1 \cos\theta_2 2\cos\theta_2 \ d\cos\theta_2 \\ &= 2\int_0^1 x^2 dx = \frac{2}{3}\left[x^3\right]_0^1 = \frac{2}{3} \end{aligned} \tag{C.18}$$

$$\begin{aligned} I_2 &= 2\int_0^1 \cos\theta_2 \ d\cos\theta_2 \\ &= 2\int_0^1 x dx = \left[x^2\right]_0^1 = 1 \end{aligned} \tag{C.19}$$

$$\langle\cos\theta_2\rangle = \frac{I_1}{I_2} = \frac{2}{3} \tag{C.20}$$

And with that we can now determine the average energy gain:

$$\begin{aligned} \langle\xi\rangle &= \gamma^2\left(1+\beta\left\langle\cos\theta_2'\right\rangle\right)\left(1-\beta\left\langle\cos\theta_1\right\rangle\right)-1 \\ &= \frac{\left(1+\beta\left\langle\cos\theta_2'\right\rangle\right)\left(1-\beta\left\langle\cos\theta_1\right\rangle\right)}{1-\beta^2}-1 \\ &= \frac{\left(1+\beta\frac{2}{3}\right)\left(1+\beta\frac{2}{3}\right)}{1-\beta^2}-1 \\ &= \frac{1+\frac{4}{3}\beta+\frac{4}{9}\beta^2}{1-\beta^2}-\frac{1-\beta^2}{1-\beta^2} \\ &= \frac{1+\frac{4}{3}\beta+\frac{4}{9}\beta^2-1+\beta^2}{1-\beta^2} \\ &= \frac{\frac{4}{3}\beta+\frac{13}{9}\beta^2}{1-\beta^2} \\ &\overset{\beta\gg\beta^2}{\approx} \frac{4}{3}\beta \end{aligned} \tag{C.21}$$

We see that ξ is linear in β which is the reason why the acceleration process is called the **first** order Fermi acceleration process.

A particle with the starting kinetic energy E_0 that crosses the shock front N times gets accelerated to the energy:

$$E_N = E_0\left(1+\langle\xi\rangle\right)^N \rightarrow N = \frac{\log\left(\frac{E_N}{E_0}\right)}{\log\left(1+\langle\xi\rangle\right)} \tag{C.22}$$

The number of particles at the energy E_N behind the shock is then calculated by:

$$Z\left(E_N\right) = \left(1-p_{\text{esc}}\right)^N \tag{C.23}$$

where we introduced the probability p_{esc} of a particle to escape the multiple scattering procedure across the shock front.

The number of particles at a certain energy E_N is described by a power law:

$$\begin{aligned}
Z\left(E_N\right) = \left(1-p_{\text{esc}}\right)^{\frac{\log \frac{E_N}{E_0}}{\log\left(1+\langle\xi\rangle\right)}} &= 10^{\log\left[\left(1-p_{\text{esc}}\right)^{\frac{\log \frac{E_N}{E_0}}{\log\left(1+\langle\xi\rangle\right)}}\right]} \\
&= 10^{\left(\frac{\log\left(\frac{E_N}{E_0}\right)}{\log(1+\langle\xi\rangle)}\cdot\log(1-p_{\text{esc}})\right)} \\
&= 10^{\left(\log\left(\frac{E_N}{E_0}\right)\cdot\frac{\log(1-p_{\text{esc}})}{\log(1+\langle\xi\rangle)}\right)} \\
&= 10^{\left(\log\left(\frac{E_N}{E_0}\right)\right)^{\frac{\log(1-p_{\text{esc}})}{\log(1+\langle\xi\rangle)}}} \\
&= \left(\frac{E_N}{E_0}\right)^{\frac{\log(1-p_{\text{esc}})}{\log(1+\langle\xi\rangle)}} \\
&\overset{\langle\xi\rangle\ll 1}{\underset{p_{\text{esc}}\ll 1}{\approx}} \left(\frac{E_N}{E_0}\right)^{\frac{p_{\text{esc}}}{\langle\xi\rangle}}
\end{aligned} \tag{C.24}$$

The number density n of the particles at the Energy E and with velocity v in an isotropic intensity I is determined by:

$$n(E) = \frac{4\pi}{v} I(E) \tag{C.25}$$

The particle flux of the upstream is calculated as an isotropic intensity through a planar area:

$$F_u(E) = \pi I(E) = \frac{\pi v n(E)}{4\pi} = \frac{v n(E)}{4} \tag{C.26}$$

Whereas the flux of the downstream is determined as a directed flux moving away from the shock with the velocity v_d by:

$$F_d(E) = v_d n\left(E\right) \tag{C.27}$$

With that we can define the escape probability p_{esc} as the ratio of the two fluxes:

$$p_{\text{esc}}(E) = p_{\text{esc}} = \frac{F_d(E)}{F_u(E)} = 4\frac{v_d}{v_u} \tag{C.28}$$

And finally, we can calculate the exponent of the resulting spectrum from eqn. (C.24):

$$\begin{aligned}
\frac{p_{\text{esc}}}{\xi} &= \frac{4\frac{v_d}{v_u}}{\frac{4}{3}\frac{v_u - v_d}{c}} \\
&= 3\frac{c\frac{v_d}{v_u}}{v_u - v_d} \\
&= 3\frac{\frac{c}{v_u}}{\frac{v_u}{v_d} - 1} \\
&\overset{v_u \approx c}{\approx} 3\frac{1}{\frac{v_u}{v_d} - 1}
\end{aligned} \tag{C.29}$$

Bibliography

Agostinelli, S. et al. (2003). “Geant4 – a simulation toolkit”. In: *Nuclear Instruments and Methods in Physics Research Section A: Accelerators, Spectrometers, Detectors and Associated Equipment* 506.3, pp. 250 –303. ISSN: 0168-9002. DOI: `10.1016/S0168-9002(03)01368-8`. URL: `http://www.sciencedirect.com/science/article/pii/S0168900203013688`.

Allison, J. et al. (Feb. 2006). “Geant4 developments and applications”. In: *Nuclear Science, IEEE Transactions on* 53.1, pp. 270 –278. ISSN: 0018-9499. DOI: `10.1109/TNS.2006.869826`.

Aschwanden, M. (2006). *Physics of the Solar Corona: An Introduction with Problems and Solutions.* Springer-Praxis Books in Astronomy and Planetary Sciences. Springer. ISBN: 9783540307655. URL: `http://books.google.de/books?id=W7FE5\_aowEQC`.

Barnett, R. M. et al. (June 1996). “Review of Particle Physics”. In: *Phys. Rev. D* 54 (1), pp. 1–708. DOI: `10.1103/PhysRevD.54.1`. URL: `http://link.aps.org/doi/10.1103/PhysRevD.54.1`.

Baumjohann, W. et al. (1996). *Basic space plasma physics.*

Bethe, H.A. (1930). “Zur Theorie des Durchgangs schneller Korpuskularstrahlen durch Materie”. In: *Annalen der Physik* 5, pp. 325–400. URL: `http://books.google.de/books?id=QzGdHAAACAAJ`.

Bruno, R. et al. (2009). “Laboratory activity at INAF-IFSI in the framework of its participation to SWA onboard ESA-Solar Orbiter .” In: *Mem. Soc. Astron. Ital.* 80, p. 239.

Burmeister, S. (Dec. 2011). *EPT DM1 Assembly Report, Issue: 1, Review: 1.*

Carr, C.M. et al. (2006). “A magnetometer for the Solar Orbiter Mission”. English. In: *Proceedings Solar Orbiter Mission Conference.* Presented at: Solar Orbiter Mission Conference : Athens, Greece, 2006. Athens, Greece.

Chen, F. F. et al. (1985). “Introduction to Plasma Physics and Controlled Fusion Volume 1: Plasma Physics, Second Edition”. In: *Physics Today* 38, p. 87. DOI: `10.1063/1.2814568`.

Chubar, Oleg et al. (May 1998). “A three-dimensional magnetostatics computer code for insertion devices”. In: *Journal of Synchrotron Radiation* 5.3, pp. 481–484. DOI: `10.1107/S0909049597013502`. URL: `http://dx.doi.org/10.1107/S0909049597013502`.

Cucinotta, F. A. et al. (Mar. 1996). “Radial dose distributions in the delta-ray theory of track structure”. In: *American Institute of Physics Conference Series.* Vol. 362. American Institute of Physics Conference Series, pp. 245–265. DOI: `10.1063/1.50083`.

Ebert, H. et al. (Sept. 1996). “Anisotropic electrical resistivity of ferromagnetic Co-Pd and Co-Pt alloys”. In: *Phys. Rev. B* 54 (12), pp. 8479–8486. DOI: `10.1103/PhysRevB.54.8479`. URL: `http://link.aps.org/doi/10.1103/PhysRevB.54.8479`.

Elleaume, P. et al. (May 1997). "Computing 3D magnetic fields from insertion devices". In: *Particle Accelerator Conference, 1997. Proceedings of the 1997*. Vol. 3, 3509 – 3511 vol.3. DOI: `10.1109/PAC.1997.753258`.

Ellison, D. C. et al. (Nov. 1985). "Shock acceleration of electrons and ions in solar flares". In: *Astrophysical Journal* 298, pp. 400–408. DOI: `10.1086/163623`.

Evans, Robley D. (1955). *The atomic nucleus*. English. McGraw-Hill, New York : 972 p.

Fermi, ENRICO (Apr. 1949). "On the Origin of the Cosmic Radiation". In: *Phys. Rev.* 75 (8), pp. 1169–1174. DOI: `10.1103/PhysRev.75.1169`. URL: `http://link.aps.org/doi/10.1103/PhysRev.75.1169`.

Gandorfer, A. et al. (Jan. 2011). "The Solar Orbiter Mission and its Polarimetric and Helioseismic Imager (SO/PHI)". In: *Journal of Physics Conference Series* 271.1, p. 012086. DOI: `10.1088/1742-6596/271/1/012086`.

Gauss, C.F. (1838). *Allgemeine Theorie des Erdmagnetismus*. In Resultate magn. Verein (Reprinted in Werke, Vol. 5, p. 121). URL: `http://books.google.de/books?id=UdCUIgAACAAJ`.

Genish, I. et al. (June 2004). "Paramagnetic anisotropic magnetoresistance in thin films of $SrRuO_3$". In: *Journal of Applied Physics* 95, pp. 6681–6683. DOI: `10.1063/1.1676052`. eprint: `arXiv:cond-mat/0311343`.

Grupen, C. (2005). *Astroparticle Physics*. Springer. DOI: `10.1007/3-540-27670-X`.

Hassler, D. M. et al. (Dec. 2011). "Investigations to Determine the Origin of the Solar Wind with the SPICE EUV Imaging Spectrograph and the Solar Orbiter Mission". In: *AGU Fall Meeting Abstracts*, B2054.

Hochedez, J.-F. et al. (Oct. 2006). "EUI, The Ultraviolet Imaging Telescopes Of Solar Orbiter". In: *Second Solar Orbiter Workshop*. Vol. 641. ESA Special Publication.

Howard, R. A. et al. (Dec. 2010). "Imaging the Solar Wind with SoloHI". In: *AGU Fall Meeting Abstracts*, B1627.

Howard, T. (May 2011). *Coronal Mass Ejections: An Introduction*. Astrophysics and Space Science Library. Springer. ISBN: 9781441987884. URL: `http://books.google.de/books?id=tKFHdIbWnZgC`.

Hurford, G. J. et al. (May 2010). "Observing Solar Hard X-rays from Heliospheric Orbits". In: *American Astronomical Society Meeting Abstracts #216*. Vol. 41. Bulletin of the American Astronomical Society, p. 404.16.

Jones, F. C. et al. (Dec. 1991). "The plasma physics of shock acceleration". In: *Space Sci. Rev.* 58, pp. 259–346. DOI: `10.1007/BF01206003`.

Kane, R. P. (Feb. 1976). "Geomagnetic field variations". In: *Space Science Reviews, vol. 18, Feb. 1976, p. 413-540* 18, pp. 413–540. DOI: `10.1007/BF00217344`.

Kerridge, David (2010). *INTERMAGNET: Worldwide near-real-time geomagnetic observatory data*. `http://www.intermagnet.org/Publications_e.php`, Retrieved on: 04.13.2012.

Knoll, Glenn F. (1989). *Radiation detection and measurement / Glenn F. Knoll*. English. 2nd ed. Wiley, New York : xix, 754 p. : ISBN: 0471815047. URL: `http://www.loc.gov/catdir/toc/onix05/88026142.html`.

Ko, H. et al. (Aug. 2011). "Simulated Effects of Secondary Particles Generated by a Space Proton Environment in the Orbit of the Aura satellite". In: *Journal of Korean Physical Society* 59, p. 674. DOI: `10.3938/jkps.59.674`.

Lario, D. et al. (Dec. 2006). “Radial and Longitudinal Dependence of Solar 4-13 MeV and 27-37 MeV Proton Peak Intensities and Fluences: Helios and IMP 8 Observations”. In: *Astrophysical Journal* 653, pp. 1531–1544. DOI: `10.1086/508982`.

Lee, Martin A. (Jan. 2000). “Acceleration of energetic particles on the Sun, in the Heliosphere, and in the Galaxy”. In: *AIP Conference Proceedings* 528.1. Ed. by Richard A. Mewaldt et al., pp. 3–18. DOI: `10.1063/1.1324276`. URL: `http://link.aip.org/link/?APC/528/3/1`.

Lenz, J. et al. (June 2006). “Magnetic sensors and their applications”. In: *Sensors Journal, IEEE* 6.3, pp. 631 –649. ISSN: 1530-437X. DOI: `10.1109/JSEN.2006.874493`.

Mapps, D.J. (Apr. 1997). “Magnetoresistive sensors”. In: *Sensors and Actuators A: Physical* 59.13. ¡ce:title¿1st European magnetic sensors and actuators conference¡/ce:title¿, pp. 9 –19. ISSN: 0924-4247. DOI: `10.1016/S0924-4247(97)80142-2`. URL: `http://www.sciencedirect.com/science/article/pii/S0924424797801422`.

Mewaldt, R. A. et al. (Sept. 2005). “Proton, helium, and electron spectra during the large solar particle events of October-November 2003”. In: *Journal of Geophysical Research (Space Physics)* 110.9, A09S18, p. 9. DOI: `10.1029/2005JA011038`.

Mueller, D. et al. (July 2012). “Solar Orbiter: Exploring the Sun-heliosphere connection”. In: *ArXiv e-prints*. arXiv: `1207.4579 [astro-ph.SR]`.

Müller-Mellin, R. et al. (Apr. 2008). “The Solar Electron and Proton Telescope for the STEREO Mission”. In: *Space Sci. Rev.* 136, pp. 363–389. DOI: `10.1007/s11214-007-9204-4`.

Okeke, F. N. et al. (Apr. 2000). “Daily variations of geomagnetic H D and Z-field at equatorial latitudes”. In: *Earth, Planets, and Space* 52, pp. 237–243.

Parker, E.N. (1965). “The passage of energetic charged particles through interplanetary space”. In: *Planetary and Space Science* 13.1, pp. 9 –49. ISSN: 0032-0633. DOI: `10.1016/0032-0633(65)90131-5`. URL: `http://www.sciencedirect.com/science/article/pii/0032063365901315`.

Plettemeier, D. et al. (Dec. 2009). “Characterization of the RPW Electric Antenna System aboard Solar Orbiter”. In: *AGU Fall Meeting Abstracts*, B1497.

Porsche, H. (1977). “General aspects of the mission Helios 1 and 2. Introduction to a special issue on initial scientific results of the Helios Mission.” In: *Journal of Geophysics Zeitschrift Geophysik* 42, pp. 551–559.

Rodriguez-Pacheco, Javier (Mar. 2011). *Experiment Interface Document Part B*.

Roelof, E. C. (1969). “Propagation of Solar Cosmic Rays in the Interplanetary Magnetic Field”. In: *Lectures in High-Energy Astrophysics*. Ed. by H. Ögelman et al., p. 111.

Russell, C.T. (2008). *The Stereo Mission*. Springer Study Edition Series. Springer. ISBN: 9780387096490. URL: `http://books.google.de/books?id=T2wnQAAACAAJ`.

Schuehle, U. (Nov. 2012). *Multi Element Telescope for Imaging and Spectroscopy*. `http://www.mps.mpg.de/en/projekte/solar-orbiter/metis/`.

Schwenn, R. et al. (1990). *Physics of the inner heliosphere*. Physics and chemistry in space Bd. 20. Springer-Verlag. ISBN: 9783540520818. URL: `http://books.google.de/books?id=LrqxAAAAIAAJ`.

Sie, D. (Oct. 2011). *EPT Demo Model Functionality Test*.

Simpson, J. A. (1983). “Elemental and Isotopic Composition of the Galactic Cosmic Rays”. In: *Annual Review of Nuclear and Particle Science* 33, pp. 323–382. DOI: `10.1146/annurev.ns.33.120183.001543`.

Solar Orbiter Team (Oct. 2011). *Experiment Interface Document Part A*.

Sullivan, J.D. (1971). “Geometric factor and directional response of single and multi-element particle telescopes”. In: *Nuclear Instruments and Methods* 95.1, pp. 5 – 11. ISSN: 0029-554X. DOI: `10.1016/0029-554X(71)90033-4`. URL: `http://www.sciencedirect.com/science/article/pii/0029554X71900334`.

Terrier, R. (2011). *Introduction to High energy Astrophysics.* `http://npac.lal.in2p3.fr/2012-2013/Cours/Astroph/lecture4.pdf`.

Thomson, W. (1856). “On the Electro-Dynamic Qualities of Metals:–Effects of Magnetization on the Electric Conductivity of Nickel and of Iron”. In: *Proceedings of the Royal Society of London* 8, pp. 546–550. DOI: `10.1098/rspl.1856.0144`. eprint: `http://rspl.royalsocietypublishing.org/content/8/546.full.pdf+html`. URL: `http://rspl.royalsocietypublishing.org/content/8/546.short`.

Tsurutani, B. T. et al. (Nov. 1997). “Some basic concepts of wave-particle interactions in collisionless plasmas”. In: *Reviews of Geophysics* 35, pp. 491–501. DOI: `10.1029/97RG02200`.

Tylka, A. J. et al. (Dec. 1997). “CREME96: a revision of the Cosmic Ray Effects on Micro-Electronics code”. In: *IEEE Transactions on Nuclear Science* 44, pp. 2150–2160. DOI: `10.1109/23.659030`.

Wimmer-Schweingruber, R. F. et al. (2010). “The Energetic Particle Detector Suite for Solar Orbiter”. In: *38th COSPAR Scientific Assembly.* Vol. 38. COSPAR Meeting, p. 3013.

Yamada, Masaaki et al. (Mar. 2010). “Magnetic reconnection”. In: *Rev. Mod. Phys.* 82 (1), pp. 603–664. DOI: `10.1103/RevModPhys.82.603`. URL: `http://link.aps.org/doi/10.1103/RevModPhys.82.603`.

Yao, W.-M. et al. (2006). “Review of Particle Physics”. In: *Journal of Physics G* 33, pp. 1+. URL: `http://pdg.lbl.gov`.

List of Figures

List of Tables

List of Acronyms and Abbreviations

ACE	Advanced Composition Explorer
AD	Analog Digital
ADC	Analog Digital Converter
AMR	Anisotropic Magnetoresistance
ASCII	American Standard Code for Information Interchange
Bi	Bismuth
BNC	Bayonet Neill Concelman / Bayonet Nut Connector / British Naval Connector
CAD	Computer Aided Design
CE	Conversion Electron
CIR	Corotating Interaction Region
CME	Coronal Mass Ejection
CREME96	Cosmic Ray Effects on Micro-Electronics Code 96
DC	Direct Current
EMMA	EPT Magnetic Field Mapping App
EPD	Energetic Particle Detector
EPT	Electron Proton Telescope
ESA	European Space Agency
ESRF	European Synchrotron Radiation Facility
EUI	Extreme Ultraviolet Imager
EUV	Extreme Ultraviolet

Geant4	Geometry and Tracking 4
GOES-11	Geostationary Operational Environmental Satellite 11
HET	High Energy Telescope
ICME	Interplanetary Coronal Mass Ejection
IMF	Interplanetary Magnetic Field
LET	Low Energy Telescope
LS	Leibnizstrasse
MAG	Magnetometer
MAG IBS	Magnetometer Inboard Sensor
MAG OBS	Magnetometer Outboard Sensor
METIS	Multi Element Telescope for Imaging and Spectroscopy
MIPS	Minimum Ionizing Particles
NASA	National Aeronautics and Space Administration
NIST	National Institute of Standards and Technology
NuDat2	Nuclear Structure and Decay Data 2
OS	Operating System
PHI	Polarimetric and Helioseismic Imager
PIPS	Passivated Ion-Implanted Silicon
RPW	Radio and Plasma Waves
SAMPEX	Solar Anomalous & Magnetospheric Particle Explorer
SEP	Solar Energetic Particle
SEPT	Solar Electron Proton Telescope
SDK	Software Development Kit

SIS	Suprathermal Ion Spectrograph
SoloHI	Solar Orbiter Heliospheric Imager
SPI	Serial Peripheral Interface
SPICE	Spectral Imaging of the Coronal Environment
SSD	Solid State Detector
STEIN	SupraThermal Electrons, Ions, & Neutrals
STEREO	Solar Terrestrial Relations Observatory
STIX	Spectrometer/Telescope for Imaging X-rays
SWA	Solar Wind Plasma Analyser
USB	Universal Serial Bus

Index

Danksagung

Zunächst möchte ich Herrn Prof. Dr. Robert F. Wimmer-Schweingruber für die Vergabe des Themas und für die sehr gute Betreuung danken. Er schaffte es, mich auch in schwierigen Phasen zu motivieren. Er gab mir immer die Freiheit, völlig selbstständig zu arbeiten, war aber bei den aufgetretenen Problemen immer bereit, den Stand der Dinge zu diskutieren und neue Denkanstöße zu geben.

Zudem möchte ich mich bei den Mitarbeitern der beiden Arbeitsgruppen von Herrn Prof. Dr. Wimmer-Schweingruber und von Herrn Prof. Dr. Heber für das angenehme und produktive Arbeitsklima bedanken. Hervorheben möchte ich dabei die beiden Doktoren Jan Köhler und Lars Berger, die stets bereit waren, mir bei auftretenden Schwierigkeiten zu helfen und die viel fachliches Wissen für mich übrig hatten.

Zusätzlichen Dank gebührt dem gesamten Solar Orbiter-Team dafür, dass ich ein Teil dieses aufregenden Projektes sein durfte. Besonderer Dank gilt dabei Dipl.-Ing. Lars Seimetz, der stets geduldig und verständnisvoll mir jeden Wunsch bezüglich CAD-Zeichnungen erfüllte und auch sonst mir jederzeit mit Rat und Tat zur Seite stand. Bedanken möchte ich mich bei Dipl.-Ing. Björn Schuster für die fruchtbare und spannende Zusammenarbeit bei der Entwicklung der EMMA-Box und bei Dr. Sönke Burmeister für die fachliche und organisatorische Unterstützung bei der Entwicklung der Magnetsysteme und von EPT im Allgemeinen. Besonderer Dank gilt auch Dipl.-Phys. Dennis Sie für die gemeinsame Arbeit am EPT-Demomodell und für seine ersten Funktionstests damit.

Für das Korrekturlesen dieser Arbeit möchte ich mich bei Dipl.-Phys. Christoph Terasa, Dipl.-Phys. Christian Drews und Dipl.-Phys. Dennis Sie bedanken.

Ganz besonders möchte ich mich bei meiner Familie bedanken: bei meinen Eltern und meinem Bruder Bernd, die mich stets unterstützt und immer an mich geglaubt haben.

Zu guter Letzt danke ich vor allem Julie, ohne die ich das alles nicht geschafft hätte.

Eidesstattliche Versicherung

Hiermit versichere ich an Eides statt, dass ich die vorliegende Arbeit abgesehen, vom Rat meiner akademischen Lehrer, ohne fremde Hilfe und lediglich unter der Verwendung der angegebenen Literatur sowie den bekannten Nachschlagewerken der Naturwissenschaften angefertigt habe, und sie nach Inhalt und Form meine eigene ist. Diese Arbeit ist unter Einhaltung der Regeln guter wissenschaftlicher Praxis entstanden.
Des weiteren versichere ich, dass diese Arbeit weder ganz noch teilweise an anderer Stelle zur Prüfung vorlag. Frühere Promotionsversuche wurden von mir nicht vorgenommen.

Kiel, den

Rolf Paspirgilis